THE UNIVERSITY OF CHICAGO

NON-EQUILIBRIUM AND HETEROGENEOUS DYNAMICS IN COLLOIDAL SUSPENSIONS

A DISSERTATION SUBMITTED TO
THE FACULTY OF THE PRITZKER SCHOOL OF MOLECULAR ENGINEERING
IN CANDIDACY FOR THE DEGREE OF
DOCTOR OF PHILOSOPHY

BY
HONGRUI HE

CHICAGO, ILLINOIS
JUNE 2025

ABSTRACT

The upgrade of 4th-generation synchrotrons has significantly enhanced X-ray coherence and flux, enabling techniques like X-ray Photon Correlation Spectroscopy (XPCS) to achieve unprecedented sensitivity. These advancements facilitate the investigation of structural dynamics across previously inaccessible time and length scales, providing new opportunities to explore complex dynamical systems. However, fully leveraging these upgrades remains challenging due to limitations in the theoretical framework for data analysis, as existing methods often distort or average out crucial dynamical information.

To address this, we developed the transport coefficient approach, which integrates internal and external forces within a Markov chain framework and introduced a universal transport coefficient to characterize microscopic dynamics. This approach is further extended to describe complex dynamics exhibiting non-Gaussian characteristics. We validate our framework using experimental and simulated systems that display non-equilibrium and non-Gaussian behavior, including relaxation, yielding, and cage confinement in colloidal suspensions. The results, including the derived transport coefficient, $J(t)$ and other relevant physical parameters, align with previous observations while offering a more detailed characterization of the underlying dynamics.

By combining this refined approach with high-coherence X-rays, we enable direct experimental studies of transient rheological phenomena. Specifically, we focus on yielding¯the transition from a solid to a liquid-like state under deformation. This fundamental process plays a central role in numerous natural and industrial applications and has been extensively explored through theoretical and simulation studies. However, experimental validation has been limited due to instrumentation challenges and system complexity, leaving critical knowledge gaps.

Using Rheo−SAXS−XPCS combined with fast lubrication dynamics (FLD) simulations, we investigate yielding transitions in colloidal suspensions, revealing time-resolved insights

into particle dynamics and structural evolution. Our study finds that repulsive suspensions yield uniformly, exhibiting Andrade-like deformation with minimal structural changes. In contrast, attractive suspensions display complex rheological behaviors, including shear banding, dynamic heterogeneity, and delayed yielding, driven by transient dynamics at shear band interfaces. These results highlight the critical role of interaction potentials in governing the yielding process, showing how attractive forces promote shear band formation and interface instability, which significantly influence macroscopic rheological response during the yielding process.

Throughout these studies, the developed approach also reveals its limitations in capturing more complex dynamics, such as memory effects, cooperative dynamics, and structure–dynamics coupling. As an outlook, future efforts should focus on explicitly incorporating these effects into the model framework. In this regard, artificial intelligence and machine learning hold significant potential for uncovering hidden patterns and enhancing the predictive capabilities of the analysis. By advancing both experimental and analytical methodologies in XPCS, this study enhances the scientific potential of next-generation synchrotrons, addressing the growing demand for high-resolution dynamical studies in soft matter and disordered materials.

To those whose track we have followed and those who will follow ours

"Thus, I have recorded it and passed it down to future generations. Scholars who appreciate antiquity will surely supplement it further."

– *Zhao Mingcheng, Introduction to the "Catalogue of Bronze and Stone Inscriptions"*

TABLE OF CONTENTS

LIST OF FIGURES x

LIST OF TABLES xxii

LIST OF VARIABLES xxiii

ACKNOWLEDGMENTS xxvii

1 OVERVIEW 1
1.1 Dynamics in Natural Physics and Materials Science 1
1.2 Foundations and Developments in the Study of Dynamics 3
1.2.1 Non-Equilibrium Dynamics 4
1.2.2 Suspension Dynamics and Rheology 6
1.2.3 Computation Modeling 7
1.3 Common Methods for Dynamics Measurement 9
1.3.1 Imaging 10
1.3.2 Time-resolved Scattering 10
1.3.3 Correlation Function 13
1.4 X-Ray Photon Correlation Spectroscopy 14
1.4.1 Physics of XPCS 15
1.4.2 XPCS in Synchrotron 17
1.4.3 Analysis Approach in XPCS 18
1.5 Research Objectives and Motivation 20

2 MATHEMATICS AND PHYSICS OF XPCS 23
2.1 Correlation Function in XPCS 23
2.2 Generalized Model: Markov Chain with Gaussian Random Walk 27
2.3 Derivation of $c_1(q, t_1, t_2)$ from Langevin Equation 31
2.4 $c_1(\vec{q}, t_1, t_2)$ in 3-Dimensional Space 37
2.5 $c_1(\vec{q}, t_1, t_2)$ in Homodyne Scattering 44
2.5.1 Generalized Equation for Homodyne Scattering 44
2.5.2 Simplified Equation for Homodyne Scattering 45
2.6 Systems with Multiple-Compositions in Non-Equilibrium 46
2.6.1 $c_2(\vec{q}, t_1, t_2)$ for Heterodyne Scattering with n-Compositions 46
2.6.2 Heterodyne Scattering with 2 Compositions 51
2.6.3 Heterodyne Scattering with 3 compositions 53
2.7 Application in Model Systems 54
2.7.1 Classical Non-Equilibrium Dynamics Model 54
2.7.2 Analysis in Transport Coefficient 59
2.8 Non-Gaussian Dynamics 63
2.8.1 The observed dynamics rate 65
2.8.2 Constant Fraction and Static system 68

2.8.3 2 Compositions system . . . 69
2.8.4 q-dependence of $J_{obs}(t)$ . . . 77
2.8.5 Connection to Heterodyne Scattering . . . 79
2.8.6 Multiple Gaussian Model to Extract Dynamics . . . 81

3 TRANSPORT COEFFICIENT APPROACH FOR CHARACTERIZING NON-EQUILIBRIUM DYNAMICS IN SOFT MATTER . . . 86
3.1 Introduction . . . 86
3.2 Materials and Method . . . 91
3.2.1 Sample Preparation . . . 91
3.2.2 Rheo-XPCS . . . 91
3.2.3 $\boldsymbol{J(t)}$ from 3 Classical Langevin Processes . . . 92
3.3 Approach Validation . . . 93
3.3.1 MD Simulation . . . 93
3.3.2 Reported Experiments . . . 96
3.4 Complex Heterogeneity Study . . . 101
3.5 Conclusion . . . 105
3.6 Appendix . . . 106
3.6.1 Formalization of Physical Parameters . . . 106
3.6.2 Molecular Dynamics Simulation . . . 109
3.6.3 Correlating Microscopic Dynamics with Macroscopic Rheology through transport coefficient ($J(t)$) in combined X-ray Photon Correlation Spectroscopy (XPCS) and *in situ* Rheology (Rheo-XPCS) . . . 111
3.6.4 Microscopically Heterogeneous Dynamics . . . 115
3.6.5 Fitting Results and Residual for Figures in main text . . . 118

4 BRIDGING MICROSCOPIC DYNAMICS AND RHEOLOGY IN THE YIELDING OF CHARGED COLLOIDAL SUSPENSIONS . . . 122
4.1 Introduction . . . 122
4.2 Results . . . 123
4.2.1 Microscopic Mechanisms Driving Yielding . . . 123
4.2.2 Microscopic Mechanisms Driving Yielding . . . 127
4.2.3 Heterogeneity in Yielding Dynamics . . . 132
4.3 Discussion . . . 134
4.3.1 Materials and Methods . . . 136
4.3.2 Simulation . . . 138
4.3.3 Characterization . . . 139
4.4 Appendix . . . 142
4.4.1 NMR Result . . . 142
4.4.2 TGA Result . . . 143
4.4.3 Static Structure and Dynamics Measurement . . . 144
4.4.4 Burger Model Fitting . . . 148
4.4.5 Zeta Potential . . . 149
4.4.6 Structure in Creep Test . . . 150

4.4.7 Analysis of second order two-time intensity autocorrelation function ($c_2(\vec{q}, t_1, t_2)$) in all directions . . . 153
4.4.8 Resolidification . . . 160
4.4.9 Delayed Yielding After Resolidification . . . 161
4.4.10 Supplementary Simulation Movies . . . 162

5 EXPLORING NON-GAUSSIAN DYNAMICS DURING YIELDING OF CHARGED COLLOIDAL SUSPENSIONS . . . 164
5.1 Introduction . . . 164
5.2 Complex Dynamics during Yielding . . . 166
5.3 Extended Transport Coefficient Approach for Simple and Homogeneous non-Gaussian Dynamics . . . 170
5.3.1 Anomalous Diffusion . . . 171
5.3.2 Cage Dynamics . . . 176
5.4 Discussion and Conclusion . . . 181
5.5 Appendix . . . 183
5.5.1 Comparison of Extracted and Reference $J(t)$ for Cage Dynamics Analyzed in Fig. 5.4 . . . 183
5.5.2 The residual of fitting from analysis in Fig. 5.4 and Fig. 5.3 . . . 184

6 OUTLOOK . . . 189
6.1 Memory Effect . . . 189
6.2 Cooperative Dynamics (cooperative dynamics (Co-Dyn)) . . . 190
6.3 Structure-Dynamics Coupling . . . 193
6.3.1 Generalized Space-Time Correlation Function . . . 194
6.4 Future Challenges in Analysis . . . 196
6.4.1 Theoretical Challenges in Modeling Memory Effects . . . 196
6.4.2 Limitations in the Description of cooperative rearrangement regions (CRR) . . . 197
6.4.3 Understanding the Space-Time Correlation . . . 198
6.5 Possible Solution: AI-Driven Method . . . 199
6.6 Closing Remarks . . . 201

REFERENCES . . . 202

LIST OF FIGURES

1.1 **Phase map of spatiotemporal techniques accessing the dynamic** [1] XPCS is a powerful technique that could cover the dynamics study in a small time and length scale. 12

2.1 **Simulation for Wiener Process / Standard Diffusion with $D = 1$ and $x_0 = 0$.** a) $P(x, t)$ represents the probability density function as time evolves. b) The figure illustrates the two-time correlation function, $c_2(q = 1, t_1, t_2)$. c) $J(t)$ is the transport coefficient described in this work. In such an equilibrium state, the dynamical transport coefficient $J(t) = 2D$ is independent of time. 60

2.2 **Simulation for Ornstein–Uhlenbeck Process with $D = 1$, $\gamma = 0.5$, $v_o = -1$ and $x_0 = 3$.** The dynamical transport coefficient $J(t) = 2D(1 - \mathrm{e}^{-\gamma t})^2$. 61

2.3 **Simulation for underdamped Brownian Oscillator with $D = 10$, $\gamma = 0.5$, $\omega_o = 1.1$, $v_o = 1$ and $x_0 = 3$.** 61

2.4 **Simulation for overdamped Brownian Oscillator with $D = 1$, $\gamma = 1.1$, $\omega_o = 0.5$, $v_o = 1$ and $x_0 = 3$.** 62

2.5 **Illustration of Non-Equilibrium Analysis Applied to a case of Non-Gaussian Dynamics.** Given by Eq. 2.163, the probablity density function (PDF) of non-Gaussian dynamics is a blend of two Gaussian dynamics, with its influence adjusted by a factor of f, as illustrated in panels A ($f = 0$), C($f = 0.5$), and E ($f = 1$). The first order two-time intensity autocorrelation function ($c_1(\vec{q}, t_1, t_2)$) at $q = 1.25$ corresponding to the non-Gaussian dynamics is computed by Eq. 2.13 and shown in upper left in panels B, D, and F. The results from the non-equilibrium approach on the $c_1(\vec{q}, t_1, t_2)$ is shown in lower right in panels B, D, and F. In panel F, the presence of noise and discontinuity in $c_1(\vec{q}, t_1, t_2)$ can be attributed to numerical resolution issues arising from the division operation involving small numbers in Eq. 2.13. 76

2.6 **Comparison between $J_{obs}(t)$ obtain from the non-equilibrium analysis (scattered dots) and the calculated by Eq. 2.164 (solid line)**. The consistency between J_{obs} demonstrates the validation of Eq. 2.148. Meanwhile, the influence of fraction (f) on the $J_{obs}(t)$ is also explored. The variation of f is represented by a color gradient of $J_{obs}(t)$, with the accompanying color bar mapping the evolution of the system dynamics from $f = 0$ to $f = 1$. 77

2.7 **Exploration of the influence of scattering vector (q) on the $J_{obs}(t)$ with $f = 0.5$.** The variation of q is represented by a color gradient of $J_{obs}(t)$, with the accompanying color bar mapping the evolution of the system dynamics from $q = 0$ to $q = 10$. 79

2.8 **Illustration of the proposed approach for extracting $S(q,t)$ to characterize non-Gaussian dynamics, exemplified by cage dynamics. A).**The simulated $c_2(\vec{q},t_1,t_2)$ at $q=6$ from the reference function, shown in the upper triangle, is analyzed by Eq. 2.131 with 2 Gaussian function, and the fitting results are shown in the lower triangle. **B).** The obtained parameters allow the reconstruction of the $S(q,t)$ at $q=6$. **C).** By analyzing many $c_2(\vec{q},t_1,t_2)$ from a range of q, the entire $S(q,t)$ varying q and t can be mapped out. The consistency between the reference and fitting results in both $c_2(\vec{q},t_1,t_2)$ and $S(q,t)$ indicates that this approach is not only compatible with analyzing the non-Gaussian dynamics observed in XPCS, but also capable of extracting genuine physical information from the dynamic process. 82

2.9 **Fitting results of simulated standard diffusion (upper triangle) using Eq. 2.135 with $n=1$.** The consistency between the simulated data (upper triangle) and the fitted $c_2(\vec{q},t_1,t_2)$ (lower triangle) indicates that the equation accurately describes the dynamic process of standard diffusion. The analyzed results are extracted to map out $S(q,t)$ in Fig. 2.10. 84

2.10 **Comparison between the PDF and $S(q,t)$ from direct computation as a reference to the analyzed results. A)** The PDF is obtained by directly computing the coordinates of the particles in the simulation boxes. It is then converted to $S(q,t)$ via a Fourier transform and plotted as a solid line in **B)**. The analyzed results of $S(q,t)$ as dashed line are closely match these reference values, with some discrepancies in the low-q regions. This is due to an insufficient number of intensity sample pixels, leading to a bias in $c_2(\vec{q},t_1,t_2)$ as a statistical property. 85

3.1 **Illustration of the XPCS experiment procedure and its analysis techniques in both equilibrium and non-equilibrium states.** (A) In a standard XPCS experiment, coherent X-rays illuminate the samples, generating speckles that reveal the spatial distribution of particles on detectors. Dynamic information about the system is obtained by calculating the temporal correlation function c_2 of these speckles, which is then converted to a one-time correlation function g_2 by averaging. Depending on whether the system is in equilibrium or not, the analysis procedure to convert from c_2 to g_2 varies: In the equilibrium case (B), g_2 (inserted figure) can be obtained by diagonally averaging c_2 at increasing value of τ (gray line); in contrast, in the non-equilibrium system (C), g_2 (inserted figure) can only be obtained by averaging c_2 within the predefined time-translation invariant zones (TIZs) (gray rectangle), where the system is assumed to be pseudo-equilibrium for a certain period within the TIZs. The color of g_2 in the inserted figure corresponds to the TIZs with lighter colors at an earlier time. (D) We introduced a transport coefficient approach to obtain the time-resolved dynamics directly by fitting c_2 without any averaging. As a result of this analysis, Γ represents the characteristic dynamics rate of the system, and its expression depends on the specific system under study. For standard diffusion, it is defined as $\Gamma = q^2 D$ in equilibrium (blue line) and $\Gamma(t) = \frac{1}{2} q^2 J(t)$ in a non-equilibrium state, where D is the diffusion constant, and $J(t)$ is the transport coefficient, as defined in Eq. 2.42. The results obtained from our newly developed non-equilibrium analysis approach (red line) offer enhanced detail and higher resolution in the time-resolved dynamics compared to conventional TIZs approaches (orange line). 90

3.2 **Simulation of a non-equilibrium system arising from temperature changes and application of transport coefficient analysis to $c_2(\vec{q}, t_1, t_2)$ extracted from different $\vec{q}$ bins.** c_2 data is extracted from three bins: (A) $\big(q_x = 6, q_y = q_z = 0\big)$, (B) $\big(q_x = q_y = 6, q_z = 0\big)$, and (C) $\big(q_x = q_y = q_z = 6\big)$. Each c_2 data set includes fitting results (lower right corner) and corresponding molecular dynamics (MD) simulation data (upper left corner) displayed on opposite sides of the diagonal. (D) Show the transport coefficient extracted through the analysis in these 3 bins, $J_x(t)$ (blue line), $J_{q_{x,y}=6}(t)$ (orange line), and $J_{q_{x,y,z}=6}(t)$ (green line), together with the J_{MD} (purple line) calculated directly from the positions of the particles in the simulation box using Eq. 2.42. The right-hand red axis illustrates the temperature variation (red line) throughout the simulation. 95

3.3 **Verification of the transport coefficient approach using experimental results from previous works.** (A) Examination of relaxation dynamics in a silica particle suspension reported in Donley et al.'s Rheo-XPCS measurement [2], and (B) corresponding results for $J(t)$ (blue line) presented in both linear-log and log-log scales (insert). The orange dots denote shear ($\dot{\gamma}(t)$) simultaneously measured from the rheometer. In the linear-log plot, the black dashed line represents the intrinsic diffusion rate (D_o) of the system under equilibrium conditions, measured at 3.1^2/s. In the log-log plot, the black solid segment depicts the trend of $J(t) \sim |\dot{\gamma}(t)| \sim t^{-1.586\pm0.003}$, serving as a visual reference. (C) and (D) Application of this non-equilibrium analysis to a gel system subjected to mechanical perturbation, as discussed in the work of Song et al. [3]. In (D), the blue line depicts the $J(t)$ derived from the non-equilibrium analysis, while the orange line indicates the smoothed $J(t)$, highlighting the relaxation trends. The avalanche dynamics are identified by a white arrow in (C), signifying an abrupt decrease followed by a rapid recovery of correlation within $c_2(\vec{q}, t_1, t_2)$. Concurrently, a black arrow in (D) marks a notable spike in $J(t)$at $t = 560s$, corresponding to the observed avalanche event. Trajectories of $\mathbb{P}(r - \mathbb{E}[r], t)$ are depicted in the inset figure at different time points: $t = 400$ s (blue line), 800 s (cyan line), 1200 s (green line), 1600 s (orange line), and 2000 s (red line), assuming δ-function at $t = 0$. In Figures A) and C), the experimental data is displayed in the upper left corner, while the fitting results are presented in the lower right corner. 97

3.4 **Application of the transport coefficient approach to a charged particle suspension undergoing shear band transitions during a creep test.** (A) Observation (upper left corner) and analysis (lower right corner) of multiple shear bands in c_2 at flow direction ($\phi = 6.3^o$) for a suspension comprising spherical silica particles surface-functionalized by L-glutathione (SiO_x-GSH) particles in a mixed salt solution (60 mM sodium nitrate ($NaNO_3$) and 10 mM magnesium sulfate ($MgSO_4$)) under constant stress of 25 Pa. The fitting results of $c_2(\vec{q}, t_1, t_2)$ in other ϕ direction are shown in Fig. 3.12 of the Appendix (App). Insets in the upper and lower corners illustrate the oscillatory features in c_2 resulting from three shear bands. (B) Comparison between rheological measurements and analysis results using the multiple-banding model. The top-to-bottom rows show changes over time in various physical parameters, including compliance (creep compliance ($\mathcal{J}(t)$)), the velocity at the outer edge of the rotor (v_{Edge}), transport coefficient $J(t)$, and fraction x_n. These measurements are obtained through direct rheological measurements (black circular markers) and non-equilibrium analysis in XPCS (solid lines), providing insights into the system's dynamics at macro and micro scales, respectively. Within the XPCS measurements, the blue, orange, and green lines specifically track the evolution of the slow, fast, and static bands in the shear banding. To facilitate a more meaningful comparison between the velocity of each band obtained from XPCS and the shear rate $\dot{\gamma}(t)$ measured by the rheometer, $\dot{\gamma}(t)$ is converted to the velocity at the outer edge of the rotor (v_{Edge}) using the equation $v_{Edge}(t) = \dot{\gamma}(t)h$. 103

3.5 **Application of the model analysis on a simulated non-equilibrium system reveals three distinct stages of temperature change, which are visually represented by the filled-in background color.** 111
3.6 **Comparative Analysis of the $J(t)$ and the $\dot{\gamma}(t)$ During the Recovery Phase of Creep Tests.** Panels A and B illustrate the relationship between $J(t)$ and $\dot{\gamma}(t)$ under an applied stress ($\sigma(t)$) of 10 Pa, while Panels C and D show the same under a $\sigma(t)$ of 100 Pa (also shown in Fig 3 A and B in the main texts). From Panels B and D, a consistent scaling relation of $\frac{k_B T}{\pi r}$ is observed between $J(t)$ and $\dot{\gamma}(t)$, independent from the applied $\sigma(t)$ in the creep test. 112
3.7 **The connection between microscopic dynamics ($J(t)$) and macroscopic properties ($\dot{\gamma}(t)$) in the recovery phase of creep tests with $\sigma(t)$ of 10Pa (blue) and 100Pa (red)**. The $J(t)$ (solid line) is derived from non-equilibrium analysis on $c_2(\vec{q}, t_1, t_2)$ measured by XPCS, and the $\dot{\gamma}(t)$ obtained from the rheometer, then scaled by a factor of $\frac{k_B T}{\pi r}$ (scattered dots), is measured from rheometer. For a better comparison, the unit for both $J(t)$ and $\dot{\gamma}(t)$ have been converted to International System of Units (S.I. Units) 114
3.8 **Illustrating microscopically heterogeneous dynamics during recovery**: By subtracting the diffusive dynamics attributed to $c_2(\vec{q}, t_1, t_2)$ based on the non-equilibrium model (Panel. A, lower right) from experimental $c_2(\vec{q}, t_1, t_2)$ measurements (Panel. A, upper left), the $c_2(\vec{q}, t_1, t_2)$ serves as evidence of microscopically heterogeneous dynamics in Panel B, indicating interference between at least two compositions with distinct dynamics in the system. The 'tailing' shape of the $c_2(\vec{q}, t_1, t_2)$ is largely attributed to the abrupt halt of a thin flow layer near the rotor during the recovery phase, mirroring the microscopically heterogeneous changes detailed in reference [2]. 116
3.9 **Illustration of the fitting results (Panels A, C, E) and residuals (Panels, B, D, F) obtained after the data fitting process shown in Fig. 3.2 of the main manuscript.** The R^2 of the fitting is shown in the title of the residual plot. 118
3.10 **Illustration of the fitting results (Panel. A) and residuals (Panel. B) obtained after the data from the [2] fitting process shown in Fig. 3.3A of the main manuscript.** The R^2 of the fitting is shown in the title of the residual plot. 119
3.11 **Illustration of fitting results (Panel. A) and residuals (Panel. B) obtained after the data from [3] fitting process shown in Fig. 3.3C of the main manuscript.** The R^2 of the fitting is shown in the title of the residual plot.119
3.12 **Comprehensive $c_2(\vec{q}, t_1, t_2)$ data across all ϕ directions from Fig. 3.4 of the manuscript.** The angle ϕ, corresponding to each bin on the field detector, is marked in the title of each panel for reference. One shown in Fig 4 of the main text is at $\phi = 6.3^o$. 120

3.13 **Presentation of the residuals resulting from the analysis conducted in CFigfig:Application of the manuscript, encompassing all ϕ directions.** The angle ϕ, corresponding to each bin on the field detector, is marked in the title of each panel for reference. 121

4.1 **Effect of interaction potential on yielding behavior.** (**A**) In charged colloidal suspensions of 116 nm spherical silica particles surface-functionalized by L-cysteine (SiO_x-Cys), changes in the interaction potential significantly affect yielding behavior through particle transport dynamics. (**B**) SAXS confirms the structural changes and potential shifts. (**C**) Two-Yukawa potentials and corresponding structure factors (inset) illustrate the transition from repulsive to attractive interactions upon adding $NaNO_3$. (**D**) The repulsive suspension exhibits classical Andrade yield behavior, where strain increases with an exponent of $\frac{1}{3}$, as the solid black line depicts. (**E**) The addition of salt induces complex rheological responses following a pre-yield behavior similar to that of the repulsive system, depicted by the solid black line. These include shear banding, delayed yielding, and resolidification, as the interaction potential evolves. 126

4.2 **combining Small Angle X-ray Scattering (SAXS), XPCS, and *in situ* rheology (Rheo-SAXS-XPCS) analysis of yielding in repulsive and attractive SiO_x-Cys suspensions.** (**A**) Flow-direction $c_2(\vec{q}, t_1, t_2)$ for the repulsive suspension during Andrade creep. (**B**, **C**, **D**) Flow-direction $c_2(\vec{q}, t_1, t_2)$ for the 100 mM $NaNO_3$ suspension under creep tests at constant stresses of 100 Pa, 110 Pa, and 120 Pa, respectively. In each panel, the upper triangle shows experimental data, and the lower triangle presents the corresponding fitted results. (**E**) Time-dependent physical parameters from rheometer measurements (markers) and XPCS analysis (solid lines) for the repulsive suspension, including shear rate ($\dot{\gamma}$), velocity at the rotor (v_{Edge}), transport coefficient (J), and fraction (x_s). (**F**, **G**, **H**) Corresponding parameters for the 100 mM $NaNO_3$ suspension. . . . 129

4.3 **FLD simulations of repulsive and attractive colloidal suspensions during creep tests.** (**A**) Repulsive colloidal suspensions exhibit homodyne scattering signals in $c_2(\vec{q}, t_1, t_2)$, corresponding to (**B**) laminar flow. (**C**) The spatial distribution of non-affine displacements (Δx_{na}) is uniform, and (**D**) its magnitude follows a Gaussian distribution. (**E**) In salted suspensions with attractive interactions, heterodyne scattering signals in $c_2(\vec{q}, t_1, t_2)$ are observed due to (**F**) shear banding, where particles flow at two distinct velocities. (**G**) The spatial distribution of Δx_{na} becomes heterogeneous, with large displacements localized at the band interface. (**H**) The Δx_{na} magnitude deviates from Gaussian behavior, exhibiting a broader, non-Gaussian distribution caused by turbulent particle motion at the interface. 131

4.4 **Microscopic mechanisms underlying complex rheological behaviors during yielding.** (**A**) Simulated creep tests replicate key rheological phenomena, including delayed yielding and resolidification, in agreement with experimental results. (**B**) Quantitative consistency between simulated and experimental physical parameters confirms the accuracy of the simulation in representing the experimental system. (**C**) Particle trajectories highlight the critical role of the interfacial junction between shear bands in governing the overall rheological response and driving behaviors such as pre-yielding, delayed yielding, and resolidification. . . 134
4.5 **NMR analysis of SiO_x-Cys.** The characteristic peaks corresponding to L-cysteine (CYS) are labeled as D and E. 142
4.6 **TGA analysis of SiO_x-Cys to determine the composition and grafting density.** The results show that 2.3% of cysteine is grafted onto the particle surface, with 2.7% water content. 143
4.7 **Small Angle X-rays Scattering (SAXS) and $c_2(\vec{q}, t_1, t_2)$ results for structural and dynamic characterization.** (**A**, **B**) 2D SAXS patterns are azimuthally integrated to obtain 1D profiles, with experimental data represented as markers in Fig. 4.1. (**C**, **D**) Dynamics are analyzed by calculating $c_2(\vec{q}, t_1, t_2)$ (Eq. 4.1) from 2D SAXS data. The equilibrated state allows for the calculation of second order one-time intensity autocorrelation function ($g_2(\vec{q}, \tau)$) through averaging, which is then used to obtain $c_2(\vec{q}, t_1, t_2)$. (**E**) The $g_2(\vec{q}, \tau)$ function is fitted with a stretched exponential to extract the relaxation time. The introduction of attractive potentials promotes the formation of internal structures, as indicated by the increased low-q intensity in SAXS profiles and longer particle relaxation times. 145
4.8 **Simulated SAXS profiles using the two-Yukawa potential for repulsive (A) and attractive (B) suspensions.** The results illustrate the shift in interparticle interactions from purely repulsive to attractive with the addition of salt. 146
4.9 **Comparison of experimental (solid lines) and simulated (dashed lines) structure factors for repulsive (A) and attractive (B) suspensions.** The good agreement confirms that the simulations effectively capture the interparticle interactions and structural features of both systems. 146
4.10 **Shear ramp measurement and modeling with Herschel–Bulkley for suspensions with attractive and repulsive interactions. (A)** Shear ramp measurements for an aqueous suspension with a repulsive potential (blue) and a salted suspension with an attractive potential (red). The addition of salt induces rheological hysteresis, as the potential changes from a repulsive to an attractive interaction potential. **(B)** The stress-shear relationship for the repulsive suspension is fitted using the Herschel–Bulkley model, where the ramp-up measurement gives a static yield stress of 24.3 Pa, and the ramp-down measurement gives a dynamic yield stress of 32.7 Pa. The close consistency between these two values indicates that the repulsive suspension behaves as a simple yielding fluid. 147

4.11 **Creep response of a repulsive suspension fitted using the Burger model.** The fitting closely matches the experimental data, indicating that the Burger model effectively captures the creep behavior under applied stress. As stress increases, the response shifts from elastic to viscous dominance. 148
4.12 **Zeta potential measurements show that the particles are negatively charged, with a monodisperse distribution centered at -31.8 mV.** . . . 149
4.13 **Flow-direction and azimuthal SAXS profiles were measured during creep tests for both repulsive and attractive suspensions.** The agreement between the flow-direction and azimuthal profiles confirms the isotropic and amorphous nature of the system. Furthermore, the lack of significant changes in the SAXS profiles suggests minimal structural evolution under creep conditions. 150
4.14 **(A) Creep test results for aqueous suspensions simulated under stress levels ranging from 0.1 to 0.4.** The black solid line indicates a strain increase following a power-law relationship, $\gamma \sim t^{\frac{1}{3}}$, corresponding to a shear rate scaling as $\dot{\gamma} \sim t^{-\frac{2}{3}}$. This behavior aligns with the characteristics of Andrade creep. (B) Structure factor evolution during the creep test. The test duration is divided into five equal intervals, with structure factors averaged within each interval. The color of each structure factor corresponds to the midpoint of the respective interval, as shown in Panel A. The results confirm the absence of significant structural changes throughout the creep test. 151
4.15 **(A) Simulated creep tests of salted suspensions under stress levels ranging from 1.1 to 1.4.** (B) Structure factors calculated during the creep tests, with the test duration divided into five equal intervals. Each structure factor is averaged over its respective interval, and the colors correspond to the midpoint of each interval as shown in Panel A. The results indicate that no significant structural changes occurred throughout the creep test. 152
4.16 $c_2(\vec{q}, t_1, t_2)$ **functions for SiO_x-Cys in aqueous suspension under a stress of 20 Pa, presented for all directions.** Experimental results are shown in the upper corners of each panel, while the corresponding fitting results are displayed in the lower corners. 154
4.17 $c_2(\vec{q}, t_1, t_2)$ **functions for SiO_x-Cys in aqueous suspension under a stress of 25 Pa, presented for all directions.** Experimental results are shown in the upper corners of each panel, while the corresponding fitting results are displayed in the lower corners. 155
4.18 $c_2(\vec{q}, t_1, t_2)$ **functions for SiO_x-Cys in aqueous suspension under a stress of 30 Pa, presented for all directions.** Experimental results are shown in the upper corners of each panel, while the corresponding fitting results are displayed in the lower corners. 156
4.19 $c_2(\vec{q}, t_1, t_2)$ **functions for SiO_x-Cys in a 100 mM $NaNO_3$ solution under a stress of 100 Pa, shown for all directions.** Experimental results are displayed in the upper corners of each panel, with the corresponding fitting results in the lower corners. 157

4.20 $c_2(\vec{q}, t_1, t_2)$ **functions for SiO_x-Cys in a 100 mM $NaNO_3$ solution under a stress of 110 Pa, shown for all directions.** Experimental results are displayed in the upper corners of each panel, with the corresponding fitting results in the lower corners. 158
4.21 $c_2(\vec{q}, t_1, t_2)$ **functions for SiO_x-Cys in a 100 mM $NaNO_3$ solution under a stress of 120 Pa, shown for all directions.** Experimental results are displayed in the upper corners of each panel, with the corresponding fitting results in the lower corners. 159
4.22 **Rheo-SAXS-XPCS results for spherical silica particles surface-functionalized by N-acetyl cysteine (SiO_x-Nac) during creep tests at applied stresses of 85, 95, and 100 Pa.** Resolidification is observed in all trials, demonstrating that this rheological phenomenon is common in charged colloidal systems. . . . 161
4.23 **Rheo-SAXS-XPCS results for spherical silica particles surface-functionalized by L-cysteine methyl ester (SiO_x-CME) in a creep test at 725 Pa, showing two instances of delayed yielding following resolidification.** 162

5.1 **Illustration of Non-Gaussian Dynamics in the Yielding Process and Their Impact on $c_2(\vec{q}, t_1, t_2)$ Observed in XPCS A)** The mean square displacement (MSD) and $J(t)$ during the three yielding phases—pre-yield, delayed yield, and resolidification (indicated by background colors) are computed using Eq. 2.42 from the PDF shown in Fig. 5.9. **B)** The $c_2(\vec{q}, t_1, t_2)$ (lower triangle) is calculated under the assumption of Gaussian dynamics, using MSD and $J(t)$ in Eq. 2.47. The resulting $c_2(\vec{q}, t_1, t_2)$ significantly deviates from the $c_2(\vec{q}, t_1, t_2)$ obtained directly from simulations using Eq. 2.14, highlighting the breakdown of Gaussian assumption. **C)** To account for non-Gaussian effects, the intermediate scattering function $S(q,t)$ is computed by Fourier transforming the PDF using Eq. 2.12. **D)** The $c_2(\vec{q}, t_1, t_2)$ is then computed from Eq. 2.13 using the refined $S(q,t)$ at $q = 7$ (solid dots at **C)**). This approach improves agreement with simulations by capturing non-Gaussian dynamics. **E)** Incorporating cooperative dynamics due to CRR further refines the $c_2(\vec{q}, t_1, t_2)$ prediction. **F)** Qualitative analysis suggests that two distinct phases of CRR (blue and red box at **E)**) contribute to correlations at high τ values. With both non-Gaussian dynamics and cooperative rearrangements included, the computed $c_2(\vec{q}, t_1, t_2)$ closely matches the simulation results. 168
5.2 **Illustration of incorporating cooperative dynamics into the analysis model improves fitting results and describes the experimental $c_2(\vec{q}, t_1, t_2)$ with higher fidelity. (A)** The $c_2(\vec{q}, t_1, t_2)$ obtained from the experiment (upper triangles) and the fitting results based on the simple transport coefficient approach. Small features in the $c_2(\vec{q}, t_1, t_2)$, such as blocks of $c_2(\vec{q}, t_1, t_2)$ that suddenly appear and disappear, are observed. However, the smooth variations predicted by the simple model fail to capture these transient features. **(B)** By incorporating Co-Dyn, the model provides a better description of the data. It reveals that these correlation blocks originate from a series of Co-Dyn events within CRR (highlighted by magenta squares). 169

5.3 **Illustration of the proposed approach for extracting $S(q,t)$ and MSD from the $c_1(\vec{q},t_1,t_2)$ with $\alpha=\frac{1}{2}$ and $D=1$. A)-C)** The $c_1(\vec{q},t_1,t_2)$ is generated from Eq. 5.6 at $q=0.5$ (**A**), 1 (**B**), and 1.5 (**C**), respectively, and is shown in the upper triangle of the $c_1(\vec{q},t_1,t_2)$. These $c_1(\vec{q},t_1,t_2)$ are analyzed using the approach proposed in Section 2.8.5, and the fitting results are plotted in the lower triangle. The consistency between the simulated and fitted $c_1(\vec{q},t_1,t_2)$ demonstrates the capability of the approach to accurately describe complex patterns. **D)** The extracted results from $c_1(\vec{q},t_1,t_2)$ for different q values ranging from 0 to 20 allow us to map $S(q,t)$ over time, indicating the dynamic changes in anomalous diffusion (Fig. 5.3 **D**). The dynamics mapped by the analysis (solid dot line) closely overlap with the reference $S(q,t)$ (faded light background) given in Eq. 5.6. **E)** By performing cumulative fitting of $S(q,t)$ in a log scale corresponding to $\frac{1}{2}q^2$ (solid line), the time-dependent physical parameters that describe the dynamics can be obtained based on Eq. 2.174. **F)** The linear parameters from a cumulant analysis, specifically MSD and $\mathbb{V}[x(t)]$, are obtained with $\alpha=0.53$ and $D=0.72$, closely matching the input values and demonstrating consistency between the analysis results and the input parameters. The observed inconsistencies might be attributed to the fact that the linear combination of Gaussian functions cannot exactly replicate the PDF of anomalous diffusion under the Riemann-Liouville (RL) operator. 174

5.4 **Illustration of the proposed approach for extracting $S(q,t)$ and MSD from the $c_1(\vec{q},t_1,t_2)$ of cage dynamics. A)-C)** The $c_1(\vec{q},t_1,t_2)$ is generated from Eq. 5.7 at $q=1$ (**A**), 10 (**B**), and 20 (**C**), respectively, and is shown in the upper triangle of the $c_1(\vec{q},t_1,t_2)$. The input parameters are set as $\epsilon=\sigma=0.1$, $\tau_o=1$, and $\tau_R=1$. The $c_1(\vec{q},t_1,t_2)$ are analyzed using the approach proposed in Section 2.8.5, and the fitting results are plotted in the lower triangle. The consistency between the simulated and fitted $c_1(\vec{q},t_1,t_2)$ demonstrates the capability of the approach to accurately describe complex patterns. **D)** The extracted results from $c_1(\vec{q},t_1,t_2)$ for different q values ranging from 0 to 30 allow us to map $S(q,t)$ over time, indicating the dynamic changes in the cage effect (**D**). The dynamics mapped by the analysis (solid scatter dots) closely overlap with the reference $S(q,t)$ (faded light background) given in Eq. 5.7. The mapped-out $S(q,t)$ can be fitted with Eq. 2.174, allowing the extraction of (**E)**) MSD and (**F)**) non-Gaussian parameter (NGP), which are then compared with the reference values. The close agreement between the extracted MSD and NGP with the input values demonstrates consistency between the analysis and the reference. The observed inconsistencies might be attributed to the fact that the linear combination of Gaussian functions cannot exactly replicate the PDF of cage dynamics. 179

5.5 **The transport coefficient $J(t)$ from reference and analysis results of cage dynamics.** The $J\,(t)(t)$ with $\epsilon = \sigma = 0.1$, $\tau_o = 1$, and $\tau_R = 1$, corresponding to the cage dynamics process in Fig. 5.4, is shown as the solid black line based on Eq. 5.11. The input parameters of the dynamics can be extracted and visualized as the transition from the ceiling of $2D$ to the baseline $2D_A$, where τ_R represents the time at which the maximum decay rate is observed. The colored dashed line represents $J_{obs}(t)$, calculated using Eq. 2.148 with parameters obtained from the proposed analysis approach. The behavior of $J_{obs}(t)$ exhibits an initial increase ($1 \leq q \leq 11$) followed by a decrease ($q \geq 11$) as q increases, consistent with the observation that cage dynamics is only prominent within a specific range of q values. 183

5.6 **Residual Analysis as a Function of n in the Gaussian Model for Cage Dynamics.** The residual decreases significantly when two Gaussian functions are used in the fitting of $c_1\,(\vec{q}, t_1, t_2)$ for cage dynamics. However, for $n = 3$ and $n = 4$, the reduction in residual is negligible, indicating that the data is already well-fitted or that additional components may lead to overfitting. Therefore, $n = 2$ is selected as the optimal choice for analyzing the $c_1\,(\vec{q}, t_1, t_2)$ of cage dynamics. This result is also physically reasonable, as it reflects the presence of two distinct dynamic processes in cage dynamics: diffusion inside and outside the cage. 184

5.7 **Residual Analysis as a Function of n in the Gaussian Model for Anomalous Diffusion.** The residual decreases significantly when more functions are used in the fitting of $c_1\,(\vec{q}, t_1, t_2)$ for anomalous diffusion. However, for $n = 4$, the reduction in residual is negligible, indicating that the data is already well-fitted or that additional components may lead to overfitting. Therefore, $n = 3$ is selected as the optimal choice for analyzing the $c_1\,(\vec{q}, t_1, t_2)$ of anomalous diffusion. 185

5.8 **Demonstration of how particle dynamics in the shear banding simulation from Section 4.2.3 deviate from Gaussian behavior over time.** The dashed lines represent the PDF computed at times $t = 1, 100, 200, 300, 400,$ and 500 by analyzing particle coordinates within the simulation boxes. The solid lines correspond to Gaussian fits. The growing discrepancy between the computed PDF and the Gaussian fits illustrates the progressive emergence of non-Gaussian dynamics over time. 186

5.9 **Evolution of the Non-Gaussian Parameter ($\alpha_2(t)$) During the Yielding Process** The $\alpha_2(t)$ is estimated by Eq. 2.176. The background color represents the three phases of the yielding process: pre-yield, delayed yield, and resolidification. The variation of $\alpha_2(t)$ highlights the changes in non-Gaussian characteristics, indicating their contribution to the yielding behavior. 187

5.10 $c_2(\vec{q}, t_1, t_2)$ **in the flow direction with consideration of non-Gaussian dynamics and CRR.** The contribution of CRR to $c_2(\vec{q}, t_1, t_2)$ is present in the flow direction, as indicated by the bright spots in $c_2(\vec{q}, t_1, t_2)$. However, due to the dominant heterodyne effects induced by flow, which manifest as an oscillation pattern, this contribution is less pronounced compared to the $c_2(\vec{q}, t_1, t_2)$ observed in the vorticity direction. 187

5.11 **Applying the non-Gaussian approach to extract dynamic information from yielding simulations. (A)** The non-Gaussian approach is applied to the $c_2(\vec{q}, t_1, t_2)$ from simulations and accurately describes the data. **(B-C)** The intermediate scattering function $S(q, t)$ extracted from the analysis (square dots) closely matches the reference computed directly from PDF of particle coordinates. 188

6.1 **Illustration of Co-Dyn Extraction and Analysis**: **A)** The $c_2(\vec{q}, t_1, t_2)$ for a relaxation process in colloidal suspension is measured from the Rheo-XPCS experiment. **B)** The $c_2(\vec{q}, t_1, t_2)$ attributed to Co-Dyn, $c_{2,\text{Co-Dyn}}$, is extracted using Eq. 6.4. **C)** The change in CRR is obtained by analyzing $c_{2,\text{Co-Dyn}}$ from **B)**. The colors of the lines indicate the individual CRR during the dynamics process, and the black line indicates the sum of all CRR over time. The fitting results of $c_{2,\text{Co-Dyn}}$ and $c_2(\vec{q}, t_1, t_2)$ are shown in the lower triangle in both **A)** and **B)**. Close agreement between $c_2(\vec{q}, t_1, t_2)$ obtained from the experiment and the analysis indicates a good model and successful analysis. 193

6.2 **Illustration of how Co-Dyn is automatically identified and quantified using machine learning (ML). A)** The experimental $c_2(\vec{q}, t_1, t_2)$ (upper triangle) is used as input and fitted (lower triangle) to **B)** a convolutional neural networks (CNN) model for feature extraction, leading to **C)** the identification and prediction of CRR events [4] and their evolution over time. 200

LIST OF TABLES

3.1 $\boldsymbol{J(t)}$ from 3 Classical Langevin Processes. 92

LIST OF VARIABLES

- **Mathematical Operation:**
  - $\mathcal{F}$: Fourier Transform
  - $\mathbb{E}$: Ensemble Average
  - $\mathbb{V}$: Variance of the quantity as $\mathbb{V}[x] = \mathbb{E}\left[x^2\right] - \mathbb{E}[x]^2$
  - Cov: Covariance of two quantities as $\mathrm{Cov}[x, y] = \mathbb{E}[xy] - \mathbb{E}[x]\,\mathbb{E}[y]$
  - $(f * g)[t]$: Convolution of function $f(t)$ and $g(t)$, equivalent to $\int_{-\infty}^{\infty} f(\tau)g(t-\tau)\,\mathrm{d}\tau$
  - $(f \star g)(\tau)$: Correlation between function $f(t)$ and $g(t)$, equivalent to $\int_{-\infty}^{\infty} f(t)g(t+\tau)dt$.
  - $\vec{u} \otimes \vec{v}$: Outer product of vector $\vec{u}$ and $\vec{v}$
  - **Re**: taking the real part from the complex composition given as $\mathbf{Re}\left[\mathrm{e}^{iA}\right] = \mathbf{Re}\left[i\sin(A) + \cos(A)\right] = \cos(A)$
  - $\underline{\mathrm{A}}^{\mathrm{T}}$: Transpose of $\underline{\mathrm{A}}$ tensor.
  - $\mathbf{E}_\alpha$: Mittag-Leffler function defined by parameter α
  - **H**: Fox **H** function.
  - $\mathbf{\Gamma}$: Gamma function
  - erf : Error function
- **Scattering:**
  - $E(\vec{q}, t)$: Scattered electromagnetic wave profile at time t
  - $I(\vec{q}, t)$: Scattered intensity profile at time t
  - $S(\vec{q}, t)$: Intermediate scattering function at time t
  - b: Scattering contrast of individual particles in the system.

- $c(\vec{r}, t_1, t_2)$: Correlation function in real space between t_1 and t_2
- $c_1(\vec{q}, t_1, t_2)$: The first-order two-time correlation function in the reciprocal space between t_1 and t_2.
- $c_2(\vec{q}, t_1, t_2)$: The second-order two-time correlation function in the reciprocal space between t_1 and t_2.
- $g_1(\vec{q}, \tau)$: The first-order one-time correlation function in the reciprocal space
- $g_2(\vec{q}, \tau)$: The second-order one-time correlation function in the reciprocal space
- β: Speckle contrast of the incident beam.
- $x_n(t)$: The fraction of the individual component n in the system at time t. Follow with the relation $1 = \sum_{n=1}^{N} x_n(t)$, with N being the total number of components.
- ϕ_n: The angle between flow velocity and scattering vector $\vec{q}$ for n.
- f: the normalization factor in a system with multiple compositions.

- **Probability:**
  - $\Delta\vec{r}(t_1, t_2)$: Displacement of a particle between t_1 and t_2.
  - $\zeta(t)$: The state variable that varies in the random process.
  - $\mathbb{P}(x, t|x_0, v_o)$: The probability density function for position of a particle (x) at time t given the initial conditions $\mathbb{P}(x, v, t = 0) = \delta(x - x_0)\delta(v - v_o)$.
  - $\mathbb{P}(\Delta x, t_1, t_2)$: Transition probability function of a particle making a displacement of Δx as time evolves from t_1 to t_2.
  - $\mathbb{P}(x_2, t_2|x_1, t_1)$: Joint probability function of $\mathbb{P}(x_1, t_1|x_0, v_o)$ and $\mathbb{P}(x_2, t_2|x_0, v_o)$.
  - Δx_{na}: Non-affine displacements calculated from FLD simulations.
  - J: Transport coefficient defined at Equation 2.42.

- $\mathcal{N}(x;\mu,\sigma^2)$: A normalized Gaussian function with respect to x with a mean of μ and a variance of σ^2.
- : $\alpha_n(t)$: The $n-$th cumulant of the distribution. When $n = 2$, $\alpha_2(t)$ is defined as the non-Gaussian parameter that characterizes the system's non-Gaussian dynamics.

- **Langevin Equation:**
  - γ: The friction coefficient or drift that characterizes the effect of friction on the particle's motion.
  - η: A 'truly random' force or noise independent of the particle's state of motion.
  - Γ: The magnitude of the random force depending on collisions between the particles and the solvent, given as $\Gamma = 2m\gamma k_B T$ for one-dimensional system.
  - ω_o: Force constant for the Brownian oscillator, given as $V(x) = \frac{1}{2}m{\omega_o}^2x^2$.
  - ω_s: The reduced frequency given as $\omega_s = \left({\omega_o}^2 - \frac{1}{4}\gamma^2\right)^{\frac{1}{2}}$.
  - γ_s: The reduced drift is given as $\gamma_s = \left(\gamma^2 - 4{\omega_o}^2\right)^{\frac{1}{2}}$.
  - D: The classical diffusion constant in the equilibrium state is defined as $D = \frac{k_B T}{m\gamma}$.
  - D_o: The intrinsic diffusion constant of the system in the equilibrium state.

- **Non-Gaussian Dynamics:**
  - $\mathcal{K}$: Memory Kernel for anomalous diffusion.
  - τ_o: the mean time between two consecutive hops in cage dynamics.
  - τ_R: the time required for the particle to explore the cage.
  - σ: the typical size of a harmonic cage confining a particle.
  - ϵ: the characteristic hopping length.

- **Rheology:**
  - γ: Strain in response to the applied deformation.
  - $\dot{\gamma}$: Shear rate in a laminar flow system.
  - σ: Stress applied to the system.
  - $\mathcal{J}$: Creep compliance, defined as γ/σ.

ACKNOWLEDGMENTS

First and foremost, I would like to express my deepest gratitude to Prof. Matthew Tirrell for his thoughtful guidance and unwavering support throughout my Ph.D. journey. I am also sincerely thankful to my advisors, Dr. Wei Chen and Dr. Suresh Narayanan, for their invaluable mentorship, boundless patience, and continual efforts in supporting both my research and personal development. Thanks also to them for providing me with a rich and free environment for learning scientific skills and doing research. Their dedications to my professional development are invaluable. I am very proud that I could have such an opportunity to work under their guidance. I also wish to thank Prof. Shrayesh Patel for serving on my committee and providing valuable insight on my research throughout its evolution. And besides, I am greatly indebted to my collaborators, Dr. Heyi Liang and Dr. Yuan Tian for their inspiring discussions and dedicated efforts in conducting the dynamics simulations.

I am particularly thankful to the members of the Dynamics and Structure group at the Advanced Photon Source: Jiang Zhang, Joseph Strzalka, Qingteng Zhang, Eric Dufresne and Ziegler Raymond for their assistance during my beamtime experiments and for demonstrating the commissioning of beamlines 8-ID and 9-ID. My experience working at these beamlines during my Ph.D. research has been highly beneficial. Miaoqi Chu has been one of the closest coworkers, offering his tremendous helps when working at python programming. Our friendship is also very important to me. Moreover, I would truly appreciate the assistance from Xiao-Min Lin from Center for Nanoscale Materials for thermogravimetric analysis and Zeta-potential measurement.

In addition, I am extremely grateful for the assistance and support from all the group members I have had the pleasure of working with: Kuang-Hao Cheng, Erwin Andrew, Jinwoo Park, Sohee Park, Hui Cao, Dean Mastropietro, and Qiming He. Their kindness, collaborative spirit, and willingness to share their knowledge have not only made the research process

smoother but also made the lab a truly enjoyable place to be. I deeply cherish the time we spent together—both the productive hours in the lab and the laughter shared outside of it. The happy memories with these wonderful people are deeply etched in my heart, and I will carry them with me as I move forward.

I would like to extend my heartfelt gratitude to my friends at Argonne National Laboratory, whose support and camaraderie have made my time there truly meaningful. Jiajun Tian, Yan Li, Xiaojian Zheng, Yusu Wang, and Xi Zhang—thank you for the insightful discussions, your generous help both inside and outside the lab, and for creating such a supportive and collaborative environment. Working alongside you has been both a privilege and a pleasure, and I am sincerely grateful for the encouragement and inspiration each of you has offered throughout my journey.

In addition, my heartfelt gratitude goes to the entire faculty in the department for their excellent teaching in the first year classes and wonderful job to create open research environments and great research facilities. My research for this dissertation was made more efficient but also much more extensive through the use of synchrotron light source and neutron scattering facility. Thus I gladly express my gratitude to Wei-Ren Chen at Oak Ridge National Laboratory, for his lecture at fundamental in scattering theories. Also, many thanks to for all of their helps in many ways with research and graduate studies. My sincere thanks further go out to everyone at PME and all others whose names I did not mention, but who contributed in any form towards the successful completion of my dissertation.

Certainly, none of this would have been possible without the financial support from the Department of Energy's Materials Research Science and Laboratory Directed Research and Development (LDRD) program at Argonne National Laboratory. This research utilized resources from the Advanced Photon Source and the Center for Nanoscale Materials, two U.S. Department of Energy (DOE) Office of Science User Facilities, which are operated by Argonne National Laboratory under Contract No. DE-AC02-06CH11357. Additionally,

we sincerely acknowledge the computing resources provided by Bebop, a high-performance computing cluster managed by the Laboratory Computing Resource Center (LCRC) at Argonne National Laboratory. This work was also partially supported by resources from the University of Chicago's Research Computing Center.

The last, and surely the most, I want to express my eternal gratitude to my family. The Ph.D. journey has not been easy, but their love and support have made it all possible.

CHAPTER 1

OVERVIEW

This chapter provides a comprehensive overview of the study of dynamics in the context of current scientific and technological advancements, emphasizing its fundamental importance across diverse scientific and industrial fields. It reviews established theoretical and experimental tools commonly used for characterizing dynamics, discussing their significant contributions and inherent limitations. Building on this foundation, the chapter highlights the transformative advancements enabled by XPCS in probing dynamic processes at the nanoscale. Finally, the discussion contextualizes the presented doctoral research within this evolving landscape, demonstrating its contributions to advancing the understanding and application of dynamics characterization.

1.1 Dynamics in Natural Physics and Materials Science

Dynamics refers to the study of motion and changes in the physical state within systems over time. It is a fundamental concept in mathematics [5, 6], physics [7, 8], chemistry [9, 10], biology [11, 12], and materials science [13, 14], providing a framework to explore how and why systems evolve under specific conditions within a given period. In natural phenomena, dynamics explain processes ranging from the molecular motion driving chemical reactions [15, 16] to the crustal movements that trigger earthquakes [17, 18] and the large-scale flows that shape planetary systems [19, 20]. In materials science, dynamics are essential for understanding how molecules [21, 22], particles [23], phases [24], and larger structures interact and rearrange [25], ultimately determining mechanical and electrical properties such as strength, elasticity, thermal conductivity, and viscosity [26, 27, 28, 29].

In materials science, dynamics span multiple interconnected scales, each influencing the others. At the molecular scale, dynamics govern the interactions and motion of particles and

molecules, driven by processes such as diffusion [30], hydrodynamic interactions [31], and interparticle forces [32]. These motions are essential in defining fundamental characteristicsn of the material, including its thermal stability [33], crystallinity [34], and chemical reactivity [35]. At the mesoscopic scale, which features systems such as colloids [36], polymers [37], and grains [38], dynamics describe how the behavior of local structures interact and respond to external forces or environmental changes, often giving rise to emergent phenomena such as self-assembly [39], heterogeneity [40], and viscoelastic behavior [41]. At the macroscopic scale, dynamics dictate bulk material behavior, including flow [42], deformation[43], and fracture [44], thereby linking microscopic mechanisms to observable properties like mechanical strength [45] and flow rates [46] in soft matter.

Understanding dynamics is pivotal in applications involving soft matter systems (e.g., gels, foams, and colloids), where material behavior arises from the intricate interplay of structure and motion across multiple length and time scales. Controlling dynamic behavior at these scales is essential for optimizing product quality, efficiency, and performance. Similarly, in glasses and amorphous solids, studying the dynamic arrest of molecules provides insight into their unique properties and long-term stability [47, 48]. In soft matter, such as emulsions or liquid crystals , dynamics play a critical role in optimizing performance for industrial and biomedical applications[49]. The shape of a gel can be manipulated by carefully tuning the strength of nano-inks and their yielding behavior during 3D printing [50]. Biomaterials, including proteins and lipid membranes, also rely heavily on dynamic processes for functionality, making the understanding of their motion vital for advancements in drug design and synthetic biology [51, 52]. By linking the temporal evolution of systems to their material properties, dynamic studies offer a powerful framework for driving innovation across diverse scientific and engineering domains.

As the demand for tailored materials and enhanced processes continues to grow, there is a pressing need to deepen our understanding of the mechanisms governing their dynamic

phenomena. The dynamics of materials are influenced by a multitude of factors, including temperature [53], pressure [54], molecular interactions [55], and the material's microstructure [56]. These factors are often interconnected, with each one affecting and being affected by the others in a complex and sometimes unpredictable ways. For instance, temperature can influence molecular mobility, which in turn affects the material's structural evolution and vice versa [57]. Similarly, the interplay between material composition and external forces can lead to non-linear behavior that are challenging to predict [58]. As these factors are highly coupled, the resulting dynamics can exhibit intricate and often non-intuitive behaviors. Therefore, studying dynamics requires significant effort to untangle these interactions and understand how they collectively govern the material's overall response. This complexity makes the study of dynamics a highly interdisciplinary and evolving field, where continuous advancements are necessary to fully capture the underlying principles that drive material behaviors across different scales.

1.2 Foundations and Developments in the Study of Dynamics

The systematic study of dynamics began in 1785, when Dutch physician Jan Ingenhousz observed the flickering motion of coal dust particles on the surface of alcohol [59]. In 1827, Scottish botanist Robert Brown noted a similar irregular movement of pollen grains under a microscope, a phenomenon now known as Brownian motion [60]. Over the years, many scientists, including Adolf Fick [61] and John William Strutt (Lord Rayleigh) [62], contributed to understanding the principles governing such dynamics. In 1905, Albert Einstein unified these earlier approaches with his groundbreaking theoretical work on Brownian motion [63], which was experimentally verified by Jean Perrin through measurements of the Avogadro number [64]. Einstein's insights laid the foundation for Langevin's treatment of Brownian motion [65], introducing the concept of an external erratic force, and spurred the development of the Fokker-Planck [66, 67], Smoluchowski [68], and Klein-Kramers equations

[69, 70]. Further advancements came from the work of Wiener [71], Ornstein, Uhlenbeck [72, 73], Chandrasekhar [74], and others.

Despite these foundational contributions, the dynamics of real systems often exhibit greater complexity due to non-equilibrium effects, cooperative dynamics and intricate microstructural changes. The following sections will explore these challenges, review their historical context, and provide insights for making quantitative predictions and guiding future research.

1.2.1 Non-Equilibrium Dynamics

Non-equilibrium dynamics describes systems that deviate from thermodynamic equilibrium due to external forces or internal fluctuations. Two major theoretical frameworks have been developed to address this rich field: the linear response theory (LRT) and fluctuation-dissipation theorem (FDT) on one hand [75, 76], and Langevin Dynamics and stochastic processes on the other [65, 70]. Each approach offers unique insights and tools to understand the behavior of complex systems driven away from equilibrium.

Fluctuation-Dissipation Theorem and Linear Response Theory

In 1931, Onsager introduced the FDT [75, 76], which Kubo later extended in 1953 by providing a general proof as the framework of LRT [77]. This proof demonstrated that the linear response of a system to an external perturbation is directly linked to the system's equilibrium fluctuation properties. Together, the FDT and LRT establish a connection between spontaneous fluctuations in equilibrium and the system's response to external forces. LRT provides a structured approach to studying systems under weak external perturbations, operating under the assumption that the response remains linear and proportional to the applied force. By employing correlation functions, LRT describes how a system relaxes back to thermal equilibrium after the external perturbation is removed. This framework enables the

extraction of non-equilibrium properties from equilibrium configurations, effectively bridging the gap between these two states. However, real-world systems often exhibit complexities such as non-linear dynamics [78, 79], many-body interactions [80], and hydrodynamic effects [81], which can limit the direct applicability of these methods. Despite these challenges, LRT remains a foundational tool for predicting first-order deviations from equilibrium in systems with weak perturbations.

Stochastic Processes and Langevin Equation

Another approach to describing non-equilibrium dynamics is the Langevin equation, a stochastic model developed by Paul Langevin in 1908 [65]. This model introduces a random force or noise, which is characterized by prescribed statistical properties. The Langevin equation describes the evolution of a system by considering both the deterministic forces acting on the system and the random fluctuations arising from the environment. This stochastic approach is particularly useful for systems where thermal fluctuations play a significant role in the dynamics, providing a framework for modeling complex systems that are far from equilibrium.

In the most common and simplest case, the Langevin equation can be framed within a Markovian chain, where the system's evolution depends solely on its current state, with no influence from its past history [82, 83]. In the Markovian process, the Chapman-Kolmogorov equation governs the evolution of the system's PDF over time [84, 85]. It expresses how the probability of being in a particular state at a later time can be derived from the distribution at an earlier time, thereby attributed to the lack of memory in the system. By applying the Langevin equation, one can derive response functions that can be compared with those obtained from LRT, providing a consistent framework for understanding non-equilibrium dynamics.

It is important to note that the results derived from Langevin equation approach will be

completely consistent with LRT. Both the stochastic approach and LRT ultimately describe the same physical phenomena but from different perspectives: the Langevin equation provides a direct method for simulating the microscopic dynamics, while LRT focuses on macroscopic properties and the system's response to perturbations. Thus, the two approaches are complementary and yield consistent results, further reinforcing the validity of the connection between fluctuations and dissipation in non-equilibrium systems.

1.2.2 Suspension Dynamics and Rheology

Starting with Einstein's relation from 1906 [63], the diffusive dynamics and effective viscosity of a suspension of spherical particles in low volume fraction is related to the fluid's viscosity and the particle volume fraction [86]. However, as the concentration of particles increases, this relationship no longer holds, and particle interactions, including hydrodynamic forces, become more significant. In concentrated suspensions, the flow field around each particle is altered by nearby particles, affecting the collective dynamics and energy dissipation [87]. This influence grows with the square of the volume fraction, and the viscosity can be described using a Taylor expansion that incorporates higher-order terms to account for increasingly complex interactions [88].

Batchelor introduced methods to calculate the higher-order viscosity corrections, considering Brownian motion and thermodynamic forces. His work led to the development of the Batchelor-Green viscosity model, which quantifies the increase in viscosity due to hydrodynamic interactions in concentrated suspensions [89]. This model provides more accurate predictions of effective viscosity in systems with significant many-body effects. Lionberger and Russel expanded on these ideas, incorporating approximations for many-body and hydrodynamic interactions, yielding numerical solutions for the zero-shear viscosity of hard-sphere dispersions that showed good agreement with experimental data [90].

An alternative approach to suspension rheology is mode-coupling theory (MCT), which

uses a microscopic theory of fluid fluctuations to model the caging behavior of particles in dense suspensions [91]. MCT predicts an ideal glass transition, where particle motion becomes highly localized due to crowding at high volume fractions. In this regime, the suspension behaves like a glass, with reduced particle mobility. MCT helps explain the dynamical transition from fluid-like to solid-like behavior as particle concentration increases, providing valuable insight into mesoscopic dynamics in concentrated suspensions [92].

Together, these models and theories offer a comprehensive understanding of suspension rheology and particle dynamics, capturing the complex interplay of particle interactions, hydrodynamic effects, and thermodynamic forces that govern particle behavior in concentrated suspensions. They bridge the gap between simple dynamics models, such as Einstein's relation, and the more complex behaviors observed in real systems [36].

1.2.3 Computation Modeling

The development of MD simulations improves the study of particle dynamics by offering computational tools to explore the behavior of systems at microscopic scales [93]. Emerging in the late 1950s, the earliest MD simulations focused on simple Lennard-Jones fluids, solving Newton's equations of motion for interacting particles [94]. This approach laid the foundation for computational studies of physical phenomena like diffusion, viscosity, and structural evolution. Early algorithms, such as the Brownian dynamics (BD) method introduced by Ermak and McCammon, bridged MD principles with approximations for hydrodynamic interactions [95]. These advancements allowed simulations of colloidal suspensions, providing insights into their equilibrium and non-equilibrium dynamics, including their diffusion and other macroscopic behaviors.

A major milestone in MD simulations came with the development of techniques to model hydrodynamic effects. Stokesian dynamics (SD), for instance, incorporated near-field lubrication corrections and far-field hydrodynamic interactions through multipole expansion of

Stokes equations [96, 97, 98]. Although computationally demanding, SD offered a highly accurate method for simulating colloidal systems under flow conditions. Subsequent refinements, such as FLD, aimed to balance accuracy and computational efficiency, making large-scale and long-time simulations more feasible. FLD simplified the computation of hydrodynamic interactions by splitting the resistance tensor into far-field isotropic contributions and near-field lubrication terms [99, 100, 101]. This approach retained the key physical accuracy of SD while significantly reducing computational costs, especially in the higher particle concentration scenarios where near-field effects dominate. FLD's computational efficiency extends MD simulations to applications involving complex microstructures and high particle concentrations. FLD has been implemented in simulation platforms like Large-scale Atomic/Molecular Massively Parallel Simulator (LAMMPS), enabling researchers to efficiently model dense colloidal suspensions and explore their dynamics in industrially relevant scenarios [102, 103].

The rise of mesoscale methods, dissipative particle dynamics (DPD)[104, 105] and multiparticle collision dynamics (MPCD) [106, 107], further enriched the capabilities of MD simulations. These methods introduced coarse-grained representations of solvent molecules, allowing for efficient modeling of solvent-particle interactions while retaining key hydrodynamic properties. For instance, DPD employs soft pairwise interactions and thermostatting to simulate fluid behavior [108], while MPCD uses a stochastic collision scheme to propagate momentum and reproduce realistic flow characteristics [109]. These approaches bridged the gap between molecular-level detail and continuum-scale predictions, enabling the study of phenomena like suspension rheology, aggregation dynamics, and microstructure formation in increasingly complex systems.

Modern MD simulations continue to develop, integrating multiscale modeling frameworks that combine atomistic, mesoscale, and continuum approaches [110]. With ongoing advancements in computational power and algorithmic efficiency, molecular dynamics simulations

are poised to tackle even more intricate problems in dynamics studies, offering predictive capabilities that are critical for both fundamental research and practical innovation.

In conclusion, the foundations and advances in dynamics have significantly shaped our understanding of both equilibrium and non-equilibrium systems. From the pioneering work on Brownian motion to the development of modern theories like Langevin dynamics and fluctuation-dissipation relations, significant strides have been made in describing particle behavior across scales. Advances in suspension dynamics, including the work on viscosity models and the application of methods like MCT, have deepened our understanding of the dynamics in complex fluid. Furthermore, the evolution of MD simulations, particularly with the introduction of methods like SD and FLD, has provided powerful computational tools to study intricate particle interactions in real systems. These advances, combined with the capabilities of platforms like LAMMPS, have opened new avenues for studying dynamics in increasingly complex systems. As computational resources continue to grow, these techniques promise to offer even more detailed insights, advancing both fundamental research and industrial applications.

1.3 Common Methods for Dynamics Measurement

To validate the results derived from dynamic theory and simulations, it is crucial to employ a range of experimental and characterization techniques to capture these dynamics in complex systems. These methods not only provide a means to directly observe and measure dynamic behavior but also offer insights into the underlying mechanisms at play. The following section provides an overview of the existing characterization methods developed and employed for dynamics studies, along with a discussion of their advantages and limitations. By addressing these factors, this section aims to provide a comprehensive understanding of the tools available for dynamic studies and their role in advancing our knowledge of complex systems.

1.3.1 Imaging

Time-resolved imaging offers a direct and intuitive way to study dynamic processes by capturing a sequence of images over time, effectively creating "movies" of system dynamics. These techniques provide detailed spatial and temporal information, making them indispensable for understanding dynamic phenomena at various scales.

Confocal microscopy uses optical sectioning to eliminate out-of-focus light, allowing for three-dimensional imaging with high spatial resolution [111, 112]. This makes confocal microscopy particularly effective for observing the motion and interactions of particles in complex environments, such as colloidal suspensions or biological systems [113, 114]. The technique can track individual particles and analyze their trajectories, but its reliance on fluorescence labeling and limited penetration depth in opaque samples can pose challenges in certain applications.

On the other hand, magnetic resonance imaging (MRI) does not require transparent samples and can probe molecular-scale dynamics in diverse environments, including solids, liquids, and complex biological tissues [115, 116]. This nuclear magnetic resonance (NMR)-based techniques excel in providing detailed information on molecular interactions, transport properties, and diffusion processes, making them invaluable for studying dynamic behavior in both materials science and biomedical research [117, 118]. Despite these strengths, the relatively low spatial resolution of NMR compared to optical methods and the need for strong magnetic fields can limit its application in certain scenarios.

1.3.2 Time-resolved Scattering

Time-resolved scattering techniques are powerful tools for investigating dynamic processes at atomic and mesoscopic scales. By capturing changes in scattering patterns over time, these methods provide insights into structural evolution, particle dynamics, and collective behaviors in various systems. Two prominent forms of time-resolved scattering are X-rays

and neutron scattering, both of which offer unique advantages in studying dynamics. Additionally, coherent diffractive imaging (CDI) and neutron backscattering (NBS) extend the capabilities of traditional scattering techniques, providing high-resolution real-space images reconstructed from diffraction data.

Time-resolved X-ray scattering in small (SAXS) and wide angle (WAXS) probes processes occurring on microscale to nanoscale, at timescales depending on the flux intensity and acquisition rate of the detector [119]. With the advent of advanced synchrotron and free-electron laser facilities, it is widely used to study structure and dynamics in materials ranging from soft matter to complex fluids and solids [120, 121, 122]. The high penetration power of X-rays makes this method suitable for studying dense and opaque samples, but radiation damage can pose challenges, particularly for biological systems. Meanwhile, neutron scattering complements X-ray scattering by offering unique advantages, such as sensitivity to lighter elements like hydrogen and isotopic contrast through deuterium labeling [123]. Time-resolved neutron scattering is particularly effective for studying soft matter, biological systems, and magnetic materials [124]. However, the relatively lower flux of neutron sources compared to X-rays limits the temporal resolution, making neutron scattering more suitable for slower processes.

CDI bridges the gap between scattering and imaging, offering the ability to reconstruct real-space images from scattering patterns [125, 126]. CDI utilizes coherent X-rays to capture high-resolution diffraction patterns, which are processed using phase retrieval algorithms to reconstruct dynamic changes in the sample's structure. Time-resolved CDI is particularly effective for visualizing nanoscale processes, such as particle assembly, phase transitions, or defect dynamics, in real time [127, 128]. While CDI eliminates the need for lenses, the requirement for highly coherent sources and complex data reconstruction algorithms can limit its accessibility and practicality.

NBS measures the energy shift of neutrons that are scattered backward from the sample,

providing information on the dynamics of atoms or molecules on timescales ranging from picoseconds to nanoseconds [129, 130]. This technique is highly sensitive to changes in the low-frequency motion of particles and offers high resolution in both time and space. NBS is particularly effective for studying molecular diffusion, glass transitions, and other relaxation processes in soft matter systems [131, 132]. One of the key advantages of NBS is its ability to directly measure the local dynamics of specific atoms, especially when combined with isotope labeling, such as deuterium substitution. However, like other neutron scattering techniques, NBS is often limited by the availability of neutron sources and the relatively low flux compared to X-ray methods, which can limit its temporal resolution for fast processes.

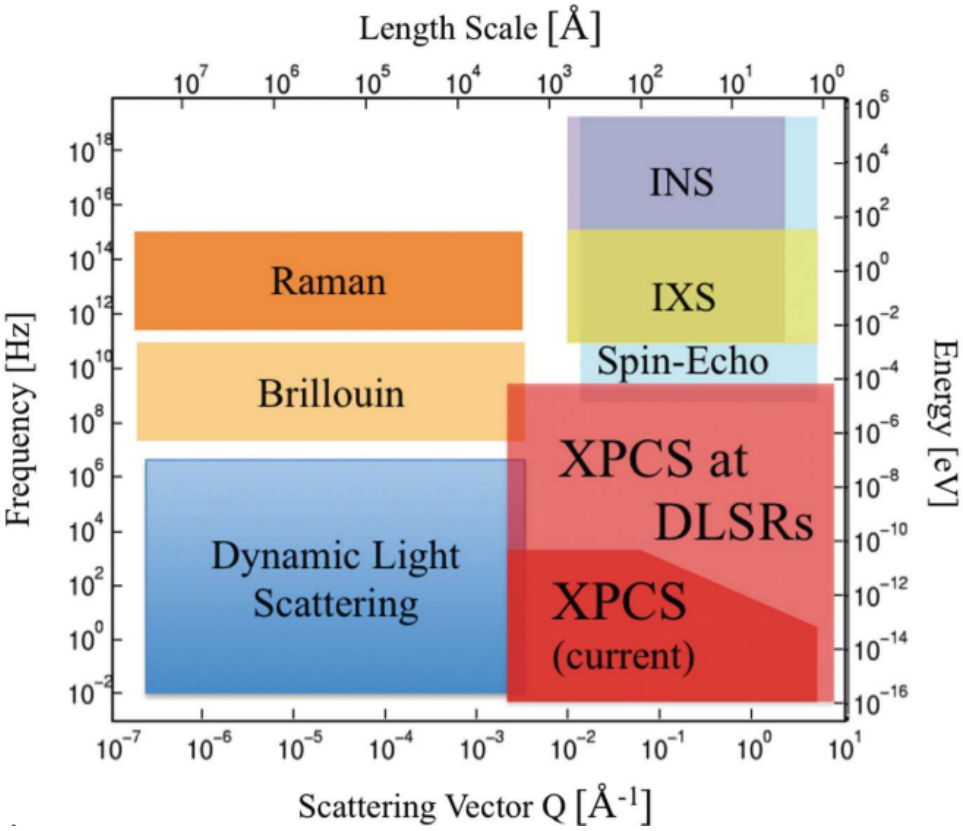

Figure 1.1: **Phase map of spatiotemporal techniques accessing the dynamic** [1] XPCS is a powerful technique that could cover the dynamics study in a small time and length scale.

1.3.3 Correlation Function

To gain deeper insights into subtle dynamics at the microscopic level, temporal correlation functions of measurement signals are essential for analyzing time-dependent phenomena. Specialized techniques are required to fully explore particle interactions, diffusion, and fluctuations, providing the sensitivity needed to uncover the underlying dynamics that govern complex systems. These techniques operate in either real or reciprocal space, enabling the analysis of dynamic processes with high precision and offering a comprehensive understanding of the intricate behaviors at play.

In the correlation in real space, fluorescence correlation spectroscopy (FCS) analyzes fluctuations in fluorescence intensity within a small observation volume [133]. FCS provides information on particle concentration, mobility, and interactions. This technique is especially valuable in biological systems, where it can probe molecular diffusion in membranes, cytoplasm, or extracellular environments [134, 135]. Despite its high sensitivity and ability to resolve real-space dynamics, FCS relies on fluorescent labeling and is limited by photobleaching and the optical properties of the sample.

In the correlation in reciprocal space, dynamics light scattering (DLS) analyzes the temporal fluctuations of the speckles from scattered light intensity caused by particle dynamics [136, 137]. It is particularly effective for colloidal suspensions and polymer systems, where it can provide insights into aggregation, stability, and rheological behavior [138, 139]. Therefore, DLS is a widely used technique for measuring particle size distributions and diffusion. However, DLS is limited in its ability to resolve complex systems with high turbidity or polydispersity.

Neutron spin echo (NSE) has a similar function but analyzes the phase shifts of neutron spin instead of the phase shifts of electromagnetic light as the "timer" of dynamics [140, 141]. NSE can probe dynamical processes such as diffusion [142], viscoelasticity [143], and relaxation [144] with nanometer spatial resolution. This technique is especially useful in

soft matter and biological systems with relatively high contrast for lighter elements, and atomic labeling [145, 146]. However, the requirement for isotopic labeling and the limited availability of neutron sources can limit its broader application.

Together, these techniques offer complementary approaches to studying dynamics using imaging and scattering. However, the spatial and temporal resolution of these techniques are limited, especially when there is a growing need to study subtle dynamics on short time scales and at small spatial scales. Therefore, there is a pressing need for the development of new techniques that can overcome these limitations and provide deeper insights into dynamic processes across various systems.

1.4 X-Ray Photon Correlation Spectroscopy

To address the challenges outlined in the previous section, XPCS is introduced and developed as a powerful tool for investigating dynamical processes. In 1991, Mark Sutton pioneered XPCS, a coherent X-ray scattering technique that enables the measurement of dynamics through the temporal autocorrelation of intensity fluctuations in space and time [147]. This method has since become invaluable for exploring nanoscale dynamics in a wide range of systems, particularly hard and soft matter systems, including oxide thin films [148], colloidal suspensions [2], polymers [149], and gels [150], providing unique insights into dynamics and structural rearrangements that are often inaccessible through other techniques.

One of the key advantages of XPCS lies in its ability to probe dynamics over a broad range of timescales, from milliseconds to hours, while simultaneously capturing information about the microstructure. This dual capability enables researchers to study processes such as particle diffusion [151], viscoelasticity [152], and phase transitions [153] in unprecedented details. Additionally, the technique is well-suited for in-situ and in-operando studies, making it a versatile tool for investigating complex materials under real-world conditions.

XPCS can be further enhanced when combined with complementary techniques such as

rheology, crystal growth studies, and measurements under electric fields. Coupling XPCS with rheology enables the investigation of microscopic dynamics alongside macroscopic mechanical properties, such as viscosity and elasticity [154]. Integrating XPCS with crystal growth studies provides insights into how nucleation and crystal formation influence material structure [155]. Additionally, combining XPCS with electrical measurements facilitates the study of dynamic processes under applied electric field, as seen in electrochemical systems [156]. This multi-modal approach connects microscopic dynamics with macroscopic properties, offering a more comprehensive understanding of how particle behavior at the microscopic scale contributes to material properties under various conditions.

1.4.1 Physics of XPCS

In a typical XPCS experiment, a coherent beam of X-rays is directed through the sample. As waves with oscillating electromagnetic fields, incident X-rays induce vibrations in the electron clouds of atoms in the scatterers. These oscillating electron cloud emit secondary radiation in all directions as they accelerate, a phenomenon known as Larmor radiation [157]. When the electrons are free or weakly bound, this emitted radiation is observed as scattered intensity and the process follows the principles of Thomson scattering [158]. In the regime of elastic scattering, the emitted radiation has the same wavelength as the incident beam. The scattered intensity is directly proportional to the size of the electron clouds, with heavier atoms, which have larger electron clouds, exhibiting stronger scattering contrast. This process provides a foundational picture of how X-rays interact with matter in the context of X-ray scattering.

In a system with many scatterers arranged in a specific spatial distribution, scattered radiation travels along distinct paths to the detector, resulting in variations in the phase angles of the scattered waves. The interference of these waves, both constructive and destructive, generates intensity fluctuations known as speckles, which encode detailed information about

the spatial arrangement of the scatterers [159]. In a XPCS experiment, speckle intensities are measured over time, either in transmission or grazing incidence geometry. By analyzing the temporal autocorrelation of the speckle intensity, subtle changes in the spatial distribution of particles can be identified, providing valuable insights into the dynamic processes within the system [147]. A detailed physical and mathematical explanation of the XPCS process will be presented in Chapter 2.

In the scattering process described above, a critical prerequisite for XPCS is the coherence of the X-rays, which fundamentally limits the resolution of the dynamics observable through this technique. Coherence describes the orderliness of incident X-rays and consists of two components: longitudinal and transverse coherence [160]. Longitudinal coherence quantifies the beam's monochromaticity, with the characteristic coherence length (l_c) defined as

$$l_c = \frac{\lambda^2}{\Delta\lambda} \tag{1.1}$$

where λ is the wavelength of the source and $\Delta\lambda$ is its bandwidth. In contrast, transverse coherence (L_T) describes how well two points in the beam are phase-correlated, directly proportional to the distance from the source to the observer (D) and inversely proportional to the source size (a), given by [161]:

$$L_T = \frac{\lambda D}{2a} \tag{1.2}$$

For example, starlight, like laser light, exhibits coherence due to its small apparent source size and large distance from the observer. In an amorphous system, without coherence in the incident X-rays, the phase angles of the scattered waves become random, leading to interference that cancels out the structure factor in the scattered signal. As a result, the absence of coherence eliminates structural information about the system from the signal, thereby significantly reducing the resolution of XPCS.

1.4.2 XPCS in Synchrotron

To achieve optimal flux and coherence, most XPCS experiments are conducted at synchrotron radiation sources around the world. A synchrotron radiation source is a facility that accelerates electrons to nearly the speed of light and uses magnetic fields to bend their path, causing the emission of highly brilliant and coherent X-rays [162]. In the United States, facilities such as the Advanced Light Source (ALS) (e.g., 12.0.2), National Synchrotron Light Source-II (NSLS-II) (e.g., 11-ID), and Advanced Photon Source (APS) (e.g., 8-ID [163]) are equipped with capabilities for supporting XPCS experiments. These synchrotron sources are designed to produce X-rays at different energies: the APS is optimal for high-energy, hard X-rays; the NSLS-II is suitable for tender X-rays; and the ALS excels in generating low-energy, soft X-rays. Notable global synchrotron facilities include the European Synchrotron Radiation Facility (ESRF) in France, PETRAIII in Germany and SPring-8 in Japan. Additionally, XPCS experiments are being explored at X-ray free-electron lasers (XFELs), although this is still an area of ongoing development [164].

Advances in accelerator technology, such as the installation of quadrupole bending magnets [165, 166] and application of swap-out injection [167, 168], have led to reduced beam sizes and increased coherence and brightness (coherent flux) in fourth-generation beamlines. The enhanced coherence improves spatial resolution, while the increased flux allows for measurements over shorter acquisition periods. These advancements enable more precise measurements of al processes, providing access to subtle dynamics that were previously difficult to observe. For example, the 8-ID beamline at APS, which features XPCS, has experienced a 100-fold increase in coherence, resulting in a 100,000-fold improvement in time resolution compared to its previous configuration [169]. Additionally, the increase in coherence has enabled other scattering beamlines, which were not originally designed for XPCS, to acquire the capability to perform XPCS measurements. These improvements, coupled with the ongoing upgrades to synchrotron facilities worldwide, are expected to significantly expand the

XPCS user community and broaden the scope of applications for this powerful technique.

1.4.3 Analysis Approach in XPCS

Despite significant advancements in XPCS, the methods used to extract dynamical information from experimental results remain relatively basic. The most widely accepted approach in XPCS is adapted from DLS, originally developed by Robert Pecora in the early 1960s [170, 171] and formalized in 1976 [172]. This method involves extracting the diffusion coefficient from $g_2(\vec{q}, \tau)$ at equilibrium. To address the complexities of more intricate systems, additional analytical techniques, such as cumulant analysis [173] and CONTIN algorithm [174], have been developed. These methods have been successfully applied to a variety of XPCS analyses, improving the ability to study more complex dynamic processes [175]. In a typical XPCS experiment, the dynamics of a non-equilibrium system are extracted by computing the $c_2(\vec{q}, t_1, t_2)$ two-time correlation function. To apply the traditional DLS method, $c_2(\vec{q}, t_1, t_2)$ is reduced to $g_2(\vec{q}, \tau)$ through averaging, and the analysis framework designed for $g_2(\vec{q}, \tau)$ is then applied to the XPCS results [176]. While the analysis techniques used in DLS can also be applied to XPCS, they often fail to capture critical details necessary for understanding the underlying dynamics.

XPCS excels at measuring more subtle dynamics on much smaller length and time scales compared to traditional methods like DLS. Beyond offering higher precision in capturing these dynamics, XPCS provides superior sensitivity to complex processes by exploiting the coherence of the X-rays beam. The dynamics observed at these scales go far beyond the simple diffusion in equilibrium typically considered in DLS analysis. Notably, when a system is subjected to changes in external conditions—such as during transitions like relaxation[177, 178], yielding [179, 180], aging [181, 182], or phase reentrance [58, 183], the system exhibits dynamic behaviors that are linked to complex phenomena at the microscopic level, including dynamical heterogeneity [179, 180] and avalanches [184, 185]. These intricate

motions, such as non-equilibrium dynamics and cooperative behavior, can be captured by XPCS but remain unresolved by DLS. As a result, the traditional DLS analysis framework does not provide a comprehensive understanding of XPCS results. With significant advances in XPCS hardware and millions of measurements performed, the analysis methods have become the limiting factor in extracting meaningful dynamical information. Consequently, the development of more efficient and effective analysis techniques has become a critical challenge in fully exploiting the potential of XPCS experiments.

Since the introduction of XPCS, many scientists have recognized its inherent challenges and have actively contributed to addressing them. Over the past few decades, several research directions have emerged, each yielding significant advancements in the analysis of complex dynamics. Notable examples include:

1. **Modification of diffusion models:** This approach focuses on enhancing the simple diffusion function. For instance, stretched exponential functions are employed to describe non-Gaussian dynamics [186], while alternative coordinate systems have been developed to improve the averaging process from $c_2\left(\vec{q}, t_1, t_2\right)$ to $g_2\left(\vec{q}, \tau\right)$ [187, 188]. Additionally, time-translation-invariant zones have been proposed to better characterize non-equilibrium dynamics[176].

2. **Development of frameworks for specific scenarios:** Efforts in this direction involve deriving specialized correlation functions to describe dynamics under unique conditions, such as homodyne and heterodyne scattering when flow is present in the system. These frameworks offer deeper insights into how scattering processes are influenced by experimental configurations [189, 190].

3. **Connection between particle simulations with experimental analysis:** This approach combines particle-level simulations with experimental data, linking observed complex dynamics to specific phenomena [191]. For example, changes in the form factor

or phase transitions can be associated with the measured scattering signals, bridging theoretical models with experimental observations [153].

Together, these approaches provide innovative solutions to address the intricate dynamics observed in XPCS, laying the foundation for more effective methodologies to analyze and interpret experimental data. This progress significantly enhances our ability to unravel the complexities of dynamic systems and expands the scope of XPCS applications.

However, the existing approaches still face notable limitations. Many are empirical in nature and lack a direct connection to fundamental physical principles, making it challenging to derive universal insights. Furthermore, these methods are often tailored to specific cases, restricting their general applicability to diverse systems and dynamic phenomena. To fully harness the potential of XPCS, there is a pressing need to develop an unified analytical framework that is both broadly applicable and grounded in fundamental physics. Such an approach would enable the extraction of key physical parameters from the complex dynamics observed in XPCS, providing deeper insights into the underlying mechanisms and advancing our understanding of a wide range of dynamic processes.

1.5 Research Objectives and Motivation

This thesis aims to address the challenges of extracting complex dynamics by developing a universal theoretical framework for dynamic analysis grounded in fundamental physical principles. By leveraging advancements in stochastic processes, the proposed approach establishes a robust and systematic connection between observed dynamics and their underlying physical mechanisms. This framework is designed to be highly versatile, allowing its application to a wide range of complex systems, including those exhibiting non-equilibrium and non-Gaussian dynamics. The framework's validity and effectiveness will be demonstrated through a combination of classical systems, MD simulations, and experimental data.

This work represents a significant advancement by unlocking the full potential of XPCS,

particularly in light of recent upgrades, and transforming it into a more powerful tool for probing dynamic behaviors in diverse systems. By broadening the applicability and precision of XPCS, this research provides a foundation for extracting deeper insights into complex systems. Ultimately, the outcome of this work is expected to have a long-term impact, benefiting the scientific community by enabling more comprehensive studies of dynamics and fostering advancements across various fields.

In Chapter 2, a detailed derivation of the fundamental mathematics and physics underlying the transport coefficient approach proposed in this work will be presented. The chapter begins with an overview of basic scattering theory and the random walk process, followed by the derivation of the theoretical framework and the dynamic parameter, $J(t)$, developed in this study. The behavior of $J(t)$ will be derived and analyzed for various classical dynamic processes, including the Wiener process (simple diffusion), Ornstein−Uhlenbeck (OU) process, and Brownian oscillators. The analysis will then be extended to dynamic systems exhibiting non-Gaussian characteristics, highlighting features observed in XPCS that deviate from the Gaussian case. Building on this understanding, a more generalized analytical approach will be discussed and presented. This analysis will emphasize the unique features of $J(t)$ in each of these processes, laying the groundwork for its application to more complex dynamics.

In Chapter 3, the transport coefficient approach is applied to Gaussian but non-equilibrium dynamics. The method is first validated using MD simulations of a system undergoing temporal temperature changes. Further verification is conducted using experimental systems reported in the literature, known for their complex non-equilibrium behavior. The results, including the derived $J(t)$ and other relevant physical parameters, not only align with previous observations but also provide deeper insights into the dynamical information of non-equilibrium states. This approach represents a significant advancement in XPCS analysis, addressing the increasing need to extract and interpret intricate non-equilibrium dynamics.

In Chapter 4, the transport coefficient approach is applied to Rheo-XPCS studies of the yielding transition in repulsive and attractive colloidal suspensions. Combining Rheo-XPCS experiments and FLD simulations, this study examines time-resolved particle dynamics and structural changes during yielding. For repulsive suspensions, uniform flow and Andrade-like yielding are observed, while attractive suspensions exhibit complex behaviors such as shear banding, dynamic heterogeneity, delayed yielding, and resolidification. Attractive interactions also drive phase separation, leading to significant dynamical heterogeneity and interfacial instability, with transient interface dynamics dominating the rheological response. These findings highlight the critical role of interaction potentials in governing yielding transitions and provide insights for tuning material properties to optimize performance in various applications.

In Chapter 5, the transport coefficient approach is extended to non-Gaussian dynamics to investigate the dynamics during the yielding of a simulated suspension. Non-Gaussian dynamics are incorporated to estimate the $c_2\left(\vec{q}, t_1, t_2\right)$, and the results are compared to the simulation. It is found that, in addition to non-Gaussian dynamics, the cooperative motion of particles must also be considered. While the particle dynamics during yielding are not fully understood, the non-Gaussian analysis approach is successfully applied to two common and simpler non-Gaussian dynamic processes: anomalous diffusion induced by memory kernels in the Generalized Langevin Equation, and hopping dynamics from an arrested cage. By comparing the dynamic parameters extracted from the proposed analysis with those from simulations, this chapter validates the approach's accuracy and versatility in analyzing simple dynamic systems with non-Gaussian characteristics. Despite the complexity of non-Gaussian dynamics, the method provides reliable physical insights into the underlying dynamics.

CHAPTER 2

MATHEMATICS AND PHYSICS OF XPCS

2.1 Correlation Function in XPCS

To understand the physical picture of XPCS, we first start with a system composed of N scattered points. The spatial distribution at time t can be described by the function denoted as:

$$\sum_{n=1}^{N} \delta(\vec{r} - \vec{r_n}(t)) \tag{2.1}$$

In real space, this position function quantifies the relation between the positions of points at different times.

The profile of its scattered electromagnetic intensity is derived through a Fourier transform ($\mathcal{F}$), expressed as:

$$\begin{aligned} E(\vec{q},t) &= \mathcal{F}\left[\sum_{n=1}^{N} b_n(t)\delta(\vec{r} - \vec{r_n}(t))\right] = \sum_{n=1}^{N} b_n(t)\mathrm{e}^{i\vec{q}\cdot\vec{r}_n(t)} \\ I(\vec{q},t) &= |E(\vec{q},t)|^2 = E(\vec{q},t)E^*(\vec{q},t) \\ &= \sum_{n=1}^{N}\sum_{m=1}^{N} b_n(t)b_m(t)\mathrm{e}^{i\vec{q}\cdot(\vec{r}_n(t)-\vec{r}_m(t))} \end{aligned} \tag{2.2}$$

where $b_n(t)$ in the equation Eq. 2.2 is defined as the unit scattering contrast and $\vec{q}$ is the scattering vector in reciprocal space.

The correlation function $c(\vec{r}, t_1, t_2)$ between t_1 and t_2 in real space could be calculated by following:

$$c(\vec{r}, t_1, t_2) = \mathbb{E}\left[\sum_{n=1}^{N}\sum_{m=1}^{N} \delta\left(\vec{r} - (\vec{r}_n(t_2) - \vec{r}_m(t_1))\right)\right] \tag{2.3}$$

where $\vec{r}_n(t_2) - \vec{r}_m(t_1)$ is the spatial correlation of any particle n and m between t_1 and t_2 and $\mathbb{E}$ denotes ensemble average .

During XPCS measurements, the $c_1(\vec{q}, t_1, t_2)$ is the temporal correlation of electromagnetic fields as the average of equation Eq. 2.3 in the reciprocal space. To match with the physical picture, a Fourier transform is applied to the correlation function in real space Eq. 2.3.

$$\mathbb{E}\left[E(\vec{q}, t_2)E^*(\vec{q}, t_1)\right] = \mathcal{F}\left[\mathbb{E}\left[c(\vec{r}, t_1, t_2)\right]\right] = \mathbb{E}\left[\sum_{n=1}^{N}\sum_{m=1}^{N} b_n(t_2)b_m(t_1)\mathrm{e}^{i\vec{q}\cdot(\vec{r}_n(t_2)-\vec{r}_m(t_1))}\right] \tag{2.4}$$

Examining Eq. 2.4, for $n \neq m$, the phase difference $\vec{q}\cdot(\vec{r}_n(t_2) - \vec{r}_m(t_1))$ has any value between $-\pi$ and $+\pi$ (modulo 2π) with equal likelihood in a homogeneous system which the particle positions are uncorrelated. The exponential function represents a point on the circumference of the unit circle in the complex plane for any choice of n, m, t_1 and t_2. But since all points on the circumference are equally probable, the expectation of the exponential function collapses to the point of origin, that is it vanishes for $n \neq m$. Therefore only terms with $n = m$ contribute to the correlation function and we obtain for a Gaussian signal [192, at eq. (11,12)]:

$$\begin{aligned}
\mathbb{E}\left[I(\vec{q}, t)\right] &= \mathbb{E}\left[\sum_{n=1}^{N} b_n(t)^2\mathrm{e}^{i\vec{q}\cdot(\vec{r}_n(t)-\vec{r}_n(t))}\right] = \mathbb{E}\left[\sum_{n=1}^{N} b_n(t)^2\mathrm{e}^{i\vec{q}\cdot\vec{0}}\right] = \mathbb{E}\left[\sum_{n=1}^{N} b_n(t)^2\right] \\
\mathbb{E}\left[E(\vec{q}, t_2)E^*(\vec{q}, t_1)\right] &= \mathbb{E}\left[\sum_{n=1}^{N} b_n(t_1)b_n(t_2)\mathrm{e}^{i\vec{q}\cdot(\vec{r}_n(t_2)-\vec{r}_n(t_1))}\right] = \mathbb{E}\left[\sum_{n=1}^{N} b_n(t_1)b_n(t_2)\mathrm{e}^{i\vec{q}\cdot\Delta\vec{r}(t_1,t_2)}\right]
\end{aligned} \tag{2.5}$$

where $\Delta\vec{r}(t_1, t_2)$ is defined as the displacement of one particle between t_1 and t_2, given by $\Delta\vec{r}(t_1, t_2) = \vec{r}_n(t_2) - \vec{r}_n(t_1)$.

According to reference [192, at eq. (11-15)], such an assumption also enables the conversion between the first-order correlation function, $c_1(\vec{q}, t_1, t_2)$, and the second-order correlation function, $c_2(\vec{q}, t_1, t_2)$, through the Siegert relation Eq. 2.6:

$$c_2(\vec{q}, t_1, t_2) = 1 + \beta |c_1(\vec{q}, t_1, t_2)|^2, \tag{2.6}$$

In the case where the system is composed of monodisperse spheres, with all particles having the same contrast and lacking any time and direction dependence as $b_n(t) = b_n$, this common factor can be extracted from the average.

$$\begin{aligned} \mathbb{E}\left[I(\vec{q}, t)\right] &= \mathbb{E}\left[\sum_{n=1}^{N} b_n^2\right] = N b_n^2 \\ \mathbb{E}\left[E(\vec{q}, t_2) E^*(\vec{q}, t_1)\right] &= \mathbb{E}\left[\sum_{n=1}^{N} b_n^2 \mathrm{e}^{i\vec{q}\cdot(\vec{r}_n(t_2) - \vec{r}_n(t_1))}\right] = N b_n^2 \mathbb{E}\left[\mathrm{e}^{i\vec{q}\cdot\Delta\vec{r}(t_1,t_2)}\right] \end{aligned} \tag{2.7}$$

Consequently, $c_1(\vec{q}, t_1, t_2)$ is obtained by normalizing the correlation function by $|b_n|^2$. [193, at eq. (3.4.14)]

$$\begin{aligned} c_1(\vec{q}, t_1, t_2) &= \frac{\mathbb{E}\left[E(\vec{q}, t_2) E^*(\vec{q}, t_1)\right]}{\left[\mathbb{E}\left[|E(\vec{q}, t_1)|^2\right] \mathbb{E}\left[|E(\vec{q}, t_2)|^2\right]\right]^{\frac{1}{2}}} = \frac{\mathbb{E}\left[E(\vec{q}, t_2) E^*(\vec{q}, t_1)\right]}{\left[\mathbb{E}\left[I(\vec{q}, t_1)\right] \mathbb{E}\left[I(\vec{q}, t_2)\right]\right]^{\frac{1}{2}}} \\ &= \frac{N b_n^2 \mathbb{E}\left[\mathrm{e}^{i\vec{q}\cdot\Delta\vec{r}(t_1,t_2)}\right]}{N b_n^2} = \mathbb{E}\left[\mathrm{e}^{i\vec{q}\cdot\Delta\vec{r}(t_1,t_2)}\right] \end{aligned} \tag{2.8}$$

To establish a correlation between $c_1(\vec{q}, t_1, t_2)$ and the dynamics of particles, we consider a system where the particle distribution at any time t after $t_0 = 0$ follows a probability density function described by $\mathbb{P}(\vec{r}, t | t_0 = 0)$. We then define $\mathbb{P}(\Delta\vec{r}, t_1, t_2)$ as the transition probability of a particle with displacement $(\Delta\vec{r} = \vec{r}_2 - \vec{r}_1)$ between time t_1 and time t_2. Then the relation between the probability distribution function at t_1 and t_2 can be connected with the convolution with transition probability as follows,

$$\begin{aligned} \mathbb{P}(\vec{r}_2, t_2 | t_0 = 0) &= \int_{-\infty}^{\infty} \mathbb{P}(\vec{r}_1, t_1 | t_0 = 0) \mathbb{P}(\Delta\vec{r}, t_1, t_2)\, \mathrm{d}\vec{r}_1 \\ &= \int_{-\infty}^{\infty} \mathbb{P}(\vec{r}_1, t_1 | t_0 = 0) \mathbb{P}(\vec{r}_2, t_2 | \vec{r}_1, t_1)\, \mathrm{d}\vec{r}_1 \end{aligned} \tag{2.9}$$

In a Markov chain, where its behavior depends only on its current state but not on its past, the variable t_1 is excluded from the computation process in Eq. 2.9. If $\mathbb{P}(\Delta r, t_1, t_2)$ is known, the $c_1(\vec{q}, t_1, t_2)$ in equation Eq. 2.8 can be expressed equivalently as follows:

$$c_1(\vec{q}, t_1, t_2) = \mathbb{E}\left[e^{i\vec{q}\cdot\Delta\vec{r}}\right] = \mathcal{F}\left[\mathbb{P}(\Delta r, t_1, t_2)\right] = \int_{-\infty}^{\infty} \mathbb{P}(\Delta r, t_1, t_2) e^{i\vec{q}\cdot\Delta\vec{r}}\, \mathrm{d}\Delta\vec{r} \tag{2.10}$$

Alternatively, $c_1(\vec{q}, t_1, t_2)$ can be expressed in another approach by substituting 2.9 into Eq. 2.10. Starting from the Fourier transform of Eq. 2.9,

$$\begin{aligned} \mathcal{F}\left[\mathbb{P}(\vec{r}_2, t_2 | t_0 = 0)\right] &= \mathcal{F}\left[\int_{-\infty}^{\infty} \mathbb{P}(\vec{r}_1, t_1 | t_0 = 0) \mathbb{P}(\Delta\vec{r}, t_1, t_2)\, \mathrm{d}\vec{r}_1\right] \\ S(\vec{q}_2, t_2) &= S(\vec{q}_1, t_1) \mathcal{F}\left[\mathbb{P}(\Delta\vec{r}, t_1, t_2)\right], \end{aligned} \tag{2.11}$$

where $S(\vec{q}, t)$ is defined as the intermediate scattering function, equivalent to the Fourier transform of $\mathbb{P}(\vec{r}, t)$ [194] as,

$$S(\vec{q}, t) = \mathcal{F}\left[\mathbb{P}(\vec{r}, t)\right] \tag{2.12}$$

Using Eq. 2.11, $c_1(\vec{q}, t_1, t_2)$ can be written as:

$$c_1(\vec{q}, t_1, t_2) = \mathcal{F}\left[\mathbb{P}(\Delta\vec{r}, t_1, t_2)\right] = \frac{S(\vec{q}, t_2)}{S(\vec{q}, t_1)}. \tag{2.13}$$

NSE measured correlation function, expressed as $\frac{S(\vec{q},t_2)}{S(\vec{q},t_1)}$, is equivalent to the $c_1(\vec{q}, t_1, t_2)$ correlation function measured in XPCS [140, 141].

By converting the $c_1(\vec{q}, t_1, t_2)$ to the second order correlation function $c_2(\vec{q}, t_1, t_2)$ with Siegert relation Eq. 2.6, we can obtain the experiment measurement of the XPCS.

$$c_2(\vec{q}, t_1, t_2) = 1 + \beta |c_1(\vec{q}, t_1, t_2)|^2 = \frac{\mathbb{E}\left[I(\vec{q}, t_1) I(\vec{q}, t_2)\right]}{\mathbb{E}\left[I(\vec{q}, t_1)\right] \mathbb{E}\left[I(\vec{q}, t_2)\right]} \tag{2.14}$$

where β is the speckle contrast range from 0-1 depending on the coherence of the incident

beam and $I(\vec{q}, t)$ is the time-resolved intensity profile at specific $\vec{q}$ and time t.

2.2 Generalized Model: Markov Chain with Gaussian Random Walk

To gain a preliminary understanding of the dynamics of a complicated non-equilibrium system, it is assumed that the particles undergo a Gaussian random walk in 1-dimension. The step size for each walk varies according to a normal distribution. This dynamic behavior is described as a Markov process, where the evolution at a certain time t for $t > t_0$ does not depend on any of the previous states the system had been in before t. Instead, it relies only on the state of the system at time t. This process represents the simplest form of a system without memory, where the present distribution defines the future distribution.

In this Markov process, the n-time probability distribution for the process, denoted as $\mathbb{P}(\zeta_n, t_n)$, is defined as [195, at eq. (5.3)].

n-component general process : $\zeta(t) = (\zeta_0(t), \ldots, \zeta_n(t))$

$$\mathbb{P}(\zeta_n, t_n) = \mathbb{P}(\zeta_n, t_n|\zeta_{n-1}, t_{n-1}) \ldots\ldots \mathbb{P}(\zeta_1, t_1|\zeta_0, t_0)\mathbb{P}(\zeta_0, t_0)$$

$$\mathbb{P}(\zeta_n, t_n) = \int_{-\infty}^{\infty} \cdots \int_{-\infty}^{\infty} \left[\prod_{t=t_0}^{t_n} \mathbb{P}(x_t, t|x_{t-1}, t_{t-1}) \right] \mathbb{P}(\zeta_0, t_0), \mathrm{d}x_{t_0} \ldots \mathrm{d}x_{t_n} \tag{2.15}$$

where $\zeta(t)$ is the state variable that varies in the random process and $\mathbb{P}(\zeta_n, t_n|\zeta_{n-1}, t_{n-1})$ is defined as the transition probability of states from time t_{n-1} to t_n.

In the Gaussian random walk model in 1-dimension, the state variable $\zeta(t)$ represents the position (x) of the particle, which varies during the random process. The transition

probability of states from time t_{n-1} to t_n, is denoted as

$$\begin{aligned}\mathbb{P}(x_n, t_n | x_{n-1}, t_{n-1}) &= \frac{1}{\sqrt{2\pi J(t_n)\Delta t}} \mathrm{e}^{-\frac{\Delta x^2}{2J(t_n)\Delta t}} = \frac{1}{\sqrt{2\pi J(t_n)\Delta t}} \mathrm{e}^{-\frac{(x_n - x_{n-1})^2}{2J(t_n)\Delta t}} \\ &\triangleq \mathcal{N}\left(x_n - x_{n-1}; \mu = 0, \sigma^2 = J(t_n)\Delta t\right) \\ &\triangleq \mathcal{N}\left(x_n; \mu = x_{n-1}, \sigma^2 = J(t_n)\Delta t\right) \\ &\triangleq \mathcal{N}\left(x_{n-1}; \mu = x_n, \sigma^2 = J(t_n)\Delta t\right)\end{aligned} \tag{2.16}$$

This transition probability is a key element in the Gaussian random walk model, where each step follows a Gaussian distribution and the state variable evolves based on these transitions. Δx is the step the particles take from t_{n-1} to t_n, defined as $\Delta x = x_n - x_{n-1}$, and Δt is the time interval between adjacent steps t_n and t_{n-1}, given by $\Delta t = t_n - t_{n-1}$. $J(t_n)\Delta t$ is the standard deviation of the step size. $J(t_n)$ is the transport coefficient corresponding to the transition step in $t_{n-1} \to t_n$. We will define $J(t)$ physically and mathematically at equation Eq. 2.42 later.

To obtain the correlation function $c_1(\vec{q}, t_1, t_2)$ for any two states at time t_2 and t_1 with an arbitrary number of steps between them, we need to calculate the transition probability $\mathbb{P}(x_2, t_2 | x_1, t_1)$. According to the Chapman-Kolmogorov Equation, $\mathbb{P}(x_2, t_2 | x_1, t_1)$ can be expressed as the product of the probabilities of propagating from t_1 to all intermediate values $t - t'$ for $t_1 < t' < t_2$, and subsequently to t_2, summed over all possible values of the intermediate state. The expression is given as:

$$\mathbb{P}(x_2, t_2 | x_1, t_1) = \int_{-\infty}^{\infty} \cdots \int_{-\infty}^{\infty} \left[\prod_{t=t_1}^{t_2 - \Delta t} \mathbb{P}(x_{t+\Delta t}, t + \Delta t | x_t, t) \right] \mathbb{P}(x_{t_1}, t_1 | x_1, t_1), \mathrm{d}x_{t_1} \ldots \mathrm{d}x_{t_2 - \Delta t} \tag{2.17}$$

where Δt is the time interval between consecutive states, and the product represents

the joint probabilities of propagating from t to $t + \Delta t$ for each intermediate time interval. This integral sums up all possible intermediate states between t_1 and t_2, and allows us to calculate the transition probability from an initial state x_1 at time t_1 to a final state x_2 at t_2 considering all possible paths and intermediate states.

In the transition probability for any two nearby steps $\mathbb{P}(x_c, t_c|x_a, t_a)$ at $t_a \to t_b$ and $t_b \to t_c$, according to equation Eq. 2.16 and Eq. 2.17, is

$$\begin{aligned}
\mathbb{P}(x_c, t_c|x_a, t_a) &= \int_{-\infty}^{\infty} \mathbb{P}(x_c, t_c|x_b, t_b)\mathbb{P}(x_b, t_b|x_a, t_a)\,\mathrm{d}x_b \\
&= \int_{-\infty}^{\infty} \mathcal{N}\left(x_c - x_b; \mu = 0, \sigma^2 = J(t_c)\Delta t\right)\mathcal{N}\left(x_b - x_a; \mu = 0, \sigma^2 = J(t_b)\Delta t\right)\,\mathrm{d}x_b \\
&= \int_{-\infty}^{\infty} \mathcal{N}\left(x_c - x_b; \mu = 0, \sigma^2 = J(t_c)\Delta t\right)\mathcal{N}\left(x_b; \mu = x_a, \sigma^2 = J(t_b)\Delta t\right)\,\mathrm{d}x_b
\end{aligned} \tag{2.18}$$

The equation Eq. 2.18 is a convolution operation of Gaussian function as $\tau = x_b$ with the property of resulting in a new Gaussian function with a mean of $\mu = \mu_f + \mu_g$ and variance of $\sigma^2 = \sigma_f^2 + \sigma_g^2$ as follow:

$$\begin{aligned}
(f * g)[t] &= \int_{-\infty}^{\infty} f(\tau)g(t - \tau)\,\mathrm{d}\tau \\
(\mathcal{N}(\tau; \mu_f, \sigma_f^2) * \mathcal{N}(t - \tau; \mu_g, \sigma_g^2))[t] &= \mathcal{N}(t; \mu_f + \mu_g, \sigma_f^2 + \sigma_g^2)
\end{aligned} \tag{2.19}$$

Substituting the relation at Eq. 2.19 to equation Eq. 2.18, $\mathbb{P}(x_c, t_c|x_a, t_a)$ is obtained as follow:

$$\begin{aligned}
\mathbb{P}(x_c, t_c|x_a, t_a) &= \mathcal{N}\left(x_c - x_b; \mu = 0, \sigma^2 = J(t_c)\Delta t\right) * \mathcal{N}\left(x_b; \mu = x_a, \sigma^2 = J(t_b)\Delta t\right)[x_c] \\
&= \mathcal{N}\left(x_c; \mu = x_a, \sigma^2 = J(t_c)\Delta t + J(t_b)\Delta t\right) \\
&= \mathcal{N}\left(x_c - x_a; \mu = 0, \sigma^2 = (J(t_c) + J(t_b))\Delta t\right)
\end{aligned} \tag{2.20}$$

Expanding the result from Eq. 2.20 to Eq. 2.17, we can obtain $\mathbb{P}(x_2, t_2|x_1, t_1)$ as follow:

$$\mathbb{P}(x_2, t_2|x_1, t_1) = \mathcal{N}\left(x_2 - x_1; \mu = 0, \sigma^2 = \Delta t \sum_{t=t_1}^{t_2} J(t)\right) \tag{2.21}$$

Adapting an assumption that step difference is infinitesimal that there is infinity t' between t_2 and t_1, the summation $\Delta t \sum_{t'=t_1}^{t_2} J(t')$ can be expressed as an integration of a continuous function $J(t)$ as:

$$\begin{aligned} \Delta t \sum_{t=t_1}^{t_2} J(t) &= \int_{t_1}^{t_2} J(t)\,\mathrm{d}t \\ \mathbb{P}(x_2, t_2|x_1, t_1) &= \mathcal{N}\left(x_2 - x_1; \mu = 0, \sigma^2 = \int_{t_1}^{t_2} J(t)\,\mathrm{d}t\right) \end{aligned} \tag{2.22}$$

where $J(t)$ is a continuous function of the change in the distribution standard deviation in $\mathbb{P}(x, t)$ as time evolves.

Considering $x_2 - x_1 = \Delta x$, we in fact obtain the $\mathbb{P}(\Delta x, t_1, t_2)$. The $c_1(q, t_1, t_2)$ is calculated according to the equation Eq. 2.4 as:

$$\begin{aligned} c_1(q, t_1, t_2) &= \int_{-\infty}^{\infty} \mathbb{P}(\Delta x, t_1, t_2) \mathrm{e}^{iq\Delta x}\,\mathrm{d}\Delta x \\ &= \int_{-\infty}^{\infty} \mathcal{N}\left(\Delta x; \mu = 0, \sigma^2 = \int_{t_1}^{t_2} J(t)\,\mathrm{d}t\right) \mathrm{e}^{iq\Delta x}\,\mathrm{d}\Delta x \\ &= \frac{1}{\sqrt{2\pi \int_{t_1}^{t_2} J(t)\,\mathrm{d}t}} \int_{-\infty}^{\infty} \mathrm{e}^{-\frac{\Delta x^2}{2\int_{t_1}^{t_2} J(t)\,\mathrm{d}t} + iq\Delta x}\,\mathrm{d}\Delta x \\ &= \mathrm{e}^{-\frac{1}{2}q^2 \int_{t_1}^{t_2} J(t)\,\mathrm{d}t} \end{aligned} \tag{2.23}$$

Considering the Siegert relation Eq. 2.6, the $c_2(q, t_1, t_2)$ obtained from XPCS measure-

ment for the Gaussian random walk process is defined as:

$$c_2(q, t_1, t_2) = 1 + \beta |c_1(q, t_1, t_2)|^2 = \beta \mathrm{e}^{-q^2 \int_{t_1}^{t_2} J(t)\,\mathrm{d}t} + 1 \tag{2.24}$$

This equation describes the $c_2(\vec{q}, t_1, t_2)$ of a system constituted of particles undergoing random Gaussian walk.

2.3 Derivation of $c_1(q, t_1, t_2)$ from Langevin Equation

Begin with Newton's equation of motion for particles in 1-dimension:

$$m\dot{v} = F(t) = F_{in}(t) + F_{ex}(t) \tag{2.25}$$

where $F(t)$ is the total force on the particles includes internal F_{in} and external F_{ex} force. When the internal force includes a random force $\eta(t)$ and a systematic force $F_{sys}(x, v, t)$ depends on the state of particle motion,

$$F_{in}(t) = F_{sys}(x, v) + \eta(t) \tag{2.26}$$

In a simple system, F_{sys} only contains a drift force $m\gamma v(t)$ act in the opposite direction to its motion to prevent large velocity fluctuations from building up. Therefore, the expression of F_{in} is

$$F_{in} = -m\gamma v(t) + \eta(t) \tag{2.27}$$

We then have the Langevin Equation as:

$$m\dot{v} = -m\gamma v(t) + \eta(t) + F_{ex}(t) \tag{2.28}$$

In this equation, v(t) represents the velocity of the particle, and m denotes its mass.

The parameter γ is a positive constant referred to as the friction coefficient or drift, which characterizes the effect of friction on the particle's motion. The term $\eta(t)$ denotes a 'truly random' force or noise independent of the state of motion of the particle. It has a 1st moment of zero and 2nd moment proportional to thermal fluctuations with a factor of Γ, which, according to fluctuation-dissipation theorem, is $\Gamma = 2m\gamma k_B T$,

$$\begin{aligned} \mathbb{E}\left[\eta(t)\right] &= 0 \\ \mathbb{E}\left[\eta(t)\eta(t')\right] &= \Gamma\delta(t-t') \end{aligned} \tag{2.29}$$

Finally, F_{ex} represents the result of all external applied forces acting on individual particles, which we consider identical throughout the paper.

From solving the Langevin Equation, the velocity of individual particle $v(t)$, mean velocity $\mathbb{E}\left[v(t)\right]$ and mean position $\mathbb{E}\left[x(t)\right]$ of the ensemble can be expressed as: [195, at eq. (2.19, 3.3 and 11.14)]

$$\begin{aligned} v(t) &= v_o \mathrm{e}^{-\gamma t} + \frac{1}{m}\int_0^t \mathrm{d}t' \mathrm{e}^{-\gamma(t-t')}\left[\eta(t') + F_{ex}(t')\right] \\ \mathbb{E}\left[v(t)\right] &= v_o \mathrm{e}^{-\gamma t} + \mathbb{E}\left[\frac{1}{m}\int_0^t \mathrm{d}t' \mathrm{e}^{-\gamma(t-t')}\left[\eta(t') + F_{ex}(t')\right]\right] \\ &= v_o \mathrm{e}^{-\gamma t} + \frac{1}{m}\int_0^t \mathrm{d}t' \mathrm{e}^{-\gamma(t-t')} F_{ex}(t') \\ \mathbb{E}\left[x(t)\right] &= x_0 + \frac{v_o}{\gamma}(1-\mathrm{e}^{-\gamma t}) + \frac{1}{m}\int_0^t \mathrm{d}t' \int_0^{t'} \mathrm{d}t'' \mathrm{e}^{-\gamma(t'-t'')} F_{ex}(t'') \end{aligned} \tag{2.30}$$

From the velocity $v(t)$, the temporal correlation of velocity $\mathbb{E}\left[v(t)v(t')\right]$, the mean square average of the position $\mathbb{E}\left[x(t)^2\right]$, and the variance of the position distribution $\mathbb{V}[x(t)]$ exhibit following relations: [195, at eq. (15.2)] [196, at eq. (2.186)]

$$\begin{aligned} \mathbb{E}\left[x(t)^2\right] &= x_0^2 + \int_0^t \mathrm{d}t_1 \int_0^t \mathrm{d}t_2\, \mathbb{E}\left[v(t_1)v(t_2)\right] \\ \mathbb{V}[x(t)] &= \mathbb{E}\left[x(t)^2\right] - \mathbb{E}\left[x(t)\right]^2 \end{aligned} \tag{2.31}$$

For any stochastic process exhibiting the Markov Chain characteristic, and when all particles in the system have the same initial conditions of position $x(t = 0) = x_0$ and velocity $v(t = 0) = v_0$, as:

$$\mathbb{P}(x, v, t = 0) = \delta(x - x_0)\delta(v - v_o) \tag{2.32}$$

the probability distribution function at any given time t can be represented by a Gaussian function. This Gaussian distribution depends on the known mean $\mathbb{E}[x(t)]$ and variance $\mathbb{V}[x(t)]$, for that specific moment.

$$\begin{aligned}
\mathbb{P}(x, t|x_0, t = 0) &= \int_{-\infty}^{\infty} \mathbb{P}(x, v, t|x_0, v_o, t = 0)\, \mathrm{d}v \\
&= \frac{1}{\sqrt{2\pi\mathbb{V}[x(t)]}} \exp\left(-\frac{[x - \mathbb{E}[x(t)]]^2}{2\mathbb{V}[x(t)]}\right) \\
&= \mathcal{N}\left(x; \mu = \mathbb{E}[x(t)], \sigma^2 = \mathbb{V}[x(t)]\right)
\end{aligned} \tag{2.33}$$

According to the Eq. 2.22, $\mathbb{P}(x, t|x_0, v_o)$ at any time t can be rewritten as:

$$\begin{aligned}
\mathbb{E}[x(t)] &= x_0 + \int_0^t \mathbb{E}[v(t)]\ \mathrm{d}t \\
\mathbb{V}[x(t)] &= \int_0^t J(t)\, \mathrm{d}t \\
\mathbb{P}(x, t|x_0, v_o) &= \mathcal{N}\left(x; \mu = x_0 + \int_0^t \mathbb{E}[v(t)]\ \mathrm{d}t, \sigma^2 = \int_0^t J(t)\, \mathrm{d}t\right)
\end{aligned} \tag{2.34}$$

with the initial conditions according to Eq. 2.32,

$$\begin{aligned}
\mathbb{E}[x(0)] &= x_0 \\
\mathbb{V}[x(0)] &= 0
\end{aligned} \tag{2.35}$$

To obtain the transition probability $\mathbb{P}(\Delta x, t_2, t_1)$ between t_1 and t_2, we apply the Fourier

transform to both sides of Eq. 2.9,

$$\mathcal{F}\left[\mathbb{P}(x_2, t_2|x_0, t=0)\right] = \mathcal{F}\left[\mathbb{P}(x_1, t_1|x_0, t=0)\right]\mathcal{F}\left[\mathbb{P}(\Delta x, t_2, t_1)\right] \tag{2.36}$$

so

$$\mathbb{P}(\Delta x, t_2, t_1) = \mathcal{F}^{-1}\left[\frac{\mathcal{F}\left[\mathbb{P}(x_2, t_2|x_0, t=0)\right]}{\mathcal{F}\left[\mathbb{P}(x_1, t_1|x_0, t=0)\right]}\right] \tag{2.37}$$

Considering the special property of Gaussian-like function in Fourier transform,

$$\mathcal{F}\left[\mathcal{N}\left(x; \mu, \sigma^2\right)\right] = \mathrm{e}^{-\frac{\sigma^2}{2}q^2 - i\mu q} \tag{2.38}$$

$\mathbb{P}(\Delta x, t_2, t_1)$ is obtained as

$$\begin{aligned}
\mathbb{P}(\Delta x, t_2, t_1) &= \mathcal{F}^{-1}\left[\frac{\exp\left(-\frac{\mathbb{V}[x(t_2)]}{2}q^2 - i\mathbb{E}\left[x(t_2)\right]q\right)}{\exp\left(-\frac{\mathbb{V}[x(t_1)]}{2}q^2 - i\mathbb{E}\left[x(t_1)\right]q\right)}\right] \\
&= \mathcal{F}^{-1}\left[\exp\left(-\frac{\left(\mathbb{V}[x(t_2)] - \mathbb{V}[x(t_1)]\right)}{2}q^2 - i\left(\mathbb{E}\left[x(t_2)\right] - \mathbb{E}\left[x(t_1)\right]\right)q\right)\right] \\
&= \mathcal{N}\left(\Delta x; \mu = \mathbb{E}\left[x(t_2)\right] - \mathbb{E}\left[x(t_1)\right], \sigma^2 = \mathbb{V}[x(t_2)] - \mathbb{V}[x(t_1)]\right)
\end{aligned} \tag{2.39}$$

The transition probability between two Gaussian-like probability functions preserves the Gaussian shape, and the resulting Gaussian function will have its mean shifted by the difference between the means of the original Gaussian functions ($\mathbb{E}\left[x(t_2)\right] - \mathbb{E}\left[x(t_1)\right]$) and its variance scaled by the difference between the variances of the original Gaussian functions ($\mathbb{V}[x(t_2)] - \mathbb{V}[x(t_1)]$) based on the specific values of the original Gaussian functions.

We then define the change in the mean position of a particle as time evolves from t_1 to t_2, $\mathbb{E}\left[x(t_2)\right] - \mathbb{E}\left[x(t_1)\right]$, as the integration of mean velocity from t_1 to t_2; the change in the variance of the position distribution $\mathbb{V}[x(t_2)] - \mathbb{V}[x(t_1)]$, as the integration of dynamical transport coefficient $J\left(t\right)$ from t_1 to t_2:

$$\mathbb{P}(\Delta x, t_1, t_2) = \mathcal{N}\left(\Delta x; \mu = \int_{t_1}^{t_2} \mathbb{E}\left[v(t)\right]\, \mathrm{d}t, \sigma^2 = \int_{t_1}^{t_2} J(t)\, \mathrm{d}t\right) \tag{2.40}$$

so that relation Eq. 2.9 is clearly satisfied as follow:

$$\begin{aligned}
\mathbb{P}(x_2, t_2 | x_0, t = 0) &= \int_{-\infty}^{\infty} \mathbb{P}(x_1, t_1 | x_0, t = 0) \mathbb{P}(\Delta x, t_1, t_2)\, \mathrm{d}x_1 \\
&= \left(\mathcal{N}\left(x_1; \mu = x_0 + \int_0^{t_1} \mathbb{E}\left[v(t)\right]\, \mathrm{d}t, \sigma^2 = \int_0^{t_1} J(t)\, \mathrm{d}t\right) * \mathcal{N}\left(\Delta x; \mu = \int_{t_1}^{t_2} \mathbb{E}\left[v(t)\right]\, \mathrm{d}t, \sigma\right.\right. \\
&= \mathcal{N}\left(x_2; \mu = x_0 + \int_0^{t_2} \mathbb{E}\left[v(t)\right]\, \mathrm{d}t, \sigma^2 = \int_0^{t_2} J(t)\, \mathrm{d}t\right)
\end{aligned} \tag{2.41}$$

which is consistent with the definition in Eq. 2.34.

In Eq. 2.40, we define the change in the mean position of a particle as time evolves from t_1 to t_2, $\mathbb{E}\left[x(t_2)\right] - \mathbb{E}\left[x(t_1)\right]$, as the integration of mean velocity from t_1 to t_2; the change in variance of the position distribution $\mathbb{V}[x(t_2)] - \mathbb{V}[x(t_1)]$, as the integration of the dynamical transport coefficient $J\left(t\right)$ from t_1 to t_2:

The mathematical and physical definition of the transport coefficient $J\left(t\right)$ is shown as:

$$\begin{aligned}
J(t) &= \frac{d}{dt}(\mathbb{V}[x(t)]) \\
&= 2\left(\mathbb{E}\left[x(t)v(t)\right] - \mathbb{E}\left[x(t)\right]\mathbb{E}\left[v(t)\right]\right) = 2\mathrm{Cov}\left[x(t), v(t)\right] \\
&= 2\left(\mathbb{E}\left[\int_0^t v(t')v(t)\, \mathrm{d}t'\right] - \mathbb{E}\left[\int_0^t v(t')\, \mathrm{d}t'\right]\mathbb{E}\left[v(t)\right]\right) \\
&= 2\left(\int_0^t \mathbb{E}\left[v(t')v(t)\right]\, \mathrm{d}t' - \int_0^t \mathbb{E}\left[v(t')\right]\mathbb{E}\left[v(t)\right]\, \mathrm{d}t'\right) \\
&= 2\int_0^t \mathrm{Cov}\left[v(t), v(t')\right]\, \mathrm{d}t'
\end{aligned} \tag{2.42}$$

where $\mathrm{Cov}\left[x(t), v(t)\right]$ is the covariance of $x(t)$ and $v(t)$ and $\int_0^t \mathrm{Cov}\left[v(t), v(t')\right]\, \mathrm{d}t'$ is a generalized form of Green-Kubo formula [195, at eq. (15.3)].

From Eq. 2.40, we have following expression:

$$\mathbb{P}(\Delta x, t_1, t_2) = \frac{1}{\sqrt{2\pi \int_{t_1}^{t_2} J(t)\,\mathrm{d}t}} \exp\left(-\frac{\left[\Delta x - \int_{t_1}^{t_2} \mathbb{E}\left[v(t)\right]\,\mathrm{d}t\right]^2}{2\int_{t_1}^{t_2} J(t)\,\mathrm{d}t} \right) \tag{2.43}$$

At the end, the two-time correlation function $c_1(q, t_1, t_2)$, at specific scattering vector q, can be expressed as:

$$\begin{aligned} c_1(q, t_1, t_2) &= \int_{-\infty}^{\infty} \mathbb{P}(\Delta x, t_1, t_2) \mathrm{e}^{iq\Delta x}\,\mathrm{d}\Delta x \\ &= \frac{1}{\sqrt{2\pi \int_{t_1}^{t_2} J(t)\,\mathrm{d}t}} \int_{-\infty}^{\infty} \exp\left(-\frac{\left[\Delta x - \int_{t_1}^{t_2} \mathbb{E}\left[v(t)\right]\,\mathrm{d}t\right]^2}{2\int_{t_1}^{t_2} J(t)\,\mathrm{d}t} + iq\Delta x \right) \mathrm{d}\Delta x \\ &= \mathrm{e}^{-\frac{1}{2}q^2 \int_{t_1}^{t_2} J(t)\,\mathrm{d}t} \mathrm{e}^{iq\int_{t_1}^{t_2} \mathbb{E}[v(t)]\,\mathrm{d}t} \end{aligned} \tag{2.44}$$

Compared to Eq. 2.39, 2.44 is equivalent to the Fourier transform of the transition probability. In other words, the correlation function measured in XPCS is the ratio between the Fourier transform of the probability function of a particle at t_1 and t_2.

$$c_1(q, t_1, t_2) = \mathcal{F}\left[\mathbb{P}(\Delta x, t_1, t_2)\right] = \frac{\mathcal{F}\left[\mathbb{P}(x_2, t_2 | x_0, t = 0)\right]}{\mathcal{F}\left[\mathbb{P}(x_1, t_1 | x_0, t = 0)\right]} \tag{2.45}$$

According to Eq. 2.44, the $c_1(q, t_1, t_2)$ could be factorized into two terms:

$$c_1(q, t_1, t_2) = c_{1,in}(q, t_1, t_2) c_{1,ex}(q, t_1, t_2) \tag{2.46}$$

where $c_{1,in}(q, t_1, t_2)$ is the correlation function attributed to internal forces, including the systematic dynamics as well as the thermal fluctuations experienced by particles, defined as:

$$c_{1,in}(q, t_1, t_2) = \mathrm{e}^{-\frac{1}{2}q^2 \int_{t_1}^{t_2} J(t)\,\mathrm{d}t} \tag{2.47}$$

and $c_{1,ex}(q,t_1,t_2)$ is the correlation function attributed to external drives defined as:

$$c_{1,ex}(q,t_1,t_2) = \mathrm{e}^{iq\int_{t_1}^{t_2}\mathbb{E}[v(t)]\,\mathrm{d}t} \tag{2.48}$$

In summary, the $c_1(q,t_1,t_2)$ is obtained by following steps:

1. Formalize Langevin equation based force profile of individual particles
2. Calculate $\mathbb{E}[v(t)]$ and $J(t)$ from Langevin equation.
3. Obtain $c_1(q,t_1,t_2)$ by substituting $\mathbb{E}[v(t)]$ and $J(t)$ into equation Eq. 2.44

Equation Eq. 2.44 is the $c_1(q,t_1,t_2)$ for the model of particles with Langevin Dynamics in 1-dimension as a fluid transports with mean velocity ($\mathbb{E}[v(t)]$) due to the bulk movement and transport coefficient $J(t)$ due to molecular random motion.

2.4 $c_1(\vec{q},t_1,t_2)$ in 3-Dimensional Space

To extend the analysis to 3-dimension and derive $c_1(\vec{q},t_1,t_2)$, we start from Langevin equation in 3 dimensions: [195, at eq. (4.9)]

$$m\dot{\vec{v}} = -m\gamma\vec{v} + \eta(t) + \vec{F}_{ex} \tag{2.49}$$

where $\vec{v}$, $\vec{\eta}$ and $\vec{F}_{ex}$ are the vectors consist all Cartesian components. It is noticed that $\vec{\eta}(t)$ is an independent Gaussian white noise. The mean and autocorrelation of the noise are given by the following straightforward generalizations according to Eq. 2.29:

$$\begin{aligned} \mathbb{E}[\vec{\eta}(t)] &= \vec{0} \\ \mathbb{E}\left[\vec{\eta}(t)\otimes\vec{\eta}(t')\right]_{ij} &= \Gamma_{ij}\delta(t-t') \end{aligned} \tag{2.50}$$

where the Cartesian indices i , j run over the values (x, y, z) and Γ_{ij} is the noise strength correlated to direction i , j.

In summary, for the case in the Ornstein–Uhlenbeck process where noises in each dimension are uncorrelated, the partial differential equation can be separated and solved independently as one in 1-dimension.

As the first step of solving $c_1(\vec{q}, t_1, t_2)$ in 3D, the velocity of individual particle $\vec{v}(t)$, mean velocity $\mathbb{E}\left[\vec{v}(t)\right]$, and mean position $\mathbb{E}\left[\vec{r}(t)\right]$ of the ensemble are solved as:

$$\begin{aligned}
\vec{v}(t) &= \vec{v}_o \mathrm{e}^{-\gamma t} + \frac{1}{m}\int_0^t \mathrm{d}t' \mathrm{e}^{-\gamma(t-t')}\left[\vec{\eta}(t') + \vec{F}_{ex}(t')\right] \\
\mathbb{E}\left[\vec{v}(t)\right] &= \vec{v}_o \mathrm{e}^{-\gamma t} + \frac{1}{m}\int_0^t \mathrm{d}t' \mathrm{e}^{-\gamma(t-t')}\vec{F}_{ex}(t') \\
\mathbb{E}\left[\vec{r}(t)\right] &= \vec{r}_o + \frac{\vec{v}_o}{\gamma}(1 - \mathrm{e}^{-\gamma t}) + \frac{1}{m}\int_0^t \mathrm{d}t' \int_0^{t'} \mathrm{d}t'' \mathrm{e}^{-\gamma(t'-t'')}\vec{F}_{ex}(t'')
\end{aligned} \tag{2.51}$$

In Ornstein–Uhlenbeck process without external forces, $F_{ex} = 0$, the mean of position at each axis, $\mathbb{E}\left[\vec{r}(t)\right]_i$, and velocity correlation function $\mathbb{E}\left[v_i(t)v_j(t')\right]$ can be written as:

$$\begin{aligned}
\mathbb{E}\left[\vec{r}(t)\right]_i &= r_{o,i} + \frac{v_{o,i}}{\gamma}(1 - \mathrm{e}^{-\gamma t}) \\
\mathbb{E}\left[\vec{v}(t) \otimes \vec{v}(t')\right]_{ij} &= v_{o,i}v_{o,j}\mathrm{e}^{-\gamma(t+t')} + \\
&\quad \frac{1}{m^2}\int_0^t \mathrm{d}t_1 \int_0^{t'} \mathrm{d}t_2 \, \mathrm{e}^{-\gamma(t-t_1)-\gamma(t'-t_2)}\mathbb{E}\left[\eta_i(t_1)\eta_j(t_2)\right]
\end{aligned} \tag{2.52}$$

The outer product of mean of velocity $\mathbb{E}\left[\vec{v}(t)\right] \otimes \mathbb{E}\left[\vec{v}(t')\right]$ can be written as:

$$\left[\mathbb{E}\left[\vec{v}(t)\right] \otimes \mathbb{E}\left[\vec{v}(t')\right]\right]_{ij} = v_{o,i}v_{o,j}\mathrm{e}^{-\gamma(t+t')} \tag{2.53}$$

The cross-covariance matrix of velocity at t and t' is calculated as:

$$\begin{aligned}
\mathrm{Cov}\left[\vec{v}(t),\vec{v}(t')\right]_{ij} &= \mathbb{E}\left[\vec{v}(t)\otimes\vec{v}(t')\right]_{ij} - \left[\mathbb{E}\left[\vec{v}(t)\right]\otimes\mathbb{E}\left[\vec{v}(t')\right]\right]_{ij} \\
&= \frac{1}{m^2}\int_0^t \mathrm{d}t_1 \int_0^{t'} \mathrm{d}t_2\, \mathrm{e}^{-\gamma(t-t_1)-\gamma(t'-t_2)}\mathbb{E}\left[\eta_i(t_1)\eta_j(t_2)\right] \\
&= \frac{\Gamma_{ij}}{m^2}\int_0^t \mathrm{d}t_1 \int_0^{t'} \mathrm{d}t_2\, \mathrm{e}^{-\gamma(t-t_1)-\gamma(t'-t_2)}\delta(t_1-t_2) \\
&= \frac{\Gamma_{ij}}{2m^2\gamma}(\mathrm{e}^{-\gamma|t-t'|} - \mathrm{e}^{-\gamma(t+t')})
\end{aligned} \tag{2.54}$$

The element $J_{ij}(t)$ in transport coefficient tensor $\underline{J}$ is calculated as:

$$\begin{aligned}
J_{ij}(t) &= 2\int_0^t \mathrm{Cov}\left[\vec{v}(t),\vec{v}(t')\right]_{ij}\,\mathrm{d}t' \\
&= \frac{\Gamma_{ij}}{m^2\gamma}\int_0^t \mathrm{e}^{-\gamma|t-t'|} - \mathrm{e}^{-\gamma(t+t')}\,\mathrm{d}t' \\
&= \frac{\Gamma_{ij}}{m^2\gamma^2}(1-2\mathrm{e}^{-\gamma t}+\mathrm{e}^{-2\gamma t})
\end{aligned} \tag{2.55}$$

Then, the covariance matrix with elements of $\mathbb{V}\left[\vec{r}(t)\right]_{ij}$ can be calculated from integrating $\mathbb{V}\left[\vec{v}(t)\otimes\vec{v}(t')\right]_{ij}$:

$$\begin{aligned}
\mathbb{V}\left[\vec{r}(t)\right]_{ij} &= \int_0^t \mathrm{d}t_1 \int_0^t \mathrm{d}t_2\, \mathrm{Cov}\left[\vec{v}(t),\vec{v}(t')\right]_{ij} \\
&= \frac{\Gamma_{ij}}{2m^2\gamma^3}(2\gamma t - 3 + 4\mathrm{e}^{-\gamma t} - \mathrm{e}^{-2\gamma t}) \\
\underline{\mathbb{V}\left[\vec{r}(t)\right]} &= \frac{1}{2m^2\gamma^3}(2\gamma t - 3 + 4\mathrm{e}^{-\gamma t} - \mathrm{e}^{-2\gamma t})\left(\underline{\Gamma}_{i=j} + \underline{\Gamma}_{i\neq j}\right) \\
\underline{\Gamma}_{i=j} = \begin{bmatrix} \Gamma_{xx} & 0 & 0 \\ 0 & \Gamma_{yy} & 0 \\ 0 & 0 & \Gamma_{zz} \end{bmatrix}, &\underline{\Gamma}_{i\neq j} = \begin{bmatrix} 0 & \Gamma_{xy} & \Gamma_{xz} \\ \Gamma_{yx} & 0 & \Gamma_{yz} \\ \Gamma_{zx} & \Gamma_{zy} & 0 \end{bmatrix}
\end{aligned} \tag{2.56}$$

where $\left(\underline{\Gamma}_{i=j}\right)$ is the variances of the individual dimension and $\underline{\Gamma}_{i\neq j}$ is the covariances across different dimensions.

If we assume the noise strength Γ in different directions are truly randomized and uncorrelated, the autocorrelation of noise $\mathbb{E}\left[\vec{\eta}(t) \otimes \vec{\eta}(t')\right]_{ij}$ can be written as: [195, at eq. (4.11)]

$$\mathbb{E}\left[\vec{\eta}(t) \otimes \vec{\eta}(t')\right]_{ij} = \Gamma_{ij}\delta_{ij}\delta(t-t') \tag{2.57}$$

δ_{ij} is the Kronecker delta.

With the uncorrelated noise assumption, the $\mathbb{V}\left[\vec{r}(t)\right]_{ij}$ can be expressed as follow, according equation (Eq. 2.56):

$$\begin{aligned}
\mathbb{V}\left[\vec{r}(t)\right]_{ij} &= \frac{1}{2m^2\gamma^3}(2\gamma t - 3 + 4\mathrm{e}^{-\gamma t} - \mathrm{e}^{-2\gamma t}) \begin{bmatrix} \Gamma_{xx} & 0 & 0 \\ 0 & \Gamma_{yy} & 0 \\ 0 & 0 & \Gamma_{zz} \end{bmatrix} \\
&= S\left(t\right) \begin{bmatrix} \Gamma_{xx} & 0 & 0 \\ 0 & \Gamma_{yy} & 0 \\ 0 & 0 & \Gamma_{zz} \end{bmatrix} \\
\mathbb{V}\left[\vec{r}(t)\right]_{ii} &= S\left(t\right)\Gamma_{ii}
\end{aligned} \tag{2.58}$$

where $S\left(t\right)$ abbreviates for $\frac{1}{2m^2\gamma^3}(2\gamma t - 3 + 4\mathrm{e}^{-\gamma t} - \mathrm{e}^{-2\gamma t})$ in Eq. 2.58.

Given the $\mathbb{E}\left[\vec{r}(t)\right]_i$ from Eq. 2.52 and $\mathbb{V}\left[\vec{r}(t)\right]_{ii}$ from Eq. 2.58, similar to Eq. 2.33, the $\mathbb{P}(\vec{r}, t)$ can be expressed as follow:

$$\begin{aligned}
\mathbb{P}(\vec{r}, t) &= \prod_{i}^{x,y,z} \mathcal{N}\left(r_i; \mu = \mathbb{E}\left[\vec{r}(t)\right]_i, \sigma^2 = \mathbb{V}\left[\vec{r}(t)\right]_{ii}\right) \\
&= \prod_{i}^{x,y,z} \mathcal{N}\left(r_i; \mu = r_{o,i} + \frac{v_{o,i}}{\gamma}(1 - \mathrm{e}^{-\gamma t}), \sigma^2 = \Gamma_{ii} S\left(t\right)\right)
\end{aligned} \tag{2.59}$$

The transition probability function

$$\mathbb{P}(\Delta\vec{r}, t_2, t_1) = \prod_i^{x,y,z} \mathcal{N}\left(\Delta r_i; \mu = \mathbb{E}\left[r_i(t_2)\right] - \mathbb{E}\left[r_i(t_1)\right], \sigma^2 = \Gamma_{ii}\left(S\left(t_2\right) - S\left(t_1\right)\right)\right) \quad (2.60)$$

The $J_{ii}(t)$ and $\mathbb{E}\left[v_i(t)\right]$ can be expressed as:

$$\begin{aligned} J_{ii}(t) &= \frac{d}{dt}\left(\Gamma_{ii} S\left(t\right)\right) = \frac{\Gamma_{ii}}{m^2\gamma^2}(1 - \mathrm{e}^{-\gamma t})^2 \\ \mathbb{E}\left[v_i(t)\right] &= \frac{d}{dt}\left(\mathbb{E}\left[r_i(t_2)\right]\right) = \frac{v_{o,i}}{\gamma}(1 - \mathrm{e}^{-\gamma t}) \end{aligned} \quad (2.61)$$

Substituting $J_{ii}(t)$ and $\mathbb{E}\left[v_i(t)\right]$ to equation Eq. 2.60, we have:

$$\mathbb{P}(\Delta\vec{r}, t_2, t_1) = \prod_i^{x,y,z} \mathcal{N}\left(\Delta r_i; \mu = \int_{t_1}^{t_2} \mathbb{E}\left[\vec{v}_i(t)\right]\, \mathrm{d}t, \sigma^2 = \int_{t_1}^{t_2} J_{ii}(t)\, \mathrm{d}t\right) \quad (2.62)$$

The two-time correlation function $c_1(\vec{q}, t_1, t_2)$ obtained through XPCS will be:

$$\begin{aligned} c_1(\vec{q}, t_1, t_2) &= \int_{-\infty}^{\infty} \mathbb{P}(\Delta\vec{r}, t_1, t_2) \mathrm{e}^{i\vec{q}\cdot\Delta\vec{r}}\, \mathrm{d}\Delta\vec{r} \\ &= \prod_i^{x,y,z} \int_{-\infty}^{\infty} \mathcal{N}\left(\Delta r_i; \mu = \int_{t_1}^{t_2} \mathbb{E}\left[v_i(t)\right]\, \mathrm{d}t, \sigma^2 = \int_{t_1}^{t_2} J_{ii}(t)\, \mathrm{d}t\right) \mathrm{e}^{iq_i\Delta r_i}\, \mathrm{d}\Delta r_i \\ &= \prod_i^{x,y,z} \int_{-\infty}^{\infty} \frac{1}{\sqrt{2\pi \int_{t_1}^{t_2} J_{ii}(t)\, \mathrm{d}t}} \exp\left(-\frac{\left[\Delta r_i - \int_{t_1}^{t_2} \mathbb{E}\left[v_i(t)\right]\, \mathrm{d}t\right]^2}{2\int_{t_1}^{t_2} J_{ii}(t)\, \mathrm{d}t} + iq_i\Delta r_i\right) \mathrm{d}\Delta r_i \\ &= \prod_i^{x,y,z} \mathrm{e}^{-\frac{1}{2}q_i^2 \int_{t_1}^{t_2} J_{ii}(t)\, \mathrm{d}t} \mathrm{e}^{iq_i \int_{t_1}^{t_2} \mathbb{E}[v_i(t)]\, \mathrm{d}t} \\ &= \mathrm{e}^{-\frac{1}{2}\int_{t_1}^{t_2}\left(q_x^2 J_{xx} + q_y^2 J_{yy} + q_z^2 J_{zz}\right)\mathrm{d}t} \mathrm{e}^{i\int_{t_1}^{t_2} q_x\mathbb{E}[v_x(t)] + q_y\mathbb{E}\left[v_y(t)\right] + q_z\mathbb{E}[v_z(t)]\, \mathrm{d}t} \\ &= \mathrm{e}^{-\frac{1}{2}\int_{t_1}^{t_2}(\vec{q}\cdot\underline{J}(t)\cdot\vec{q}^{\mathrm{T}})\mathrm{d}t} \mathrm{e}^{i\vec{q}\cdot\int_{t_1}^{t_2}\mathbb{E}[\vec{v}(t)]\, \mathrm{d}t} \end{aligned} \quad (2.63)$$

where transport coefficient tensor $\underline{J}$ is defined as:

$$\underline{J}(t) = \begin{bmatrix} J_{xx}(t) & 0 & 0 \\ 0 & J_{yy}(t) & 0 \\ 0 & 0 & J_{zz}(t) \end{bmatrix} \tag{2.64}$$

If we have assumed that the noise strength is isotropic ($\Gamma_{ii} = 2m\gamma k_B T$) and transport coefficient is the same for all the components $\left(J = 3J_{xx} = 3J_{yy} = 3J_{zz}\right)$ without external drive $\left(\mathbb{E}\left[v_x(t)\right] = \mathbb{E}\left[v_y(t)\right] = \mathbb{E}\left[v_z(t)\right] = 0\right)$, based on equation Eq. 2.61, $c_1(\vec{q}, t_1, t_2)$ can be expressed as:

$$c_1(\vec{q}, t_1, t_2) = \mathrm{e}^{-\frac{1}{6}(q_x^2+q_y^2+q_z^2)\int_{t_1}^{t_2} J(t)\,\mathrm{d}t} \tag{2.65}$$

The term

$$q^2 = |\vec{q}|^2 = q_x^2 + q_y^2 + q_z^2 \tag{2.66}$$

defines an Ewald sphere in the reciprocal space where $c_1(\vec{q}, t_1, t_2)$ measured from any point in the sphere are equivalent in the isotropic system.

The $c_2\left(\vec{q}, t_1, t_2\right)$ can then be expressed using the Siegert relation Eq. 2.6 as follows:

$$c_2(\vec{q}, t_1, t_2) = 1 + \beta \mathrm{e}^{-\frac{1}{3}(q_x^2+q_y^2+q_z^2)\int_{t_1}^{t_2} J(t)\,\mathrm{d}t} \tag{2.67}$$

In the Ornstein−Uhlenbeck process, assuming noise strength in each direction equals to the case in 1-dimension, $\Gamma_{ii} = 2m\gamma k_B T$, J(t) can be expressed as:

$$J(t) = 3J_{ii}(t) = 6\frac{k_B T}{m\gamma}(1 - \mathrm{e}^{-\gamma t})^2 \tag{2.68}$$

Substituting the diffusion constant defined as $D = \frac{k_B T}{m\gamma}$, the $J(t)$ is obtained as:

$$J(t) = 6D(1 - \mathrm{e}^{-\gamma t})^2 \tag{2.69}$$

As $t \to \infty$ where the system reaches equilibrium, $J\,(t)$ equals to

$$J(t) = 6D \tag{2.70}$$

Based on the equation, we can conclude that, under the conditions of isotropic and uncorrelated noise, the transport coefficient $J\,(t)$ in 3-dimensional space is related to the transport coefficient in 1-dimension, $J_{ii}(t) = 2D$, as follows,

$$J(t) = nJ_{ii}(t) \triangleq J_n(t) \tag{2.71}$$

where n stands for the number of dimensions in the system.

Therefore, substituting the equation Eq. 2.71 to equation Eq. 2.63, the $c_1(\vec{q}, t_1, t_2)$ in 3 dimensions with isotropic and uncorrelated noise in each direction can be expressed as:

$$\begin{aligned} c_1(\vec{q}, t_1, t_2) &= \mathrm{e}^{-\frac{1}{2}q^2 \int_{t_1}^{t_2} (nJ_{ii}(t))\,\mathrm{d}t} \mathrm{e}^{i\vec{q}\cdot\int_{t_1}^{t_2} \mathbb{E}[\vec{v}(t)]\,\mathrm{d}t} \\ &= \mathrm{e}^{-\frac{1}{2}q^2 \int_{t_1}^{t_2} J_{nD}(t)\,\mathrm{d}t} \mathrm{e}^{i\vec{q}\cdot\int_{t_1}^{t_2} \mathbb{E}[\vec{v}(t)]\,\mathrm{d}t} \end{aligned} \tag{2.72}$$

Here, we expand the physical picture from 1 dimension to 3 dimensions. The equation Eq. 2.72 is fundamental for further derivation for the equilibrium systems in complex fluid environments, such as laminar or shear banding flow.

2.5 $c_1(\vec{q}, t_1, t_2)$ in Homodyne Scattering

2.5.1 Generalized Equation for Homodyne Scattering

In the Rheo-XPCS experiment, the laminar flow system can be conceptualized as comprising ensembles of flow layers across the gap ($0 \leq y \leq h$), each possessing the same transport coefficient $J(t)$ but different mean velocities $\mathbb{E}[\vec{v}(y,t)]$. The correlation function can be expressed as:

$$\begin{aligned} c_1(\vec{q}, t_1, t_2) &= \sum_{y_1=1}^{h} \sum_{y_2=1}^{h} \frac{\Delta y_1}{h} \frac{\Delta y_2}{h} c_{1,y_1-y_2}(\vec{q}, t_1, t_2) \\ &= \frac{1}{h^2} \sum_{y_1=1}^{h} \sum_{y_2=1}^{h} \mathrm{e}^{-\frac{1}{2}q^2 \int_{t_1}^{t_2} J(t)\,\mathrm{d}t} \mathrm{e}^{i\vec{q}\cdot\int_{t_1}^{t_2} \mathbb{E}[\vec{v}(y_1,t)]-\mathbb{E}[\vec{v}(y_2,t)]\,\mathrm{d}t} \Delta y_1 \Delta y_2 \\ &= \frac{1}{h^2} \int_0^h \int_0^h \mathrm{e}^{-\frac{1}{2}q^2 \int_{t_1}^{t_2} J(t)\,\mathrm{d}t} \mathrm{e}^{i\vec{q}\cdot\int_{t_1}^{t_2} \mathbb{E}[\vec{v}(y_1,t)]-\mathbb{E}[\vec{v}(y_2,t)]\,\mathrm{d}t} \,\mathrm{d}y_1 dy_2 \end{aligned} \tag{2.73}$$

where $c_{1,y_1-y_2}(\vec{q}, t_1, t_2)$ denotes as the correlation function between ensembles at position y_1 and y_2 in the gap.

Depending on its position in the gap (y) between the rotor and stator and taking into account the non-equilibrium nature of the system, where the shear rate changes over time, the velocity can be mathematically expressed as follows:

$$\vec{v}(y,t) = v_x(y,t) = \dot{\gamma}(t) y \tag{2.74}$$

Based on the aforementioned equation, the particle mean displacement in Equation Eq. 2.34 can be derived as follows:

$$\int_{t_1}^{t_2} \mathbb{E}\left[\vec{v}(y,t)\right]\,\mathrm{d}t = \int_{t_1}^{t_2} v_x(t)\,\mathrm{d}t = y \int_{t_1}^{t_2} \dot{\gamma}(t)\,\mathrm{d}t \tag{2.75}$$

In a homogeneous system with laminar flow that produces homodyne scattering, the

integration of all the ensemble coordinates in Equation Eq. 2.73 can be transformed from individual particles to spatial coordinates across the gap in the Couette geometry from 0 to h.

$$\begin{aligned} c_1(\vec{q},t_1,t_2) &= \frac{1}{h^2}\int_0^h\int_0^h \mathrm{e}^{-\frac{1}{2}q^2\int_{t_1}^{t_2}J(t)\,\mathrm{d}t}\mathrm{e}^{i\vec{q}\cdot\int_{t_1}^{t_2}\mathbb{E}[\vec{v}(y_1,t)]-\mathbb{E}[\vec{v}(y_2,t)]\,\mathrm{d}t}\,\mathrm{d}y_1 dy_2 \\ &= \left[\mathrm{e}^{-\frac{1}{2}q^2\int_{t_1}^{t_2}J(t)\,\mathrm{d}t}\right]\frac{1}{h^2}\int_0^h\int_0^h \mathrm{e}^{\left[iq\int_{t_1}^{t_2}\dot{\gamma}(t)\cos(\phi(t))\,\mathrm{d}t\right](y_1-y_2)}\,\mathrm{d}y_1 dy_2 \\ &= \left[\mathrm{e}^{-\frac{1}{2}q^2\int_{t_1}^{t_2}J(t)\,\mathrm{d}t}\right]\mathrm{sinc}^2\left[\frac{1}{2}qh\int_{t_1}^{t_2}\dot{\gamma}(t)\cos(\phi(t))\,\mathrm{d}t\right] \end{aligned} \tag{2.76}$$

where ϕ is the angle between shear/flow direction and $\vec{q}$.

With Siegert Relation Eq. 2.6, the $c_2(\vec{q},t_1.t_2)$ can be expressed as:

$$\begin{aligned} c_2(\vec{q},t_1,t_2) &= 1+\beta|c_1(\vec{q},t_1,t_2)|^2 \\ &= 1+\beta\left[\mathrm{e}^{-q^2\int_{t_1}^{t_2}J(t)\,\mathrm{d}t}\right]\mathrm{sinc}^4\left[\frac{1}{2}qh\int_{t_1}^{t_2}\dot{\gamma}(t)\cos(\phi\,(t))\,\mathrm{d}t\right] \end{aligned} \tag{2.77}$$

2.5.2 Simplified Equation for Homodyne Scattering

In the Rheo-XPCS experiment for system under strong deformation, the ensembles at different positions exhibit a great difference in velocity. Therefore, Eq. 2.73 is simplified by ignoring the cross-correlation between different layers where $y_1 \neq y_2$,

$$\begin{aligned} c_1(\vec{q},t_1,t_2) &= \sum_{y=y_1=y_2=1}^{h}\frac{\Delta y}{h}c_{1,y}(\vec{q},t_1,t_2) = \frac{1}{h}\sum_{y=1}^{h}\mathrm{e}^{-\frac{1}{2}q^2\int_{t_1}^{t_2}J(t)\,\mathrm{d}t}\mathrm{e}^{i\vec{q}\cdot\int_{t_1}^{t_2}\mathbb{E}[\vec{v}(y,t)]\,\mathrm{d}t}\Delta y \\ &= \frac{1}{h}\int_0^h \mathrm{e}^{-\frac{1}{2}q^2\int_{t_1}^{t_2}J(t)\,\mathrm{d}t}\mathrm{e}^{i\vec{q}\cdot\int_{t_1}^{t_2}\mathbb{E}[\vec{v}(y,t)]\,\mathrm{d}t}\,\mathrm{d}y \\ &= \left[\mathrm{e}^{-\frac{1}{2}q^2\int_{t_1}^{t_2}J(t)\,\mathrm{d}t}\right]\frac{1}{h}\int_0^h \mathrm{e}^{\left[q\int_{t_1}^{t_2}\dot{\gamma}(t)\cos(\phi(t))\,\mathrm{d}t\right]iy}\,\mathrm{d}y \\ &= \left[\mathrm{e}^{-\frac{1}{2}q^2\int_{t_1}^{t_2}J(t)\,\mathrm{d}t}\right]\mathrm{sinc}\left[\frac{1}{2}qh\int_{t_1}^{t_2}\dot{\gamma}(t)\cos(\phi(t))\,\mathrm{d}t\right]\mathrm{e}^{i\frac{1}{2}qh\int_{t_1}^{t_2}\dot{\gamma}(t)\cos(\phi(t))\,\mathrm{d}t} \end{aligned} \tag{2.78}$$

where ϕ is the angle between shear/flow direction and $\vec{q}$.

With Siegert Relation Eq. 2.6, the $c_2(\vec{q}, t_1.t_2)$ can be expressed as:

$$\begin{aligned} c_2(\vec{q}, t_1, t_2) &= 1 + \beta |c_1(\vec{q}, t_1, t_2)|^2 \\ &= 1 + \beta \left[\mathrm{e}^{-q^2 \int_{t_1}^{t_2} J(t)\, \mathrm{d}t} \right] \mathrm{sinc}^2 \left[\frac{1}{2} qh \int_{t_1}^{t_2} \dot{\gamma}(t) \cos\left(\phi\left(t\right)\right) \mathrm{d}t \right] \end{aligned} \tag{2.79}$$

To consider the equilibrium condition of standard diffusion under constant shear where shear rate is constant as $\dot{\gamma}(t) \cos\left(\phi\left(t\right)\right) = \dot{\gamma} \cos\left(\phi\right)$ and $J(t) = 6D$, the $c_2(\vec{q}, t_1, t_2)$ can be expressed as:

$$c_2(\vec{q}, t_1, t_2) = 1 + \beta \left[\mathrm{e}^{-6q^2 D(t_2 - t_1)} \right] \mathrm{sinc}^2 \left[\frac{1}{2} qh \cos\left(\phi\right) \dot{\gamma}(t_2 - t_1) \right] \tag{2.80}$$

Substituting the absolute time (t_2, t_1) by delayed time $\tau = t_2 - t_1$, the $c_2(\vec{q}, t_1, t_2)$ is reduced to the one-time correlation function, $g_2(\vec{q}, \tau)$ as:

$$g_2(\vec{q}, \tau) = 1 + \beta \left[\mathrm{e}^{-6q^2 D\tau} \right] \mathrm{sinc}^2 \left[\frac{1}{2} qh \cos\left(\phi\right) \dot{\gamma}\tau \right] \tag{2.81}$$

The Eq. 2.81 mentioned above is a commonly used homodyne equation that has been widely applied in various studies.

2.6 Systems with Multiple-Compositions in Non-Equilibrium

2.6.1 $c_2(\vec{q}, t_1, t_2)$ for Heterodyne Scattering with n-Compositions

We can extend the analysis to include the time-dependent fraction of each composition, $x_n(t)$. The total scattered electromagnetic wave, $E(\vec{q}, t)$, at a given time t can then be expressed as a compositionally weighted contribution from the scattered electromagnetic fields of each

composition, $E_n(\vec{q},t)$, as follows:

$$\begin{aligned} E(\vec{q},t) &= \sum_{n=1}^{N} x_n(t) E_n(\vec{q},t) \\ 1 &= \sum_{n=1}^{N} x_n(t) \end{aligned} \tag{2.82}$$

The ensemble average intensity could be calculated as follows:

$$\begin{aligned} \mathbb{E}\left[I(\vec{q},t)\right] &= \mathbb{E}\left[E(\vec{q},t)E^*(\vec{q},t)\right] \\ &= \mathbb{E}\left[\sum_{n=1}^{N} x_n(t)E_n(\vec{q},t) \sum_{m=1}^{N} x_m(t)E_m^*(\vec{q},t)\right] \\ &= \sum_{n=1}^{N} x_n^2(t)\mathbb{E}\left[\left|E_n(\vec{q},t)\right|^2\right] + \sum_{n=1}^{N}\sum_{m\neq n}^{N} x_n(t)x_m(t)\mathbb{E}\left[E_n(\vec{q},t)E_m^*(\vec{q},t)\right] \end{aligned} \tag{2.83}$$

To simply the equation above, let's consider the following assumptions:

1. The average intensity produced by each scatterer is determined by a consistent unit scattering contrast, as all the scatterers are composed of the same materials. This unit scattering contrast remains constant across all scatterers and does not vary with time.

$$\mathbb{E}\left[I_n(\vec{q},t)\right] = \mathbb{E}\left[\left|E_n(\vec{q},t)\right|^2\right] = \mathbb{E}\left[|b|^2\right] \tag{2.84}$$

2. The electromagnetic field scattered from different compositions does not correlate with each other if the signals come from different compositions:

$$\sum_{n=1}^{N}\sum_{m\neq n}^{N} x_n(t)x_m(t)\mathbb{E}\left[E_n(\vec{q},t)E_m(\vec{q},t)\right] = 0 \tag{2.85}$$

With these two conditions, the average intensity could be written as

$$\mathbb{E}\left[I(\vec{q},t)\right] = \mathbb{E}\left[|b|^2\right] \sum_{n=1}^{N} x_n(t)^2 \tag{2.86}$$

The correlation function between time t_1 and t_2 could be computed as:

$$c_1(\vec{q},t_1,t_2) = \frac{\mathbb{E}\left[E(\vec{q},t_2)E^*(\vec{q},t_1)\right]}{\left[\mathbb{E}\left[|E(\vec{q},t_1)|^2\right]\mathbb{E}\left[|E(\vec{q},t_2)|^2\right]\right]^{\frac{1}{2}}} \tag{2.87}$$

Substituting the fractional relation Eq. 2.82 to the previous correlation function:

$$\begin{aligned} c_1(\vec{q},t_1,t_2) &= \frac{\mathbb{E}\left[\sum_{m=1}^{N} x_m(t_2)E_m(\vec{q},t_2) \sum_{n=1}^{N} x_n(t_1)E_n^*(\vec{q},t_1)\right]}{\left[\mathbb{E}\left[I(\vec{q},t_1)\right]\mathbb{E}\left[I(\vec{q},t_2)\right]\right]^{\frac{1}{2}}} \\ &= \frac{\left[\begin{array}{l} \sum_{n=1}^{N} x_n(t_2)x_n(t_1)\mathbb{E}\left[E_n(\vec{q},t_2)E_n^*(\vec{q},t_1)\right] + \\ \sum_{n=1}^{N}\sum_{m\neq n}^{N} x_m(t_2)x_n(t_1)\mathbb{E}\left[E_m(\vec{q},t_2)E_n^*(\vec{q},t_1)\right] \end{array}\right]}{\left[\sum_{n=1}^{N} x_n(t_1)^2\mathbb{E}\left[I_n(\vec{q},t_1)\right] \sum_{n=1}^{N} x_n(t_2)^2\mathbb{E}\left[I_n(\vec{q},t_2)\right]\right]^{\frac{1}{2}}} \end{aligned} \tag{2.88}$$

The correlation function above could be interpreted as the sum of two components: the self-correlating terms for each component plus their cross-term. To simplify and rationalize the correlation function, we assume no spatial correlation of $E(\vec{q},t)$ between scatterers in different composition ($n \neq m$) at different time:

$$\sum_{n=1}^{N}\sum_{m\neq n}^{N} x_n(t_1)x_m(t_2)\mathbb{E}\left[E_m(\vec{q},t_2)E_n^*(\vec{q},t_1)\right] = 0 \tag{2.89}$$

Now, introducing the compositional temporal correlation function, $c_{1,n}(\vec{q},t_1,t_2)$, with

form shown in Eq. 2.72,

$$
\begin{aligned}
c_{1,n}(\vec{q},t_1,t_2) &= \frac{\mathbb{E}\left[E_n(\vec{q},t_2)E_n^*(\vec{q},t_1)\right]}{\left[\mathbb{E}\left[E_n(\vec{q},t_2)\right]^2\mathbb{E}\left[E_n^*(\vec{q},t_1)\right]^2\right]^{\frac{1}{2}}} = \frac{\mathbb{E}\left[E_n(\vec{q},t_2)E_n^*(\vec{q},t_1)\right]}{\mathbb{E}\left[I(\vec{q},t)\right]} \\
&= \mathrm{e}^{-\frac{1}{2}q^2\int_{t_1}^{t_2}J_n(t)\,\mathrm{d}t}\mathrm{e}^{i\vec{q}\cdot\int_{t_1}^{t_2}\mathbb{E}[\vec{v}_n(t)]\,\mathrm{d}t}
\end{aligned}
\tag{2.90}
$$

the self-correlation part of $c_1(\vec{q},t_1,t_2)$ can be written as follows:

$$
\begin{aligned}
\sum_{n=1}^{N}x_n(t_1)x_n(t_2)\mathbb{E}\left[E_n(\vec{q},t_2)E_n^*(\vec{q},t_1)\right] &= \mathbb{E}\left[I(\vec{q},t)\right]\sum_{n=1}^{N}x_n(t_1)x_n(t_2)c_{1,n}(\vec{q},t_1,t_2) \\
&= \mathbb{E}\left[|b|^2\right]\sum_{n=1}^{N}x_n(t_1)x_n(t_2)\mathrm{e}^{-\frac{1}{2}q^2\int_{t_1}^{t_2}J_n(t)\,\mathrm{d}t}\mathrm{e}^{i\vec{q}\cdot\int_{t_1}^{t_2}\mathbb{E}[\vec{v}_n(t)]\,\mathrm{d}t}
\end{aligned}
\tag{2.91}
$$

The correlation function thus could be simplified as:

$$
\begin{aligned}
c_1(\vec{q},t_1,t_2) &= \frac{\mathbb{E}\left[|b|^2\right]\sum\limits_{n=1}^{N}x_n(t_1)x_n(t_2)c_{1,n}(\vec{q},t_1,t_2)}{\mathbb{E}\left[|b|^2\right]\left[\sum\limits_{n=1}^{N}x_n(t_1)^2\sum\limits_{n=1}^{N}x_n(t_2)^2\right]^{\frac{1}{2}}} \\
&= \frac{\sum\limits_{n=1}^{N}x_n(t_1)x_n(t_2)c_{1,n}(\vec{q},t_1,t_2)}{\left[\sum\limits_{n=1}^{N}x_n(t_1)^2\sum\limits_{n=1}^{N}x_n(t_2)^2\right]^{\frac{1}{2}}} \\
&= \frac{1}{f}\sum_{n=1}^{N}x_n(t_1)x_n(t_2)c_{1,n}(\vec{q},t_1,t_2) \\
&= \frac{1}{f}\sum_{n=1}^{N}x_n(t_1)x_n(t_2)\mathrm{e}^{-\frac{1}{2}q^2\int_{t_1}^{t_2}J_n(t)\,\mathrm{d}t}\mathrm{e}^{i\vec{q}\cdot\int_{t_1}^{t_2}\mathbb{E}[\vec{v}_n(t)]\,\mathrm{d}t}
\end{aligned}
\tag{2.92}
$$

Let the normalization factor f define as $f = \left[\sum\limits_{n=1}^{N}x_n(t_1)^2\sum\limits_{n=1}^{N}x_n(t_2)^2\right]^{\frac{1}{2}}$.

We then apply the Siegert relation Eq. 2.6 to obtain the $c_2(\vec{q},t_1,t_2)$ function measured

from the XPCS experiment under speckle contrast of β:

$$\begin{aligned} c_2(\vec{q},t_1,t_2) &= 1+\beta|c_1(\vec{q},t_1,t_2)|^2 \\ &= 1+\beta\left[c_1(\vec{q},t_1,t_2)c_1^*(\vec{q},t_1,t_2)\right] \\ &= 1+\beta\left[\sum_{n=1}^{N} x_n(t_1)x_n(t_2)c_{1,n}\sum_{m=1}^{N} x_m(t_1)x_m(t_2)c_{1,m}^*\right] \\ &= 1+\frac{\beta}{f^2}\sum_{n=1}^{N}\sum_{m=1}^{N} x_n(t_1)x_n(t_2)x_m(t_1)x_m(t_2)c_{1,n}c_{1,m}^* \end{aligned} \tag{2.93}$$

Subsequently, $c_2(\vec{q},t_1,t_2)$ is obtained by substituting from equation Eq. 2.90:

$$c_2(\vec{q},t_1,t_2) = 1+\frac{\beta}{f^2}\sum_{n=1}^{N}\sum_{m=1}^{N}\begin{bmatrix} x_n(t_1)x_n(t_2)x_m(t_1)x_m(t_2)\times \\ \mathrm{e}^{-\frac{1}{2}q^2\int_{t_1}^{t_2} J_n(t)+J_m(t)\,\mathrm{d}t}\times \\ \mathrm{e}^{i\vec{q}\cdot\int_{t_1}^{t_2}\mathbb{E}[\vec{v}_n(t)]-\mathbb{E}[\vec{v}_m(t)]\,\mathrm{d}t} \end{bmatrix} \tag{2.94}$$

In the XPCS experiment, only the real part in the Eq. 2.94 can be observed:

$$\begin{aligned} c_2(\vec{q},t_1,t_2) &= 1+\frac{\beta}{f^2}\sum_{n=1}^{N}\sum_{m=1}^{N}\mathbf{Re}\begin{bmatrix} x_n(t_1)x_n(t_2)x_m(t_1)x_m(t_2)\times \\ \mathrm{e}^{-\frac{1}{2}q^2\int_{t_1}^{t_2} J_n(t)+J_m(t)\,\mathrm{d}t}\times \\ \mathrm{e}^{i\vec{q}\cdot\int_{t_1}^{t_2}\mathbb{E}[\vec{v}_n(t)]-\mathbb{E}[\vec{v}_m(t)]\,\mathrm{d}t} \end{bmatrix} \\ &= 1+\frac{\beta}{f^2}\sum_{n=1}^{N}\sum_{m=1}^{N}\begin{bmatrix} x_n(t_1)x_n(t_2)x_m(t_1)x_m(t_2)\times \\ \mathrm{e}^{-\frac{1}{2}q^2\int_{t_1}^{t_2} J_n(t)+J_m(t)\,\mathrm{d}t}\times \\ \mathbf{Re}\left[\mathrm{e}^{i\vec{q}\cdot\int_{t_1}^{t_2}\mathbb{E}[\vec{v}_n(t)]-\mathbb{E}[\vec{v}(t)_m]}\right] \end{bmatrix} \end{aligned} \tag{2.95}$$

The term **Re** denotes taking the real part from the complex term of $\mathrm{e}^{i\vec{q}\cdot\int_{t_1}^{t_2}\mathbb{E}[\vec{v}_n(t)]-\mathbb{E}[\vec{v}(t)_m]}$, the cosine part,

$$\mathbf{Re}\left[\mathrm{e}^{i\vec{q}\cdot\int_{t_1}^{t_2}\mathbb{E}[v_n(t)]-\mathbb{E}[v_m(t)]\,\mathrm{d}t}\right] = \cos\left[\vec{q}\cdot\int_{t_1}^{t_2}\mathbb{E}\left[\vec{v}_n(t)\right]-\mathbb{E}\left[\vec{v}_m(t)\right]\,\mathrm{d}t\right] \tag{2.96}$$

For the self-interference part as $n = m$, this term equalizes to 1:

$$\begin{aligned}\mathbf{Re}\left[\mathrm{e}^{i\vec{q}\cdot\int_{t_1}^{t_2}\mathbb{E}[v_n(t)]-\mathbb{E}[v_n(t)]\,\mathrm{d}t}\right] &= \cos\left[\vec{q}\cdot\int_{t_1}^{t_2}\mathbb{E}\left[\vec{v}_n(t)\right]-\mathbb{E}\left[\vec{v}_n(t)\right]\,\mathrm{d}t\right] \\ &= \cos\left[0\right]=1\end{aligned} \tag{2.97}$$

As we further consider that the displacement of each composition is attributed to the flow along direction $\phi_n(t)$ relative to scattering vector $\vec{q}$, the interference term can be simplified as:

$$\mathbf{Re}\left[\mathrm{e}^{i\vec{q}\cdot\int_{t_1}^{t_2}\mathbb{E}[\vec{v}_n(t)]-\mathbb{E}[\vec{v}_m(t)]\,\mathrm{d}t}\right]=\cos\left[q\int_{t_1}^{t_2}\mathbb{E}\left[v_n(t)\right]\cos\left(\phi_n(t)\right)-\mathbb{E}\left[v_m(t)\right]\cos\left(\phi_m(t)\right)\mathrm{d}t\right] \tag{2.98}$$

The completed form of the time correlation function with heterodyne scattering under time-dependent change in fraction and relative velocity is written as follows:

$$c_2(\vec{q},t_1,t_2)=1+\frac{\beta}{f^2}\sum_{n=1}^{N}\sum_{m=1}^{N}\left[\begin{array}{c}x_n(t_1)x_n(t_2)x_m(t_1)x_m(t_2)\times \\ \mathrm{e}^{-\frac{1}{2}q^2\int_{t_1}^{t_2}J_n(t)+J_m(t)\,\mathrm{d}t}\times \\ \cos\left[q\int_{t_1}^{t_2}\mathbb{E}\left[v_n(t)\right]\cos\left(\phi_n(t)\right)-\mathbb{E}\left[v_m(t)\right]\cos\left(\phi_m(t)\right)\mathrm{d}t\right]\end{array}\right] \tag{2.99}$$

2.6.2 Heterodyne Scattering with 2 Compositions

To verify the equation in general form, we consider a simpler case. In this context, the heterodyne equation in the system with 2 compositions, static reference (r) and sample (s), consistently moving with relative speed $\mathbb{E}\left[v\right]$ and direction ϕ concerning scattering vector $\vec{q}$,

the equation could be simplified as:

$$c_2(\vec{q},t_1,t_2) = 1 + \frac{\beta}{f^2}\begin{bmatrix} [x_r(t_1)x_r(t_2)]^2\,\mathrm{e}^{-q^2\int_{t_1}^{t_2} J_r(t)\,\mathrm{d}t} + \\ [x_s(t_1)x_s(t_2)]^2\,\mathrm{e}^{-q^2\int_{t_1}^{t_2} J_s(t)\,\mathrm{d}t} + \\ 2x_r(t_1)x_r(t_2)x_s(t_1)x_s(t_2)\mathrm{e}^{-\frac{1}{2}q^2\int_{t_1}^{t_2} J_s(t)+J_r(t)\,\mathrm{d}t}\cos\left[q\cos(\phi)\int_{t_1}^{t_2}\mathbb{E}\left[v\right]\,\mathrm{d}t\right] \end{bmatrix}$$
$$f^2 = \left[x_s(t_1)^2 + x_r(t_1)^2\right]\left[x_s(t_2)^2 + x_r(t_2)^2\right] \tag{2.100}$$

To further consider the equilibrium conditions in the Wiener process or standard diffusion, in which all parameters, including x_s, x_r and v, are independent of time and $J_n(t) = 6D_n$, the equation could be further simplified as:

$$c_2(\vec{q},t_1,t_2) = 1 + \frac{\beta}{f^2}\begin{bmatrix} x_r^4\mathrm{e}^{-6q^2D_r(t_2-t_1)} + x_s^4\mathrm{e}^{-6q^2D_s(t_2-t_1)} + \\ 2x_r^2x_s^2\mathrm{e}^{-3q^2(D_r+D_s)(t_2-t_1)}\cos\left[q\cos(\phi)\mathbb{E}\left[v\right](t_2-t_1)\right] \end{bmatrix}$$
$$f^2 = \left[x_s^2 + x_r^2\right]^2 \tag{2.101}$$

Further apply the condition for the composition (x) and delayed time (τ):

$$x = \frac{I_s}{I_s + I_r} = \frac{x_s^2\mathbb{E}\left[I\right]}{x_s^2\mathbb{E}\left[I\right] + x_r^2\mathbb{E}\left[I\right]} = \frac{x_s^2}{x_s^2 + x_r^2} = \frac{x_s^2}{f}$$
$$\tau = t_2 - t_1 \tag{2.102}$$

The one-time correlation equation for heterodyne scattering $g_2(\vec{q},\tau)$ is shown as:

$$g_2(\vec{q},\tau) = 1 + \beta\begin{bmatrix} (1-x)^2\mathrm{e}^{-6q^2D_r\tau} + x^2\mathrm{e}^{-6q^2D_s\tau} + \\ 2x(1-x)\mathrm{e}^{-3q^2(D_r+D_s)\tau}\cos\left[q\cos(\phi)\mathbb{E}\left[v\right]\tau\right] \end{bmatrix} \tag{2.103}$$

The equation Eq. 2.103 above is a commonly used heterodyne equation that has been widely applied in various studies.

2.6.3 Heterodyne Scattering with 3 compositions

We further consider a system constituted of 3 compositions with 2 flowing components as $(1,2)$ and 1 static component as (r). The flowing composition moves with velocity (v_1, v_2) and direction (ϕ_1, ϕ_2) relative to the $\vec{q}$. The heterodyne equation could be expressed as follows:

$$c_2(\vec{q}, t_1, t_2) = 1 + \frac{\beta}{f(t_1, t_2)^2}[c_{2,self} + c_{2,cross}] \tag{2.104}$$

with the normalization factor written as:

$$f(t_1, t_2)^2 = \left[x_1(t_1)^2 + x_2(t_1)^2 + x_r(t_1)^2\right]\left[x_1(t_2)^2 + x_2(t_2)^2 + x_r(t_2)^2\right] \tag{2.105}$$

and $c_{2,self}$ and $c_{2,cross}$ denoted as the self-correlation and cross-correlation between different compositions, respectively. These correlation functions are defined as follows:

$$\begin{aligned}
c_{2,self} = & \begin{bmatrix} [x_r(t_1)x_r(t_2)]^2\, \mathrm{e}^{-q^2\int_{t_1}^{t_2} J_r(t)\,\mathrm{d}t} + \\ [x_1(t_1)x_1(t_2)]^2\, \mathrm{e}^{-q^2\int_{t_1}^{t_2} J_1(t)\,\mathrm{d}t} + \\ [x_2(t_1)x_2(t_2)]^2\, \mathrm{e}^{-q^2\int_{t_1}^{t_2} J_2(t)\,\mathrm{d}t} + \end{bmatrix} \\
c_{2,cross} = & \begin{bmatrix} 2x_r(t_1)x_r(t_2)x_1(t_1)x_1(t_2)\mathrm{e}^{-\frac{1}{2}q^2\int_{t_1}^{t_2} J_r(t)+J_1(t)\,\mathrm{d}t} \times \\ \cos\left[q\int_{t_1}^{t_2}\mathbb{E}\left[v_1(t)\right]\cos\left(\phi_1(t)\right)\mathrm{d}t\right] + \\ 2x_r(t_1)x_r(t_2)x_2(t_1)x_2(t_2)\mathrm{e}^{-\frac{1}{2}q^2\int_{t_1}^{t_2} J_r(t)+J_2(t)\,\mathrm{d}t} \times \\ \cos\left[q\int_{t_1}^{t_2}\mathbb{E}\left[v_2(t)\right]\cos\left(\phi_2(t)\right)\mathrm{d}t\right] + \\ 2x_1(t_1)x_1(t_2)x_2(t_1)x_2(t_2)\mathrm{e}^{-\frac{1}{2}q^2\int_{t_1}^{t_2} J_2(t)+J_1(t)\,\mathrm{d}t} \times \\ \cos\left[q\int_{t_1}^{t_2}\mathbb{E}\left[v_1(t)\right]\cos\left(\phi_1(t)\right) - \mathbb{E}\left[v_2(t)\right]\cos\left(\phi_2(t)\right)\mathrm{d}t\right] \end{bmatrix}
\end{aligned} \tag{2.106}$$

The equation shown above represents the heterodyne scattering function for a system with three components, and its calculation involves a large number of parameters. Due to the complexity of this calculation, it becomes challenging to directly extract the physical parameters from the measured data using this equation. To overcome this difficulty, it is

necessary to employ approximations based on the specific characteristics of the physical system. The following approximations are commonly utilized:

1. The intrinsic dynamics of the reference position is much slower than that of the flowing composition as $J_r = 0$ and, therefore, $c_{1,r} = 1$.

2. The flow direction of each composition is dominated at the horizontal direction and, therefore, $\phi_1 = \phi_2 = \theta$, where θ is the angle between $\vec{q}$ and the horizontal reference of $\theta = 0$.

With all the reasonable assumptions above, the final form of the heterodyne scattering function for 3 flowing bands, which will be utilized for analysis in this paper, is as follows:

$$
\begin{aligned}
c_{2,self} = & \begin{bmatrix} [x_r(t_1)x_r(t_2)]^2 + \\ [x_1(t_1)x_1(t_2)]^2 \, \mathrm{e}^{-q^2 \int_{t_1}^{t_2} J_1(t)\,\mathrm{d}t} + \\ [x_2(t_1)x_2(t_2)]^2 \, \mathrm{e}^{-q^2 \int_{t_1}^{t_2} J_2(t)\,\mathrm{d}t} + \end{bmatrix} \\
c_{2,cross} = & \begin{bmatrix} 2x_r(t_1)x_r(t_2)x_1(t_1)x_1(t_2)\mathrm{e}^{-\frac{1}{2}q^2 \int_{t_1}^{t_2} J_1(t)\,\mathrm{d}t} \times \\ \cos\left[q\cos(\theta)\int_{t_1}^{t_2} \mathbb{E}\left[v_1(t)\right]\,\mathrm{d}t\right] + \\ 2x_r(t_1)x_r(t_2)x_2(t_1)x_2(t_2)\mathrm{e}^{-\frac{1}{2}q^2 \int_{t_1}^{t_2} J_2(t)\,\mathrm{d}t} \times \\ \cos\left[q\cos(\theta)\int_{t_1}^{t_2} \mathbb{E}\left[v_2(t)\right]\,\mathrm{d}t\right] + \\ 2x_1(t_1)x_1(t_2)x_2(t_1)x_2(t_2)\mathrm{e}^{-\frac{1}{2}q^2 \int_{t_1}^{t_2} J_2(t)+J_1(t)\,\mathrm{d}t} \times \\ \cos\left[q\cos(\theta)\int_{t_1}^{t_2} \mathbb{E}\left[v_1(t)\right] - \mathbb{E}\left[v_2(t)\right]\,\mathrm{d}t\right] \end{bmatrix}
\end{aligned}
\tag{2.107}
$$

2.7 Application in Model Systems

2.7.1 Classical Non-Equilibrium Dynamics Model

In the following section, we apply equation Eq. 2.72 to several classical processes that match the description of Langevin dynamics, including the Wiener process (standard diffusion), Ornstein–Uhlenbeck process, and Brownian oscillator. By analyzing these dynamic pro-

cesses, we can estimate the transport coefficients and, hopefully, gain insight into how this physical parameter represents the dynamic behavior of the system.

Wiener Process / Standard Diffusion

In this case of 1-dimensional Wiener process or standard diffusion, fluctuations ($\zeta(t)$) exist at the velocity level as $\Gamma = 2D$. Under such conditions, the Langevin equation of the Wiener process can be expressed as [195, at eq. (9.2)]:

$$\dot{x} = v_o + R(t) = v_o + \sqrt{2D}\zeta(t) \tag{2.108}$$

Here, $R(t)$ represents a random fluctuation in velocity attributed to a stationary, Gaussian, δ-correlated, Markov process $\zeta(t)$. It possesses the following properties:

$$\mathbb{E}\left[\zeta(t)\zeta(t')\right] = \delta(t - t') \tag{2.109}$$

where v_o and x_0 are the initial velocity and position for the process.

The mean velocity $\mathbb{E}\left[v(t)\right]$, mean position $\mathbb{E}\left[x(t)\right]$, variance of position $\mathbb{V}[x(t)]$ and transport coefficient $J\left(t\right)$ of the ensemble are obtained as:

$$\begin{aligned}
\mathbb{E}\left[v(t)\right] &= v_o \\
\mathbb{E}\left[v(t)v(t')\right] &= v_o^2 + 2D\delta(t - t') \\
\mathbb{E}\left[x(t)\right] &= x_0 + v_o t \\
\mathbb{V}[x(t)] &= \mathbb{E}\left[x(t)^2\right] - \mathbb{E}\left[x(t)\right]^2 = 2Dt \\
J(t) &= \frac{d}{dt}\left(\mathbb{V}[x(t)]\right) = 2D
\end{aligned} \tag{2.110}$$

Substituting the value of $\mathbb{E}\left[v(t)\right]$ and $\mathbb{V}[x(t)]$ from equation Eq. 2.110 to equation Eq.

2.44, the $c_1(q, t_1, t_2)$ is obtained based on as:

$$c_1(q, t_1, t_2) = \mathrm{e}^{-q^2 D(t_2 - t_1)} \mathrm{e}^{iqv_o(t_2 - t_1)} \tag{2.111}$$

Eq. 2.111 is the $c_1(q, t_1, t_2)$ for the model of Advection-Diffusion in 1-dimension, a fluid transports with external driven bulk movement (v_o) and diffusion (D) of the substance due to molecular random motion.

Considering the case in equilibrium state as changing the absolute time (t_1, t_2) to delayed time τ as $\tau = t_2 - t_1$:

$$g_1(q, \tau) = \mathrm{e}^{-q^2 D\tau} \mathrm{e}^{iqv_o\tau} \tag{2.112}$$

Further considering diffusion is the only dynamics in the system and there is no bulk movement in the system as $v_o = 0$, the Eq. 2.112 can be reduced to the simplest model that commonly applied in XPCS analysis:

$$g_1(q, \tau) = \mathrm{e}^{-q^2 D\tau} \tag{2.113}$$

Ornstein−Uhlenbeck Process

In Ornstein−Uhlenbeck process, the external force (F_{ex}) is set to zero while the drift coefficient (γ) remains non-zero. This configuration gives rise to an Ornstein–Uhlenbeck process. The Ornstein–Uhlenbeck process exhibits a mean-reverting behavior and is commonly used to model systems with a tendency to return to equilibrium. In such a case, the Langevin equation is given by [195, at eq. (6.1)]:

$$m\dot{v} = -m\gamma v(t) + \eta(t) \tag{2.114}$$

In the Ornstein–Uhlenbeck process, the thermal fluctuation noise in velocity is attributed to collisions between particles and solvent with the level of $\Gamma = 2m\gamma k_B T$. Then, the mean

velocity $\mathbb{E}[v(t)]$, mean position $\mathbb{E}[x(t)]$ and variance of position $\mathbb{V}[x(t)]$ of the ensemble is solved as:

$$\begin{aligned}
\mathbb{E}[v(t)] &= v_o \mathrm{e}^{-\gamma t} \\
\mathbb{E}[x(t)] &= x_0 + \frac{v_o}{\gamma}(1 - \mathrm{e}^{-\gamma t}) \\
\mathbb{V}[x(t)] &= \mathbb{E}\left[x(t)^2\right] - \mathbb{E}[x(t)]^2 = \frac{k_B T}{m\gamma^2}(2\gamma t - 3 + 4\mathrm{e}^{-\gamma t} - \mathrm{e}^{-2\gamma t}) \\
&= \frac{D}{\gamma}(2\gamma t - 3 + 4\mathrm{e}^{-\gamma t} - \mathrm{e}^{-2\gamma t})
\end{aligned} \tag{2.115}$$

where D is defined as the diffusion constant of the system and is equal to $D = \frac{k_B T}{m\gamma}$

The dynamical transport coefficient $J(t)$ is defined as:

$$\begin{aligned}
J(t) = \frac{d}{dt}(\mathbb{V}[x(t)]) &= \frac{d}{dt}\left(\frac{D}{\gamma}(2\gamma t - 3 + 4\mathrm{e}^{-\gamma t} - \mathrm{e}^{-2\gamma t})\right) \\
&= 2D(1 - 2\mathrm{e}^{-\gamma t} + \mathrm{e}^{-2\gamma t}) \\
&= 2D\left(1 - \mathrm{e}^{-\gamma t}\right)^2
\end{aligned} \tag{2.116}$$

The two-time correlation function $c_1(q, t_1, t_2)$ obtained through XPCS will be:

$$\begin{aligned}
c_1(q, t_1, t_2) &= \mathrm{e}^{-\frac{1}{2}q^2 \int_{t_1}^{t_2} J(t)\,\mathrm{d}t} \mathrm{e}^{iq \int_{t_1}^{t_2} \mathbb{E}[v(t)]\,\mathrm{d}t} \\
&= \mathrm{e}^{-q^2 D \int_{t_1}^{t_2} \left(1 - \mathrm{e}^{-\gamma t}\right)^2 \mathrm{d}t} \mathrm{e}^{iqv_o \int_{t_1}^{t_2} \exp(-\gamma t)\,\mathrm{d}t}
\end{aligned} \tag{2.117}$$

Brownian Oscillator

In a Brownian oscillator with potential of $V(x) = \frac{1}{2}m{\omega_o}^2 x^2$, the conservative force in the particle is $m{\omega_o}^2 x$ as $-\frac{\partial V(x)}{\partial x} = -m{\omega_o}^2 x$. Therefore, the Langevin Equation (LE) for the Brownian oscillator is: [195, at eq. (13.1)]

$$m\dot{v} = -m\gamma v + \eta(t) - m{\omega_o}^2 x \tag{2.118}$$

For the Brownian oscillator with initial conditions of $x(0) = x_0$ and $v(0) = v_o$, the value of $\mathbb{E}[v(t)]$,$\mathbb{E}[x(t)]$ and $\mathbb{V}[x(t)]$ is solved as: [195, at eq. (13.17, 13.20)] [74, at eq. (214)]

$$\begin{aligned}
\mathbb{E}[v(t)] &= \frac{\mathrm{e}^{-\gamma t/2}}{\omega_s}\left[-x_0\left({\omega_o}^2\sin(\omega_s t)\right) + v_o\left(\omega_s\cos(\omega_s t) - \frac{1}{2}\gamma\sin(\omega_s t)\right)\right] \\
\mathbb{E}[x(t)] &= \frac{\mathrm{e}^{-\gamma t/2}}{\omega_s}\left[x_0\left(\omega_s\cos(\omega_s t) + \frac{1}{2}\gamma\sin(\omega_s t)\right) + v_o\left(\sin(\omega_s t)\right)\right] \\
\mathbb{V}[x(t)] &= \frac{k_B T}{m{\omega_o}^2}\left[\,1 - \mathrm{e}^{-\gamma t}\left(\frac{\gamma^2}{2\omega_s^2}\sin^2(\omega_s t) + \frac{\gamma}{2\omega_s}\sin(2\omega_s t) + 1\right)\right]
\end{aligned} \tag{2.119}$$

where ω_s is the reduced frequency given as:

$$\omega_s = \left({\omega_o}^2 - \frac{1}{4}\gamma^2\right)^{\frac{1}{2}} \tag{2.120}$$

With the knowledge of $\mathbb{V}[x(t)]$ and $\mathbb{V}[v(t)]$, the transport coefficient $J(t)$ for Brownian oscillator can be written as: [74, at eq. (213)]

$$J(t) = \frac{d}{dt}\left(\mathbb{V}[x(t)]\right) = \frac{2D\gamma^2}{{\omega_s}^2}\mathrm{e}^{-\gamma t}\sin^2(\omega_s t) \tag{2.121}$$

Substituting the value of $\mathbb{E}[v(t)]$ and $J(t)$ from equations Eq. 2.119 and Eq. 2.121 to equation Eq. 2.44, the two-time correlation function for XPCS, $c_1(t_1, t_2)$, becomes,

$$\begin{aligned}
c_1(q, t_1, t_2) &= \mathrm{e}^{-\frac{1}{2}q^2\int_{t_1}^{t_2} J\,\mathrm{d}t}\mathrm{e}^{iq\int_{t_1}^{t_2}\mathbb{E}[v(t)]\,\mathrm{d}t} \\
&= \exp\left(-\frac{D\gamma^2 q^2}{{\omega_s}^2}\int_{t_1}^{t_2}\mathrm{e}^{-\gamma t}\sin^2(\omega_s t)\,\mathrm{d}t\right) \\
&\times \exp\left(i\frac{q\mathrm{e}^{-\gamma t/2}}{\omega_s}\int_{t_1}^{t_2} -x_0\left({\omega_o}^2\sin(\omega_s t)\right) + v_o\left(\omega_s\cos(\omega_s t) - \frac{1}{2}\gamma\sin(\omega_s t)\right)\,\mathrm{d}t\right)
\end{aligned} \tag{2.122}$$

2.7.2 Analysis in Transport Coefficient

If the internal and external forces, such as conservative forces or hydrodynamic forces, are described by complicated functions, $J(t)$ and $\mathbb{V}[x(t)]$ are not analytically solvable. Therefore, we propose to extract $J(t)$ with arbitrary profile functions (e.g., Eq. 3.2 in chapter 3 later) to capture non-equilibrium dynamics in such systems. However, the physical interpretation of $J(t)$ and $\mathbb{V}[x(t)]$ are not clear. On the other hand, throughout the derivations in the previous 2.7.1, the $J(t)$ and $\mathbb{V}[x(t)]$ are analytically resolved from the Langevin equation for well-defined models of the Wiener process, Ornstein−Uhlenbeck process, and Brownian oscillator. Below, we will show that the estimation of $J(t)$ and $\mathbb{V}[x(t)]$ from these models facilitates a better understanding of their physics.

Wiener Process / Standard Diffusion

For Wiener process, $J(t)$ is obtained as:

$$J(t) = 2D \tag{2.123}$$

Since there are no drift or external forces applied to the particles, the system is in equilibrium and the dynamics of the particles are independent of time. Therefore, the obtained $J(t)$ correlates with the diffusion constant.

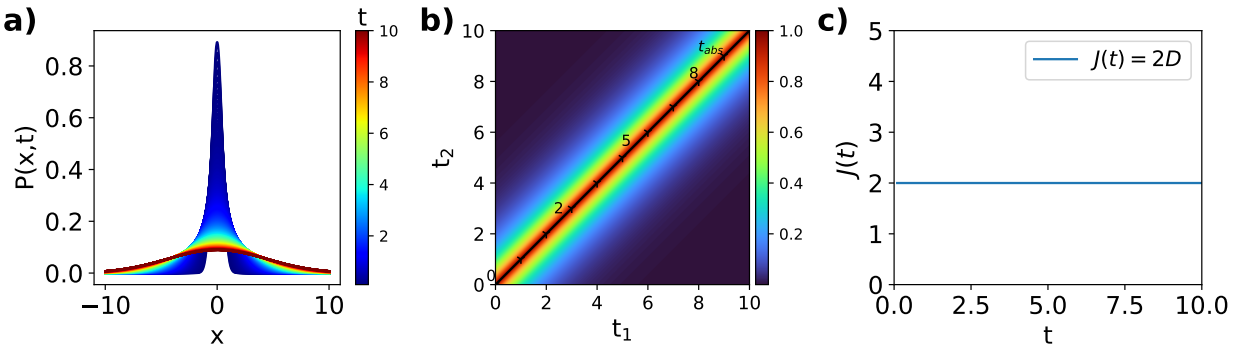

Figure 2.1: **Simulation for Wiener Process / Standard Diffusion with $D = 1$ and $x_0 = 0$.** a) $P(x,t)$ represents the probability density function as time evolves. b) The figure illustrates the two-time correlation function, $c_2(q = 1, t_1, t_2)$. c) $J(t)$ is the transport coefficient described in this work. In such an equilibrium state, the dynamical transport coefficient $J(t) = 2D$ is independent of time.

Ornstein−Uhlenbeck Process

For Ornstein−Uhlenbeck process, $J(t)$ is obtained as:

$$J(t) = 2D(1 - \mathrm{e}^{-\gamma t})^2 \tag{2.124}$$

In the Ornstein−Uhlenbeck process, a drift acts on the particles. At $t = 0$, when the velocity of the particles is at maximum, the drift force is also maximized. $J(t)$ starts at 0, and particles have a uniform bulk movement with v_o. As time evolves, the velocity of the particles and the effect of drift gradually decreases. As the results show, $J(t)$ gradually increases. Eventually, the system reaches equilibrium and the drift effect is minimized after a long time. In this case, $J(t)$ reaches a plateau at $2D$, indicating that the system is at equilibrium just like the result from the Wiener process.

$$J_{eq}(t) = \lim_{t\to\infty} 2D(1 - \mathrm{e}^{-\gamma t})^2 \quad = 2D \tag{2.125}$$

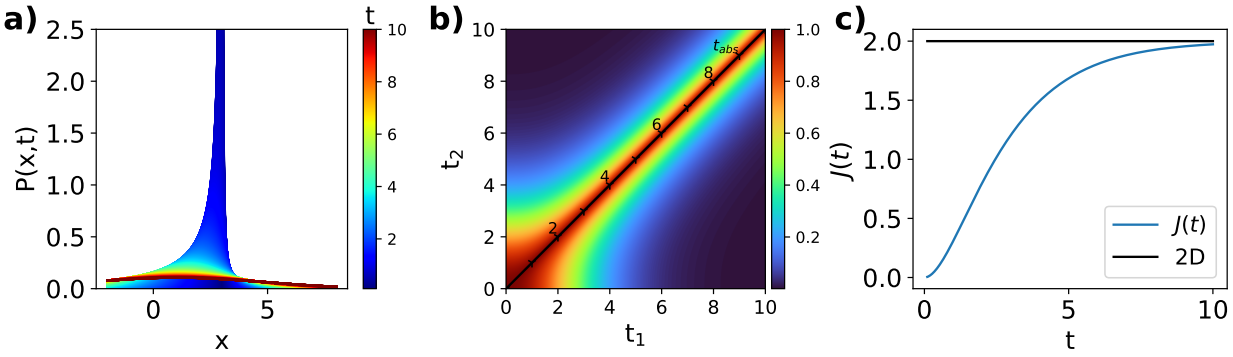

Figure 2.2: **Simulation for Ornstein–Uhlenbeck Process with** $D = 1$**,** $\gamma = 0.5$**,** $v_o = -1$ **and** $x_0 = 3$**.** The dynamical transport coefficient $J(t) = 2D(1 - \mathrm{e}^{-\gamma t})^2$.

Brownian Oscillator

For Brownian oscillator, $J(t)$ is obtained as:

$$J(t) = \frac{2D\gamma^2}{{\omega_s}^2}\mathrm{e}^{-\gamma t}\sin^2(\omega_s t) \tag{2.126}$$

Recall that ω_s is a reduced frequency defined in Equation Eq. 2.120 as $\omega_s = \left({\omega_o}^2 - \frac{1}{4}\gamma^2\right)^{\frac{1}{2}}$. In the case of underdamping oscillator as $\omega_o > \frac{1}{2}\gamma$, ω_s is a real and positive value.

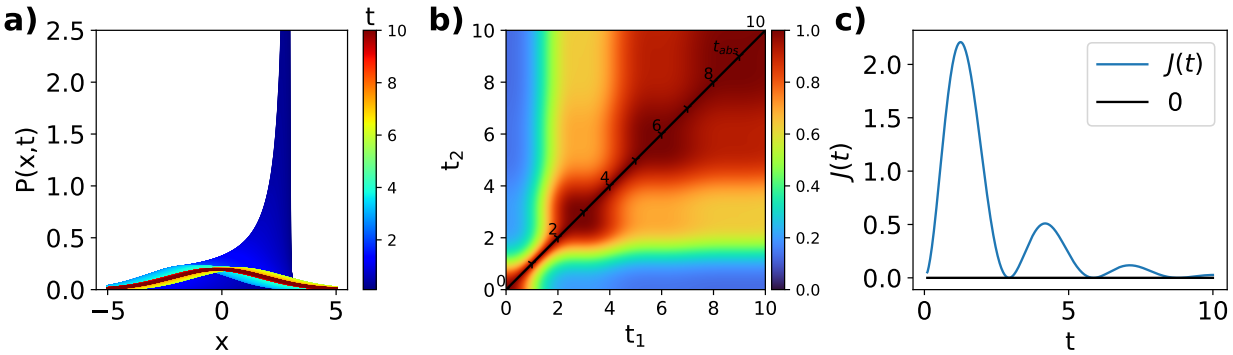

Figure 2.3: **Simulation for underdamped Brownian Oscillator with** $D = 10$**,** $\gamma = 0.5$**,** $\omega_o = 1.1$**,** $v_o = 1$ **and** $x_0 = 3$**.**

However, in the case of an overdamped oscillator with $\omega_o < \frac{1}{2}\gamma$, ω_s is an imaginary number, and the trend of equation Eq. 2.126 is less obvious. Instead, we define a new

simplified term of "simplified drift" as $\gamma_s = \left(\gamma^2 - 4{\omega_o}^2\right)^{\frac{1}{2}}$. The term is a real and positive number when $\omega_o < \frac{1}{2}\gamma$ and consists of relations with ω_s as $\gamma_s = i2\omega_s$. Substituting γ_s into equation Eq. 2.126 and applying a relation $\sin(ix) = i\sinh(x)$, we have an equivalent equation for an overdamped oscillator:

$$J(t) = \frac{8D\gamma^2}{\gamma_s^2} \mathrm{e}^{-\gamma t} \sinh^2\left(\frac{1}{2}\gamma_s t\right) \tag{2.127}$$

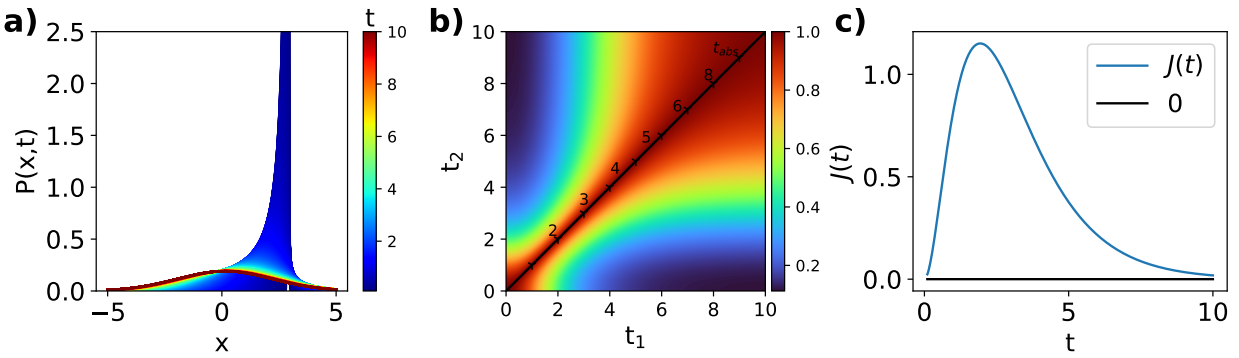

Figure 2.4: **Simulation for overdamped Brownian Oscillator with** $D = 1$, $\gamma = 1.1$, $\omega_o = 0.5$, $v_o = 1$ **and** $x_0 = 3$.

With Eq. 2.126 and Eq. 2.127, the dynamics of the Brownian oscillator are obvious. For $t \to \infty$, the term of $\mathrm{e}^{-\gamma t}$ dominates $J(t)$ and $J(t) = 0$. This means that the drift force and elastic force cancel out at equilibrium and the system remains static. For $t \to 0$, the oscillation term $\left(\sin^2(\omega_s t)\right)$ in Eq. 2.126 or $\left(\sinh^2\left(\frac{1}{2}\gamma_s t\right)\right)$ in Eq. 2.127 dominates $J(t)$. However, $J(t)$ as shown in Fig. 2.3 and Fig. 2.4 , the oscillation signals vanish much faster for $\left(\sinh^2\left(\frac{1}{2}\gamma_s t\right)\right)$, as the drift force prevails in the overdamped oscillator.

To reduce the Brownian oscillator to the Ornstein−Uhlenbeck process, we have no elastic force in the system as

$$\begin{aligned} m\omega_o^2 x = \omega_o &= 0 \\ \gamma_s = \left(\gamma^2 - 4{\omega_o}^2\right)^{\frac{1}{2}} &= \gamma \end{aligned} \tag{2.128}$$

Substituting $\gamma_s = \gamma$, the expression of $J(t)$ can be written as:

$$\begin{aligned} J(t) &= \frac{8D\gamma^2}{\gamma^2}\mathrm{e}^{-\gamma t}\sinh^2\left(\frac{1}{2}\gamma t\right) \\ &= 8D\mathrm{e}^{-\gamma t}\left(\frac{1-\mathrm{e}^{-\gamma t}}{2\mathrm{e}^{-\frac{1}{2}\gamma t}}\right)^2 \\ &= 2D\left(1-\mathrm{e}^{-\gamma t}\right)^2 \end{aligned} \tag{2.129}$$

By setting ω_0 to 0, we simplify the dynamics from a Brownian Oscillator to an Ornstein−Uhlenbeck process. Additionally, if the system reaches equilibrium as t tends to infinity as in equation (Eq. 2.125), the dynamical process further simplifies from an Ornstein−Uhlenbeck process to a Wiener process, which is the most fundamental stochastic dynamics process.

2.8 Non-Gaussian Dynamics

In Section 2.2, the assumption of Gaussian dynamics is introduced, where dynamic fluctuations are memoryless and the future PDF depends only on the current state Eq. 2.15. Under this assumption, the PDF can be expressed as a Gaussian function (Eq. 2.16), and the subsequent derivation proceeds accordingly. However, in reality, not all dynamic processes exhibit Gaussian behavior. In the presence of time and state dependent noise, the PDF may deviate from a Gaussian form and take on an arbitrary shape. The following section explores the observation of non-Gaussian dynamics in XPCS. Through mathematical and physical derivations, we will examine the expected features of non-Gaussian dynamics and present a general analytical approach that can effectively handle these non-Gaussian processes.

As a simple example of non-Gaussian dynamics, consider a one-dimensional process consisting of N subensembles, each undergoing Gaussian dynamics. In this case, the PDF at

any time t is a superposition of N Gaussian functions, which can be expressed as:

$$\begin{aligned} \mathbb{P}(x,t) &= \sum_{n=1}^{N} x_n(t)\mathcal{N}\left(x;\mu_n\left(t\right),\sigma_n^2\left(t\right)\right) \\ 1 &= \sum_{n=1}^{N} x_n(t) \end{aligned} \tag{2.130}$$

where $\mu_n(t)$, $\sigma_n^2(t)$ and $x_n(t)$ represent the mean, variance and fraction of the nth Gaussian function at time t, respectively.

According to Eq. 2.13, The $c_1\left(\vec{q},t_1,t_2\right)$ is then expressed as:

$$\begin{aligned} c_1\left(q,t_1,t_2\right) &= \frac{\mathcal{F}\left[\mathbb{P}(x,t_2)\right]}{\mathcal{F}\left[\mathbb{P}(x,t_1)\right]} \\ &= \frac{\sum\limits_{n=1}^{N} x_n(t_2)\mathcal{F}\left[\mathcal{N}\left(x;\mu_n\left(t_2\right),\sigma_n^2\left(t_2\right)\right)\right]}{\sum\limits_{n=1}^{N} x_n(t_1)\mathcal{F}\left[\mathcal{N}\left(x;\mu_n\left(t_1\right),\sigma_n^2\left(t_1\right)\right)\right]} \\ &= \frac{\sum\limits_{n=1}^{N} x_n(t_2)\exp\left(-\frac{1}{2}q^2\sigma_n^2(t_2)-iq\mu_n(t_2)\right)}{\sum\limits_{n=1}^{N} x_n(t_1)\exp\left(-\frac{1}{2}q^2\sigma_n^2(t_1)-iq\mu_n(t_1)\right)} \end{aligned} \tag{2.131}$$

In the actual XPCS experiment, the quantity measured is $c_2\left(\vec{q},t_1,t_2\right)$. Acorrding to Siegart relation in Eq. 2.131, the $c_2\left(\vec{q},t_1,t_2\right)$ for non-Gaussian dynamics is computed as ,

$$\begin{aligned} c_2(q,t_1,t_2) &= 1+\beta\left|\frac{\sum\limits_{n=1}^{N} x_n(t_2)\exp\left(-\frac{1}{2}q^2\sigma_n^2(t_2)-iq\mu_n(t_2)\right)}{\sum\limits_{n=1}^{N} x_n(t_1)\exp\left(-\frac{1}{2}q^2\sigma_n^2(t_1)-iq\mu(t_1)\right)}\right|^2 \\ &= 1+\beta\left(\frac{\sum\limits_{n=1}^{N}\sum\limits_{m=1}^{N} x_n(t_2)x_m(t_2)\exp\left(-\frac{1}{2}q^2\left(\sigma_n^2(t_2)+\sigma_m^2(t_2)\right)-iq\left(\mu_n(t_2)-\mu_m(t_2)\right)\right)}{\sum\limits_{n=1}^{N}\sum\limits_{m=1}^{N} x_n(t_1)x_m(t_1)\exp\left(-\frac{1}{2}q^2\left(\sigma_n^2(t')+\sigma_m^2(')\right)-iq\left(\mu_n(t')-\mu_m(t')\right)\right)}\right) \end{aligned} \tag{2.132}$$

Applying

$$\begin{aligned} \frac{d}{dt}\left(\mu_n(t)\right) &= v_n(t) \\ \mu_n(t) &= \int_{-\infty}^{t} v_n\left(t'\right)\, dt' \\ \frac{d}{dt}\left(\sigma_n^2(t)\right) &= J_n(t) \\ \sigma_n^2(t) &= \int_{-\infty}^{t} J_n\left(t'\right)\, dt' \end{aligned} \tag{2.133}$$

and considering

$$\begin{aligned} J_{nm}(t) &= \frac{1}{2}\left(J_n(t) + J_m(t)\right) \\ v_{nm}(t) &= v_n(t) - v_m(t) \end{aligned} \tag{2.134}$$

we have,

$$c_2(q,t_1,t_2) = 1 + \beta \left(\frac{\sum_{n=1}^{N}\sum_{m=1}^{N} x_n(t_2)x_m(t_2)\exp\left(\int_{-\infty}^{t_2} -q^2 J_{nm}(t') - iqv_{nm}(t')\,dt'\right)}{\sum_{n=1}^{N}\sum_{m=1}^{N} x_n(t_1)x_m(t_1)\exp\left(\int_{-\infty}^{t_1} -q^2 J_{nm}(t') - iqv_{nm}(t')\,dt'\right)} \right) \tag{2.135}$$

2.8.1 The observed dynamics rate

Assuming $c_2\left(\vec{q},t_1,t_2\right)$ could be accurately characterized by applying the non-equilibrium approach, we have observed the observed dynamics coefficient ($\Gamma_{obs}(q,t)$) from the analysis of $c_2\left(\vec{q},t_1,t_2\right)$ from theXPCS measurement as,

$$c_2(q,t_1,t_2) = 1 + \beta \exp\left(-\int_{t_1}^{t_2} \Gamma_{obs}(q,t)\,dt\right) \tag{2.136}$$

It is imperative to interpret the physical significance of $\Gamma_{obs}(q,t)$ by establishing connections to $\mu_n(t)$, $\sigma_n^2(t)$, and $x_n(t)$ as follow,

$$1+\beta\exp\left(-\int_{t_1}^{t_2}\Gamma_{obs}(t)\,dt\right)=1+\beta\left(\frac{\sum_{n=1}^{N}\sum_{m=1}^{N}x_n(t_2)x_m(t_2)\exp\left(\int_{-\infty}^{t_2}-q^2J_{nm}(t')-iqv_{nm}(t')\,dt'\right)}{\sum_{n=1}^{N}\sum_{m=1}^{N}x_n(t_1)x_m(t_1)\exp\left(\int_{-\infty}^{t_1}-q^2J_{nm}(t')-iqv_{nm}(t')\,dt'\right)}\right) \tag{2.137}$$

Conduct $\ln\left(\frac{c_2(q,t_1,t_2)-1}{\beta}\right)$

$$-\int_{t_1}^{t_2}\Gamma_{obs}(t)\,dt=\ln\left(\frac{\sum_{n=1}^{N}\sum_{m=1}^{N}x_nx_m\exp\left(-q^2\int_{-\infty}^{t_2}J_{nm}(t')-iqv_{nm}(t')\,dt'\right)}{\sum_{n=1}^{N}\sum_{m=1}^{N}x_nx_m\exp\left(-q^2\int_{-\infty}^{t_1}J_{nm}(t')-iqv_{nm}(t')\,dt'\right)}\right) \tag{2.138}$$

We further extend the derivation on the term of $\ln\left(\frac{\sum\cdots}{\sum\cdots}\right)$,

$$\begin{aligned}
&\ln\left(\frac{\sum_{n=1}^{N}\sum_{m=1}^{N}x_n(t_2)x_m(t_2)\exp\left(-q^2\int_{-\infty}^{t_2}J_{nm}(t')-iqv_{nm}(t')\,dt'\right)}{\sum_{n=1}^{N}\sum_{m=1}^{N}x_n(t_1)x_m(t_1)\exp\left(-q^2\int_{-\infty}^{t_1}J_{nm}(t')-iqv_{nm}(t')\,dt'\right)}\right)\\
&=\ln\left(\sum_{n=1}^{N}\sum_{m=1}^{N}x_n(t_2)x_m(t_2)\mathrm{e}^{-q^2\int_{-\infty}^{t_2}J_{nm}(t')-iqv_{nm}(t')\,dt'}\right)\\
&-\ln\left(\sum_{n=1}^{N}\sum_{m=1}^{N}x_n(t_1)x_m(t_1)\mathrm{e}^{-q^2\int_{-\infty}^{t_1}J_{nm}(t')-iqv_{nm}(t')\,dt'}\right)\\
&=\int_{t_1}^{t_2}\frac{d}{dt}\left(\ln\left(\sum_{n=1}^{N}\sum_{m=1}^{N}x_n(t)x_m(t)\mathrm{e}^{-q^2\int_{-\infty}^{t}J_{nm}(t')-iqv_{nm}(t')\,dt'}\right)\right)\,dt
\end{aligned} \tag{2.139}$$

Compared to the expression of $\Gamma_{obs}(q,t)$, we obtained that,

$$\Gamma_{obs}(q,t)=-\frac{d}{dt}\left(\ln\left(\sum_{n=1}^{N}\sum_{m=1}^{N}x_n(t)x_m(t)\mathrm{e}^{-q^2\int_{-\infty}^{t}J_{nm}(t')-iqv_{nm}(t')\,dt'}\right)\right) \tag{2.140}$$

Continue derivation of $\Gamma_{obs}(q,t)$,

$$\begin{aligned}\Gamma_{obs}(q,t) =& -\frac{d}{dt}\left(\ln\left(\sum_{n=1}^{N}\sum_{m=1}^{N} x_n(t)x_m(t)\mathrm{e}^{-q^2\int_{-\infty}^{t} J_{nm}(t')-iqv_{nm}(t')\,dt'}\right)\right)\\ =& -\frac{\sum_{n=1}^{N}\sum_{m=1}^{N}\begin{bmatrix} x_n(t)x_m(t)\left(-q^2J_{nm}(t)-iqv_{nm}(t)\right)+\\ \frac{d}{dt}\left(x_n(t)x_m(t)\right)\end{bmatrix}\exp\left(-q^2\int_{-\infty}^{t} J_{nm}(t')-iqv_{nm}(t')\,dt'\right)}{\sum_{n=1}^{N}\sum_{m=1}^{N} x_n(t)x_m(t)\exp\left(-q^2\int_{-\infty}^{t} J_{nm}(t')-iqv_{nm}(t')\,dt'\right)}\end{aligned} \tag{2.141}$$

Considering the fraction change composition as,

$$F(t)=\frac{d}{dt}\left(x_n(t)x_m(t)\right)=\frac{d}{dt}\left(x_n(t)\right)x_m(t)+\frac{d}{dt}\left(x_m(t)\right)x_n(t) \tag{2.142}$$

The equation is simplified as,

$$\Gamma_{obs}(q,t) =\frac{\sum_{n=1}^{N}\sum_{m=1}^{N}\left(x_n(t)x_m(t)\left(q^2J_{nm}(t)+iqv_{nm}(t)\right)-F(t)\right)\exp\left(-q^2\int_{-\infty}^{t} J_{nm}(t')-iqv_{nm}(t')\,dt'\right)}{\sum_{n=1}^{N}\sum_{m=1}^{N} x_n(t)x_m(t)\exp\left(-q^2\int_{-\infty}^{t} J_{nm}(t')-iqv_{nm}(t')\,dt'\right)} \tag{2.143}$$

Since we only observe the real part in experiment, equation is further simplified as,

$$\Gamma_{obs}(q,t) =\frac{\sum_{n=1}^{N}\sum_{m=1}^{N}\begin{bmatrix} x_n(t)x_m(t)\begin{bmatrix} q^2J_{nm}(t)\cos\left(q\int_{-\infty}^{t} v_{nm}(t')\,dt'\right)\\ qv_{nm}(t)\sin\left(q\int_{-\infty}^{t} v_{nm}(t')\,dt'\right)\end{bmatrix}\\ -F(t)\cos\left(q\int_{-\infty}^{t} v_{nm}(t')\,dt'\right)\end{bmatrix}\exp\left(-q^2\int_{-\infty}^{t} J_{nm}(t')\,dt'\right)}{\sum_{n=1}^{N}\sum_{m=1}^{N} x_n(t)x_m(t)\exp\left(-q^2\int_{-\infty}^{t} J_{nm}(t')\,dt'\right)\cos\left(q\int_{-\infty}^{t} v_{nm}(t')\,dt'\right)} \tag{2.144}$$

It should be emphasized that Eq. 2.144, derived from Eq. 2.130, is only valid under strict conditions and assumptions. Often, these assumptions may not hold in real systems. Specifically, it assumes a homogeneous system while also considering multiple independent

sub-ensembles, where the positions of individual particles are uncorrelated. In reality, this is rarely the case, as particles with different characteristics tend to assembly into structures to achieve a thermodynamically favorable state, driven by either entropic or enthalpic effects. This assembly structure often introduces heterodyne scattering in the system (See Section 2.6.1), violating the assumptions of Eq. 2.136. Nevertheless, Eq. 2.144 provides a simplified and idealized expectation of the $c_2\left(\vec{q}, t_1, t_2\right)$ observed for non-Gaussian dynamics in XPCS and may not always be valid under all experimental conditions. Despite these limitations, it remains a valuable model for gaining insights into the expected behavior of non-Gaussian dynamics in XPCS.

2.8.2 Constant Fraction and Static system

To better understand non-Gaussian dynamics observed in XPCS through the property of $\Gamma_{obs}(q,t)$, let's greatly simply the system to a static system with constant fraction. In such assumption, the following conditions is applied,

$$\begin{aligned} v_n = v_m \rightarrow v_{nm} = 0 \\ F(t) = \frac{d}{dt}\left(x_n(t)\right) = \frac{d}{dt}\left(x_m(t)\right) = 0 \end{aligned} \tag{2.145}$$

In such case, $\Gamma_{obs}(q,t)$ is reduced to,

$$\Gamma_{obs}(q,t) = q^2 \frac{\sum_{n=1}^{N}\sum_{m=1}^{N} x_n x_m J_{nm}(t) \exp\left(-q^2 \int_{-\infty}^{t} J_n\left(t'\right)\, dt'\right)}{\sum_{n=1}^{N}\sum_{m=1}^{N} x_n x_m \exp\left(-q^2 \int_{-\infty}^{t} J_{nm}\left(t'\right)\, dt'\right)} \tag{2.146}$$

To make a better comparison, we define observed tranpsort coefficient ($J_{obs}(q,t)$) as,

$$J_{obs}(q,t) = \frac{\Gamma_{obs}(q,t)}{q^2} = \frac{\sum_{n=1}^{N}\sum_{m=1}^{N} x_n x_m J_{nm}(t) \exp\left(-q^2 \int_{-\infty}^{t} J_{nm}\left(t'\right)\, dt'\right)}{\sum_{n=1}^{N}\sum_{m=1}^{N} x_n x_m \exp\left(-q^2 \int_{-\infty}^{t} J_{nm}\left(t'\right)\, dt'\right)} \tag{2.147}$$

Compare to the $J_{obs}(q,t)$ obtained from any of the Markov chain processes, such as Wiener (Eq. 2.110), Ornstein–Uhlenbeck (Eq. 2.124), and Brownian oscillator (Eq. 2.127 Eq. 2.126), $J_{obs}(q,t)$ of non-Gaussian process in Eq. 2.147 consists a term of $\exp\left(-\frac{1}{2}q^2 \int_{-\infty}^{t} J_{nm}\left(t'\right)\, dt'\right)$, leading to two major differences as

1. a history-dependence as $\exp\left(-\frac{1}{2}q^2 \underline{\int_{-\infty}^{t} J_{nm}\left(t'\right)\, dt'}\right)$
2. a q-dependence as $\exp\left(-\frac{1}{2}\underline{q^2} \int_{-\infty}^{t} J_{nm}\left(t'\right)\, dt'\right)$

We would further explore and elaborate how such differences influence the observation of $\Gamma_{obs}(q,t)$ observed in XPCS experiment in the following sections.

2.8.3 2 Compositions system

If there is a 2 composition system, $J(t)$ and fraction of each composition is given as $J_1(t)$, $J_2(t)$, f and $1-f$, respectively, given by Eq. 2.147, $J_{obs}(t)$ we observed is expressed as,

$$J_{obs}(t) = \frac{\begin{bmatrix} f^2 J_1(t) \exp\left(-q^2 \int_{-\infty}^{t} J_1\left(t'\right)\, dt'\right) + \\ (1-f)^2 J_2(t) \exp\left(-q^2 \int_{-\infty}^{t} J_2\left(t'\right)\, dt'\right) + \\ f(1-f) J_{12}(t) \exp\left(-q^2 \int_{-\infty}^{t} J_{12}\left(t'\right)\, dt'\right) \end{bmatrix}}{\begin{bmatrix} f^2 \exp\left(-q^2 \int_{-\infty}^{t} J_1\left(t'\right)\, dt'\right) + \\ (1-f)^2 \exp\left(-q^2 \int_{-\infty}^{t} J_2\left(t'\right)\, dt'\right) + \\ 2f(1-f) \exp\left(-q^2 \int_{-\infty}^{t} J_{12}\left(t'\right)\, dt'\right) \end{bmatrix}} \tag{2.148}$$

Connection to Gaussian Dynamics

For Eq. 2.148, it is foreseen the non-Gaussian dynamics is reduced to Gaussian dynamics in the following instance,

1. Both compositon 1 and 2 have no memory for their dynamics so that the transport dynamics average out to be 0 after a long time.

$$\begin{aligned} \int_{-\infty}^{t} J_1\left(t'\right)\, dt' &= \int_{-\infty}^{t} J_2\left(t'\right)\, dt' = 0 \\ \int_{-\infty}^{t} J_{12}\left(t'\right)\, dt' &= \int_{-\infty}^{t} \frac{1}{2}\left(J_1\left(t'\right) + J_1\left(t'\right)\right)\, dt' = 0 \end{aligned} \tag{2.149}$$

2. There is only 1 dominated composition in the system,

$$\begin{aligned} f &= 1 \\ (1-f) &= 0 \end{aligned} \tag{2.150}$$

3. The dynamics of the second composition is too slow compared to the dynamics of the first composition, i.e., molecules in solid container compared to the scatters,

$$J_1(t) \gg J_2(t) \approx 0 \tag{2.151}$$

4. The dynamics of the second composition is faster than the dynamics of the first composition,

$$J_1(t) < J_2(t) \tag{2.152}$$

and meanwhile time approaches $t \to \infty$

In case 1,

$$\begin{aligned} J_{obs}(t) &= \frac{f^2 J_1(t)\exp\left(-q^2 0\right) + (1-f)^2 J_2(t)\exp\left(-q^2 0\right) + 2f(1-f)J_{12}(t)\exp\left(-q^2 0\right)}{f^2\exp\left(-q^2 0\right) + (1-f)^2\exp\left(-q^2 0\right) + 2f(1-f)\exp\left(-q^2 0\right)} \\ &= \frac{f^2 J_1(t) + (1-f)^2 J_2(t) + 2f(1-f)J_{12}(t)}{(f-(1-f))^2} \\ &= f^2 J_1(t) + (1+f^2-2f)J_2(t) + \Big(fJ_1(t) + fJ_2(t) - f^2 J_1(t) - f^2 J_2(t)\Big) \\ &= fJ_1(t) + (1-f)J_2(t) \end{aligned} \tag{2.153}$$

In case 2-3,

$$J_{obs}(t) = \frac{\exp\left(-q^2\int_{-\infty}^{t} J_1\left(t'\right)\,dt'\right)J_1(t)}{\exp\left(-q^2\int_{-\infty}^{t} J_1\left(t'\right)\,dt'\right)} = J_1(t) \tag{2.154}$$

In either of the cases, J_{obs} can accurately describes the transport dynamics of the system without any memory effects based on the $c_2\left(\vec{q}, t_1, t_2\right)$ measured from XPCS experiment.

In the listed instance, the fourth case seems contradicts the description of the third case and is less mathematically evident. Indeed, the fourth case can be attributed to the central limits theorem, a concept we will elaborate on in the subsequent section.

Central Limit Theorem

It is pertinent to consider the implications of the central limit theorem (CLT) in the context. In CLT, consider a series of stochastic processes [197],

$$X_1, X_2, ...X_t \tag{2.155}$$

where each $X_{t'}$ represents a random variable that can follow any distribution with a finite mean ($\mu_{t'}$) and variance ($\sigma_{t'}$). Regardless of the specific distribution of these variables, the sum Z_n, defined as

$$Z_t = \sum_{t'=1}^{t} X_{t'} \tag{2.156}$$

tends to a Gaussian distribution as the number of variables increases. Mathematically, this convergence is expressed as:

$$\lim_{t\to\infty} \frac{Z_t - \sum\limits_{t'=1}^{t} \mu_{t'}}{\sqrt{\sum\limits_{t'=1}^{t} \sigma_{t'}^2}} = \mathcal{N}(\mu = 0, \sigma^2 = 1). \tag{2.157}$$

This theorem suggests that while our approach may not initially capture the dynamics of a system with non-Gaussian behavior accurately, it becomes more applicable over an extended period.

After a brief review, we then corporate the picture of CLT into the non-Gaussian dynamics. In CLT, each step of random walk follows a finite distribution and, therefore, PDF of the state will only gets broader over time. As the rate of change in broadness of distribution, $J_n(t)$ is always a positive number over the interval of t. In Eq. 2.148, assuming $J_1 < J_2$, as $t \to \infty$, we have,

$$\lim_{t\to\infty} \int_{-\infty}^{t} J_2\left(t'\right)\, dt' \gg \lim_{t\to\infty} \int_{-\infty}^{t} J_{12}\left(t'\right)\, dt' \gg \lim_{t\to\infty} \int_{-\infty}^{t} J_1\left(t'\right)\, dt' \tag{2.158}$$

Therefore,

$$\lim_{t\to\infty} \exp\left(-q^2 \int_{-\infty}^{t} J_2\left(t'\right)\, dt'\right) \ll \lim_{t\to\infty} \exp\left(-q^2 \int_{-\infty}^{t} J_{12}\left(t'\right)\, dt'\right) \ll \lim_{t\to\infty} \exp\left(-q^2 \int_{-\infty}^{t} J_1\left(t'\right)\, dt'\right) \tag{2.159}$$

Therefore, Eq. 2.148 is simplified as,

$$\lim_{t\to\infty} J_{obs}(t) = \lim_{t\to\infty} \frac{\exp\left(-q^2 \int_{-\infty}^{t} J_1\left(t'\right)\, dt'\right) J_1(t)}{\exp\left(-q^2 \int_{-\infty}^{t} J_1\left(t'\right)\, dt'\right)} = \lim_{t\to\infty} J_1(t) \tag{2.160}$$

Similar idea can be extended to Eq. 2.147 for a generalized system with N composition and following equation is obtained,

$$\begin{aligned}
\lim_{t\to\infty} J_{obs}(t) &= \lim_{t\to\infty} \frac{\sum_{n=1}^{N}\sum_{m=1}^{N} x_n x_m J_{nm}(t) \exp\left(-q^2 \int_{-\infty}^{t} J_{nm}\left(t'\right)\, dt'\right)}{\sum_{n=1}^{N}\sum_{m=1}^{N} x_n x_m \exp\left(-q^2 \int_{-\infty}^{t} J_{nm}\left(t'\right)\, dt'\right)} \\
&= \frac{x_n^2 J_n(t) \exp\left(-q^2 \int_{-\infty}^{t} J_n\left(t'\right)\, dt'\right)}{x_n^2 \exp\left(-q^2 \int_{-\infty}^{t} J_n\left(t'\right)\, dt'\right)} \\
&= \min\left[J_n(t)\right]
\end{aligned} \tag{2.161}$$

The observation of Eq. 2.161 is consistent with the description of CLT that PDF can be approximated to Gaussian dynamics and our non-equilibrium approach again becomes valid to accurately capture the transport dynamics of the system.

Visualization of 2 Compositions System

To better understand the physical significant of $J_{obs}(t)$ elaborated in Eq. 2.148, we present a simulated system with well-defined $J_1(t)$ and $J_2(t)$ as follow,

$$J_1(t) = \begin{cases} 0, t < 0 \\ J_{1,\infty}, t \geq 0 \end{cases}, J_2(t) = \begin{cases} 0, t < 0; \\ J_{2,0}\mathrm{e}^{\Gamma t} + J_{2,\infty}, t \leq 0 \end{cases} \tag{2.162}$$

where $J_1(t)$ represents the unperturbed component of the system, maintaining a constant diffusivity $J_{1,0}$ over time, while $J_2(t)$ characterizes the system component undergoing relaxation with an exponential decay rate of Γ.

Based on Eq. 2.130, PDF is defined as,

$$\begin{aligned}\mathbb{P}(x,t) &= f\mathcal{N}\left(x;\mu=0,\sigma^2(t)=\int_{-\infty}^{t} J_1\left(t'\right)\,dt'\right)+(1-f)\mathcal{N}\left(x;\mu=0,\sigma^2(t)=\int_{-\infty}^{t} J_2\left(t'\right)\,dt'\right)\\ &= f\mathcal{N}\left(x;\mu=0,\sigma^2(t)=J_1 t\right)+(1-f)\mathcal{N}\left(x;\mu=0,\sigma^2(t)=\frac{J_{2,0}}{\Gamma}\left(1-\mathrm{e}^{\Gamma t}\right)+J_{2,\infty}t\right)\end{aligned} \tag{2.163}$$

By applying the given conditions Eq. 2.162 to Eq. 2.148, $J_{obs}(t)$ is analytically expressed as,

$$J_{obs}(t)=\frac{\begin{bmatrix} f^2 J_{1,0}\exp\left(-q^2 J_{1,\infty}t\right)+\\ (1-f)^2\left(J_{2,0}\mathrm{e}^{\Gamma t}+J_{2,\infty}\right)\exp\left(-q^2\left(\frac{J_{2,0}}{\Gamma}\left(\mathrm{e}^{\Gamma t}-1\right)+J_{2,\infty}t\right)\right)+\\ f(1-f)\left(J_{2,0}\mathrm{e}^{\Gamma t}+J_{2,\infty}+J_{1,0}\right)\exp\left(-\frac{1}{2}q^2\left(\frac{J_{2,0}}{\Gamma}\left(\mathrm{e}^{\Gamma t}-1\right)+\left(J_{2,\infty}+J_{1,0}\right)t\right)\right)\end{bmatrix}}{\begin{bmatrix} f^2\exp\left(-q^2 J_{1,\infty}t\right)+\\ (1-f)^2\exp\left(-q^2\left(\frac{J_{2,0}}{\Gamma}\left(\mathrm{e}^{\Gamma t}-1\right)+J_{2,\infty}t\right)\right)+\\ 2f(1-f)\exp\left(-\frac{1}{2}q^2\left(\frac{J_{2,0}}{\Gamma}\left(\mathrm{e}^{\Gamma t}-1\right)+\left(J_{2,\infty}+J_{1,0}\right)t\right)\right)\end{bmatrix}} \tag{2.164}$$

To visualize both PDF and $J_{obs}(t)$, we numerically define $J_{1,\infty}$, $J_{2,0}$, $J_{2,\infty}$ and Γ as,

$$\begin{aligned} J_{1,\infty}=J_{2,\infty}&=0.01\\ J_{2,0}&=10\\ \Gamma&=-2.5\end{aligned} \tag{2.165}$$

so that,

$$\begin{aligned} J_1(t)&=0.01\\ J_2(t)&=10\mathrm{e}^{-2.5t}+0.01\end{aligned} \tag{2.166}$$

With the numerical conditions in Eq. 2.166, PDF is shown in panels A, C, and E of Fig. 2.5 within the range of $0\leq t\leq 10$, considering the cases where f equals 0, 0.5, and 1.

With the knowledge of PDF, $c_1(\vec{q}, t_1, t_2)$ at $q = 1.25$ is calculated by Eq. 2.13 and shown in upper left in panels B, D, and F of Fig. 2.5. The non-equilibrium approach is then applied to the simulated $c_1(\vec{q}, t_1, t_2)$ and analysis results shown in lower right in panels B, D, and F of Fig. 2.5.

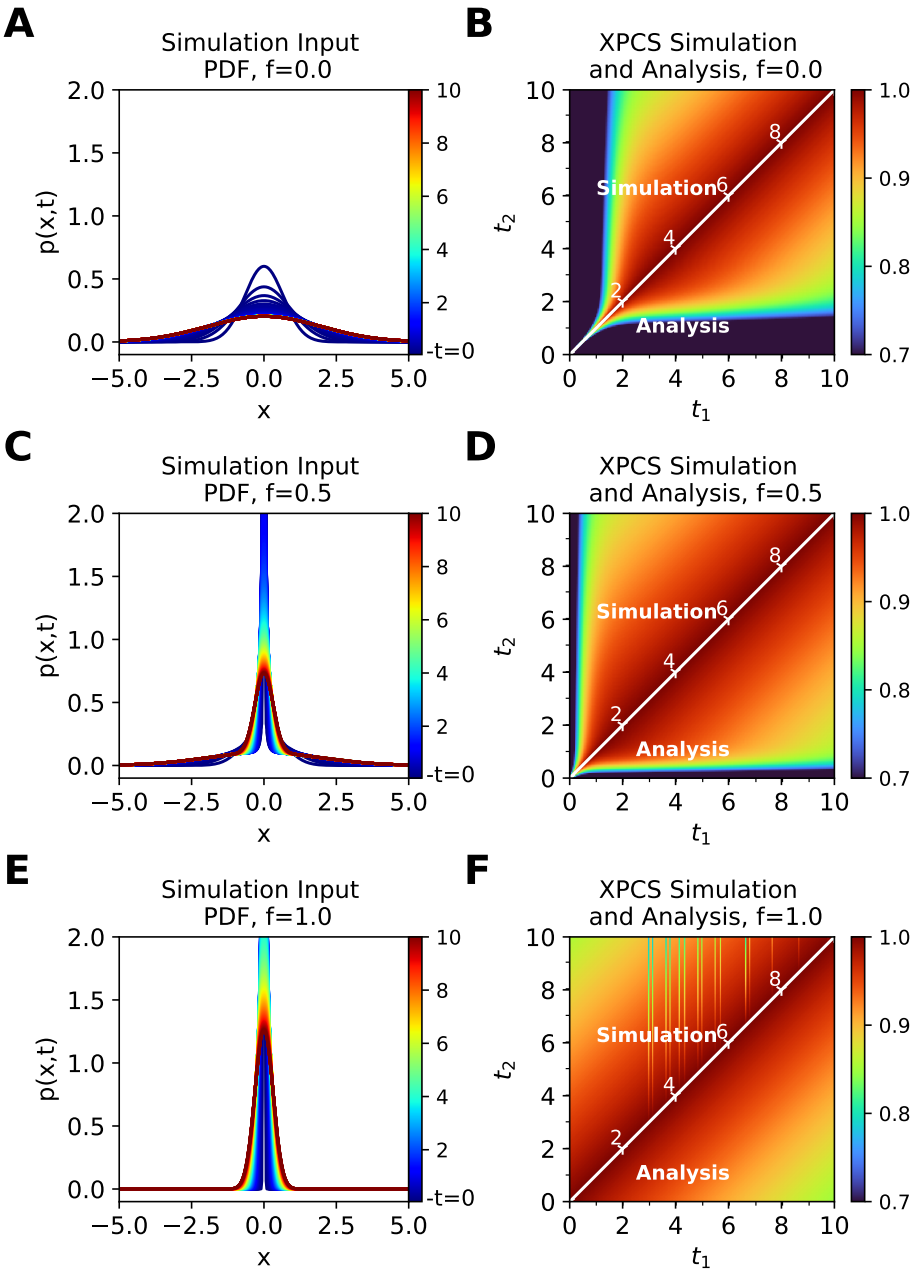

Figure 2.5: **Illustration of Non-Equilibrium Analysis Applied to a case of Non-Gaussian Dynamics.** Given by Eq. 2.163, the PDF of non-Gaussian dynamics is a blend of two Gaussian dynamics, with its influence adjusted by a factor of f, as illustrated in panels A ($f = 0$), C($f = 0.5$), and E ($f = 1$). The $c_1(\vec{q}, t_1, t_2)$ at $q = 1.25$ corresponding to the non-Gaussian dynamics is computed by Eq. 2.13 and shown in upper left in panels B, D, and F. The results from the non-equilibrium approach on the $c_1(\vec{q}, t_1, t_2)$ is shown in lower right in panels B, D, and F. In panel F, the presence of noise and discontinuity in $c_1(\vec{q}, t_1, t_2)$ can be attributed to numerical resolution issues arising from the division operation involving small numbers in Eq. 2.13.

In Fig. 2.6, we compare $J_{obs}(t)$ obtain from the non-equilibrium analysis and direct computation by Eq. 2.148. Across different values of f, the alignment of J_{obs} affirms the validity of Eq. 2.148, shedding light on the suitability of the non-equilibrium approach in capturing non-Gaussian dynamics.

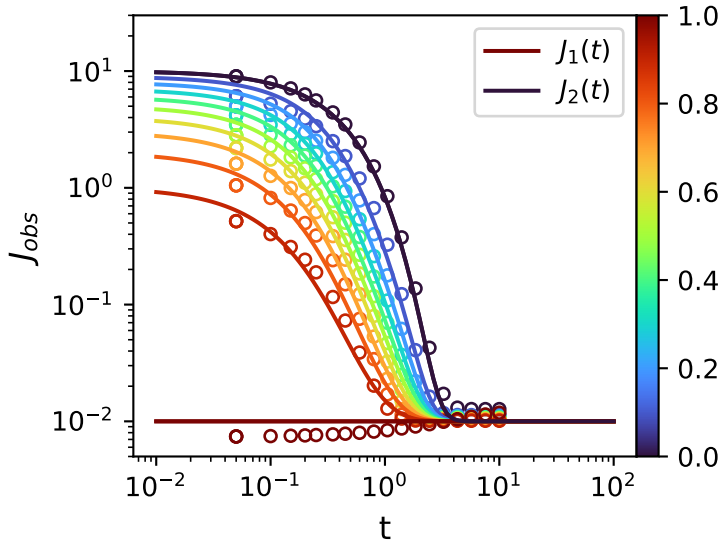

Figure 2.6: **Comparison between $J_{obs}(t)$ obtain from the non-equilibrium analysis (scattered dots) and the calculated by Eq. 2.164 (solid line)**. The consistency between J_{obs} demonstrates the validation of Eq. 2.148. Meanwhile, the influence of fraction (f) on the $J_{obs}(t)$ is also explored. The variation of f is represented by a color gradient of $J_{obs}(t)$, with the accompanying color bar mapping the evolution of the system dynamics from $f = 0$ to $f = 1$.

2.8.4 q-dependence of $J_{obs}(t)$

Another noticeable property of J_{obs} is its q-dependence attributed to the term of $\exp\left(-\frac{1}{2}q^2 \int_{-\infty}^{t} J_n\left(t'\right)\, dt'\right)$. In another words, different dynamics is obtained by the measurement of $c_1\left(\vec{q}, t_1, t_2\right)$ in different q regions.

Starting from $q = 0$, Eq. 2.147 is reduced to,

$$\begin{aligned} J_{obs}(q=0,t) &= \frac{\sum_{n=1}^{N}\sum_{m=1}^{N} x_n x_m J_{nm}(t) \exp\left(-0^2 \int_{-\infty}^{t} J_{nm}\left(t'\right)\, dt'\right)}{\sum_{n=1}^{N}\sum_{m=1}^{N} x_n x_m \exp\left(-0^2 \int_{-\infty}^{t} J_{nm}\left(t'\right)\, dt'\right)} \\ &= \frac{\sum_{n=1}^{N}\sum_{m=1}^{N} x_n x_m J_{nm}(t)}{\sum_{n=1}^{N}\sum_{m=1}^{N} x_n x_m} \\ &= \frac{\frac{1}{2}\sum_{n=1}^{N}\sum_{m=1}^{N} x_n x_m \left(J_n(t) + J_m(t)\right)}{\sum_{n=1}^{N} x_n \sum_{m=1}^{N} x_m} \\ &= \frac{1}{2}\left(\sum_{n=1}^{N} x_m \sum_{m=1}^{N} x_n J_n(t) + \sum_{n=1}^{N} x_n \sum_{m=1}^{N} x_m J_m(t)\right) \\ &= \sum_{n=1}^{N} x_n J_n(t) \end{aligned} \tag{2.167}$$

Based on the Eq. 2.167, at $q = 0$, $J_{obs}(t)$ is simply the linear combination of $J_n(t)$ at any time t, resemble the case without memory effect.

However, as q increases, the contribution from the part with faster dynamics vanish as $\exp\left(-\frac{1}{2}q^2 \int_{-\infty}^{t} J_n\left(t'\right)\, dt'\right)$ rapidly approaches to 0. Eventually, at $q \to \infty$, only the slowest dynamics is observed.

$$\lim_{q\to\infty} J_{obs}(t) = \lim_{q\to\infty} \frac{\sum_{n=1}^{N}\sum_{m=1}^{N} x_n x_m J_{nm}(t) \exp\left(-q^2 \int_{-\infty}^{t} J_{nm}\left(t'\right)\, dt'\right)}{\sum_{n=1}^{N}\sum_{m=1}^{N} x_n x_m \exp\left(-q^2 \int_{-\infty}^{t} J_{nm}\left(t'\right)\, dt'\right)} = \min\left[J_n(t)\right] \tag{2.168}$$

The q-dependence of $J_{obs}(t)$ is similar to the description of CLT explained in previous

section.

To delve deeper into the q-dependence of $J_{obs}(t)$, we utilize the simulated system described in Eq. 2.162 and illustrate the variation of $J_{obs}(t)$ across different q values in Fig. 2.7.

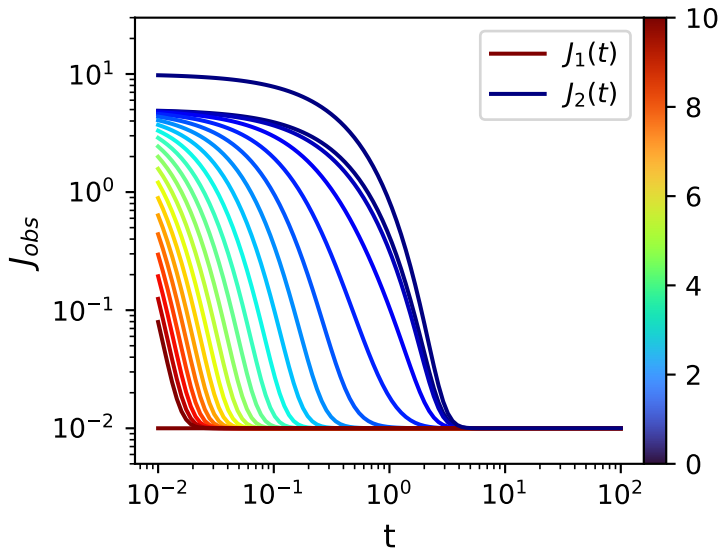

Figure 2.7: **Exploration of the influence of scattering vector (q) on the $J_{obs}(t)$ with $f = 0.5$.** The variation of q is represented by a color gradient of $J_{obs}(t)$, with the accompanying color bar mapping the evolution of the system dynamics from $q = 0$ to $q = 10$.

As shown in Fig. 2.7, $J_{obs}(t)$ observed in high q rapidly approaches to $J_1(t)$, the slow dynamics in the system compared to $J_2(t)$. Such observation confirm the results in Eq. 2.168.

2.8.5 Connection to Heterodyne Scattering

When multiple components with discrete dynamics are present in the system, the scattering signals can interfere with each other, resulting in heterodyne scattering signals in $c_2(\vec{q}, t_1, t_2)$. Such a system is a classical non-Gaussian system that has been well-described in the literature. Our proposed model can be reduced to account for heterodyne scattering, providing a good example to validate the effectiveness of our model.

With heterodyne scattering, our assumption in 2.136 is no longer valid. Therefore, the dynamics of the system can be simplified and extracted by a single parameter, $\Gamma(q,t)$. Instead, our derivation starts from 2.135.

$$c_2(q,t_1,t_2) = 1 + \beta \left(\frac{\sum_{n=1}^{N}\sum_{m=1}^{N} x_n x_m \exp\left(\int_{-\infty}^{t_2} -q^2 J_{nm}(t') - iqv_{nm}(t')\,dt'\right)}{\sum_{n=1}^{N}\sum_{m=1}^{N} x_n x_m \exp\left(\int_{-\infty}^{t_1} -q^2 J_{nm}(t') - iqv_{nm}(t')\,dt'\right)} \right) \tag{2.169}$$

In the classical derivation of heterodyne scattering function, there is an important assumption that the system has no memory effect, the transport dynamics and flow motion is average to 0 as,

$$\int_{-\infty}^{t_1} -q^2 J_{nm}(t') - iqv_{nm}(t')\,dt' = 0 \tag{2.170}$$

We got the equation as,

$$\begin{aligned} c_2(q,t_1,t_2) &= 1 + \frac{\beta}{f}\sum_{n=1}^{N}\sum_{m=1}^{N} x_n x_m \exp\left(\int_{t_1}^{t_2} -q^2 J_{nm}(t') - iqv_{nm}(t')\,dt'\right) \\ f &= \sum_{n=1}^{N}\sum_{m=1}^{N} x_n x_m = \sum_{n=1}^{N} x_n \sum_{m=1}^{N} x_m = 1 \end{aligned} \tag{2.171}$$

Since only the real part is measureable in XPCS experiment, the equation is reduced to,

$$c_2(q,t_1,t_2) = 1 + \beta \sum_{n=1}^{N}\sum_{m=1}^{N} x_n x_m \exp\left(\int_{t_1}^{t_2} -q^2 J_{nm}(t)\,dt'\right) \cos\left(\int_{t_1}^{t_2} qv_{nm}(t')\,dt'\right) \tag{2.172}$$

This is the heterodyne scattering equation. If there are 2 compositions in the system,

the $c_2\left(\vec{q}, t_1, t_2\right)$ is written as,

$$c_2(q, t_1, t_2) = 1 + \beta \left[\begin{array}{c} x_1^2 \exp\left(- \int_{t_1}^{t_2} q^2 J_1(t')\, dt' \right) + \\ x_2^2 \exp\left(- \int_{t_1}^{t_2} q^2 J_2(t')\, dt' \right) + \\ 2x_1 x_2 \exp\left(-\frac{1}{2} q^2 \int_{t_1}^{t_2} J_1(t') + J_2(t)\, dt' \right) \cos\left(q \int_{t_1}^{t_2} v_o(t')\, dt' \right) \end{array} \right] \tag{2.173}$$

2.8.6 Multiple Gaussian Model to Extract Dynamics

Among the many types of non-Gaussian dynamics, only a few cases can be analytically solved under certain approximations. For most systems, however, the PDF of particle dynamics may take on complex or even arbitrary forms. To accommodate such complexity, the PDF at any given time can be approximated as a linear combination of N Gaussian functions Eq. 2.130. Using this approximation, and according to Eq. 2.13, the $c_1\left(\vec{q}, t_1, t_2\right)$ can be expressed as Eq. 2.131 and $c_1\left(\vec{q}, t_1, t_2\right)$ measured from XPCS can be expressed as Eq. 2.135.

In terms of physical significance, Eq. 2.131 is, in fact, a model with n components, each undergoing simple diffusion. In certain cases analogous to this model, such as a binary mixture of active and non-active particles, the $c_2\left(\vec{q}, t_1, t_2\right)$ across all q ranges can be fitted using a single set of parameters $\mu_n(t)$, $\sigma_n^2(t)$, and $x_n(t)$ [198]. However, given the broad nature of non-Gaussian dynamics, some $c_2\left(\vec{q}, t_1, t_2\right)$ results cannot be adequately described by a single set of parameters. In such cases, $c_2\left(\vec{q}, t_1, t_2\right)$ at each q is analyzed separately to obtain $S(\vec{q}, t)$ from Eq. 2.13 over time at that specific q. A reverse Fourier transform can be applied to recover the PDF. This approach allows us to characterize the dynamics through the evolution of the PDF, without further requiring a predefined model prior to the analysis.

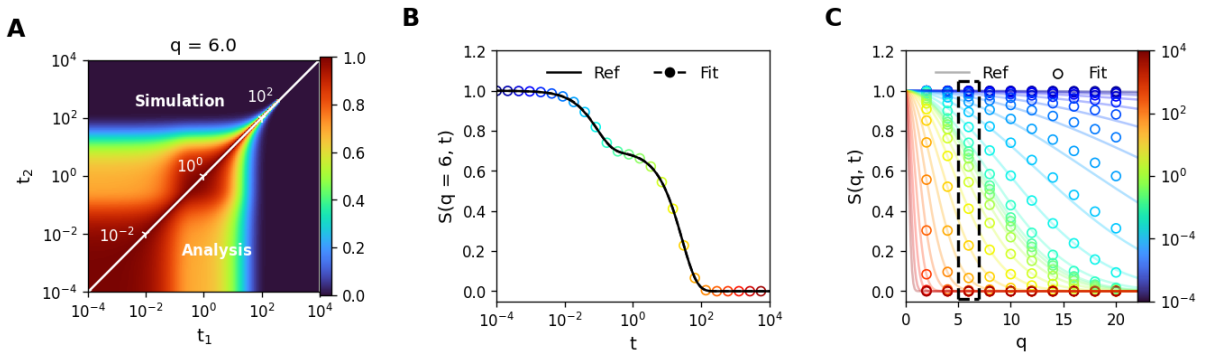

Figure 2.8: **Illustration of the proposed approach for extracting $S(q,t)$ to characterize non-Gaussian dynamics, exemplified by cage dynamics. A).** The simulated $c_2\left(\vec{q},t_1,t_2\right)$ at $q=6$ from the reference function, shown in the upper triangle, is analyzed by Eq. 2.131 with 2 Gaussian function, and the fitting results are shown in the lower triangle. **B).** The obtained parameters allow the reconstruction of the $S(q,t)$ at $q=6$. **C).** By analyzing many $c_2\left(\vec{q},t_1,t_2\right)$ from a range of q, the entire $S(q,t)$ varying q and t can be mapped out. The consistency between the reference and fitting results in both $c_2\left(\vec{q},t_1,t_2\right)$ and $S(q,t)$ indicates that this approach is not only compatible with analyzing the non-Gaussian dynamics observed in XPCS, but also capable of extracting genuine physical information from the dynamic process.

By combining these results of $S\left(q,t\right)$ and the comprehensive picture of the dynamics, the fundamental parameters that describe non-Gaussian dynamics can be obtained. Once $S(\vec{q},t)$ is determined, various physical parameters characterizing the dynamic process can be extracted, such as the transport coefficient, mean square displacement, and non-Gaussian parameter. A well-established approach for studying non-Gaussian dynamics is to expand $S(q,t)$ in a series of even Hermite polynomials [199].

$$S(q,t)=\mathrm{e}^{-\frac{1}{2}q^2\mathbb{V}[x(t)]}\left[1+\alpha_2(t)\frac{\left(\frac{1}{2}q^2\mathbb{V}[x(t)]\right)^2}{2!}-\left(\alpha_3(t)-3\alpha_2(t)\right)\frac{\left(\frac{1}{2}q^2\mathbb{V}[x(t)]\right)^3}{3!}.....\right] \tag{2.174}$$

where $\alpha_n(t)$ are cumulant defined as:

$$\alpha_n(t)=\frac{\mathbb{E}\left[x^{2n}\right]}{\frac{2n+1}{3^n}\mathbb{E}\left[x^2\right]^n}-1 \tag{2.175}$$

When $n = 2$, the first cumulant $\alpha_2(t)$ is obtained, often referred to as the NGP, which describes the change in kurtosis behavior in a non-Gaussian distribution.

$$\alpha_2(t) = \frac{\mathbb{V}[x(t)^2]}{3\mathbb{V}[x(t)]^2} - 1 \tag{2.176}$$

To better extract the fundamental physical parameter, Eq. 2.175 is taken as log scale, expanding $\ln(S(q,t))$ at small q while ignoring the higher order terms. In such case, the following expression is obtained [200],

$$\ln(S(q,t)) = -\mathbb{V}[x(t)]\left(\frac{1}{2}q^2\right) + \left(\mathbb{V}[x(t)^2] - 3\mathbb{V}[x(t)]^2\right)\left(\frac{1}{2}q^2\right)^2 \tag{2.177}$$

These fundamental parameters, including MSD and $\alpha_2(t)$, can characterize and provide insight into the non-Gaussian dynamics obtained from XPCS.

Validation of the Model Using Gaussian Dynamics

To demonstrate the efficiency and validity of our model, we simulate non-interacting particles exhibiting standard diffusive dynamics. The PDF follows a Gaussian distribution. As shown in Fig. 2.10, our model, given by Eq. 2.131 with $n = 1$, effectively analyzes the simulated $c_2(\vec{q}, t_1, t_2)$, and the extracted $S(q,t)$ closely matches the reference obtained by Fourier transforming the PDF computed directly from the particle coordinates. Some discrepancies appear in the low-q regions, which stem from inherent limitations in $c_2(\vec{q}, t_1, t_2)$ computation in both XPCS experiments and simulations. These discrepancies arise due to an insufficient number of intensity sample pixels at low q, leading to a statistical bias in $c_2(\vec{q}, t_1, t_2)$.

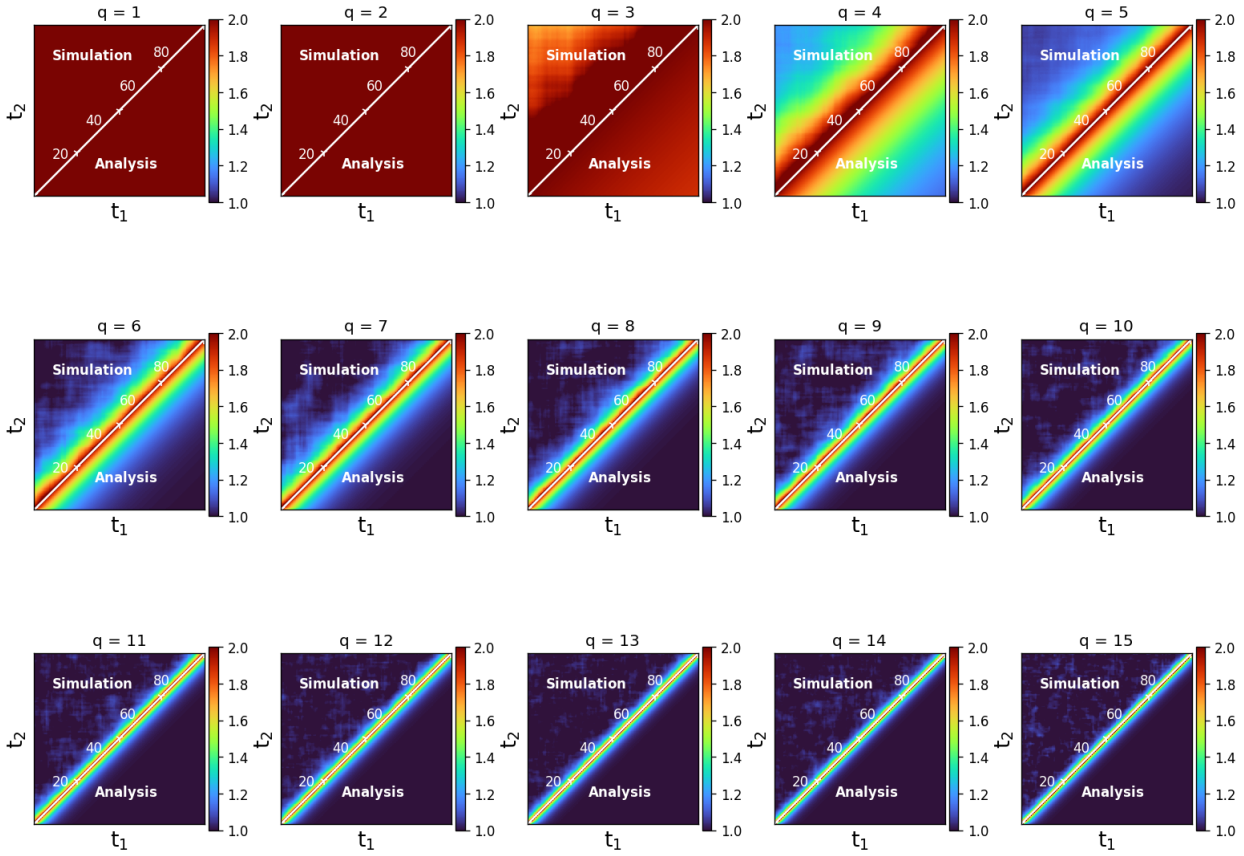

Figure 2.9: **Fitting results of simulated standard diffusion (upper triangle) using Eq. 2.135 with** $n = 1$**.** The consistency between the simulated data (upper triangle) and the fitted $c_2(\vec{q}, t_1, t_2)$ (lower triangle) indicates that the equation accurately describes the dynamic process of standard diffusion. The analyzed results are extracted to map out $S(q, t)$ in Fig. 2.10.

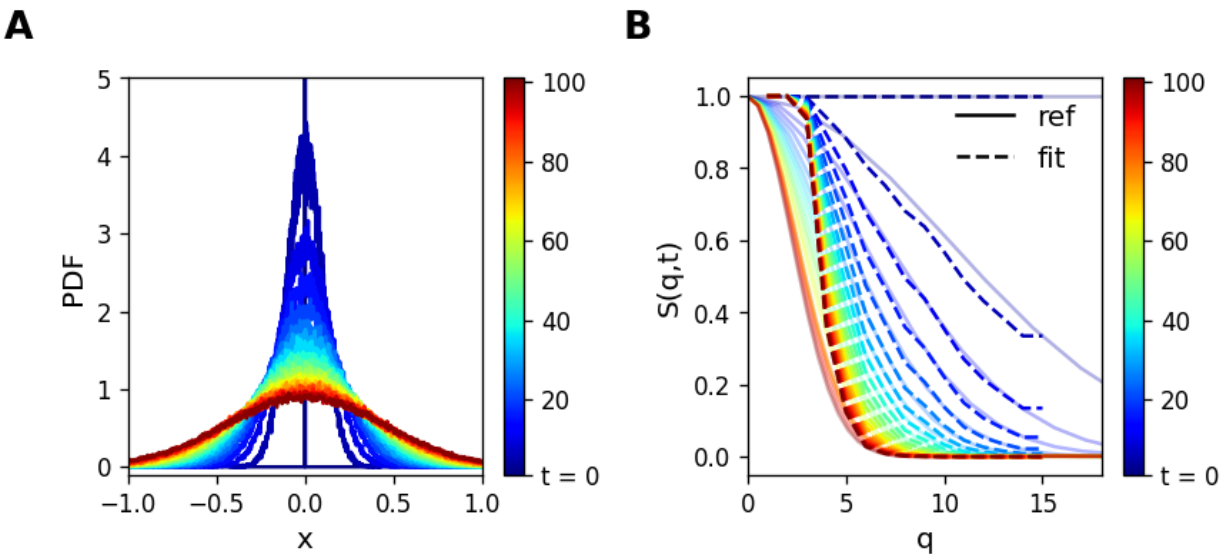

Figure 2.10: **Comparison between the PDF and $S(q,t)$ from direct computation as a reference to the analyzed results. A)** The PDF is obtained by directly computing the coordinates of the particles in the simulation boxes. It is then converted to $S(q,t)$ via a Fourier transform and plotted as a solid line in **B)**. The analyzed results of $S(q,t)$ as dashed line are closely match these reference values, with some discrepancies in the low-q regions. This is due to an insufficient number of intensity sample pixels, leading to a bias in $c_2\left(\vec{q},t_1,t_2\right)$ as a statistical property.

CHAPTER 3

TRANSPORT COEFFICIENT APPROACH FOR CHARACTERIZING NON-EQUILIBRIUM DYNAMICS IN SOFT MATTER

3.1 Introduction

Soft materials, including colloidal suspensions [201, 202], polymers[191, 203], gels [204, 205], and biological materials [206, 207], often exist in non-equilibrium states, a crucial aspect of their practical applications and scientific studies. These non-equilibrium states arise due to external factors, including mechanical forces, temperature fluctuations, or chemical reactions, necessitating an understanding of how these materials respond to such stimuli. Although classical theories such as mean-field theory [208, 209], renormalization group [210, 211], and universality [210, 212] have contributed significantly to our understanding of particle and atomic behavior within complex systems, they fall short when these materials deviate from equilibrium under external influences. Non-equilibrium dynamics introduce intriguing phenomena, including transitions between metastable states [213, 214], dynamical heterogeneity [179, 180], aging [181, 182], yielding [215, 216], avalanches [184, 185], and phase reentrance [58, 183]. Real-time measurements serve as a valuable tool to unravel the kinetics and mechanisms governing these transitions, facilitating improved control and predictability [217, 218]. Consequently, it becomes imperative to develop robust *in situ* tools and analysis models that enable us to investigate the dynamic behavior of complex materials [219, 220], validate theoretical constructs [221, 222], and engineer functional materials for a variety of applications within these soft matter systems.

In this pursuit, various *in situ* techniques, including scattering [223, 224, 121], imaging [225, 226, 227], spectroscopy [228, 229, 230, 231], and force measurements [232, 233], emerge as effective tools for investigating non-equilibrium phenomena. Among these techniques,

XPCS, a coherent x-ray scattering method capable of measuring dynamics through the temporal autocorrelation function of intensity fluctuations in space and time, has shone since its introduction in 1991 [147]. It offers exceptional spatial and temporal resolution, making it ideal for investigating the unique insight of non-equilibrium dynamics at the nanoscale in diverse soft matter systems. In a typical XPCS experiment (Fig. 3.1A), a series of x-ray scattering intensities (speckles) $I(\vec{q}, t)$ is collected with a 2D detector as a function of time. To extract the dynamics from a non-equilibrium system, a $c_2\left(\vec{q}, t_1, t_2\right)$ is computed according to the Eq. 2.14 [234].

In a system containing a large number of independent scatters with randomized scattered phases, the scattered fields are generated by Gaussian processes. This condition enables the application of the Siegert relation, and $c_2\left(\vec{q}, t_1, t_2\right)$ is written as follows Eq. 2.14 [137].

A common approach to analyzing equilibrium dynamics $c_2\left(\vec{q}, t_1, t_2\right)$ starts with its conversion to a $g_2\left(\vec{q}, \tau\right)$. In equilibrium, $g_2\left(\vec{q}, \tau\right)$ is calculated by diagonal averaging of $c_2\left(\vec{q}, t_1, t_2\right)$ along the axis of delayed time τ as shown in Fig. 3.1B. However, for non-equilibrium dynamical evolution, diagonal averaging fails, and this conversion thereby involves dividing the absolute time of the experiment into distinct regions, as demonstrated in Fig. 3.1C. These regions are known as TIZs [176]. Within these TIZs, it is assumed that the system is in a pseudo-equilibrium state. $g_2\left(\vec{q}, \tau\right)$ is then calculated by averaging over the delay time $\tau = |t_2 - t_1|$ in either the vertical/horizontal direction or the diagonal direction. Subsequent analysis involves fitting the one-time correlation function with a specific model of the correlation function tailored to the characteristics of the system under investigation. The choice of an appropriate model depends on the properties and behaviors of the system. For example, a simple exponential function describes the diffusion dynamics with a single relaxation time [235]. A Kohlrausch–Williams–Watts (KWW) function has been shown to describe systems that exhibit anomalous diffusion [186], a sinc function for a fluid that undergoes homogeneous shear [189], or a heterodyne scattering function for a system composed of two

components with well-separated dynamical time scales [190].

However, XPCS analyses in non-equilibrium systems present significant challenges. Reported studies have treated such systems by approximating the system to be in equilibrium system within TIZs, which is a shortcoming in systems characterized by strongly varying non-equilibrium conditions, such as the Rheo-XPCS experiments conducted under external stimulus [154]. Conversion of $c_2\left(\vec{q}, t_1, t_2\right)$ into $g_2\left(\vec{q}, \tau\right)$ by averaging over τ can potentially distort or overlook intricate time-dependent variations in the data, leading to the loss of crucial information about the dynamics of the system [187]. Moreover, current XPCS analyses struggle to decipher complex patterns observed in the two-time correlation function, such as "square", "wings" or "tail-like" features [153, 236, 3]. Predominant explanations have focused on "backflow" where particles move relative to their neighbors, leading to jammed and disordered arrangements at irregular intervals [176], or abrupt phase transitions of the entire system [153]. Such models often overlook the influence of factors such as structural dynamics, particle interactions, and other time-dependent effects that play an important role in shaping the observed patterns. The incomplete consideration of these elements in the current analyses hinders our comprehensive understanding of the underlying dynamics.

Advancing XPCS analysis methodologies in non-equilibrium systems to overcome some of the above limitations is important in deepening our understanding of complex dynamic processes in soft matter. The advancement presented in this work enables the direct extraction of valuable information from $c_2\left(\vec{q}, t_1, t_2\right)$ without the need for any temporal averaging. We present a transport coefficient method for characterizing non-equilibrium dynamics in soft matter. Our approach formulates a Langevin dynamics model that considers particle dynamics comprising two constituents: intrinsic random motion and externally driven motion. By assuming a Markovian process without memory for non-equilibrium dynamics, we derive the transition probability $\mathbb{P}(\Delta x, t_1, t_2)$, which connects the probability distribution ($\mathbb{P}$) of position (x) at time t_1 and t_2 within the dynamic process. We then convert this

probability to $c_2(\vec{q}, t_1, t_2)$ using a Fourier transform. To validate our model, we initially applied it to a molecular dynamics simulation system with known physical parameters. This involves comparing the transport coefficient $J(t)$ obtained from the simulation trajectory with the values extracted from the analysis of $c_2(\vec{q}, t_1, t_2)$. Subsequently, we employ this analysis methodology on XPCS results from two sources in the literature that have used existing methodologies: one that involves relaxation of a colloidal system after applied creep [2] and another that involves a gel system subjected to internal stresses [3]. Furthermore, we extend our analysis methodology to include complex fluids characterized by even more complex dynamics. In this context, we explore a system involving a suspension of charged colloids in salt solutions. Using a combination of creep measurements and Rheo-XPCS, we delve into the dynamics of deformation and relaxation, allowing us to observe phenomena such as complex patterns in the $c_2(\vec{q}, t_1, t_2)$ and multiple shear bands. Subsequently, we interpret and rationalize these complex rheological phenomena by extracting time-dependent physical quantities using the developed approach. This advancement not only enhances the data accuracy of XPCS analysis (Fig. 3.1D) but also offers significant insight into the dynamical properties of the system that are overlooked by the existing methods.

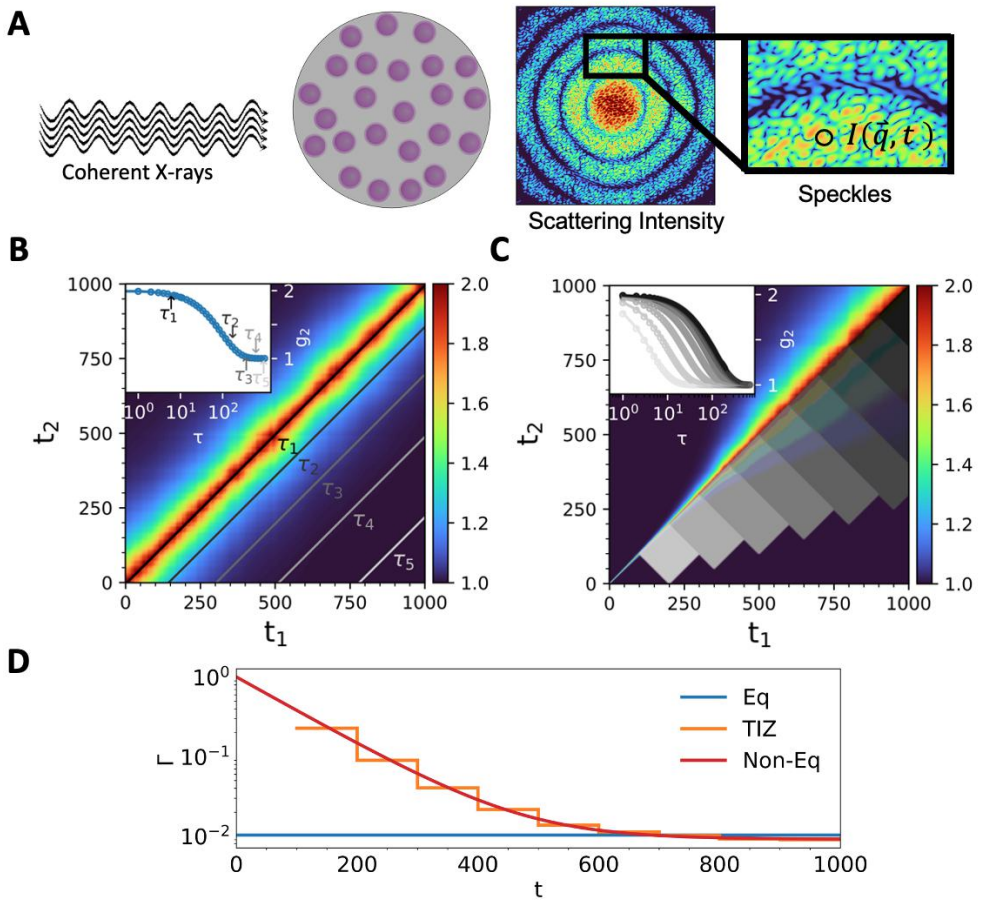

Figure 3.1: **Illustration of the XPCS experiment procedure and its analysis techniques in both equilibrium and non-equilibrium states.** (A) In a standard XPCS experiment, coherent X-rays illuminate the samples, generating speckles that reveal the spatial distribution of particles on detectors. Dynamic information about the system is obtained by calculating the temporal correlation function c_2 of these speckles, which is then converted to a one-time correlation function g_2 by averaging. Depending on whether the system is in equilibrium or not, the analysis procedure to convert from c_2 to g_2 varies: In the equilibrium case (B), g_2 (inserted figure) can be obtained by diagonally averaging c_2 at increasing value of τ (gray line); in contrast, in the non-equilibrium system (C), g_2 (inserted figure) can only be obtained by averaging c_2 within the predefined TIZs (gray rectangle), where the system is assumed to be pseudo-equilibrium for a certain period within the TIZs. The color of g_2 in the inserted figure corresponds to the TIZs with lighter colors at an earlier time. (D) We introduced a transport coefficient approach to obtain the time-resolved dynamics directly by fitting c_2 without any averaging. As a result of this analysis, Γ represents the characteristic dynamics rate of the system, and its expression depends on the specific system under study. For standard diffusion, it is defined as $\Gamma = q^2 D$ in equilibrium (blue line) and $\Gamma(t) = \frac{1}{2} q^2 J(t)$ in a non-equilibrium state, where D is the diffusion constant, and $J(t)$ is the transport coefficient, as defined in Eq. 2.42. The results obtained from our newly developed non-equilibrium analysis approach (red line) offer enhanced detail and higher resolution in the time-resolved dynamics compared to conventional TIZs approaches (orange line).

3.2 Materials and Method

3.2.1 Sample Preparation

The charged colloidal systems are created through a chemical process involving the grafting of charged molecules, specifically L-glutathione (GSH), onto the surfaces of 120nm spherical silica particles (SiO_x) particles using click chemistry. Once these desired charged particles are obtained, they are suspended in salt solutions (48 v%) comprising 60 mM $NaNO_3$ + 10 mM $MgSO_4$. The suspensions are then subjected to an ultrasonic treatment. The volume fraction of the system is intentionally designed to strike a delicate balance—it is sufficiently high to encourage the development of an internal structure, yet low enough to prevent occurrences of glass transition and crystallization.

3.2.2 Rheo-XPCS

The XPCS experiment takes place at 8ID-I at Advanced Photon Source in Argonne National Laboratory, with a sample-to-detector distance of 8 m, X-ray energy set at 7.35 keV, and data acquisition at a rate of 10 Hz. Simultaneously, a Rheo-XPCS experiment is conducted by performing a creep test. This approach allows for the measurement of both deformation under constant applied stress and the subsequent recovery after stress removal, enabling a comprehensive study of the system's yielding behaviors. In the context of charged colloids that exist under complex ionic conditions, this setup anticipates a range of intricate rheological phenomena, including delayed yielding, resolidification, and shear banding. In the Rheo-XPCS experiment, the creep test is performed on SiO_x-GSH in a solution consisting of 60 mM $NaNO_3$ + 10 mM $MgSO_4$. In particular, the deformation behavior of SiO_x-GSH in this specific ionic environment exhibits heterodyne scattering signals characterized by multiple shear bands, as illustrated in Fig. 3.4A. Given the complexity of this phenomenon, more in-depth analysis and interpretation are warranted, using the non-equilibrium analysis

of XPCS as described in this study.

3.2.3 $\boldsymbol{J(t)}$ *from 3 Classical Langevin Processes*

Table 3.1: $\boldsymbol{J(t)}$ from 3 Classical Langevin Processes.

Langevin Process	$J(t)$
Wiener / Standard Diffusion	$2D$
Ornstein–Uhlenbeck	$2D\left(1-\mathrm{e}^{-\gamma t}\right)^2$
Brownian Oscillator: Underdamped $\left(\omega_o > \frac{\gamma}{2}\right)$	$2D\frac{\gamma^2}{\omega_s}\mathrm{e}^{-\gamma t}\sin\left(\omega_s t\right)^2$
Brownian Oscillator: Overdamped $\left(\omega_o < \frac{\gamma}{2}\right)$	$8D\frac{\gamma^2}{\gamma_s}\mathrm{e}^{-\gamma t}\sinh\left(\gamma_s t\right)^2$

Table 3.1 presents the formulations for the $J(t)$s derived from three classical Langevin dynamics. In this context, D represents the classical diffusion constant in the equilibrium state. The symbol γ denotes the drift velocity, indicative of the average directional motion, while ω_o represents the angular frequency associated with the harmonic oscillator's oscillations. The terms γ_s and ω_s are dimensionless parameters corresponding to scaled versions of γ and ω_o.

In the case of an underdamped Brownian oscillator, where the influence of the elastic force surpasses that of the drift force $\left(\omega_o > \frac{\gamma}{2}\right)$, $J(t)$ oscillates over time due to the $\sin\left(\omega_s t\right)^2$ component. Conversely, in an overdamped oscillator scenario $\left(\omega_o < \frac{\gamma}{2}\right)$ characterized by the predominance of the drift force, the oscillatory behavior of $J(t)$, driven by $\sinh\left(\frac{1}{2}\gamma_s t\right)^2$, dissipates more rapidly. Further elaboration on this topic is provided in Section 2.7.2 of the Chapter 2.

3.3 Approach Validation

3.3.1 MD Simulation

To validate the theoretical framework described above in Chapter 2, Section 2.4, we performed MD simulations involving non-interacting particles (i.e., phantom particles) within a non-equilibrium system created by varying the temperature. As shown in Fig. 3.2D, the temperature was initially maintained at a high value, followed by a linear decrease to a stable lower value. The transport coefficient, $J_{\vec{q}}$, was determined by $c_2(\vec{q}, t_1, t_2)$ using Eq. 2.67. To streamline the fitting process, we represented the trend of the transport coefficient using the error function (see Eq. 3.2 in the App). For a better comparison, in each figure of $c_2(\vec{q}, t_1, t_2)$, the data obtained from experiments and simulation is presented in the upper left, while the fitting results are displayed in the lower right. In Fig. 3.2A - C, $c_2(\vec{q}, t_1, t_2)$ obtained from simulation trajectories with different scattering vectors demonstrates good agreement with the simulated data. According to Eq. 2.67, the correlation functions obtained at higher values of $\left(q_x^2 + q_y^2 + q_z^2\right)$ exhibit a faster decay. This trend is evident starting with $\left(q_x = q_y = q_z = 6\right)$ in Fig. 3.2A, followed by $\left(q_x = q_y = 6, q_z = 0\right)$ in Fig. 3.2B, and subsequently by $\left(q_x = 6, q_y = q_z = 0\right)$ in Fig. 3.2C. Despite these differences, the transport coefficient extracted from $c_2(\vec{q}, t_1, t_2)$ measured with different scattering vectors, namely $J_{q_x=6}(t)$, $J_{q_{x,y}=6}(t)$, and $J_{q_{x,y,z}=6}(t)$, is anticipated to be identical, as they originate from the particle dynamics of the same simulation. This consistency is observed in Fig. 3.2D, where all transport coefficients overlap and follow the same decreasing trend over time. Similar results are also observed for other scattering vectors, as shown in Fig. 3.5 from App.

In a system without external drive, the transport coefficient can also be obtained directly from simulation trajectories using the time derivative of the mean-squared displacement of particles, denoted as J_{MD} and given by Eq. 2.42. This parameter serves as a validation

measure for the analysis of $c_2(\vec{q}, t_1, t_2)$. As illustrated in Fig. 3.2D, the transport coefficients obtained by fitting $c_2(\vec{q}, t_1, t_2)$ with different scattering vectors agree with the reference J_{MD}. The slight discrepancy observed for $J_{q_{x,y,z}=6}(t)$ during $t < 100$ can be attributed to two reasons: (1) the absence of valid data to describe the rapid dynamics in the high q regions during the high-temperature period and (2) the selected equation did not accurately capture the actual change in $J\,(t)$ over time. Despite these imperfections, this result provides evidence that $J\,(t)$ accurately reflects the actual physical quantity in the system, thus validating the approach of extracting $J\,(t)$.

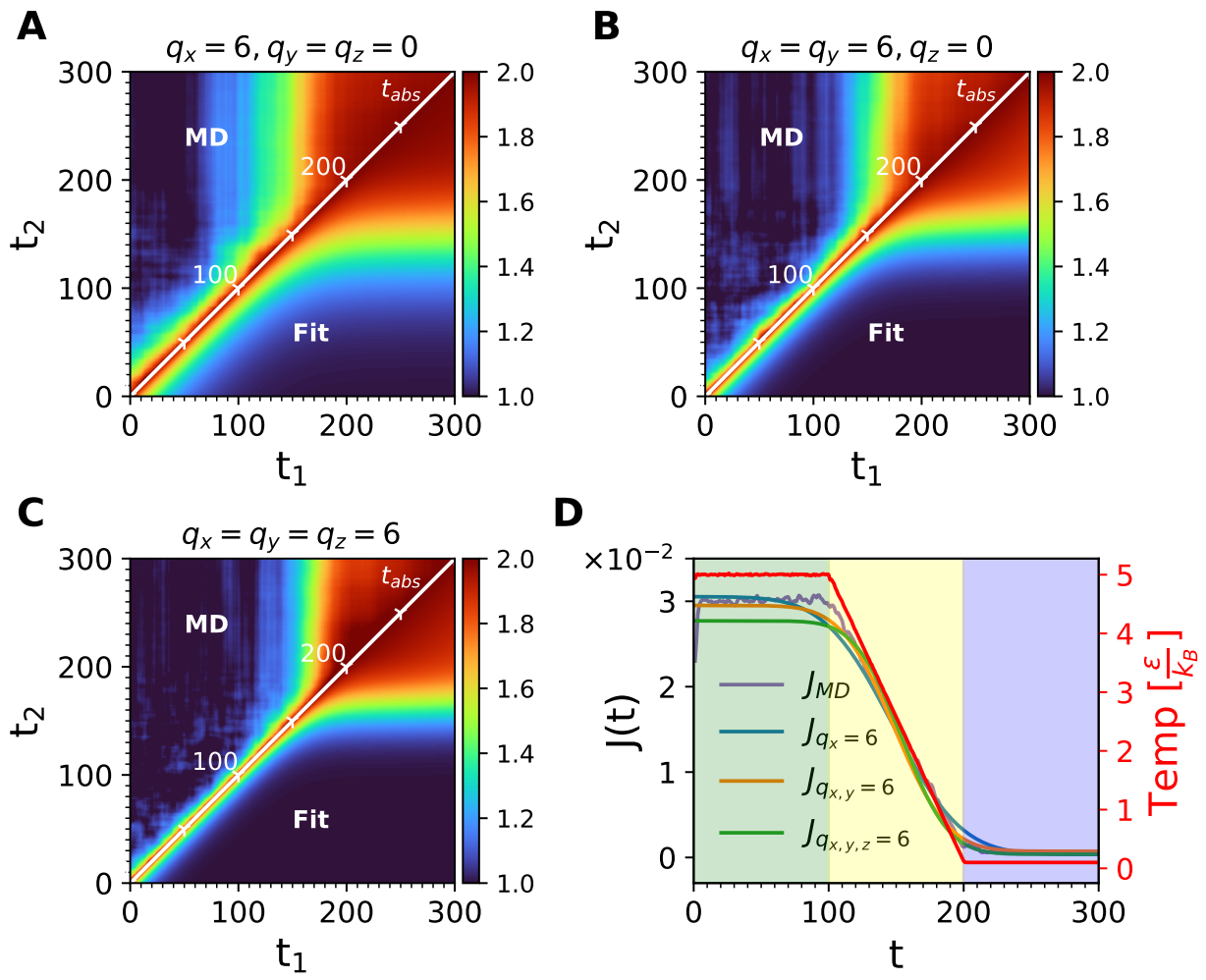

Figure 3.2: **Simulation of a non-equilibrium system arising from temperature changes and application of transport coefficient analysis to $c_2(\vec{q}, t_1, t_2)$ extracted from different $\vec{q}$ bins.** c_2 data is extracted from three bins: (A) $(q_x = 6, q_y = q_z = 0)$, (B) $(q_x = q_y = 6, q_z = 0)$, and (C) $(q_x = q_y = q_z = 6)$. Each c_2 data set includes fitting results (lower right corner) and corresponding MD simulation data (upper left corner) displayed on opposite sides of the diagonal. (D) Show the transport coefficient extracted through the analysis in these 3 bins, $J_x(t)$ (blue line), $J_{q_{x,y}=6}(t)$ (orange line), and $J_{q_{x,y,z}=6}(t)$ (green line), together with the J_{MD} (purple line) calculated directly from the positions of the particles in the simulation box using Eq. 2.42. The right-hand red axis illustrates the temperature variation (red line) throughout the simulation.

.

3.3.2 Reported Experiments

After validating the proposed analysis approach through MD simulations, we then confirmed its applicability to the results of previous experiments [2, 3]. The relaxation dynamics described in these two respective papers exhibit intriguing dynamic phenomena under non-equilibrium conditions. The extracted $J(t)$ from our analysis not only corroborates the conclusions presented in the articles but also provides new insights into how the particle interactions and drifts resulting from the motion of the particles govern the relaxation dynamics. This is evident from the comparison with the classical model of the Brownian oscillator shown in Section 2.7.2 of the Chapter 2.

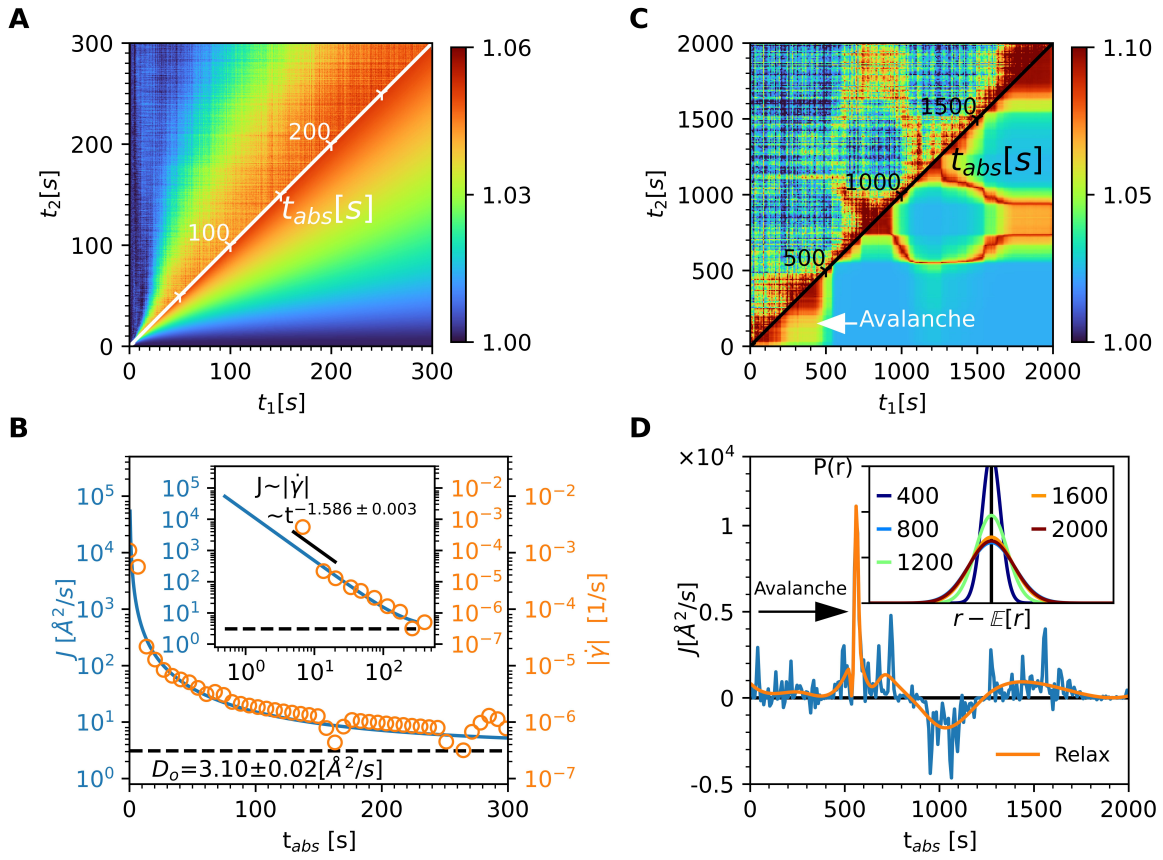

Figure 3.3: **Verification of the transport coefficient approach using experimental results from previous works.** (A) Examination of relaxation dynamics in a silica particle suspension reported in Donley et al.'s Rheo-XPCS measurement [2], and (B) corresponding results for $J(t)$ (blue line) presented in both linear-log and log-log scales (insert). The orange dots denote $\dot{\gamma}(t)$ simultaneously measured from the rheometer. In the linear-log plot, the black dashed line represents the intrinsic diffusion rate (D_o) of the system under equilibrium conditions, measured at 3.1^2/s. In the log-log plot, the black solid segment depicts the trend of $J(t) \sim |\dot{\gamma}(t)| \sim t^{-1.586\pm0.003}$, serving as a visual reference. (C) and (D) Application of this non-equilibrium analysis to a gel system subjected to mechanical perturbation, as discussed in the work of Song et al. [3]. In (D), the blue line depicts the $J(t)$ derived from the non-equilibrium analysis, while the orange line indicates the smoothed $J(t)$, highlighting the relaxation trends. The avalanche dynamics are identified by a white arrow in (C), signifying an abrupt decrease followed by a rapid recovery of correlation within $c_2(\vec{q}, t_1, t_2)$. Concurrently, a black arrow in (D) marks a notable spike in $J(t)$at $t = 560s$, corresponding to the observed avalanche event. Trajectories of $\mathbb{P}(r - \mathbb{E}[r], t)$ are depicted in the inset figure at different time points: $t = 400$ s (blue line), 800 s (cyan line), 1200 s (green line), 1600 s (orange line), and 2000 s (red line), assuming δ-function at $t = 0$. In Figures A) and C), the experimental data is displayed in the upper left corner, while the fitting results are presented in the lower right corner.

Overdamped Relaxation

The non-equilibrium analysis was applied to investigate relaxation dynamics in a silica particle suspension, as described in recent work by Donley et al. [2]. Their data were collected by performing a creep/recovery rheological test with applied stress ranging from 7.5 to 100 Pa for 100 s in a concentrated (42 v%) and disordered suspension of charged silica nanoparticles.

The recovery phase of the creep tests, conducted under stresses of 100 Pa and 10 Pa, was monitored using $c_2\left(\vec{q}, t_1, t_2\right)$, which are depicted in Fig. 3.3A and Fig. 3.6A, respectively. To interpret this data, a power-law model was applied, encapsulating the relationship between the transport coefficient ($J\left(t\right)$) and time (t), referring to Eq. 3.3 in the App. Analysis revealed that $J \sim t^{-1.586}$ accurately represents the transport dynamics during relaxation from the 100 Pa creep/recovery test (Fig. 3.3B), while $J \sim t^{-1.972}$ suitably characterizes the dynamics from the 10 Pa test (in the App). The observed exponential relaxation of $J\left(t\right)$ to intrinsic diffusivity of equilibrium (D_o) aligns with the overdamped behavior of a Brownian oscillator (see 3.1 in Materials and Methods and Fig. 2.4 and Eq. 2.127 in the Chapter 2), indicating dominance by systematic drift. This inference is congruent with a system characterized by soft repulsive interactions. The observed power-law decrease of $J\left(t\right)$ correlates with the rheometric shear rate via a scaling factor $\frac{k_B T}{\pi r}$, assuming $r = 10$nm and $T = 298$K, as specified in the experiments (See Fig. 3.7 at Section 3.7.3 in the App). It is suspected that external shear induces systematic forces by complex potentials, including frictional and interparticle forces, thereby influencing transport dynamics.

Analysis revealed that $J \sim t^{-1.586}$ accurately represents the transport dynamics during relaxation from the 100 Pa creep/recovery test (Fig. 3.3B), while $J \sim t^{-1.972}$ suitably characterizes the dynamics from the 10 Pa test (Fig. 3.6B in the App). The observed exponential relaxation of $J\left(t\right)$ to intrinsic diffusivity of equilibrium (D_o) aligns with the overdamped behavior of a Brownian oscillator (see Fig. 3.1 in Materials and Methods and Fig. 2.4 and Eq. 2.127 in the Chapter 2, indicating dominance by systematic drift. This

inference is congruent with a system characterized by soft repulsive interactions. The observed power-law decrease of $J(t)$ correlates with the rheometric shear rate via a scaling factor $\frac{k_B T}{\pi r}$, assuming $r = 10\text{nm}$ and $T = 298\text{K}$). It is suspected that external shear induces systematic forces by complex potentials, including frictional and interparticle forces, thereby influencing transport dynamics.

Lastly, the presence of microscopically heterogeneous dynamics is visually substantiated in Fig. 3.8 of the App Section 3.7.4. The distinct 'tailing' in Fig. 3.8B indicates the emergence of shear banding, likely due to the abrupt cessation of a thin flow layer near the surface of the rotor in the recovery phase. This observation is in alignment with the previously discussed microscopically heterogeneous dynamics by Donley et al. [2].

Underdamped Relaxation

The results from Fig. 3.3C illustrate the application of non-equilibrium analysis to a polymer-particle gel system under mechanical perturbation. This system experienced mechanical perturbation by overloading the cell with the *ex situ* gelled material, resulting in a compressive strain of approximately 10 % [3]. Our study focused on investigating the dynamics and its evolution over time in this gel system. To capture the intricate changes in dynamics, $J(t)$ was determined separately for each experimental time point, modeling $c_2(\vec{q}, t_1, t_2)$ by Eq. 3.1 as detailed in App Section 3.7.1. The observed consistency between the experimental data and the fitting results indicates the successful capture of the dynamic changes as time progresses through non-equilibrium analysis.

The complex shape of $c_2(\vec{q}, t_1, t_2)$ can be attributed to the fluctuation of $J(t)$ in both directions around 0 as the system relaxes from the mechanical perturbation. Experimental $c_2(\vec{q}, t_1, t_2)$ displays a distinctive "wings" feature, and the correlation function undergoes non-monotonic changes as the delay time increases. This phenomenon is elucidated by considering the change in the probability density function of particle displacement, denoted

as $\mathbb{P}(r - \mathbb{E}[r], t)$. As shown in the inset of Fig. 3.3D, $\mathbb{P}(r - \mathbb{E}[r], t)$ initially broadens ($t = 0 \rightarrow 800$ s) as the system relaxes, but later narrows ($t = 800 \rightarrow 1200$ s) due to the systematic force, reversing its evolution over time. Such behavior in $\mathbb{P}(r - \mathbb{E}[r], t)$ can lead to an initial decrease and subsequent increase in the correlation function without requiring particles to return to their exact positions at earlier times, as observed in previous work [237]. The fitting of $J(t)$ reveals that this change in $\mathbb{P}(r - \mathbb{E}[r], t)$ occurs when $J(t)$ becomes negative between 800 and 1200 s. Notably, $\mathbb{P}(r - \mathbb{E}[r], t)$ at $t = 800$ s and $t = 1600$ s overlaps, indicating that $\mathbb{P}(r - \mathbb{E}[r], t)$ returns to its initial configuration after completing a period of oscillations. The behavior of $J(t)$ is similar to the dissipation dynamics in an underdamped Brownian oscillator when the elastic force dominates the drift force, as shown in 3.1 in Materials and Methods and Fig. 2.3 and Eq. 2.126 in the Chapter 2. However, in this system, F_{sys} is far more complex than a Brownian oscillator potential and drift force, leading to deviations from the classical model, such as $J(t)$ dropping below 0 and its modulation of frequency over time (Fig. 3.3D). However, these oscillations subside, and $J(t)$ approaches 0 at long times, consistent with the predictions of the Brownian oscillator model, aligning with the conclusion that the system returns to equilibrium.

Furthermore, our methodology effectively identifies the occurrence of avalanche dynamics, evidenced at ($t = 560s$) by a pronounced surge in $J(t)$, as indicated by black arrows in Fig. 3.3D), accompanied by a transient decrease in correlation, swiftly followed by recovery within $c_2(\vec{q}, t_1, t_2)$, as denoted by white arrows in Fig. 3.3C). These avalanche dynamics typically involve the rapid and transient rearrangement of particles, which serves to release the built-up internal stress during the relaxation phase [238], manifesting as a sharp increase in $J(t)$ in XPCS experiments.

In summary, compared to traditional analysis like TIZs approach, our method offers two primary advantages. Firstly, it provides a more granular and quantitatively rich insight into the temporal evolution of system dynamics, as exemplified by the detailed capture of

avalanche dynamics at ($t = 560s$) in Fig. 3.3C, where the enhanced resolution enables the detection and quantification of such intricate phenomena. Secondly, our technique is particularly adept at uncovering subtle patterns within $c_2(\vec{q}, t_1, t_2)$, such as the 'tails' observed in Fig. 3.3A and the 'wings' patterns in Fig. 3.3C, thereby offering a comprehensive view of the dynamic landscape.

3.4 Complex Heterogeneity Study

After validating the proposed analysis approach through MD simulations and experimental results from the previous sections, we applied it to a system that exhibits not only significant non-equilibrium characteristics but also heterogeneous dynamic phenomena, such as multiple shear band transitions [239]. Investigating the fine dynamics in each shear band of such an opaque colloidal system over time, including its fraction, relative velocity, and rate of intrinsic dynamics, has always been challenging because of limitations in spatiotemporal resolution and penetration depth of instrumental optics, as well as the shortcomings of existing analysis approaches. However, when combined with Rheo-XPCS, our analysis allowed us to explore how $J(t)$ and other physical parameters reflect these complex processes by revealing variations over time that were previously unattainable using conventional analysis methods.

In Fig. 3.4A, we employed non-equilibrium analysis to gain deeper insights into the dynamics of a chosen heterogeneous system. Our focus falls on the shear banding phenomenon observed in Rheo-XPCS experiments, where this approach holds substantial promise for elucidating its underlying mechanisms. This system consists of a combination of SiO_x-GSH in a salt suspension containing 60 mM $NaNO_3$ and 10 mM $MgSO_4$, with an applied stress of 25 Pa. The Rheo-XPCS measurement of the system displays prominent characteristics of heterodyne scattering as evidenced by the oscillation of the $c_2(\vec{q}, t_1, t_2)$ along the delay time direction. There are two discrete frequencies in oscillations before 15 s and after 40 s, as

shown in the zoomed-in section of Fig. 3.4A, indicating the presence of three compositions in the shear banding within these time intervals. The variation in these frequencies over time indicates that the fraction and relative velocity of each composition consistently varies, even diminishes, throughout the creep test. While rheometer measurements yield a standard compliance curve under deformation, the dynamic behaviors provided by Rheo-XPCS, including the velocity (v_{Edge}), fraction(x_n), and transport coefficient (J) of each shear band, once are inaccessible to us due to a lack of an appropriate analysis approach. Therefore, it stands as a compelling example to demonstrate the capabilities of our developed approach to characterize the detailed insights as the change of these physical parameters over time.

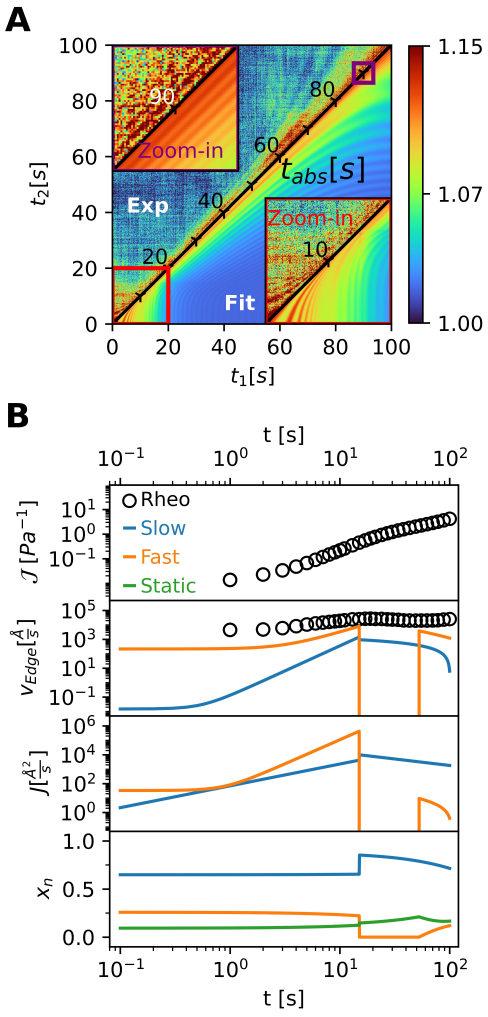

Figure 3.4: **Application of the transport coefficient approach to a charged particle suspension undergoing shear band transitions during a creep test.** (A) Observation (upper left corner) and analysis (lower right corner) of multiple shear bands in c_2 at flow direction ($\phi = 6.3^o$) for a suspension comprising SiO_x-GSH particles in a mixed salt solution (60 mM $NaNO_3$ and 10 mM $MgSO_4$) under constant stress of 25 Pa. The fitting results of $c_2\left(\vec{q}, t_1, t_2\right)$ in other ϕ direction are shown in Fig. 3.12 of the App. Insets in the upper and lower corners illustrate the oscillatory features in c_2 resulting from three shear bands. (B) Comparison between rheological measurements and analysis results using the multiple-banding model. The top-to-bottom rows show changes over time in various physical parameters, including compliance ($\mathcal{J}(t)$), the velocity at the outer edge of the rotor (v_{Edge}), transport coefficient $J\left(t\right)$, and fraction x_n. These measurements are obtained through direct rheological measurements (black circular markers) and non-equilibrium analysis in XPCS (solid lines), providing insights into the system's dynamics at macro and micro scales, respectively. Within the XPCS measurements, the blue, orange, and green lines specifically track the evolution of the slow, fast, and static bands in the shear banding. To facilitate a more meaningful comparison between the velocity of each band obtained from XPCS and the shear rate $\dot{\gamma}(t)$ measured by the rheometer, $\dot{\gamma}(t)$ is converted to the velocity at the outer edge of the rotor (v_{Edge}) using the equation $v_{Edge}(t) = \dot{\gamma}(t)h$.

In our analysis of non-equilibrium dynamics, we assumed that the system could be represented as comprising a static reference with $v_r = 0$ and $J_r = 0$, along with two components flowing horizontally with mean ensemble velocities of v_1 and v_2, each possessing their respective transport coefficients $J_1(t)$ and $J_2(t)$. We ensured that the angles ϕ_1 and ϕ_2 between the scattering vector $\vec{q}$ and the reference line were equal and denoted as θ, where θ represents the angle concerning $\theta = 0$. These specified conditions allowed us to simplify Eq. 2.104 and reduce the number of adjustable parameters, as explained in detail in Eq. 2.107 in the Chapter 2. Greater details of the relationship between these physical parameters and time are demonstrated by Eq. 3.4 and Fig. 3.5 in the Section 3.6.1 App and the fitting results of $c_2\left(\vec{q}, t_1, t_2\right)$ in all ϕ directions are shown Fig. 3.12 in the App.

Under the applied stress, the system exhibited a heterogeneous deformation, marked by the formation of three distinct bands: a slow-flowing band, a fast-flowing band, and a static band close to the stator. This formation of three bands can be attributed to the strong attraction between the particles, leading to dense structures in the static and slow-flowing bands and the localization of deformation primarily in the fast-flowing band. As illustrated in Fig. 3.4B, 15 seconds after initiation of the applied stress ($t = 15s$), a significant event occurred within the fast moving band. Most of the particles in this band merged into the slow-moving and static bands, leading to the loss of the fast-moving band as the lubrication layer in the deformation process. Consequently, the entire fast-flowing band transitioned to the slow-flowing state, resulting in a dramatic increase in the fraction of the slow-flowing band. Simultaneously, the increase in shear rate reached a plateau value, and the $\mathcal{J}(t)$ increased at a slower rate. After 40 seconds, the continuously applied stress led to the destruction of the internal structure. Some parts of the static bands started flowing again, with velocities comparable to their pre-jamming state. Consequently, the fraction of the fast-flowing band gradually increased but velocity decreased over time. Through non-equilibrium analysis, we effectively analyzed the complex dynamics of the multiple shear

banding transitions, providing insights into the formation, jamming, and reflow phenomena occurring within the system under applied stress.

3.5 Conclusion

The proposed transport coefficient, $J(t)$, serves as a comprehensive measure that encapsulates the collective influence of both random and systematic forces on the internal particle dynamics observed in XPCS. This analysis approach for extracting $J(t)$ not only enables us to quantify and understand non-equilibrium dynamics effectively but also allows for a genuine characterization of the system. We have rigorously evaluated its capabilities using both molecular dynamics (MD) simulations and experimental data from previous research. The $J(t)$ obtained through this analysis not only represents the system's underlying physics but also provides nuanced insights beyond the scope of current methodologies.

To further demonstrate its potential, we have applied this method to investigate a complex case that is currently beyond the reach of existing analysis techniques and experiments: a heterogeneous system characterized by shear banding involving three bands, as observed in Rheo-XPCS. We have successfully captured the detailed changes in dynamics within these shear bands, shedding light on how microscale dynamics contribute to the macroscopic rheological response, including shear rate and strain.

In conclusion, our presented method represents a significant advancement in the field of non-equilibrium dynamics analysis and modeling, offering both efficiency and accuracy. Such an advanced approach helps us to better study and understand the intriguing phenomena induced by non-equilibrium dynamics. This understanding can not only be applied to optimizing soft materials in various fields [50, 240], but also holds great potential for exploring natural phenomena [241, 184]. Another exciting prospect for future development lies in its potential application to generate extensive datasets, facilitating the training of artificial intelligence (AI) systems to extract non-equilibrium dynamics effectively right after an ex-

periment. This AI tool could prove invaluable in future XPCS beamlines, enabling users to not only optimize experimental conditions before conducting experiments but also provide real-time results and feedback on dynamic systems during XPCS scans. As synchrotron light sources undergo upgrades, offering greater flux and coherence, finer dynamics become accessible in XPCS. In light of these forthcoming advances, our analysis approach holds tremendous promise for immediate application in XPCS studies across a wide range of samples, allowing us to probe subtle non-equilibrium dynamics that were previously inaccessible.

3.6 Appendix

3.6.1 Formalization of Physical Parameters

Analysis in Fig. 3.3 Panels C and D

In an ideal situation of a non-equilibrium model, various time-dependent parameters $p(t)$ within the model, such as $J(t)$, $\dot{\gamma}(t)$ and $\mathbb{E}[v(t)]$, should be continuous arbitrary where each frame of t corresponds to a specific value. Consequently, to accurately capture the dynamics evolution over time, the fitting process should involve thousands of parameters that correspond to each measured frame, as follows:

$$p(t) : p(t=0), p(1), p(2) \cdots\cdots p(t) \tag{3.1}$$

This analysis approach is employed in the results shown in Fig. 3.3 Panels C and D of the manuscript. However, when practically analyzing extended time procedures, for the sake of streamlining the fitting process and minimizing the parameter count, these time-dependent parameters can be effectively approximated using various functions.

Analysis in Fig. 3.2

In the analysis of our MD simulation, where the system is homogeneous and the temperature exhibits a smooth transition from high to low, the trend of the $J\,(t)$ is represented by the error function (erfc) as follow:

$$J(t) = J_{scale}\text{erfc}\left(t_{scale}(t - t_{shift})\right) + J_{shift} \tag{3.2}$$

which J_{scale}, J_{shift}, t_{scale} and t_{shift} are parameters to either stretch or shift the error function in different axis to accommodate the actual change of $J\,(t)$ along time.

Analysis in Fig. 3.3 Panels A and B

To more effectively model the intrinsic dynamics observed during the relaxation process using a simplified approach, we have represented the trend of $J(t)$ through a power law that incorporates three parameters: the scale factor (J_o), the exponent (b), and a vertical shift (D_o),

$$J(t) = J_o\, t^b + D_o \tag{3.3}$$

was utilized to formalize the relation between $J\,(t)$ and time t. In Eq. 3.3, J_o represents the scaling of the transport coefficient, and D_o signifies the intrinsic diffusion rate of the system at equilibrium. The exponent b delineates the power-law behavior.

Analysis inFig. 3.4

In the analysis of multiple-banding system, the function of the physical parameters for the two flowing components, including mean velocity $v_1(t)$ and $v_2(t)$, transport coefficient $J_1(t)$ and $J_2(t)$, and fraction $x_1(t)$ and $x_2(t)$, are divided into 2 segments at $t = 15$ when the dynamics process changes its trend. This segmentation in the dynamics analysis arises from

the non-monotonic behavior observed in the variables $J(t)$,v, and x_n, where each displays a pattern of increase followed by a decrease. Such trends complicate the use of a single function to precisely capture these variations accurately. Consequently, $c_2(\vec{q}, t_1, t_2)$ was segmented into two parts at the $t = 15s$, each modeled by distinct functions. To describe v_1 and v_2, $J_1(t)$ and $J_2(t)$ at different segments, a power law is utilized as:

$$
\begin{aligned}
J_1(t) &= \begin{cases} a_{J,1,1}t^{b_{J,1,1}} + c_{J,1,1} & : t < 15 \\ a_{J,1,2}t^{b_{J,1,2}} + c_{J,1,2} & : t \geq 15 \end{cases} \\
J_2(t) &= \begin{cases} a_{J,2,1}t^{b_{J,2,1}} + c_{J,2,1} & : t < 15 \\ a_{J,2,2}t^{b_{J,2,2}} + c_{J,2,2} & : t \geq 15 \end{cases} \\
v_1(t) &= \begin{cases} a_{v,1,1}t^{b_{v,1,1}} + c_{v,1,1} & : t < 15 \\ a_{v,1,2}t^{b_{v,1,2}} + c_{v,1,2} & : t \geq 15 \end{cases} \\
v_2(t) &= \begin{cases} a_{v,2,1}t^{b_{v,2,1}} + c_{v,2,1} & : t < 15 \\ a_{v,2,2}t^{b_{v,2,2}} + c_{v,2,2} & : t \geq 15 \end{cases}
\end{aligned}
\tag{3.4}
$$

where scale (a), exponent (b), and vertical shift (c) are fitting parameters of the power law and labeled by subscript corresponding to its (Parameters, Segment, Component).

Additional constraints are imposed on the fitting process for $x_1(t)$ and $x_2(t)$, taking into account the inherent limits of fraction growth and reduction, which are confined within the range of 0 and 1.

$$
\begin{aligned}
x_1(t) &= \begin{cases} d_{x,1,1} - a_{x,1,1}\mathrm{e}^{b_{x,1,1}(t-c_{x,1,1})} & : t < 15 \\ a_{x,1,2}\mathrm{e}^{b_{x,1,2}(t-c_{x,1,2})} & : t \geq 15 \end{cases} \\
x_2(t) &= \begin{cases} d_{x,2,1} - a_{x,2,1}\mathrm{e}^{b_{x,2,1}(t-c_{x,2,1})} & : t < 15 \\ a_{x,2,2}\mathrm{e}^{b_{x,2,2}(t-c_{x,2,2})} & : t \geq 15 \end{cases}
\end{aligned}
\tag{3.5}
$$

Any negative values in $x_1(t)$ and $x_2(t)$ is substituted by 0.

The interpretation of the physical parameters in these model functions could vary depending on the specific context of their application. For instance, b_n in Eq. 3.3 could relate to the exponent that characterizes the time dependency of the dynamics rate as $\dot{\gamma} \sim t^{b_n}$ when it is extracted from a system undergoes relaxations or deformations.

3.6.2 Molecular Dynamics Simulation

To verify the proposed model, we simulate a solution of non-interacting particles (phantom particles) in a non-equilibrium system. The solvent is implicitly modeled by the Langevin thermostat, and the equation of motion of the n-th particle is,

$$\dot{\vec{v}}_n = -\gamma \vec{v}_n + \frac{\vec{\eta}_n(t)}{m} \tag{3.6}$$

where the mass, m, is set to unity for all particles, $\vec{v}_n(t)$ is the velocity of the n-th particle. The stochastic force acting on the n-th particle, $\vec{\eta}_n(t)$, satisfies the following conditions,

$$\begin{aligned} \mathbb{E}\left[\vec{\eta}_n(t)\right] &= \vec{0} \\ \mathbb{E}\left[\vec{\eta}_n(t) \otimes \vec{\eta}_n(t')\right]_{ij} &= 6k_B T\gamma\delta_{ij}\delta(t-t') \end{aligned} \tag{3.7}$$

The friction coefficient, γ, is set to $\gamma = 1000\frac{m}{\tau}$, where $\tau = \sigma\left(\frac{m}{\epsilon}\right)^{\frac{1}{2}}$ is the reduced time, σ and ϵ are reduced length and energy, respectively. The velocity-Verlet algorithm is used to integrate the equation of motion, with an integration time step $\Delta t = 0.001\tau$. The simulation consists of three stages with different temperatures:

1. The temperature was kept constant at $T = 5\frac{\epsilon}{k_B}$.
2. The temperature linear decreased with time from $T = 5\frac{\epsilon}{k_B}$ to $T = 0.1\frac{\epsilon}{k_B}$.
3. The temperature was maintained constant at $T = 0.1\frac{\epsilon}{k_B}$.

Each stage lasts for 1τ, that is, 1000 simulation steps. All simulations were performed using the LAMMPS [102] under periodic boundary conditions.

In the Chapter 3, $c_2(\vec{q}, t_1, t_2)$ and its corresponding analysis for bins at $q_x = 6$, $q_y = q_x = 6$ and $q_x = q_y = q_z = 6$ have been demonstrated. Here, we provide the bins at $q_x = 3$, $q_y = q_x = 3$ and $q_x = q_y = q_z = 3$ to further verify the non-equilibrium analysis approach. Again, $J(t)$ obtained from two respective approaches, derived from analyzing $c_2(\vec{q}, t_1, t_2)$ of XPCS and spatial averaging of the particle positions in the simulation box, shows consistency. This result provides evidence that $J(t)$ accurately reflects the actual physical quantity in the system, validating the extraction approach of $J(t)$.

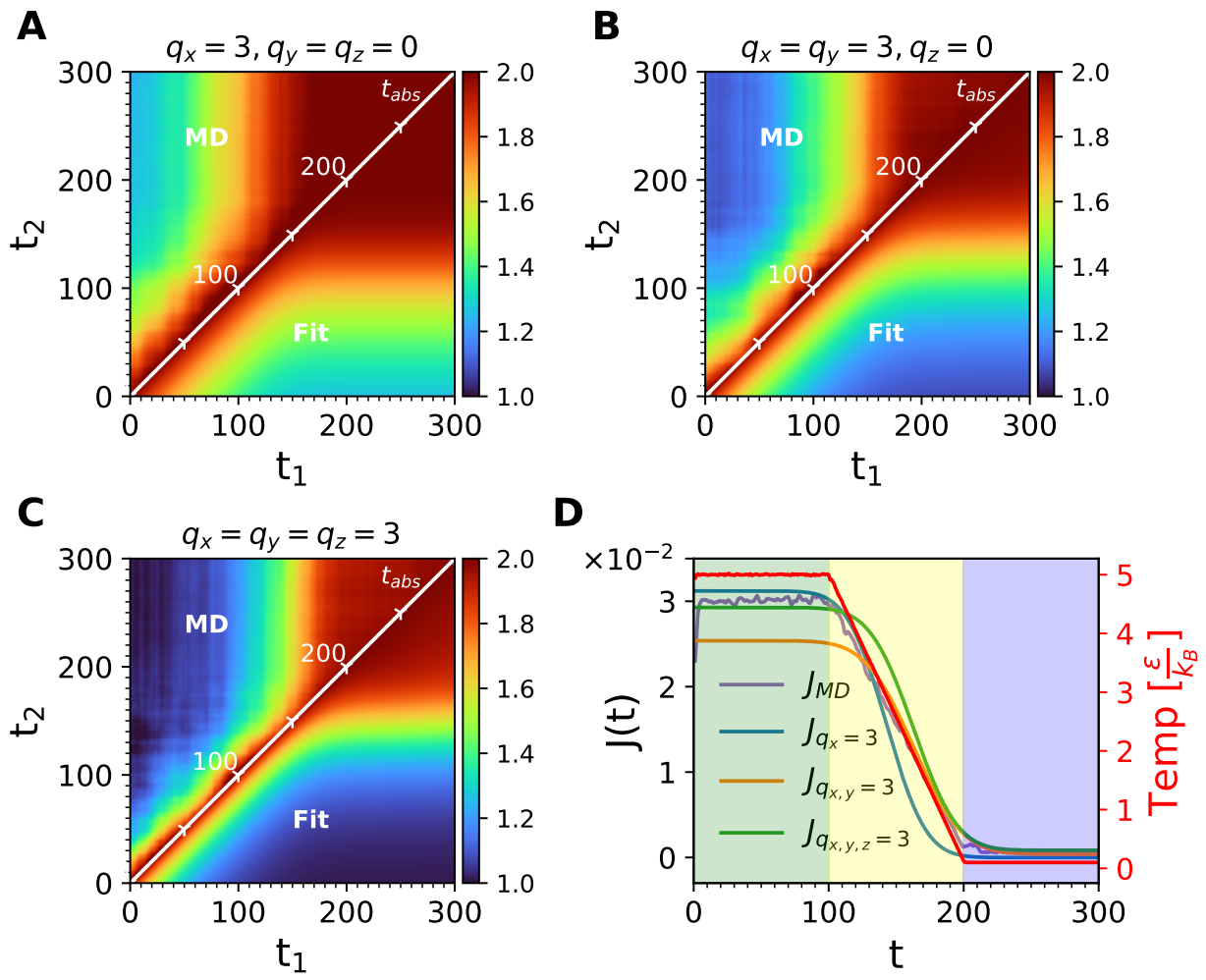

Figure 3.5: **Application of the model analysis on a simulated non-equilibrium system reveals three distinct stages of temperature change, which are visually represented by the filled-in background color.**

3.6.3 Correlating Microscopic Dynamics with Macroscopic Rheology through $J(t)$ in Rheo-XPCS

Supplementary Results: Recovery following a 10 Pa Creep Test

Beyond the relaxation data for the 100 Pa creep test illustrated in Fig. 3.6A and C of the primary manuscript, we further examined the XPCS data derived from a 10 Pa creep test, as detailed in Fig. 3.2 as reference [2]. The aggregated findings of the 10 Pa and 100 Pa

creep tests are presented in Fig. 3.6 in this document.

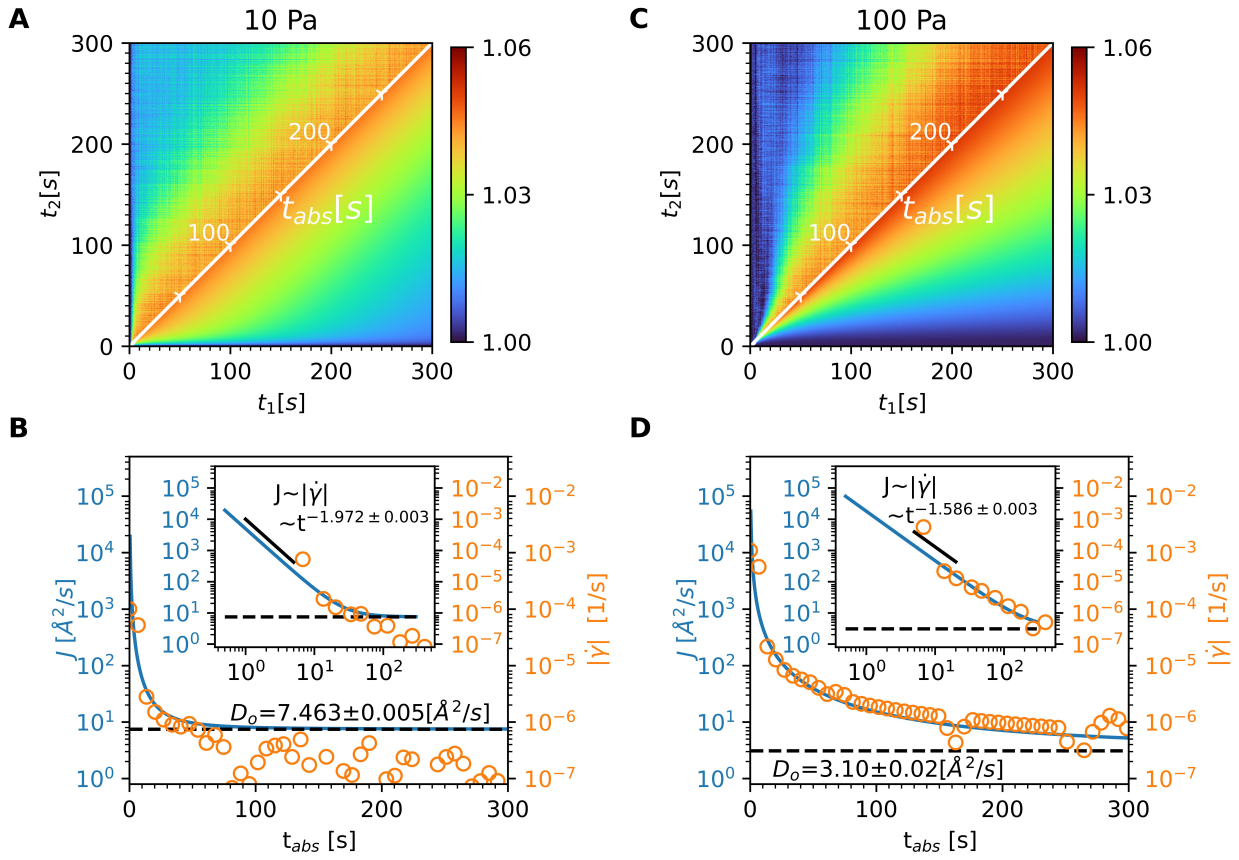

Figure 3.6: **Comparative Analysis of the $J(t)$ and the $\dot{\gamma}(t)$ During the Recovery Phase of Creep Tests.** Panels A and B illustrate the relationship between $J(t)$ and $\dot{\gamma}(t)$ under an applied $\sigma(t)$ of 10 Pa, while Panels C and D show the same under a $\sigma(t)$ of 100 Pa (also shown in Fig 3 A and B in the main texts). From Panels B and D, a consistent scaling relation of $\frac{k_BT}{\pi r}$ is observed between $J(t)$ and $\dot{\gamma}(t)$, independent from the applied $\sigma(t)$ in the creep test.

Analysis of Fig. 3.6 yields several key insights:

1. During the creep tests, the $J(t)$ diminishes more swiftly at the lower stress level (10 Pa) with an exponent of -1.972, in contrast to the -1.586 exponent observed under the higher stress condition (100 Pa). This trend aligns with the results of both XPCS, evidenced by a pronounced increase in $c_2(\vec{q}, t_1, t_2)$ along the t_{abs} diagonal, and rheological data, which show $\dot{\gamma}(t)$ approaching zero as the strain quickly returns to the

baseline level of irrecoverable strain.

2. The estimated values of D_o from both creep tests are similar in magnitude. However, the lack of extended $c_2(\vec{q}, t_1, t_2)$ data for the 100 Pa creep test compromises the precision of D_o, leading to the observed variance in the values D_o between panels B and D.

3. The rapid recovery observed in the 10 Pa creep test results in a rapid decrease in $\dot{\gamma}(t)$, potentially falling below the sensitivity range of the measurement instruments, thus casting doubt on the reliability of the data points with $\dot{\gamma} < 10^{-6}$. Despite this, Fig. 3.6 generally demonstrates a consistent scaling relation between $J(t)$ and $\dot{\gamma}(t)$.

In the following section, we will concentrate on the third conclusion to further explore the intrinsic relationship between the $J(t)$ and $\dot{\gamma}(t)$.

$J(t)$ and $\dot{\gamma}(t)$ in micro-rheology

To elucidate this phenomenon, we used Equation (9) to correlate the variance in position ($\mathbb{V}[x(t)]$) and $\mathcal{J}(t)$ from reference [242], which is presented as follows:

$$\mathbb{V}[x(t)] = \frac{k_B T}{\pi r}\mathcal{J}(t) = \frac{k_B T}{\pi r \sigma}\gamma(t) \tag{3.8}$$

where r represents the radius of the particles involved. By differentiating both sides for time, we derive an expression that links $J(t)$ and $\dot{\gamma}(t)$ through a scaling factor of $\frac{k_B T}{\pi r \sigma}$,

$$J(t) = \frac{k_B T}{\pi r \sigma}\dot{\gamma}(t) \tag{3.9}$$

However, the scaling between $J(t)$ and $\dot{\gamma}(t)$ obtained from reference [2] and as shown in Fig. 3.6 of our manuscript does not align with Eq. 3.9. As indicated in reference [242], the theoretical derivations in micro-rheology suggest a scaling factor of $\frac{k_B T}{\pi r \sigma}$, indicating dis-

crepancies attributable to the recovery-phase measurements of viscoelastic materials, which deviate from the assumed creeping flow conditions.

Interestingly, through our analysis, we observed a power-law decrease of $J(t)$ correlates with the rheometric shear rate via a scaling factor $\frac{k_B T}{\pi r}$, assuming $r = 10\text{nm}$ and $T = 298\text{K}$, as specified in the experiments from reference [2]. Ignoring the units for a moment, this leads us to an empirical formulation:

$$J(t) \approx \frac{k_B T}{\pi r} |\dot{\gamma}(t)| \tag{3.10}$$

This empirical relation, although not theoretically derived, offers a pragmatic approximation under the specific conditions of our experiments.Fig. 3.7 is corroborated by the results of the creep test performed under a lower stress of 10 Pa, indicating that the observed scaling between $J(t)$ and $\dot{\gamma}(t)$ is not affected by the magnitude of the applied creep stress.

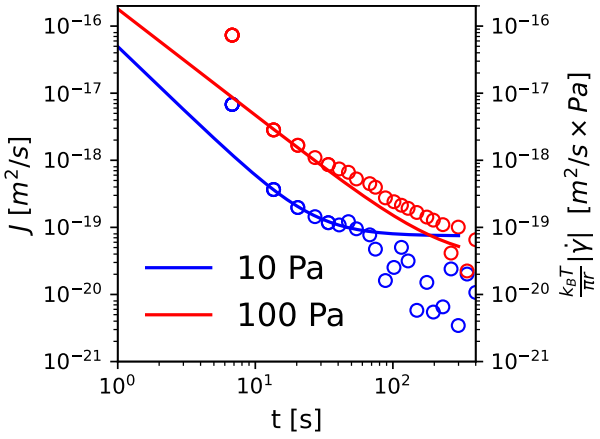

Figure 3.7: **The connection between microscopic dynamics ($J(t)$) and macroscopic properties ($\dot{\gamma}(t)$) in the recovery phase of creep tests with $\sigma(t)$ of 10Pa (blue) and 100Pa (red)**. The $J(t)$ (solid line) is derived from non-equilibrium analysis on $c_2(\vec{q}, t_1, t_2)$ measured by XPCS, and the $\dot{\gamma}(t)$ obtained from the rheometer, then scaled by a factor of $\frac{k_B T}{\pi r}$ (scattered dots), is measured from rheometer. For a better comparison, the unit for both $J(t)$ and $\dot{\gamma}(t)$ have been converted to International System of Units (S.I. Units)

Our ongoing research is focused on elucidating these findings and developing a theoretical framework to accurately describe them. In simulations involving phantom particles, we

observed that the variations in $J(t)$ and $\dot{\gamma}(t)$ over time are decoupled; the shear rate induces affine transformations that alter the central positioning of the intensity profile $\mathbb{IP}(x,t)$ without affecting the distribution breadth and, consequently, $J(t)$. A preliminary hypothesis suggests that external deformation in such systems, characterized by complex potentials, can induce systematic forces, including frictional and interparticle forces, thereby influencing transport dynamics. We are actively working to further explore and define these dynamics and to develop a comprehensive theoretical model. Our goal is to bridge microscopic $J(t)$, as determined by XPCS, with macroscopic rheological properties, such as the complex shear modulus ($G^*(\omega)$) and the stress relaxation modulus ($G_r(t)$), using the principles of microrheology discussed in [243].

3.6.4 Microscopically Heterogeneous Dynamics

In reference [2], the microscopically heterogeneous dynamics is quantified using the ratio of the recovery to quiescence phases in $c_2(\vec{q}, t_1, t_2)$, denoted as $c_{\text{ratio}}(t_1, t_2 = 0)$ in equation [3] from their paper.

Our methodology introduces an alternative approach for assessing the microscopically heterogeneous dynamics. As delineated in the derivations Eq. 2.4 and Eq. 2.5, our model assumes random, homogeneous, and independent particle dynamics. This assumption leads to the simplification where terms involving $n \neq m$ average to zero, yielding our non-equilibrium model. Given this foundation, the correlations we analyzed pertain mainly to diffusive and nonaffine dynamics, denoted $c_{2,\text{Homo}}$, and do not directly correspond to the microscopically heterogeneous dynamics described in the paper [2].

However, our current work has devised a method to discern such complex dynamics. To elucidate the contributions from heterogeneous dynamics ($c_{2,\text{Hetero}}$), we employ the following expression:

$$c_{2,\text{Hetero}} \sim \mathbb{E}\left[\sum_{n=1}^{N}\sum_{m\neq n}^{N} \mathrm{e}^{i\vec{q}\cdot(\vec{r}_n(t_2)-\vec{r}_m(t_1))}\right] = c_{2,\text{exp}} - c_{2,\text{Homo}} \tag{3.11}$$

This approach involves subtracting the component of homogeneous dynamics from the total experimental correlation, thus isolating the residuals that reflect heterogeneous dynamics, as demonstrated in Fig. 3.8.

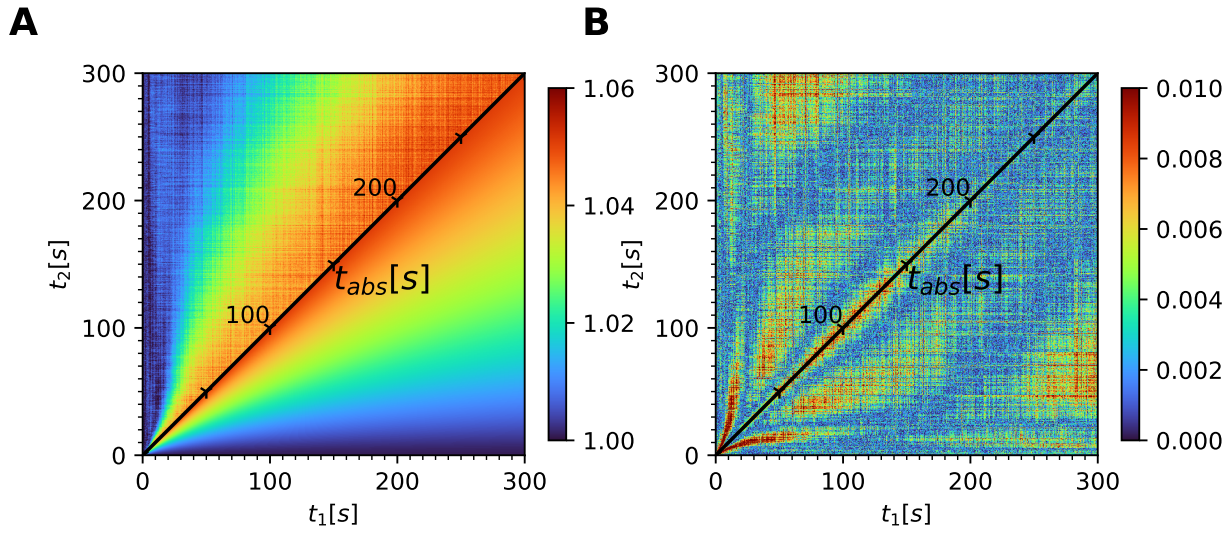

Figure 3.8: **Illustrating microscopically heterogeneous dynamics during recovery**: By subtracting the diffusive dynamics attributed to $c_2\left(\vec{q}, t_1, t_2\right)$ based on the non-equilibrium model (Panel. A, lower right) from experimental $c_2\left(\vec{q}, t_1, t_2\right)$ measurements (Panel. A, upper left), the $c_2\left(\vec{q}, t_1, t_2\right)$ serves as evidence of microscopically heterogeneous dynamics in Panel B, indicating interference between at least two compositions with distinct dynamics in the system. The 'tailing' shape of the $c_2\left(\vec{q}, t_1, t_2\right)$ is largely attributed to the abrupt halt of a thin flow layer near the rotor during the recovery phase, mirroring the microscopically heterogeneous changes detailed in reference [2].

The temporal patterns observed in the residuals of $c_2\left(\vec{q}, t_1, t_2\right)$ shown in Fig. 3.8 suggest the presence of microscopically heterogeneous dynamics, as previously noted by [2]. The pronounced 'tailing' pattern evident in Fig. 3.8B is indicative of shear banding, potentially resulting from the sudden stop of a thin flow layer near the rotor's surface during the recovery phase. This aligns with the heterogeneous dynamics discussed in [2]. We are currently enhancing our methods to more effectively formalize these relationships, accurately describe

the patterns seen in $c_2(\vec{q}, t_1, t_2)$, and quantify the associated heterogeneous dynamics.

3.6.5 *Fitting Results and Residual for Figures in main text*

Fitting Residual for Fig. 3.2

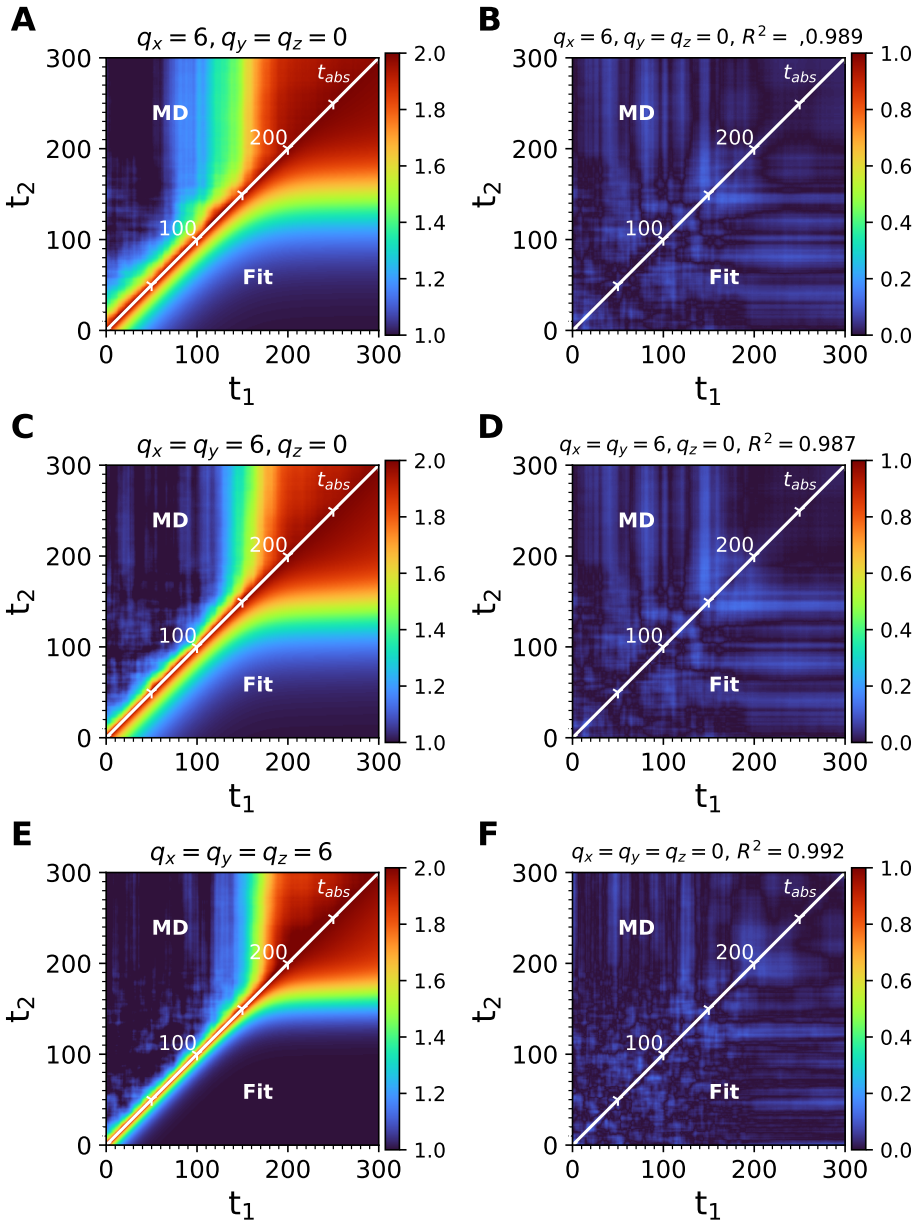

Figure 3.9: **Illustration of the fitting results (Panels A, C, E) and residuals (Panels, B, D, F) obtained after the data fitting process shown in Fig. 3.2 of the main manuscript.** The R^2 of the fitting is shown in the title of the residual plot.

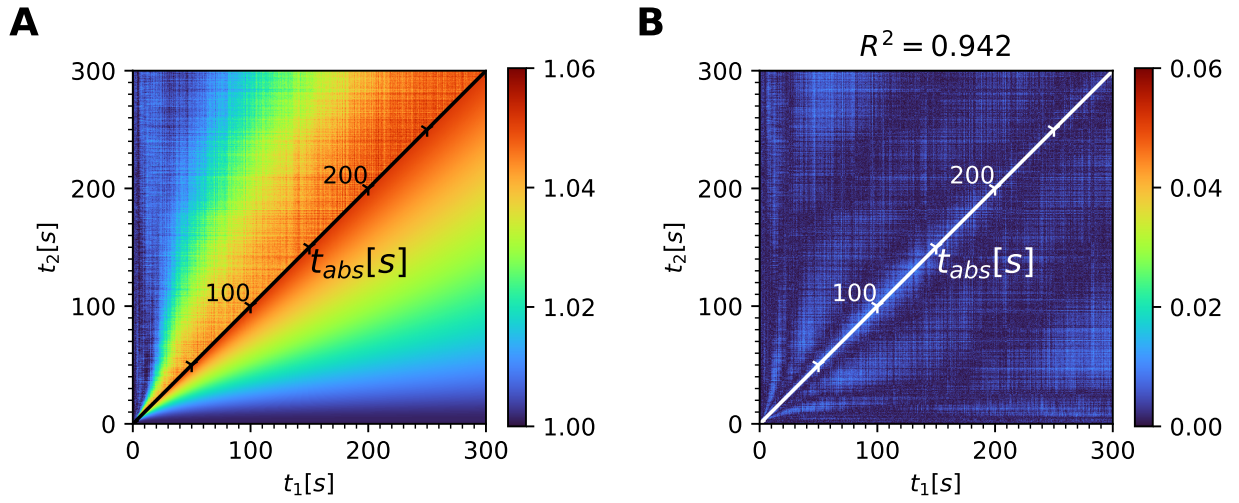

Figure 3.10: **Illustration of the fitting results (Panel. A) and residuals (Panel. B) obtained after the data from the [2] fitting process shown in Fig. 3.3A of the main manuscript.** The R^2 of the fitting is shown in the title of the residual plot.

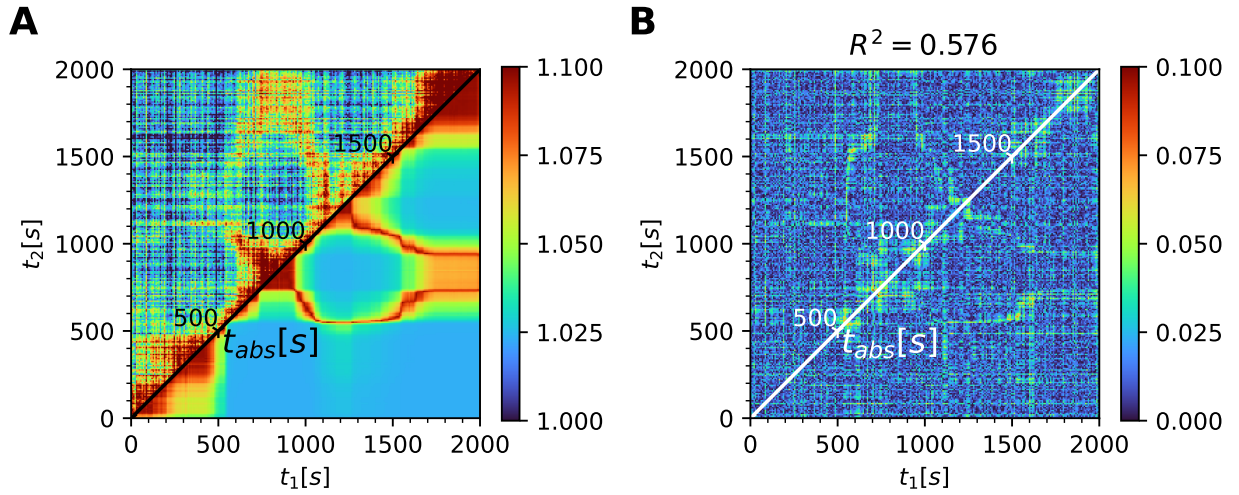

Figure 3.11: **Illustration of fitting results (Panel. A) and residuals (Panel. B) obtained after the data from [3] fitting process shown in Fig. 3.3C of the main manuscript.** The R^2 of the fitting is shown in the title of the residual plot.

Fitting Result and Residual for Fig. 3.4 in all ϕ directions

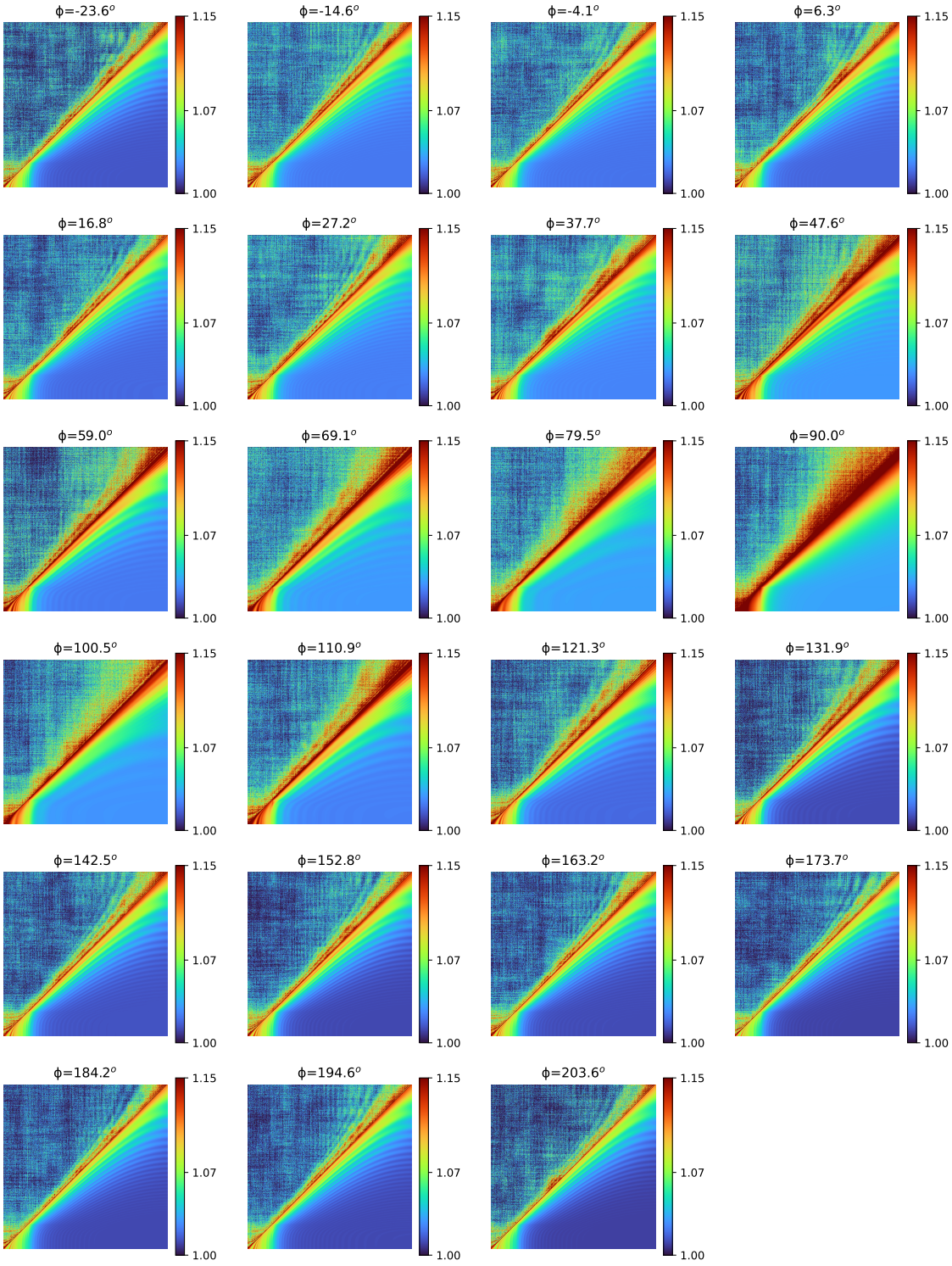

Figure 3.12: **Comprehensive $c_2\left(\vec{q}, t_1, t_2\right)$ data across all ϕ directions from Fig. 3.4 of the manuscript.** The angle ϕ, corresponding to each bin on the field detector, is marked in the title of each panel for reference. One shown in Fig 4 of the main text is at $\phi = 6.3^o$.

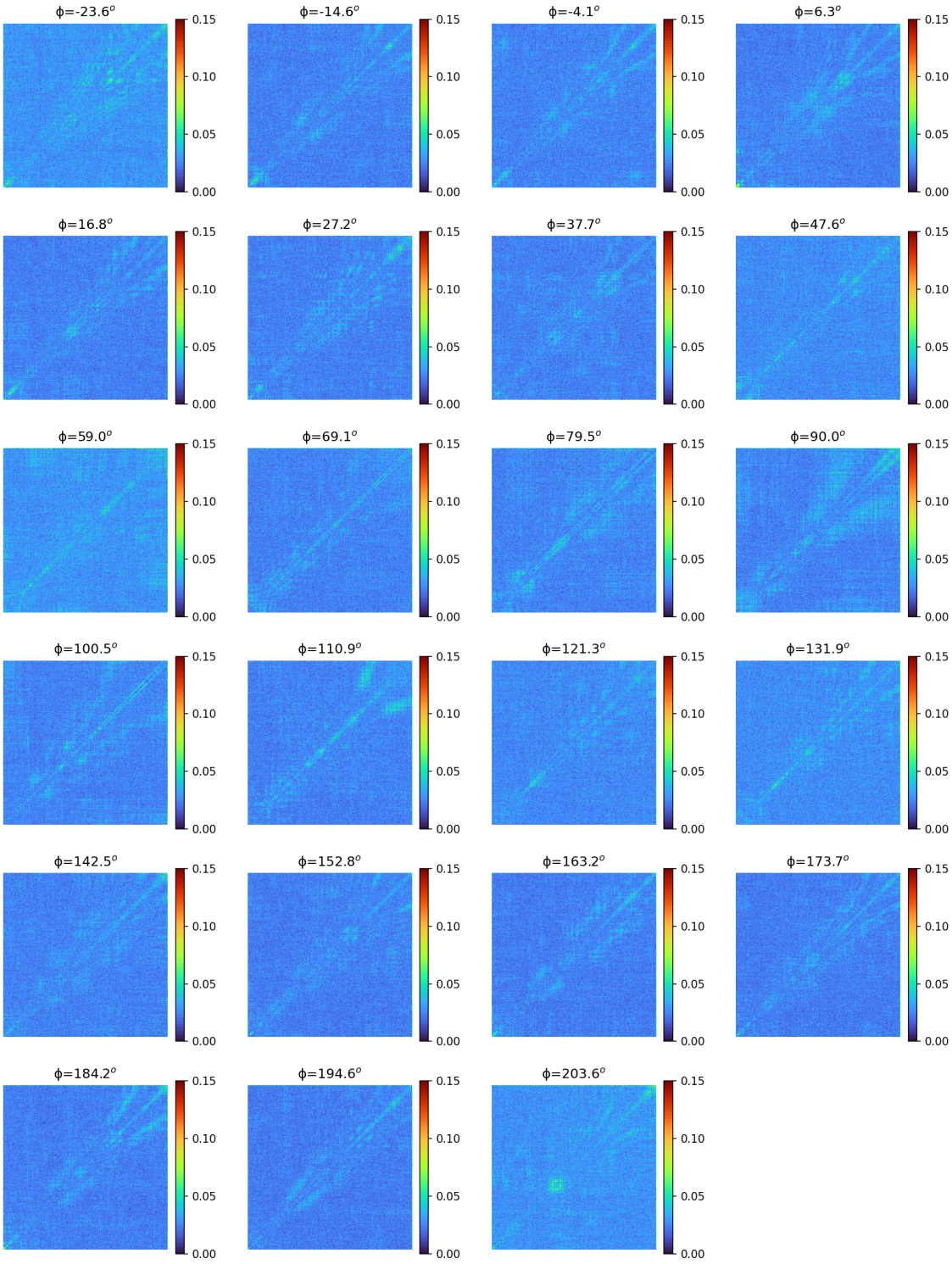

Figure 3.13: **Presentation of the residuals resulting from the analysis conducted in CFigfig:Application of the manuscript, encompassing all ϕ directions.** The angle ϕ, corresponding to each bin on the field detector, is marked in the title of each panel for reference.

CHAPTER 4

BRIDGING MICROSCOPIC DYNAMICS AND RHEOLOGY IN THE YIELDING OF CHARGED COLLOIDAL SUSPENSIONS

4.1 Introduction

Disordered materials play a vital role in various products and processes, ranging from everyday items like toothpaste, face creams, and foods (e.g., mayonnaise, ketchup, yogurt) to structural materials such as concrete and mortar. They are also essential in industrial applications involving slurries, coatings, and composites [244, 245, 246]. Under stress, these materials undergo yielding, a significant transition from elastic energy storage to plastic deformation once a critical load is exceeded [247, 248, 249]. This transition is key to optimizing material properties for applications such as improving handling [250], ensuring formulation consistency [251], and enabling controlled reactions [252]. Understanding and controlling the yielding process is fundamental for enhancing manufacturing efficiency, improving product performance, and achieving desired functionalities [253, 254, 255]. However, the microscopic mechanisms underlying yielding remain poorly understood, largely due to challenges in linking structural and dynamic changes at the particle level to macroscopic rheological behaviors.

To address these challenges, advanced techniques are necessary to explore particle-level structures and dynamics during yielding. SAXS provides structural insights spanning nanoscale to microscale, while XPCS offers high spatiotemporal resolution of particle dynamics through the $c_2\left(\vec{q}, t_1, t_2\right)$. Integrating these methods in a Rheo-SAXS-XPCS framework enables simultaneous investigation of structural changes, dynamic evolution, and macroscopic rheological responses [189]. Complementary computational methods, such as Stokesian Dynamics and FLD simulations [101, 99, 93], provide real-space insights into particle dynamics and their implications for rheological behavior, bridging gaps in experimental observations.

This study employs Rheo-SAXS-XPCS and FLD simulations to examine yielding behav-

ior in charged colloidal suspensions under rheological creep tests. Zwitterionic SiO_x-Cys particles were dispersed in aqueous solutions and 100 mM $NaNO_3$ solutions to tune interparticle forces from repulsive to weakly attractive (Fig. 4.1A). While SAXS measurements indicated minimal static structural changes, significant variations in particle dynamics, captured through the $J(t)$, were closely linked to complex rheological phenomena, including shear banding [256, 257, 258], delayed yielding [259], and resolidification [183]. Dynamical heterogeneity emerged as a central factor driving these behaviors, highlighting the intricate interplay between microscopic rearrangements and macroscopic responses. By connecting rheological observations to microscopic dynamics and structural evolution, the findings provide new insights into energy dissipation, structural adaptation, and particle transport in disordered materials under stress, advancing our understanding of yielding mechanisms and informing the design of materials with tailored properties.

4.2 Results

4.2.1 Microscopic Mechanisms Driving Yielding

The rheological behaviors of repulsive and attractive SiO_x-Cys suspensions differ significantly, despite both exhibiting Andrade creep during creep tests. In repulsive suspensions, the microscopic dynamics align with laminar flow, as evidenced by the angular dependence of the $c_2(\vec{q}, t_1, t_2)$ (**Movie S2** in the App). The fastest decay occurs along the flow direction (Fig. 4.16), supported by homodyne scattering patterns in experiments (Fig. 4.2A) and simulations (Fig. 4.3A). The sinc function form of $c_2(\vec{q}, t_1, t_2)$ (Eq. 2.78) and flow velocity snapshots confirm that particle velocities vary linearly with their positions within the gap, illustrating a homogeneous flow profile (Fig. 4.3B).

To quantify these dynamics, a transport coefficient approach [260] applied *via* Eq. 2.78 revealed a consistent scaling between $\dot{\gamma}(t)$ and the transport coefficient ($J(t)$) (Fig. 4.2E).

Over time, $J(t)$ decreases, reflecting stress dissipation and stabilizing at $J(t \to \infty) = 0$, marking complete relaxation and a new steady state. Spatial analysis of Δx_{na} from FLD simulations further highlights the homogeneity of repulsive suspensions, with no discernible spatial correlations. Particles with varying Δx_{na} values are randomly distributed (Fig. 4.3C), and the Gaussian distribution of Δx_{na} broadens over time (Fig. 4.3D), reflecting the Markovian dynamics typical of homogeneous systems.

In contrast, attractive suspensions exhibit more complex behaviors due to attractive interparticle interactions (**Movie S3** in the App). These interactions result in shear banding, with dense shear bands separated by low-density interfacial regions (Fig. 4.3F and G). The $c_2(\vec{q}, t_1, t_2)$ function displays pronounced oscillations, appearing as stripe patterns during Andrade creep (Fig. 4.2B). These oscillations, indicative of heterodyne scattering, stem from relative motion between system components, contributing a cosine term to $c_2(\vec{q}, t_1, t_2)$ (Eq. 2.100). Simulations corroborate this behavior, showing particle segregation into phases with differing flow velocities and the formation of voids at interfaces (Fig. 4.3F). Velocity mapping reveals distinct shear bands: an upper band flows at a shear rate of approximately 0.0125, while the lower band remains nearly stagnant. This phenomenon arises from the rearrangement of soft regions with weak connectivity and significant local free volume [261, 262].

At low stresses, attractive suspensions display Andrade creep, while higher stresses lead to delayed yielding and resolidification. These transitions are reflected in the $c_2(\vec{q}, t_1, t_2)$, where oscillation frequencies correspond to changes in flow velocity. During delayed yielding, oscillation periods decrease (e.g., from 25 s in Fig. 4.2C to 10 s in Fig. 4.2D). During resolidification, periods increase (e.g., from 75 s to 40 s). Quantitative analysis links flow dynamics to parameters such as relative velocity between shear bands(v_{edge}), fraction of flowing components (x_s), and the transport coefficient ($J(t)$) (Fig. 4.2F, G, and H). Agreement between XPCS and rheological measurements confirms the relationship between microscopic parti-

cle dynamics and macroscopic rheological responses, cross-validating the experimental and simulation results.

The distinct dynamics in salted suspensions further manifest in the heterogeneity of transport processes, as shown by spatial variations in Δx_{na}. Simulations indicate increased Δx_{na} near low-density interface layers compared to shear bands, driven by increased particle mobility around voids (Fig. 4.3G). This mobility, influenced by Eshelby quadrupoles, creates correlated displacement fields that localize shear within interfacial regions [263, 264]. Over time, Δx_{na} distributions transition from Gaussian to power-law forms (Fig. 4.3H), with long tails (the inset of Fig. 4.3H), reflecting non-Markovian dynamics. Despite this heterogeneity, interface particles contribute minimally to $J(t)$ due to their small population. By excluding tail regions, Δx_{na} distributions can be approximated as Gaussian, enabling simplified analysis of transport dynamics and providing insights into the interplay between structural heterogeneity and particle transport during yielding. This analysis underscores the critical role of interparticle interactions and structural organization in governing the rheological responses of salted suspensions.

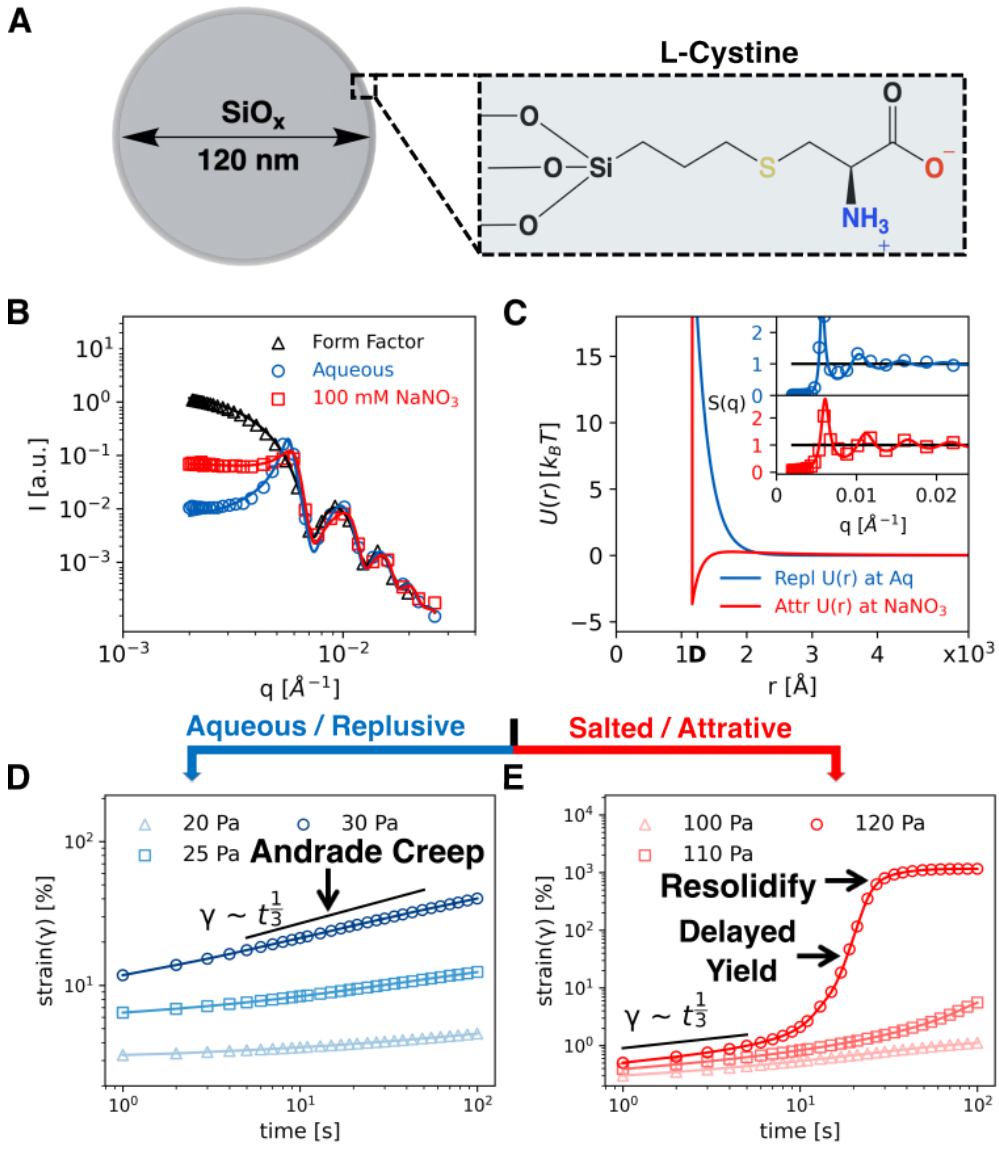

Figure 4.1: **Effect of interaction potential on yielding behavior.** (**A**) In charged colloidal suspensions of 116 nm SiO_x-Cys, changes in the interaction potential significantly affect yielding behavior through particle transport dynamics. (**B**) SAXS confirms the structural changes and potential shifts. (**C**) Two-Yukawa potentials and corresponding structure factors (inset) illustrate the transition from repulsive to attractive interactions upon adding $NaNO_3$. (**D**) The repulsive suspension exhibits classical Andrade yield behavior, where strain increases with an exponent of $\frac{1}{3}$, as the solid black line depicts. (**E**) The addition of salt induces complex rheological responses following a pre-yield behavior similar to that of the repulsive system, depicted by the solid black line. These include shear banding, delayed yielding, and resolidification, as the interaction potential evolves.

4.2.2 Microscopic Mechanisms Driving Yielding

The rheological behaviors of aqueous and salted SiO_x-Cys suspensions differ significantly, despite both exhibiting Andrade creep during creep tests. In aqueous suspensions, the microscopic dynamics align with laminar flow, as evidenced by the angular dependence of the $c_2(\vec{q}, t_1, t_2)$ function (**Movie S2** in the App). The fastest decay occurs along the flow direction (Fig. 4.16), supported by homodyne scattering patterns in experiments (Fig. 4.2A) and simulations (Fig. 4.3A). The sinc function form of $c_2(\vec{q}, t_1, t_2)$ (Eq. 2.78) and flow velocity snapshots confirm that particle velocities vary linearly with their positions within the gap, illustrating a homogeneous flow profile (Fig. 4.3B).

To quantify these dynamics, a transport coefficient approach [260] applied *via* Eq. 2.78 revealed a consistent scaling between shear stress ($\dot{\gamma}(t)$) and the transport coefficient ($J(t)$) (Fig. 4.2E). Over time, $J(t)$ decreases, reflecting stress dissipation and stabilizing at $J(t \rightarrow \infty) = 0$, marking complete relaxation and a new steady state. Spatial analysis of Δx_{na} from FLD simulations further highlights the homogeneity of aqueous suspensions, with no discernible spatial correlations. Particles with varying Δx_{na} values are randomly distributed (Fig. 4.3C), and the Gaussian distribution of Δx_{na} broadens over time (Fig. 4.3D), reflecting the Markovian dynamics typical of homogeneous systems.

In contrast, salted suspensions exhibit more complex behaviors due to attractive interparticle interactions (**Movie S3** in the App). These interactions result in shear banding, with dense shear bands separated by low-density interfacial regions (Fig. 4.3F and G). The $c_2(\vec{q}, t_1, t_2)$ function displays pronounced oscillations, appearing as stripe patterns during Andrade creep (Fig. 4.2B). These oscillations, indicative of heterodyne scattering, stem from relative motion between system components, contributing a cosine term to $c_2(\vec{q}, t_1, t_2)$ (Eq. 2.100). Simulations corroborate this behavior, showing particle segregation into phases with differing flow velocities and the formation of voids at interfaces (Fig. 4.3F). Velocity mapping reveals distinct shear bands: an upper band flows at a shear rate of approximately

0.0125, while the lower band remains nearly stagnant. This phenomenon arises from the rearrangement of soft regions with weak connectivity and significant local free volume [261, 262].

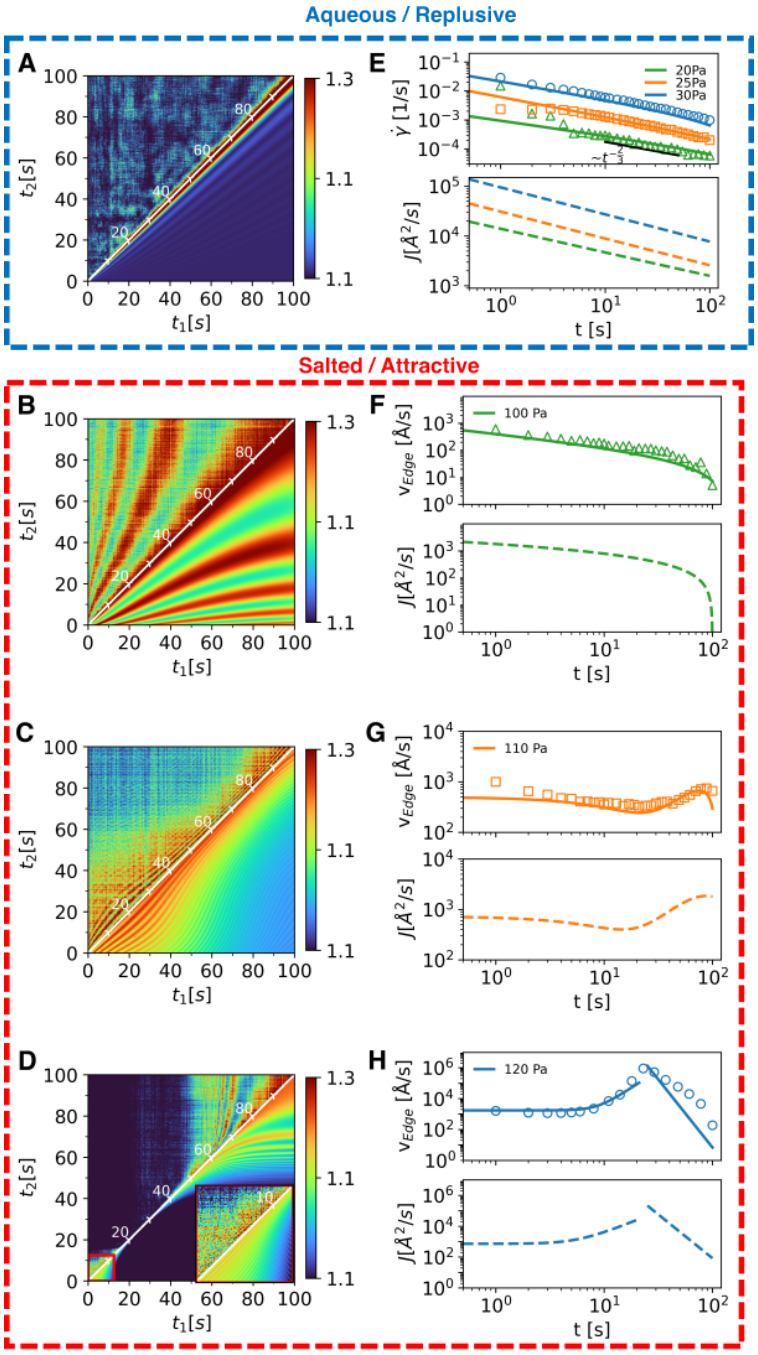

Figure 4.2: **Rheo-SAXS-XPCS analysis of yielding in repulsive and attractive SiO_x-Cys suspensions.** (**A**) Flow-direction $c_2\left(\vec{q}, t_1, t_2\right)$ for the repulsive suspension during Andrade creep. (**B**, **C**, **D**) Flow-direction $c_2\left(\vec{q}, t_1, t_2\right)$ for the 100 mM $NaNO_3$ suspension under creep tests at constant stresses of 100 Pa, 110 Pa, and 120 Pa, respectively. In each panel, the upper triangle shows experimental data, and the lower triangle presents the corresponding fitted results. (**E**) Time-dependent physical parameters from rheometer measurements (markers) and XPCS analysis (solid lines) for the repulsive suspension, including shear rate ($\dot{\gamma}$), velocity at the rotor (v_{Edge}), transport coefficient (J), and fraction (x_s). (**F**, **G**, **H**) Corresponding parameters for the 100 mM $NaNO_3$ suspension.

At low stresses, attractive suspensions display Andrade creep, while higher stresses lead to delayed yielding and resolidification. These transitions are reflected in the $c_2(\vec{q}, t_1, t_2)$, where oscillation frequencies correspond to changes in flow velocity. During delayed yielding, oscillation periods decrease (e.g., from 25 s in Fig. 4.2C to 10 s in Fig. 4.2D). During resolidification, periods increase (e.g., from 75 s to 40 s). Quantitative analysis links flow dynamics to parameters such as relative velocity between shear bands(v_{edge}), fraction of flowing components (x_s), and the transport coefficient ($J(t)$) (Fig. 4.2F, G, and H). Agreement between XPCS and rheological measurements confirms the relationship between microscopic particle dynamics and macroscopic rheological responses, cross-validating the experimental and simulation results.

The distinct dynamics in salted suspensions further manifest in the heterogeneity of transport processes, as shown by spatial variations in Δx_{na}. Simulations indicate increased Δx_{na} near low-density interface layers compared to shear bands, driven by increased particle mobility around voids (Fig. 4.3G). This mobility, influenced by Eshelby quadrupoles, creates correlated displacement fields that localize shear within interfacial regions [263, 264]. Over time, Δx_{na} distributions transition from Gaussian to power-law forms (Fig. 4.3H), with long tails (the inset of Fig. 4.3H), reflecting non-Markovian dynamics. Despite this heterogeneity, interface particles contribute minimally to $J(t)$ due to their small population. By excluding tail regions, Δx_{na} distributions can be approximated as Gaussian, enabling simplified analysis of transport dynamics and providing insights into the interplay between structural heterogeneity and particle transport during yielding. This analysis underscores the critical role of interparticle interactions and structural organization in governing the rheological responses of salted suspensions.

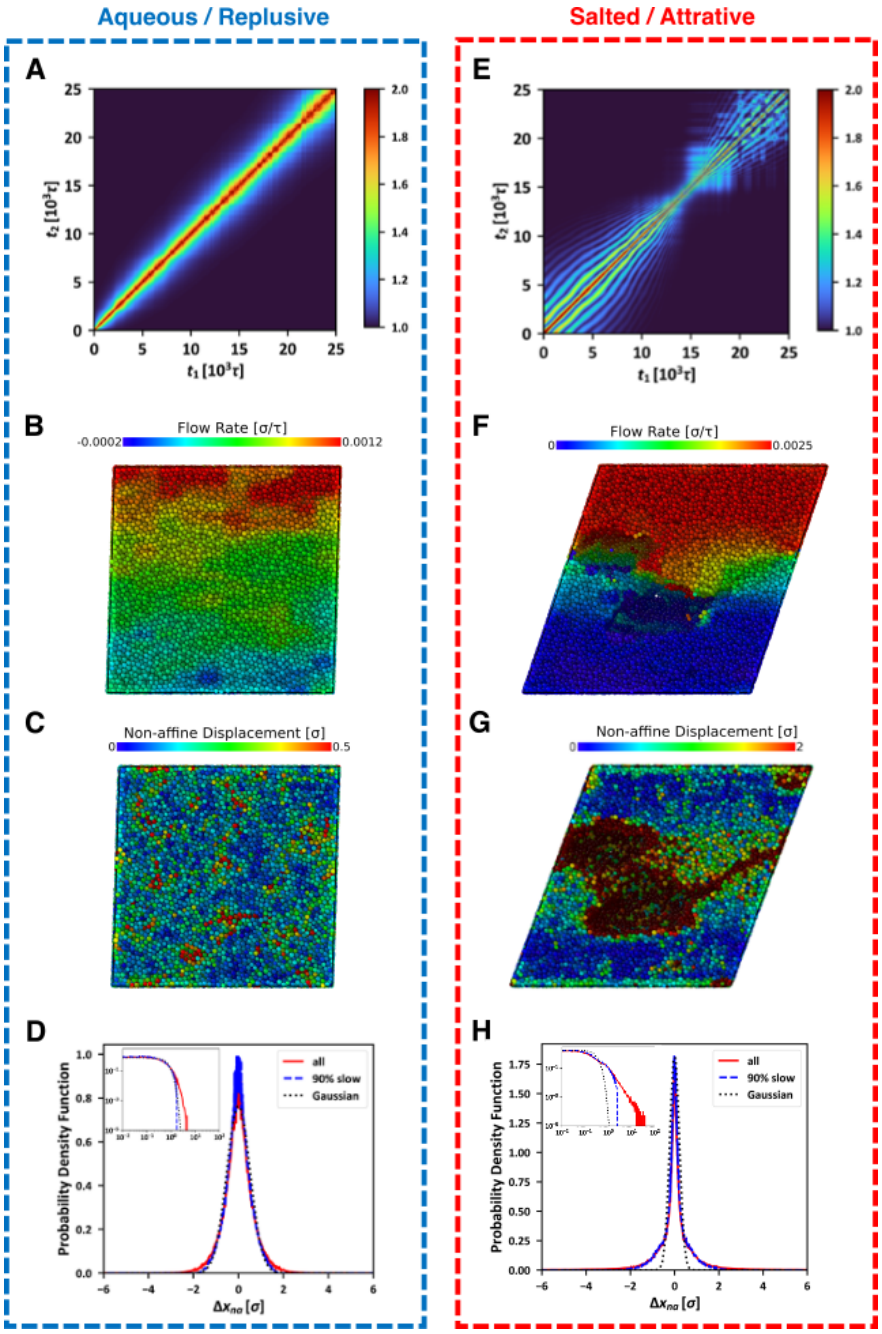

Figure 4.3: **FLD simulations of repulsive and attractive colloidal suspensions during creep tests.** (**A**) Repulsive colloidal suspensions exhibit homodyne scattering signals in $c_2\left(\vec{q}, t_1, t_2\right)$, corresponding to (**B**) laminar flow. (**C**) The spatial distribution of Δx_{na} is uniform, and (**D**) its magnitude follows a Gaussian distribution. (**E**) In salted suspensions with attractive interactions, heterodyne scattering signals in $c_2\left(\vec{q}, t_1, t_2\right)$ are observed due to (**F**) shear banding, where particles flow at two distinct velocities. (**G**) The spatial distribution of Δx_{na} becomes heterogeneous, with large displacements localized at the band interface. (**H**) The Δx_{na} magnitude deviates from Gaussian behavior, exhibiting a broader, non-Gaussian distribution caused by turbulent particle motion at the interface.

4.2.3 Heterogeneity in Yielding Dynamics

The interplay between microscopic structural rearrangements and dynamic processes introduces significant heterogeneity in these systems, directly influencing the complex rheological phenomena observed during yielding. In suspensions with repulsive interactions, particles remain well-dispersed, preserving structural homogeneity (Fig. 4.3B and C). However, when interactions become attractive, particles aggregate, forming dense, particle-rich regions interspersed with voids (Fig. 4.3F and G). Under applied stress, these structural inhomogeneities evolve dynamically, as shear flow expels colloid-depleted voids from dense regions and elongates them into interfacial layers.

These void-generated interfacial layers play a critical role by acting as lubricants between adjacent dense regions, reducing friction and facilitating differential motion. This mechanism results in the development of shear bands—distinct regions with varying flow velocities—that characterize yielding in systems with attractive interactions (**Movie S1** in the SI). The dynamic heterogeneity associated with shear banding is evidenced by heterodyne scattering patterns in XPCS measurements, which capture the velocity differences within these bands (Fig. 4.3B, C, and D).

Further insights into these processes are provided by simulations, which highlight the role of shear band junctions during yielding (Fig. 4.4, **Movie S3** in the SI). These interfaces, composed of junctions with fewer bonds, serve as mechanically weaker regions that localize strain under applied stress, significantly shaping the rheological response. At low strain levels, such as at a stress of 1.1 (Fig. 4.4A), deformation is concentrated within these junctions through particle adhesion, resulting in a plateau in strain and shear rate. As strain increases, these junctions rupture, enabling shear bands to slide relative to one another and triggering delayed yielding (Fig. 4.4B, at $250 \leq t \leq 300s$). Continued deformation leads to the collapse of fragmented junctions and the formation of new ones, driving resolidification (Fig. 4.4B, at $t \geq 300s$). This cyclic bond rupture and reformation process underlies the

observed delayed yielding and resolidification behaviors.

The transport coefficient ($J(t)$) emerges as a critical parameter for validating the consistency between experiments and simulations. Across the pre-yielding, delayed yielding, and resolidification stages (Fig. 4.4C), $J(t)$ exhibits similar trends in both experiments and simulations, highlighting a strong agreement (Fig. 4.4B). This alignment underscores the dynamic equilibrium between bond formation and rupture, which dictates the macroscopic rheological response. The transition to solid-like behavior is characterized by an increasing bond density and the establishment of new junctions, reflected in a decreasing $J(t)$. Conversely, bond rupture and junction failure correspond to fluidization, marked by an increase in $J(t)$. Together, these dynamic processes define the intricate rheological behavior of salted colloidal suspensions during yielding, bridging structural evolution and macroscopic flow properties.

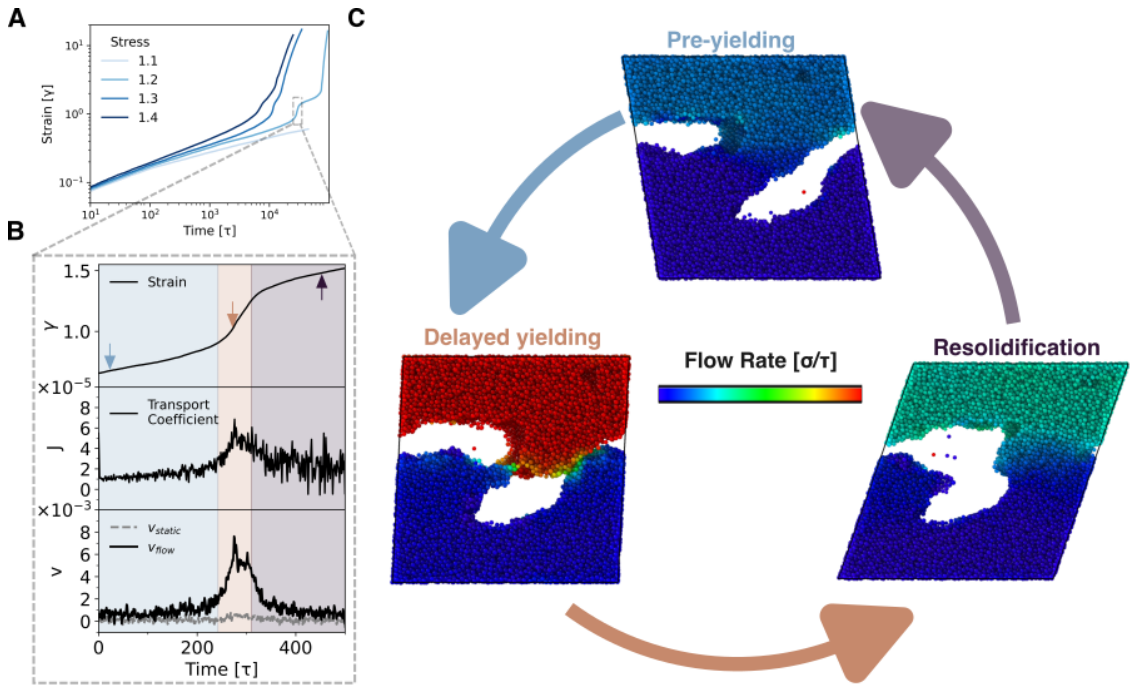

Figure 4.4: **Microscopic mechanisms underlying complex rheological behaviors during yielding.** (**A**) Simulated creep tests replicate key rheological phenomena, including delayed yielding and resolidification, in agreement with experimental results. (**B**) Quantitative consistency between simulated and experimental physical parameters confirms the accuracy of the simulation in representing the experimental system. (**C**) Particle trajectories highlight the critical role of the interfacial junction between shear bands in governing the overall rheological response and driving behaviors such as pre-yielding, delayed yielding, and resolidification.

4.3 Discussion

The integration of Rheo-SAXS-XPCS and FLD simulations provides a cohesive framework that links microscopic particle interactions to macroscopic rheological behavior during yielding. By combining rheological measurements, structural insights, and dynamic analysis, this study highlights how particle-scale processes—such as bond formation and rupture, particle aggregation, and interfacial dynamics—drive phenomena like stress relaxation and fluidization. These findings emphasize the multiscale nature of yielding in colloidal suspensions.

In systems dominated by salt-induced attractive interactions, yielding behavior differs significantly from that in aqueous systems governed by repulsive forces, giving rise to complex

rheological phenomena such as shear banding [256], delayed yielding [259], coarsening [265], and resolidification [183]. Previous experimental and simulation studies have linked these behaviors to distinct mechanisms, including two-step yielding [266, 267], phase separation [268], heterogeneous fluidization [269], and shear banding [270]. However, a unified and comprehensive framework that connects these mechanisms remains elusive due to the lack of direct experimental evidence and a clear physical picture. Thus, developing a systematic approach based on time-resolved local measurements of structural changes is essential. In our study, while both systems exhibit similar creeping dynamics during the pre-yielding phase, attractive interactions introduce pronounced structural and dynamical heterogeneity [271]. These interactions lead to phase separation, creating diluted regions that form cavitated interfaces and densified regions that develop into shear bands under deformation [272, 273, 261]. Dynamically, particles in densified regions experience arrested motion due to deeper potential wells, while those near interfaces exhibit enhanced mobility and strong displacement fields [274, 275]. This heterogeneity governs plastic deformation, stress localization, and flow intermittency [276, 277], as demonstrated by simulation results (Fig. 4.3) and validated by experimental data (Fig. 4.2 and Fig. 4.4). Together, these observations provide a detailed understanding of the role of structural and dynamical heterogeneity in complex rheological phenomena.

At the microscopic level, the behavior of shear band junctions plays a critical role in the yielding process. Junction rupture acts as a precursor to macroscopic failure, initiating complex rheological responses. Visualizing these events at the scale of individual junctions is essential for identifying localized deformation and rupture mechanisms during yielding [278]. The breaking of bonds at junctions mirrors the behavior observed in shear banding, where the deformability of soft regions facilitates shear localization and promotes band flow [279]. Notably, even minimal bond breakage—less than 1 %—can trigger significant structural and dynamical changes [58], highlighting the sensitivity of the macroscopic response

to microscopic rearrangements. Under these conditions, delayed yielding and resolidification persist indefinitely due to the continuous cycle of junction rupture and reconstruction, with fluidization only occurring when shear rates exceed a critical threshold after prolonged stress application [280].

Connecting particle-level mechanisms to bulk rheological behavior offers a powerful framework for understanding and predicting yielding dynamics. Future studies aim to modulate the balance between repulsive and attractive interactions to explore transitions from homogeneous to heterogeneous responses, leveraging both simulations and experiments [266, 281, 282]. Enhanced XPCS experiments, utilizing higher coherence and flux, will enable the capture of subtle particle dynamics and their direct correlation with macroscopic properties [283, 284]. These advancements promise deeper insights into the mechanisms underlying structural and dynamical heterogeneity.

Such an integrated approach holds significant potential for optimizing material performance in diverse applications. From industrial processing of complex fluids to adaptive soft robotics and biomedical innovations such as targeted therapies and tissue engineering, understanding and manipulating yielding behavior will pave the way for next-generation functional materials with precisely tunable properties.

4.3.1 Materials and Methods

Sample Preparation

This study investigates concentrated charged colloids with varying interaction potentials by preparing two systems: a simple fluid and a complex fluid. The simple fluid system consists of 116 nm SiO_x-Cys particles suspended in water, while the complex fluid system uses the same particles suspended in a 100 mM $NaNO_3$ solution to modify interaction potentials while maintaining physical and chemical similarity.

The SiO_x-Cys particles were synthesized by grafting CYS onto silica surfaces *via* thiol-ene

click chemistry. This process involved introducing allyl groups through allyl trimethoxysilane, followed by a thiol-ene reaction to form a charged monolayer. The particles were dispersed in an aqueous solution using an ultrasonic bath, ensuring uniform suspension. The volume fraction was optimized to form internal structures while avoiding glass transition and crystallization.

NMR spectroscopy confirmed the chemical structure of SiO_x-Cys (Fig. 4.5), and zeta potential measurements indicated a slightly negative surface charge of -31.8 mV (Fig. 4.12). Details of the physical properties of SiO_x-Cys in both systems are presented in the Characterization section of the App.

Rheo-SAXS-XPCS Measurement

The rheological procedure for Rheo-SAXS-XPCS measurements follows a standardized protocol to ensure reproducibility. The sample is loaded into the Taylor-Couette geometry and subjected to a pre-shear of 100 % strain amplitude at 1 rad/s for 200 seconds to eliminate shear history. After pre-shear, the sample rests at zero stress ($\sigma = 0$) for 600 seconds to reach a steady state, followed by an XPCS measurement to capture the reference structure and intrinsic dynamics in the quiescent state.

For creep tests, which measure deformation under constant stress, the pre-shear procedure ensures a consistent initial state. A relaxation step then allows the sample to rest at zero strain ($\gamma = 0$) for 200 seconds, with residual stresses released by briefly setting $\sigma = 0$ for 0.1 seconds before applying the stress.

Under applied deformation, the system's non-equilibrium response prevents converting the $c_2\left(\vec{q}, t_1, t_2\right)$ function into a one-time correlation without losing time-dependent dynamics. Therefore, the full $c_2\left(\vec{q}, t_1, t_2\right)$ function is analyzed. Yield stress fluids under stress exhibit combined isotropic intrinsic dynamics and shear-induced dynamics along the flow direction, causing ϕ-dependent asymmetry in the XPCS autocorrelation function due to faster decay.

To resolve this asymmetry, the intensity profile within the q range is divided into 23 bins at 10.5^o intervals relative to the ϕ angle, generating a ϕ-dependent $c_2(\vec{q}, t_1, t_2)$ function. Cooperative particle dynamics are analyzed within the q range of 0.0048–0.0060 Å^{-1}. A q value of 0.054 Å^{-1} is used, corresponding to the particle structure peak and de Gennes narrowing.

4.3.2 Simulation

Dense colloidal suspensions were simulated using LAMMPS [102] to investigate the effects of inter-particle potentials on rheological behavior. Particle diameters followed a normal distribution, $\mathcal{N}(\sigma, (0.07\sigma)^2)$, with a fixed volume fraction of 48 %, consistent with experimental conditions. Here, σ represents the average particle diameter and serves as the unit length. The inter-particle interactions were modeled using the DLVO potential in LAMMPS [93], with parameters obtained by fitting two-Yukawa potentials (Fig. 4.1C and Fig. 4.8). Hydrodynamic interactions were incorporated *via* FLD [101, 99, 93], a simplified version of Stokesian dynamics. FLD separates hydrodynamic interactions into near-field lubrication forces and far-field many-body effects. Based on lubrication theory, lubrication forces account for hydrodynamic effects arising from confined solvents between moving particles [285]. Far-field interactions are approximated by applying linear viscous forces, reflecting mean particle mobility [101, 99]. In dense suspensions, screened far-field interactions make near-field lubrication dominant, validating the use of FLD in this context. At equilibrium, the simulations accurately reproduced the static microstructure of both attractive and repulsive suspensions observed experimentally, as confirmed by the agreement in scattering structure factors (Fig. 4.9).

The simulations were conducted in a $6\mu m \times 6\mu m \times 6\mu m$ periodic simulation box (**Movie S1, S2** and **S3** in the App). Although this size is much smaller than the experimental gap, it captures key phenomena such as laminar flow in repulsive suspensions and shear

banding in attractive suspensions. Direct comparisons of $c_2(\vec{q}, t_1, t_2)$, calculated from simulated scattering intensity autocorrelations, with experimental XPCS measurements revealed checkerboard patterns in addition to homodyne and heterodyne signals. These patterns, attributed to collective dynamics, appear with stronger amplitude in simulations due to the small system size, resulting in noise that obscures transport dynamics.

To isolate transport dynamics, $c_2(\vec{q}, t_1, t_2)$ was recalculated using the theoretical model in Eq. 2.100. The simulation box was divided into components based on flow conditions: 10 evenly spaced layers for repulsive suspensions and two bands (fast and slow) for attractive suspensions, classified by flow rates. For each component, the composition ($x(t)$), flow rate ($v(t)$), and effective transport coefficient ($J(t)$) were determined. Flow rates were derived from collective bead motion, while $J(t)$ was calculated as the time derivative of the variance of particle positions due to thermal motion, $J(t) = \frac{d\mathbb{V}[x(t)]}{dt}$. The values of $x(t)$, $v(t)$ and $J(t)$ were then used in Eq. 2.100 to compute $c_2(\vec{q}, t_1, t_2)$.

4.3.3 Characterization

Colloidal suspensions were prepared by dispersing SiO_x-Cys particles with a diameter of $d = 116\,\text{nm}$ and a dispersity of $\Delta r/r = 0.07$ into either deionized water or a 100 mM $NaNO_3$ solution. Samples were studied at a volume fraction of 0.48 (Fig. 4.1A), which allows the development of internal structures associated with complex rheological responses while remaining below the jamming threshold. The chemical structure of the CYS ligands grafted onto the SiO_x-Cys surface was verified by NMR (Fig. 4.5), and the grafting density was determined to be 2.3% by weight from TGA measurements. Zeta potential analysis showed a surface potential of $-31.8\,\text{mV}$, and the surface charge density was measured as $-0.19\,\mu\text{equi/g}$. Rheological measurements fitted with the Herschel-Bulkley model yielded a dynamic yield stress of 32.7 Pa, consistent with the static yield stress (24.3 Pa), indicating that the repulsive suspension behaves as a simple yield stress fluid (Fig. 4.10B).

Structural and dynamic characterizations were performed using SAXS and XPCS at beamline 8-ID-I of the Advanced Photon Source (APS). The static structure was examined using coherent X-ray scattering intensity ($I(\vec{q},\tau)$) profiles (Fig. 4.1B), and equilibrium dynamics were assessed through intensity autocorrelation functions ($g_2(\vec{q},\tau)$) (Fig. 4.7E). The SAXS profiles showed a Guinier region at $q > 0.005\,\text{Å}^{-1}$ and Bessel-type oscillations, consistent with monodisperse SiO_x particles coated with CYS. In the salted suspension, increased intensity at $q > 0.003\,\text{Å}^{-1}$ indicated aggregation and structure formation due to attractive interactions. The $I(\vec{q},\tau)$ data were analyzed using a two-Yukawa potential model to extract interaction parameters describing the strength and range of interparticle forces [286]. The resulting interaction potentials (inset of Fig. 4.1C) and structure factors (Fig. 4.1C) show a clear transition from repulsive to attractive interactions with the addition of $NaNO_3$.

The system's dynamics were quantified using the intensity-intensity autocorrelation function ($c_2(\vec{q},t_1,t_2)$), derived from 2D raw detector images (Fig. 4.7C, D):

$$c_2(\vec{q},t_1,t_2) = \frac{\mathbb{E}\left[I(\vec{q},t_1)I(\vec{q},t_2)\right]}{\mathbb{E}\left[I(\vec{q},t_1)\right]\mathbb{E}\left[I(\vec{q},t_2)\right]} \tag{4.1}$$

The resulting $c_2(\vec{q},t_1,t_2)$ matrices exhibited a Toeplitz-like structure, indicating stationary equilibrium conditions. This confirms that the intrinsic dynamics of SiO_x-Cys particles in both suspensions followed Brownian motion. The $c_2(\vec{q},t_1,t_2)$ was transformed into the $g_2(\vec{q},\tau)$ function through diagonal averaging (Fig. 4.1F):

$$g_2(\vec{q},\tau) = \frac{\mathbb{E}\left[I(\vec{q},t)I(\vec{q},t+\tau)\right]}{\mathbb{E}\left[I(\vec{q},t)\right]\mathbb{E}\left[I(\vec{q},t+\tau)\right]} \tag{4.2}$$

The $g_2(\vec{q},\tau)$ function was fitted using a stretched exponential function:

$$g_2(\vec{q},\tau) = 1 + \beta e^{-2\left(\frac{\tau}{\tau_o}\right)^{\alpha}} \tag{4.3}$$

Here, τ_o is the relaxation time, α is the stretching exponent representing the distribution of relaxation times, and β is the speckle contrast, which depends on the coherence of the

incident beam.

The relaxation time τ_o in the attractive suspension was slightly longer than in the repulsive suspension, indicating the formation of larger aggregates with slower dynamics. This observation aligns with SAXS results, confirming that attractive interactions promote aggregate formation. These findings underscore the impact of interparticle potentials on the structural and dynamic properties of colloidal suspensions.

4.4 Appendix

4.4.1 NMR Result

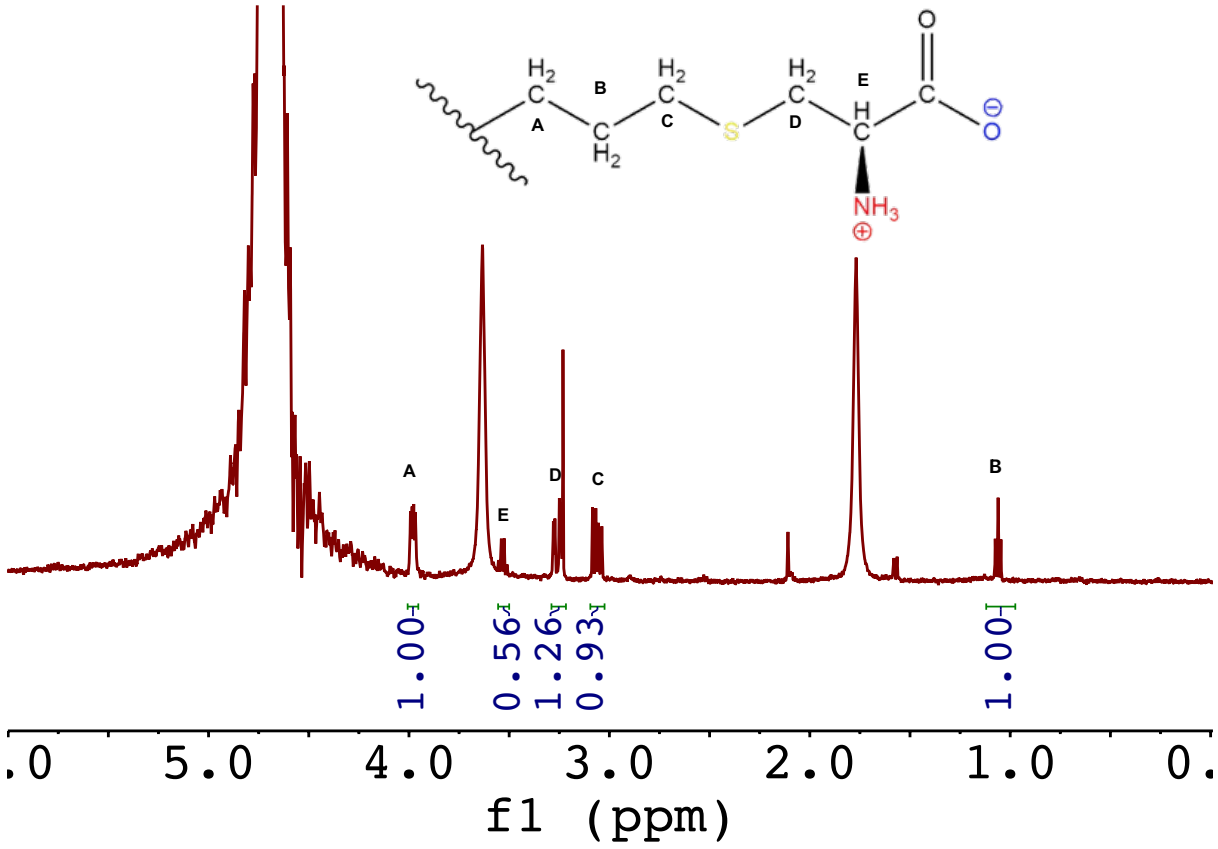

Figure 4.5: **NMR analysis of SiO_x-Cys.** The characteristic peaks corresponding to CYS are labeled as D and E.

4.4.2 TGA Result

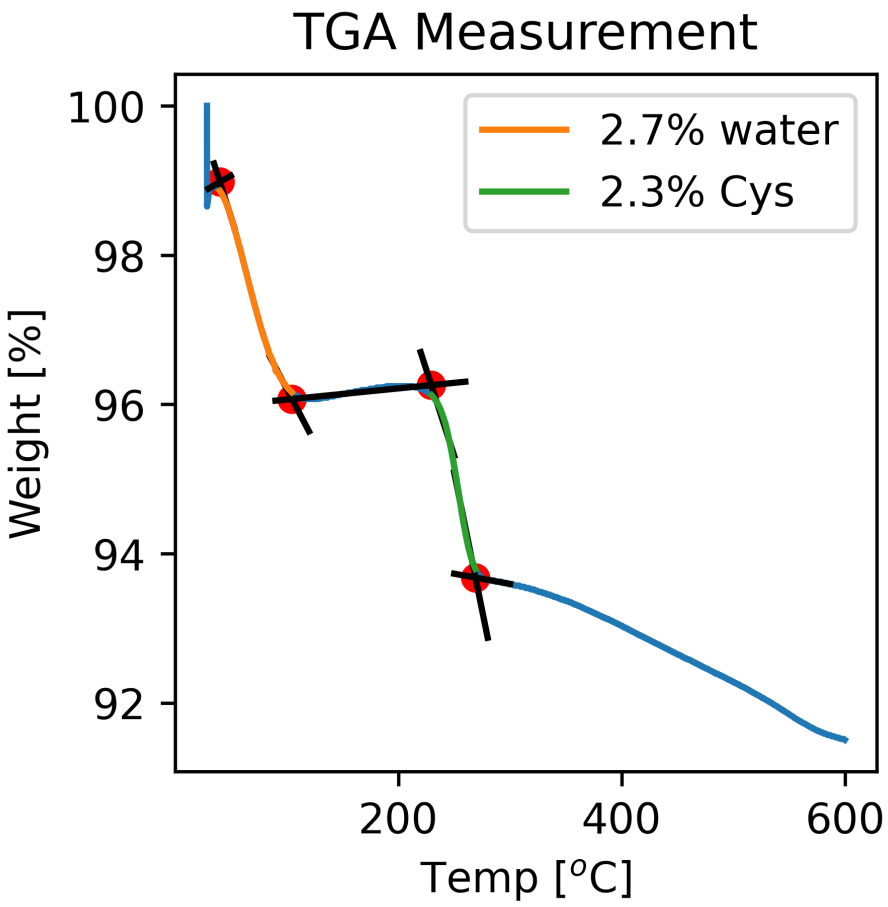

Figure 4.6: **TGA analysis of SiO_x-Cys to determine the composition and grafting density.** The results show that 2.3% of cysteine is grafted onto the particle surface, with 2.7% water content.

4.4.3 Static Structure and Dynamics Measurement

The static structure and equilibrium dynamics measurements demonstrate that the introduction of an attractive potential leads to the formation of internal structures in the system. This is supported by the increased low-q intensity in the SAXS profile, longer particle relaxation times, and a larger hysteresis area observed in shear sweep measurements.

The rheological hysteresis observed during the shear ramp measurement (Fig. 4.10A) further supports the idea that the addition of salts transforms a simple fluid of repulsive colloids into a system exhibiting complex rheological behavior. The structural and dynamic changes revealed by SAXS and XPCS (Fig. 4.1) correlate with the rheological data, where SiO_x-Cys in a salt solution shows significant hysteresis. In contrast, the stress curves during shear sweep up and down are identical in the repulsive suspension, indicating the absence of hysteresis.

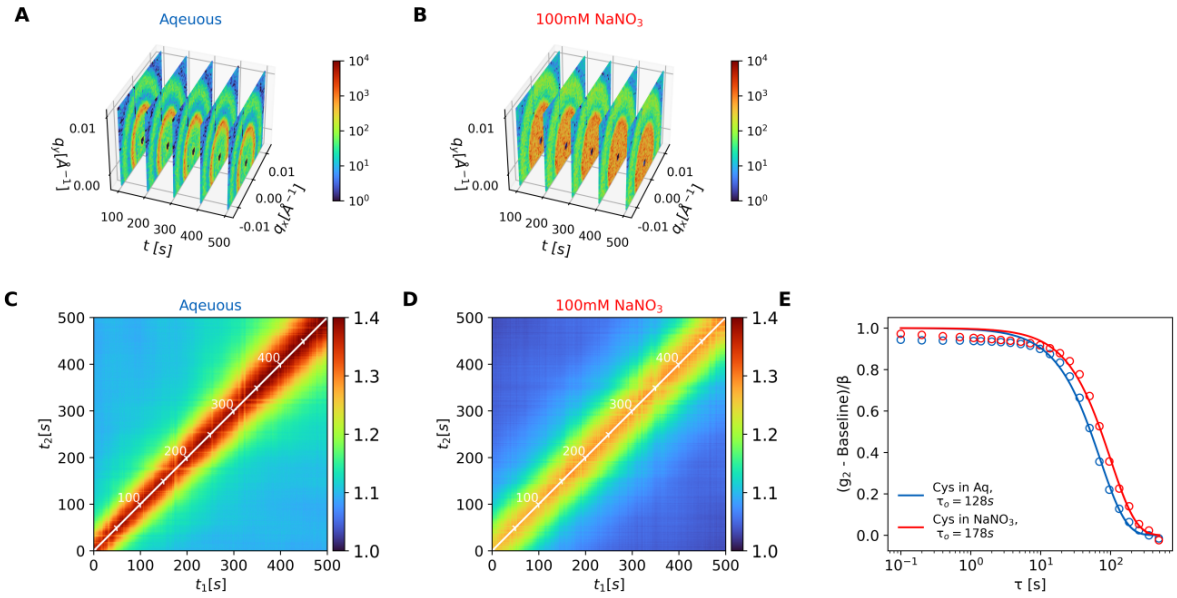

Figure 4.7: **SAXS and $c_2(\vec{q}, t_1, t_2)$ results for structural and dynamic characterization.** (**A**, **B**) 2D SAXS patterns are azimuthally integrated to obtain 1D profiles, with experimental data represented as markers in Fig. 4.1. (**C**, **D**) Dynamics are analyzed by calculating $c_2(\vec{q}, t_1, t_2)$ (Eq. 4.1) from 2D SAXS data. The equilibrated state allows for the calculation of $g_2(\vec{q}, \tau)$ through averaging, which is then used to obtain $c_2(\vec{q}, t_1, t_2)$. (**E**) The $g_2(\vec{q}, \tau)$ function is fitted with a stretched exponential to extract the relaxation time. The introduction of attractive potentials promotes the formation of internal structures, as indicated by the increased low-q intensity in SAXS profiles and longer particle relaxation times.

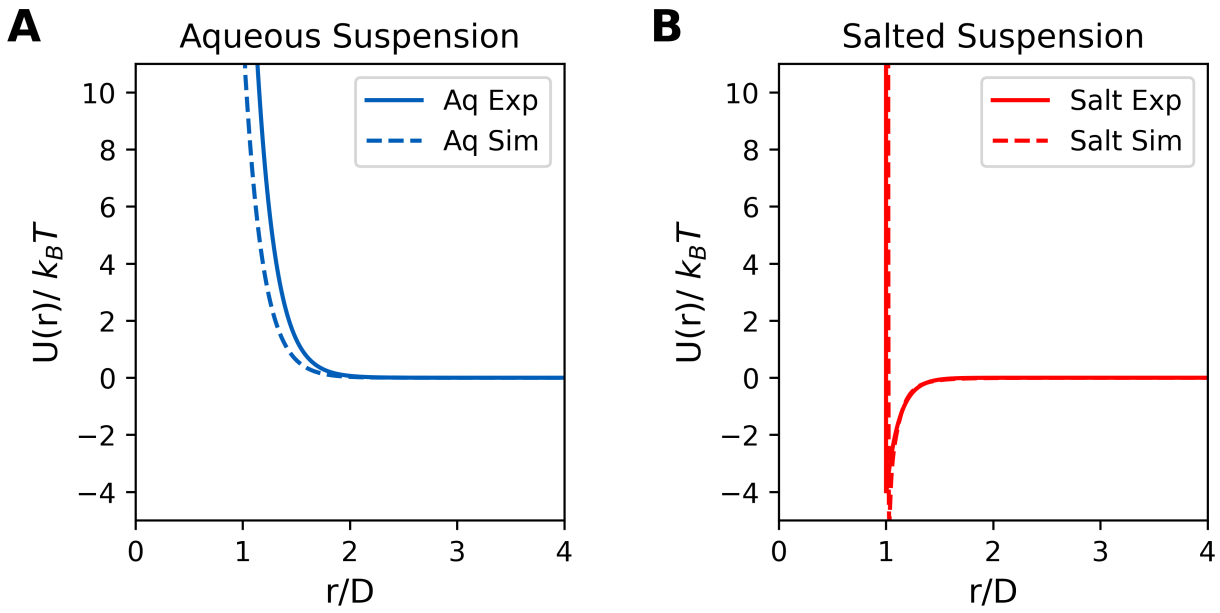

Figure 4.8: **Simulated SAXS profiles using the two-Yukawa potential for repulsive (A) and attractive (B) suspensions.** The results illustrate the shift in interparticle interactions from purely repulsive to attractive with the addition of salt.

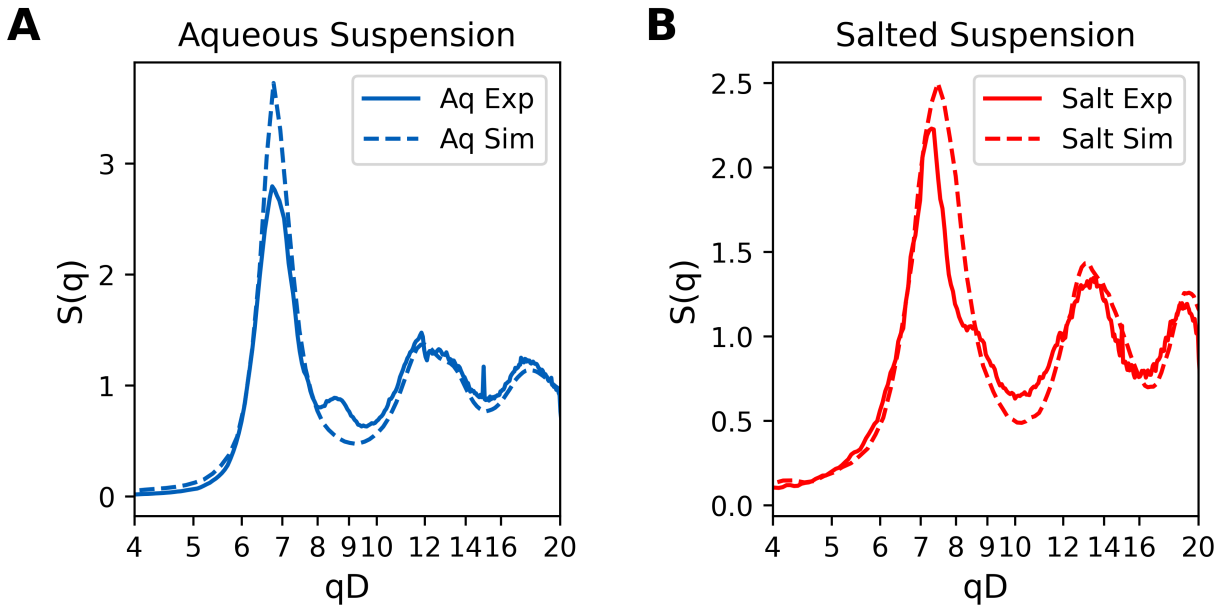

Figure 4.9: **Comparison of experimental (solid lines) and simulated (dashed lines) structure factors for repulsive (A) and attractive (B) suspensions.** The good agreement confirms that the simulations effectively capture the interparticle interactions and structural features of both systems.

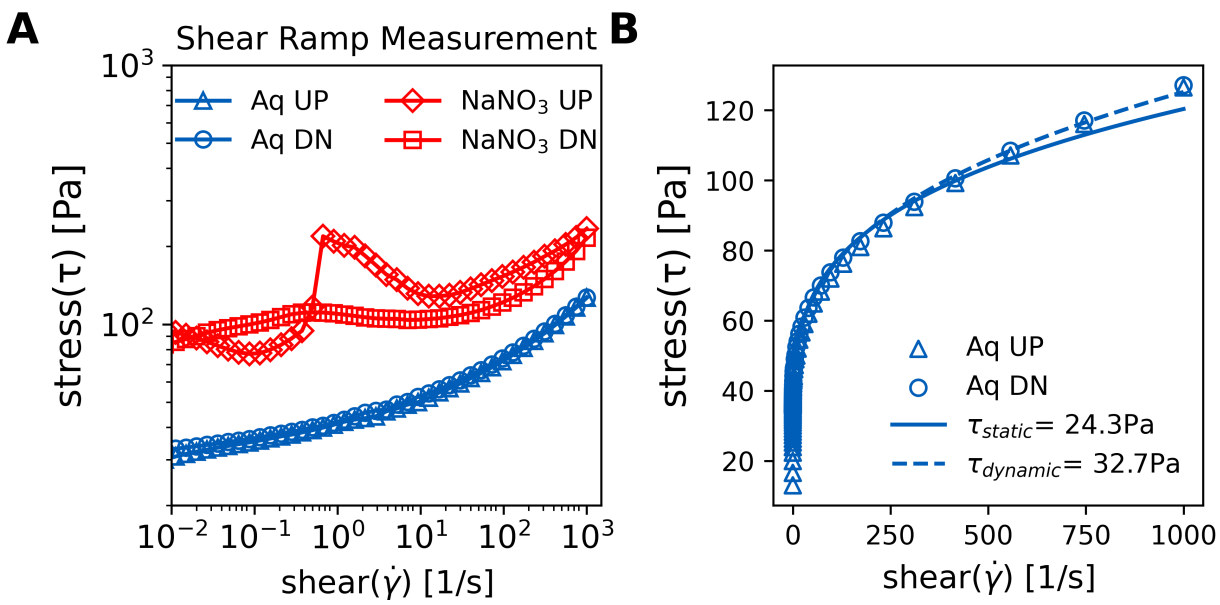

Figure 4.10: **Shear ramp measurement and modeling with Herschel–Bulkley for suspensions with attractive and repulsive interactions.** **(A)** Shear ramp measurements for an aqueous suspension with a repulsive potential (blue) and a salted suspension with an attractive potential (red). The addition of salt induces rheological hysteresis, as the potential changes from a repulsive to an attractive interaction potential. **(B)** The stress-shear relationship for the repulsive suspension is fitted using the Herschel–Bulkley model, where the ramp-up measurement gives a static yield stress of 24.3 Pa, and the ramp-down measurement gives a dynamic yield stress of 32.7 Pa. The close consistency between these two values indicates that the repulsive suspension behaves as a simple yielding fluid.

4.4.4 Burger Model Fitting

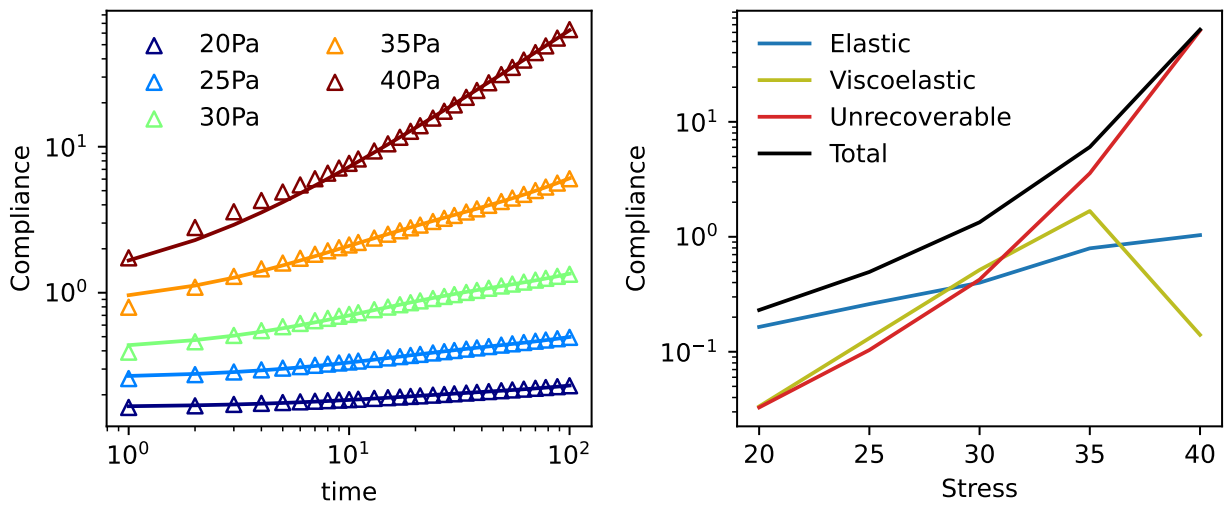

Figure 4.11: **Creep response of a repulsive suspension fitted using the Burger model.** The fitting closely matches the experimental data, indicating that the Burger model effectively captures the creep behavior under applied stress. As stress increases, the response shifts from elastic to viscous dominance.

4.4.5 Zeta Potential

Zeta Potential Report
v2.3

Malvern

Malvern Instruments Ltd - © Copyright 2008

Sample Details

Sample Name:	120nm_SiOx_Cys_01 1		
SOP Name:	mansettings.nano		
General Notes:			
File Name:	120nm_SiOx_Particle.dts	**Dispersant Name:**	Water
Record Number:	28	**Dispersant RI:**	1.330
Date and Time:	Tuesday, February 1, 2022 1:58:4...	**Viscosity (cP):**	0.8872
		Dispersant Dielectric Constant:	78.5

System

Temperature (°C):	25.0	**Zeta Runs:**	12
Count Rate (kcps):	334.0	**Measurement Position (mm):**	2.00
Cell Description:	Clear disposable zeta cell	**Attenuator:**	9

Results

			Mean (mV)	Area (%)	St Dev (mV)
Zeta Potential (mV):	-31.8	**Peak 1:**	-31.8	100.0	5.71
Zeta Deviation (mV):	5.71	**Peak 2:**	0.00	0.0	0.00
Conductivity (mS/cm):	0.0158	**Peak 3:**	0.00	0.0	0.00
Result quality :	Good				

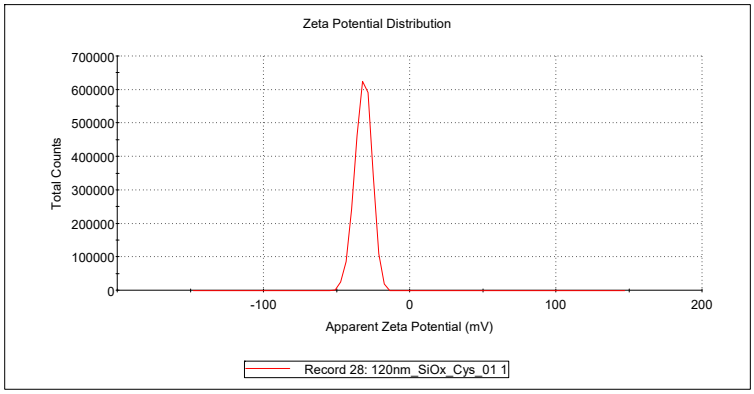

Malvern Instruments Ltd
www.malvern.com

Zetasizer Ver. 7.12
Serial Number : MAL1013322

File name: 120nm_SiOx_Particle.dts
Record Number: 28
01 Feb 2022 2:23:49 PM

Figure 4.12: **Zeta potential measurements show that the particles are negatively charged, with a monodisperse distribution centered at -31.8 mV.**

4.4.6 Structure in Creep Test

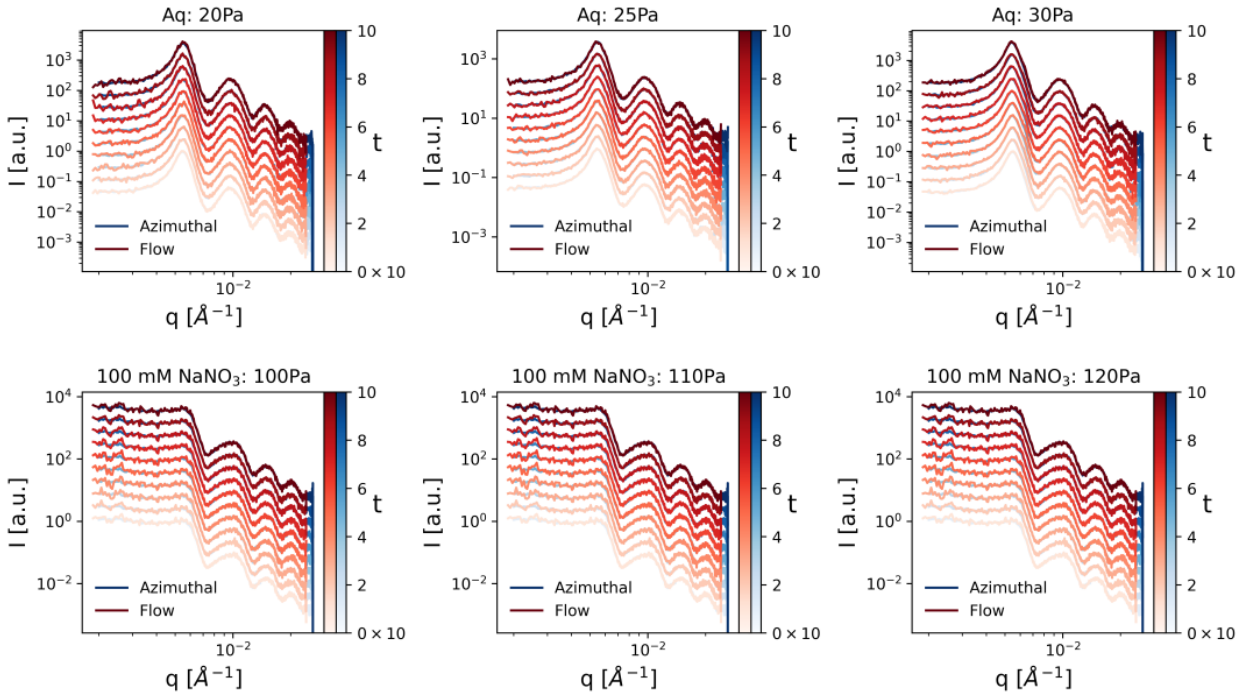

Figure 4.13: **Flow-direction and azimuthal SAXS profiles were measured during creep tests for both repulsive and attractive suspensions.** The agreement between the flow-direction and azimuthal profiles confirms the isotropic and amorphous nature of the system. Furthermore, the lack of significant changes in the SAXS profiles suggests minimal structural evolution under creep conditions.

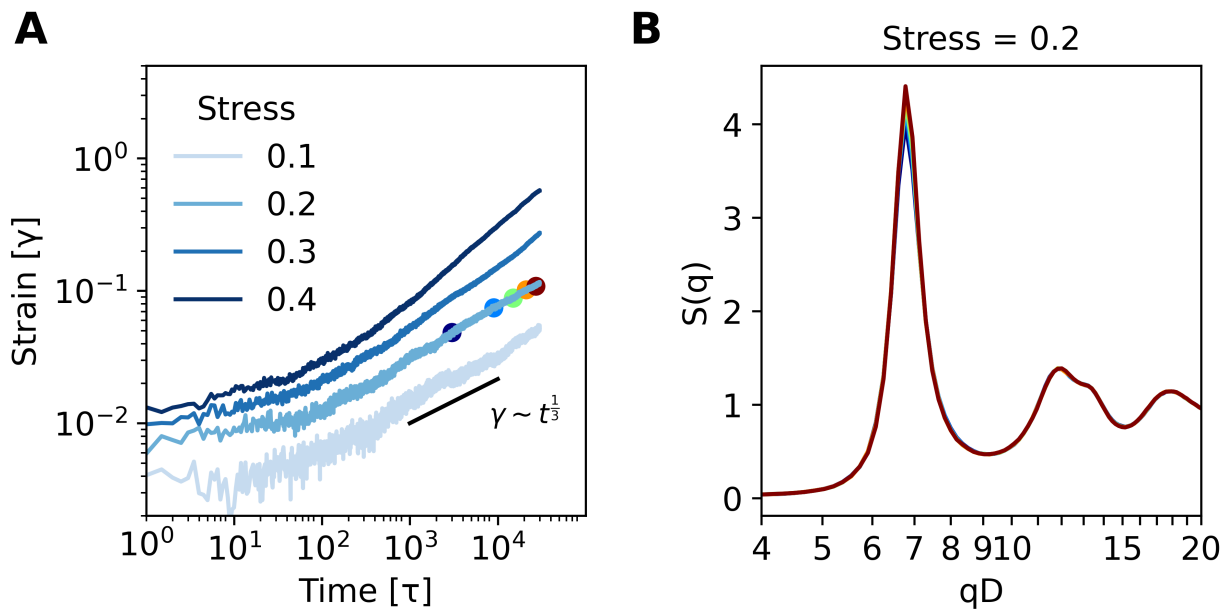

Figure 4.14: **(A) Creep test results for aqueous suspensions simulated under stress levels ranging from 0.1 to 0.4.** The black solid line indicates a strain increase following a power-law relationship, $\gamma \sim t^{\frac{1}{3}}$, corresponding to a shear rate scaling as $\dot{\gamma} \sim t^{-\frac{2}{3}}$. This behavior aligns with the characteristics of Andrade creep. (B) Structure factor evolution during the creep test. The test duration is divided into five equal intervals, with structure factors averaged within each interval. The color of each structure factor corresponds to the midpoint of the respective interval, as shown in Panel A. The results confirm the absence of significant structural changes throughout the creep test.

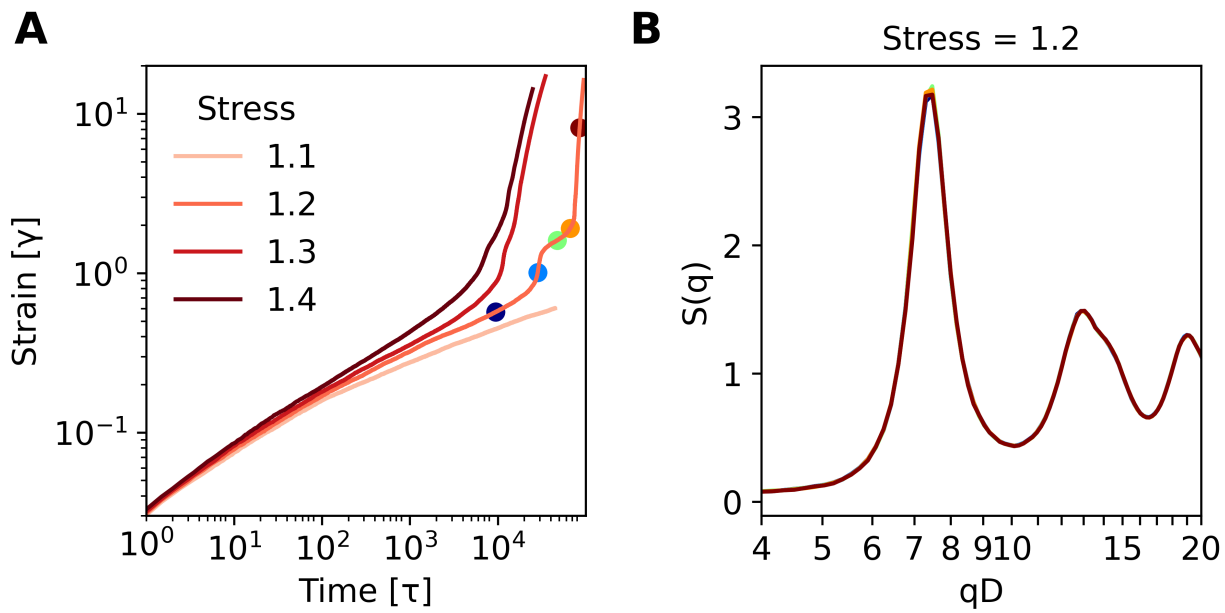

Figure 4.15: **(A) Simulated creep tests of salted suspensions under stress levels ranging from 1.1 to 1.4.** (B) Structure factors calculated during the creep tests, with the test duration divided into five equal intervals. Each structure factor is averaged over its respective interval, and the colors correspond to the midpoint of each interval as shown in Panel A. The results indicate that no significant structural changes occurred throughout the creep test.

4.4.7 Analysis of $c_2(\vec{q}, t_1, t_2)$ in all directions

Aqueous suspension

During creep measurements under horizontally applied stress, the $c_2(\vec{q}, t_1, t_2)$ decay exhibits a significantly faster rate in the horizontal direction. This anisotropic behavior gradually decreases as the observation angle moves away from the horizontal axis, reaching its slowest decay in the vertical direction (Fig. 4.16, Fig. 4.17, and Fig. 4.18).

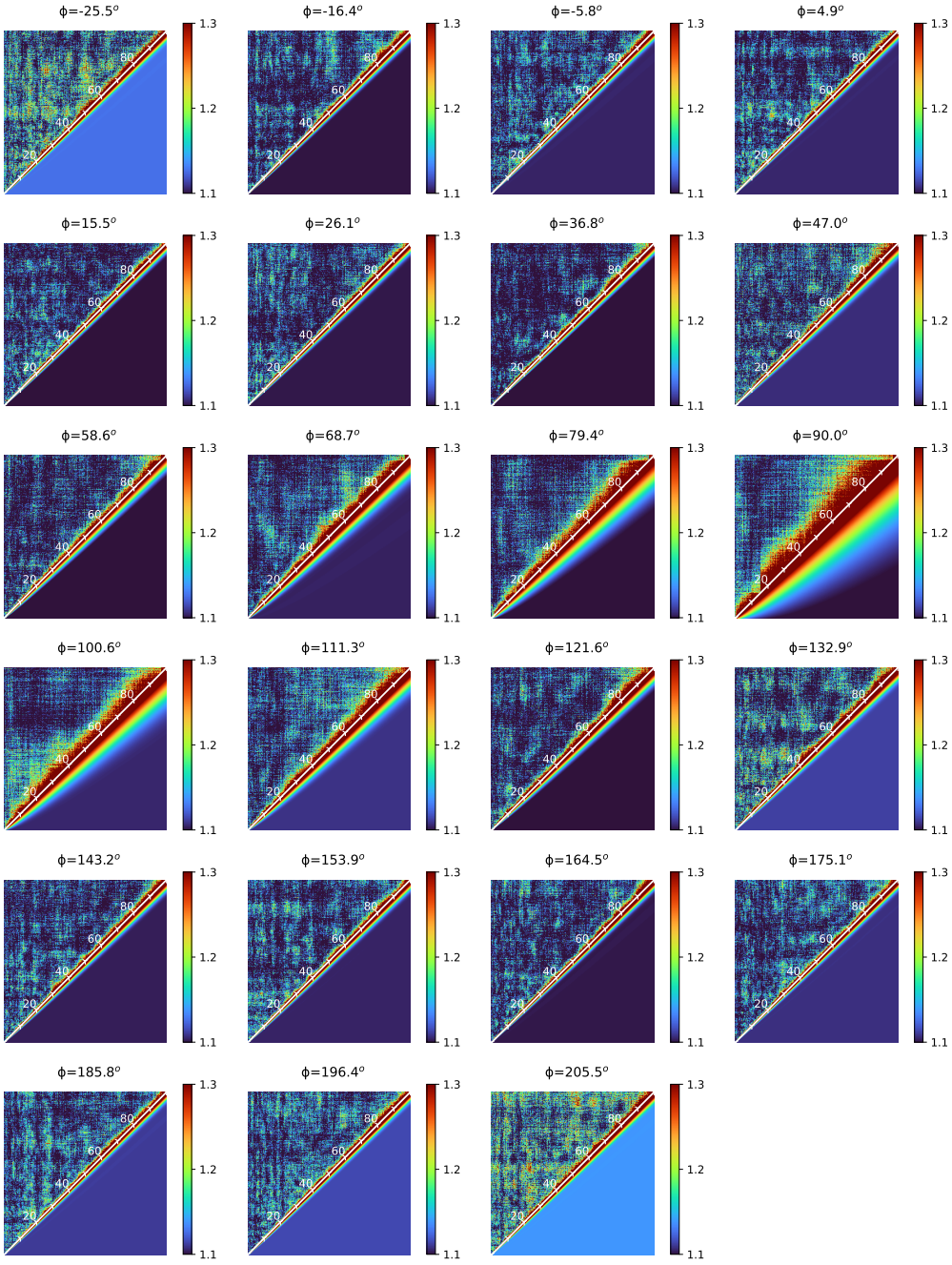

Figure 4.16: $c_2(\vec{q}, t_1, t_2)$ **functions for SiO_x-Cys in aqueous suspension under a stress of 20 Pa, presented for all directions.** Experimental results are shown in the upper corners of each panel, while the corresponding fitting results are displayed in the lower corners.

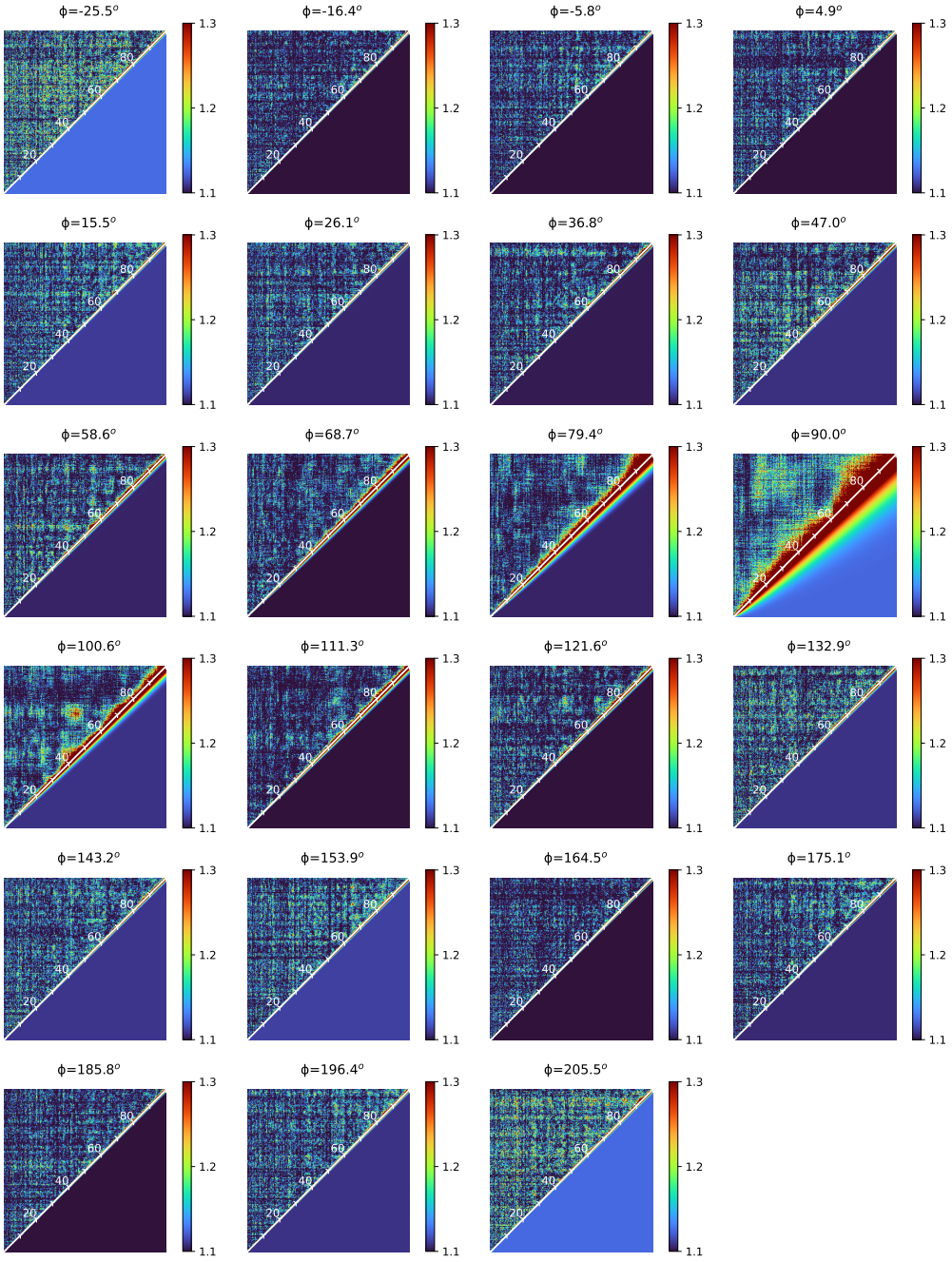

Figure 4.17: $c_2\left(\vec{q}, t_1, t_2\right)$ **functions for SiO_x-Cys in aqueous suspension under a stress of 25 Pa, presented for all directions.** Experimental results are shown in the upper corners of each panel, while the corresponding fitting results are displayed in the lower corners.

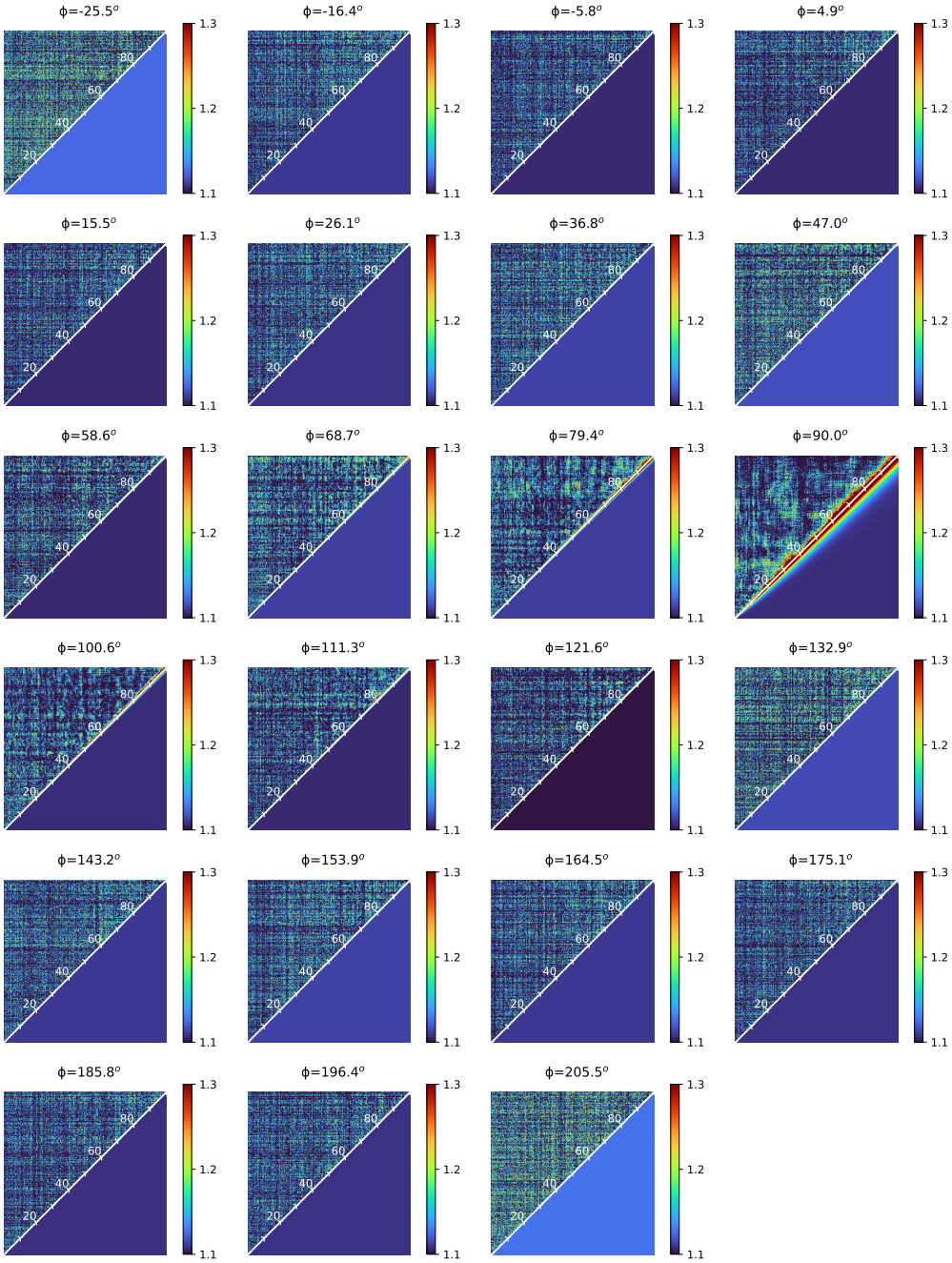

Figure 4.18: $c_2\left(\vec{q}, t_1, t_2\right)$ **functions for SiO_x-Cys in aqueous suspension under a stress of 30 Pa, presented for all directions.** Experimental results are shown in the upper corners of each panel, while the corresponding fitting results are displayed in the lower corners.

Suspension in 100 mM $NaNO_3$

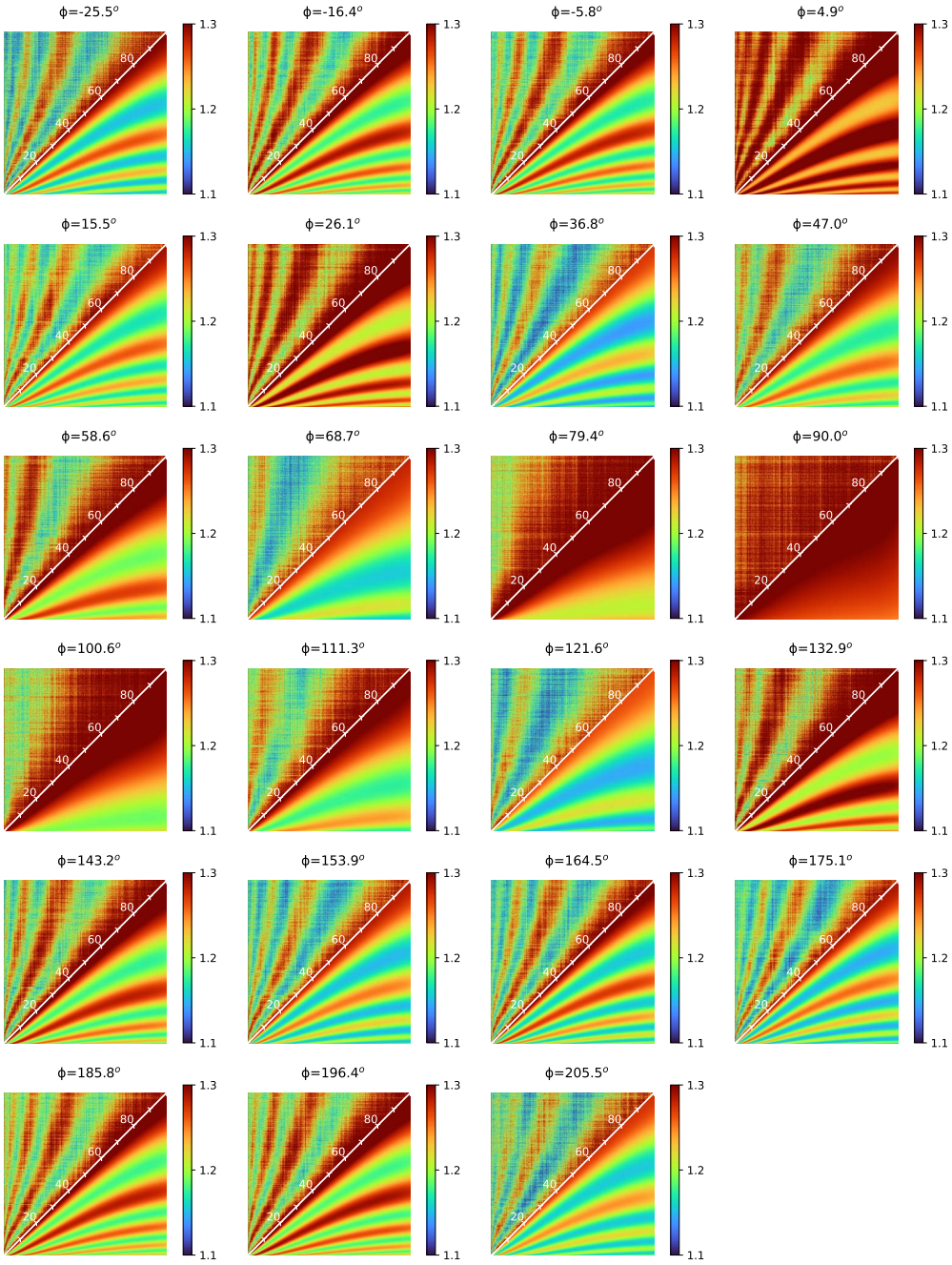

Figure 4.19: $c_2\left(\vec{q}, t_1, t_2\right)$ **functions for SiO_x-Cys in a 100 mM $NaNO_3$ solution under a stress of 100 Pa, shown for all directions.** Experimental results are displayed in the upper corners of each panel, with the corresponding fitting results in the lower corners.

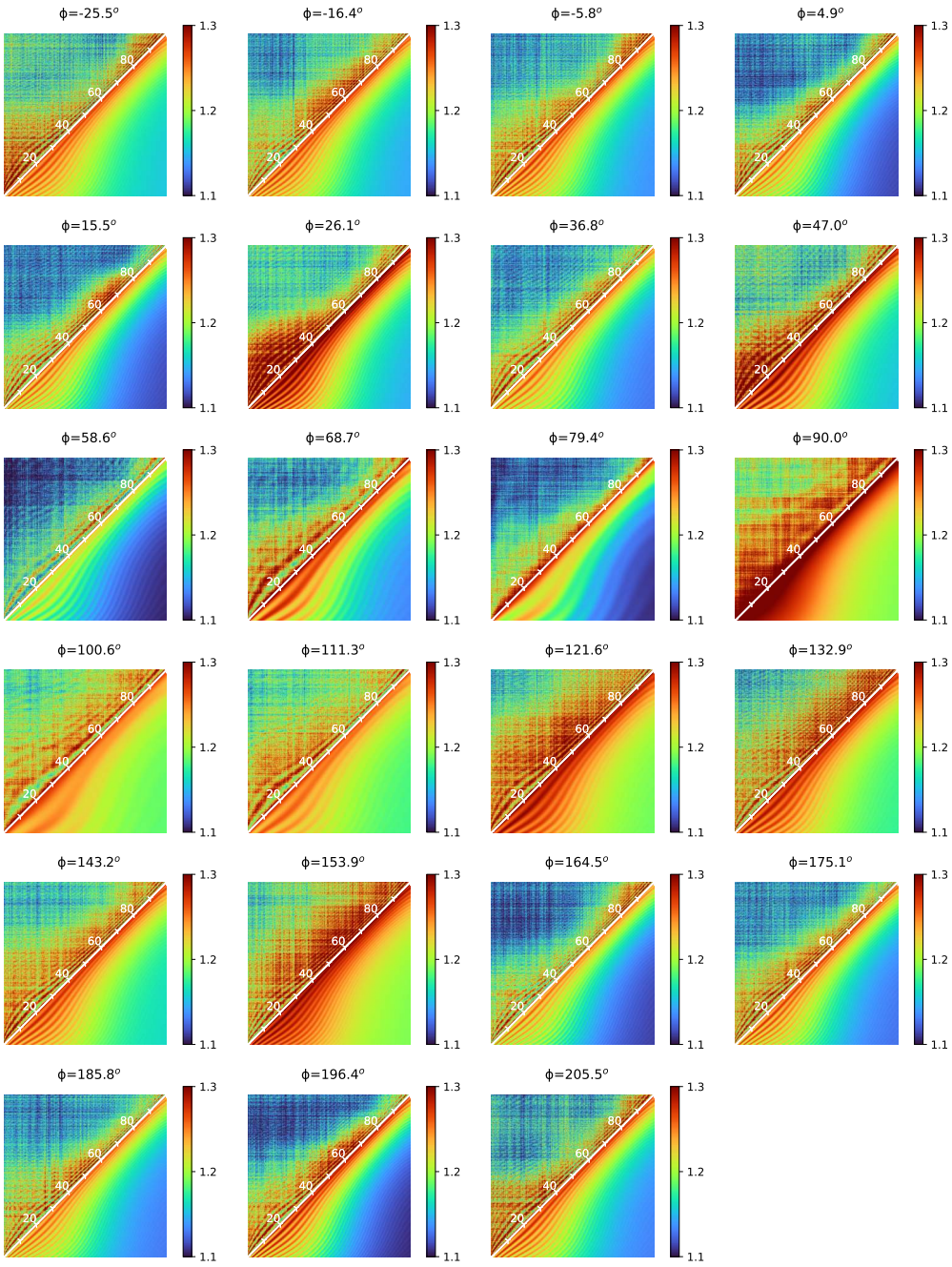

Figure 4.20: $c_2\left(\vec{q}, t_1, t_2\right)$ **functions for SiO_x-Cys in a 100 mM $NaNO_3$ solution under a stress of 110 Pa, shown for all directions.** Experimental results are displayed in the upper corners of each panel, with the corresponding fitting results in the lower corners.

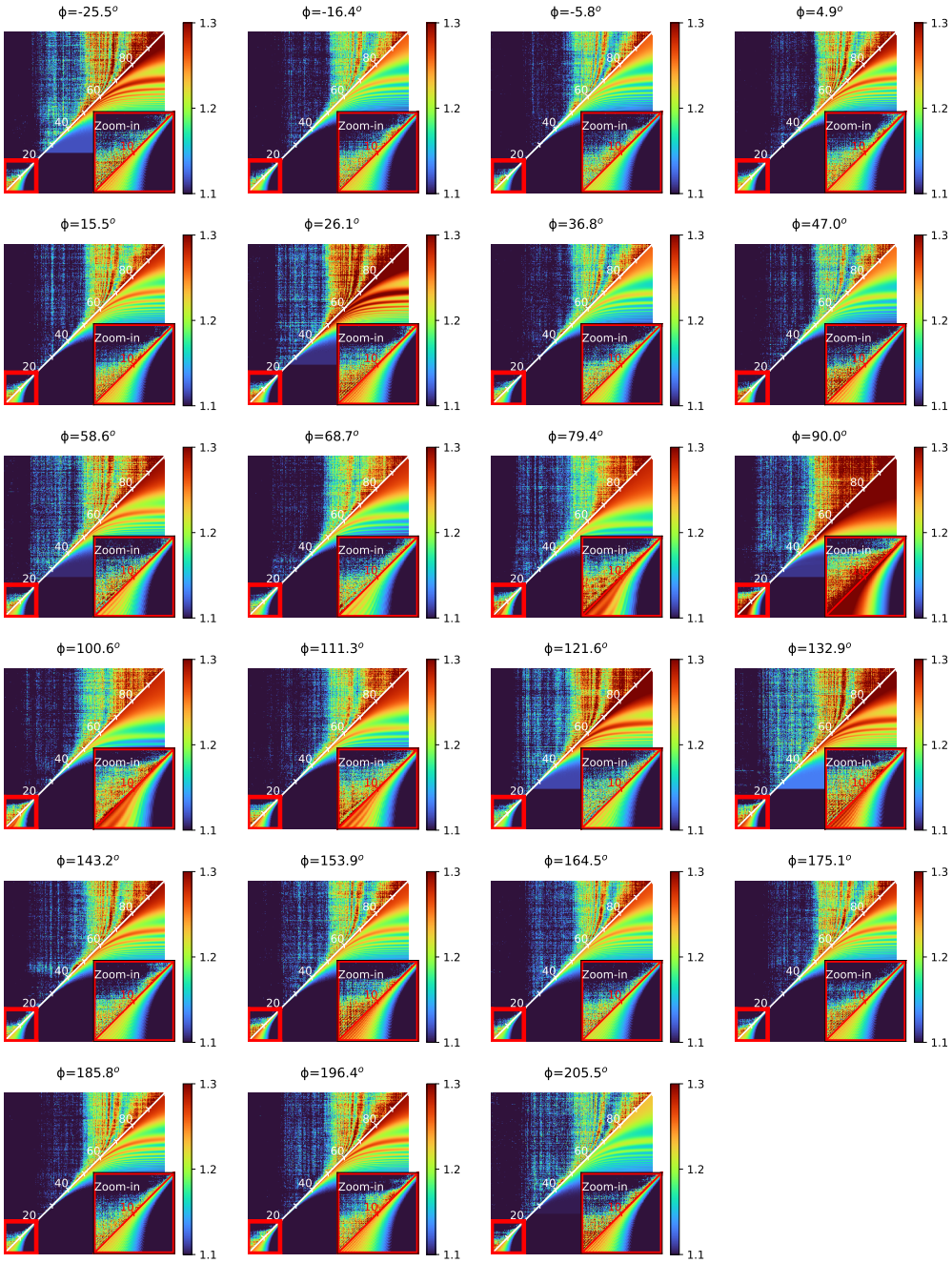

Figure 4.21: $c_2\left(\vec{q}, t_1, t_2\right)$ **functions for SiO_x-Cys in a 100 mM $NaNO_3$ solution under a stress of 120 Pa, shown for all directions.** Experimental results are displayed in the upper corners of each panel, with the corresponding fitting results in the lower corners.

4.4.8 Resolidification

In this experiment, we also investigated the yielding behavior of another salted colloidal suspension, SiO_x-Nac (negatively charged), in 10 mM magnesium nitrate ($Mg(NO_3)_2$) and 70 mM $NaNO_3$ during a creep test using Rheo-SAXS-XPCS. The ionic conditions were carefully controlled to match the ionic strength used for SiO_x-Cys. Under these conditions, $Mg(NO_3)_2$ induces both a screening and crosslinking effect, enhancing attractive interactions between the colloidal surfaces. This attraction results in complex rheological behaviors, including delayed yielding and resolidification, which are similar to those observed for SiO_x-Cys. These findings suggest that such rheological phenomena are common across charged colloidal systems.

At the microscopic level, resolidification occurs when the system transitions from net bond loss to bond formation. Upon cessation of flow, these bonds rapidly decrease as the force chains lock in place. However, as energy storage saturates and applied stress resumes, particle mobility is restored, leading to a reversal in bond dynamics. This process results in cycles of delayed yielding and resolidification, as demonstrated by the oscillatory shear observed in the flow rate, shown in Fig. 4.2.

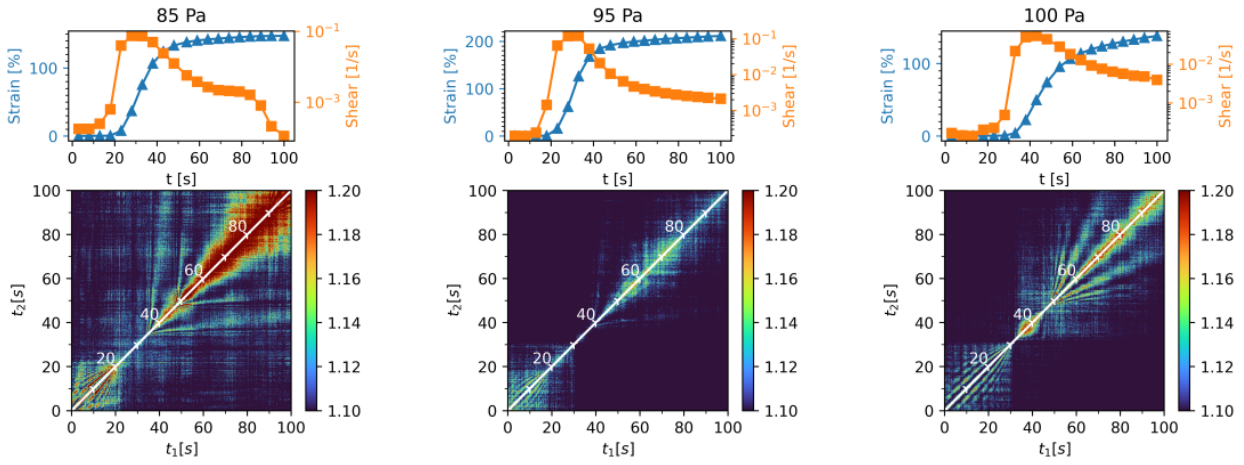

(a) (b) (c)

Figure 4.22: **Rheo-SAXS-XPCS results for SiO_x-Nac during creep tests at applied stresses of 85, 95, and 100 Pa.** Resolidification is observed in all trials, demonstrating that this rheological phenomenon is common in charged colloidal systems.

4.4.9 Delayed Yielding After Resolidification

In addition to studying neutral (SiO_x-Cys) and negatively charged (SiO_x-Nac) colloidal suspensions, we also examined a positively charged colloidal suspension, SiO_x-CME. This suspension exhibits higher viscosity, likely due to interactions between the positively charged molecules and the negatively charged surface of SiO_x. Despite the increased viscosity, complex rheological phenomena were observed during yielding in its salted suspension (10 mM sodium nitrate ($NaSO_4$) and 70 mM $NaNO_3$).

In the creep test with Rheo-SAXS-XPCS, we observed a second instance of delayed yielding following resolidification. This twice-delayed yielding aligns with the microscale picture of junctions between shear bands. After resolidification, the rebuilt junctions are unable to sustain the applied stress, resulting in the breakdown of these junctions and the subsequent delayed yielding.

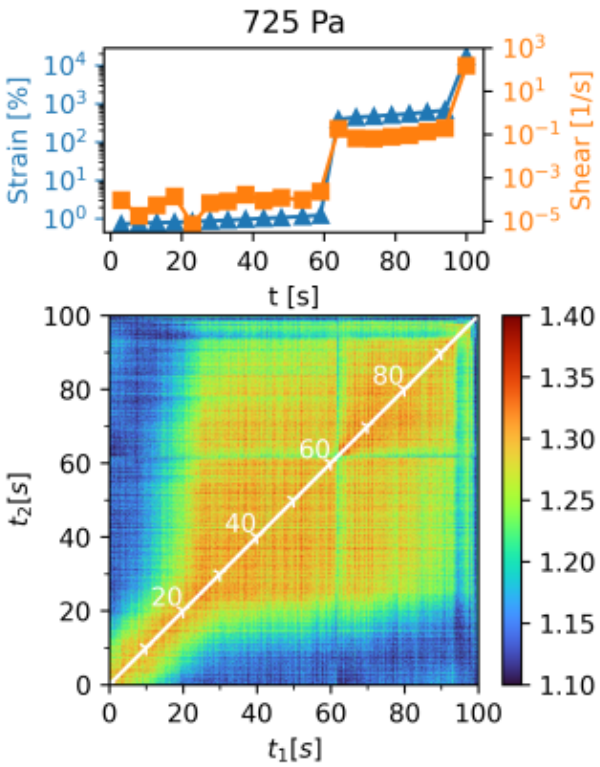

Figure 4.23: **Rheo-SAXS-XPCS results for SiO_x-CME in a creep test at 725 Pa, showing two instances of delayed yielding following resolidification.**

4.4.10 Supplementary Simulation Movies

The following movies visualize the simulated dynamics of colloidal suspensions under shear, illustrating the impact of interparticle interactions on the yielding process and shear band formation. Each simulation highlights key features of the system's response to applied stress, ranging from homogeneous flow in repulsive systems to complex rheological phenomena such as shear banding, delayed yielding, and resolidification in attractive systems. Particles are color-coded based on their shear rate to enhance visualization of flow characteristics. Detailed descriptions of each movie are provided below.

Movie S1. Shear band formation in an attractive suspension. The gray surface represents void regions initially distributed uniformly. As deformation progresses, a concentrated shear band layer emerges, driven by attractive interactions that squeeze voids out of the

interface, forming low-density regions. These regions are mechanically weaker, leading to strain localization.

Movie S2. Yielding process of a repulsive suspension with repulsive interactions under a stress of 0.1. Particles are color-coded by their shear rate. Due to the repulsive potential, the shear rate remains homogeneously distributed, exhibiting a linear profile across the gap, characteristic of laminar flow.

Movie S3. Yielding process of an attractive suspension with attractive interactions under a stress of 1.3. Particles are color-coded by their shear rate. The attractive potential induces shear banding, where distinct bands exhibit different flow velocities. During yielding, the junction between the shear bands becomes critical, as delayed yielding and resolidification are governed by the breaking and reforming of this junction.

CHAPTER 5

EXPLORING NON-GAUSSIAN DYNAMICS DURING YIELDING OF CHARGED COLLOIDAL SUSPENSIONS

5.1 Introduction

Gaussian dynamics refer to the motion of particles in systems where force fluctuations are truly random, and the system evolves as a Markovian process with no memory of the past states. In such systems, the probability distribution functions (PDFs) of particle positions and velocities are well-formulated by a Gaussian, enabling straightforward analytical treatment and modeling [82, 83, 287]. Such dynamics typically arise in idealized systems where particle interactions are negligible or occur over short timescales, making Gaussian approximation highly effective. The simplicity and generality of Gaussian dynamics have made them fundamental across various disciplines, including statistical mechanics, materials science, and fluid dynamics, where they provide accurate description of numerous natural and engineered processes. For example, in the design of novel materials [288, 14], drug delivery systems [289, 290], and energy storage technologies [291, 292], models of Gaussian dynamics offer a robust framework for characterizing particle behavior, facilitating predictive insights and systematic optimization of system performance.

In many real-world systems, Gaussian approximations break down due to complex interparticle interactions, long-range correlations, and memory-dependent fluctuations. These systems exhibit non-Gaussian dynamics, where fluctuations depend on the system's history or the particle states, invalidating the assumption of a lack of memory in the system, where applicable. Such behaviors are widespread across complex systems, ranging from soft matter to biological environments. For example, in concentrated suspensions, particles experience transient confinement by their neighbors, leading to cage dynamics that evolve over time that depend on the local environment [293, 294]. Similarly, in entangled polymer systems, repta-

tion describes the motion of polymer chains constrained by surrounding chains, resulting in intricate, non-Markovian behavior [295, 296]. Beyond structural constraints in specific systems, even a system that is consistent with the picture of Gaussian dynamics can transition to non-Gaussian dynamics due to its dynamic history, with transient responses to external forces or collective particle behaviors driving this crossover. Such non-Gaussian phenomena highlight the complexity of real-world systems, where memory-dependent fluctuations play a crucial role in shaping their dynamics.

In Chapter 4, significant non-Gaussian dynamics is observed during the yielding of an attractive colloidal suspension (Fig. 4.3H). Without a proper approach, the dynamics must be approximated as Gaussian, limiting comparisons with experimental results to a purely qualitative level using the transport coefficient ($J(t)$). While this may suffice for qualitative analysis, such oversimplification can potentially obscure key physical insights into yielding, especially when deviations from Gaussian statistics are fundamental to the dynamics. More broadly, non-Gaussian dynamics are often misinterpreted within traditional analysis frameworks, hindering a comprehensive understanding of their physical significance. Addressing these challenges requires a refined theoretical framework capable of fully capturing non-Gaussian fluctuations.

To address this gap, we extend our previously introduced transport coefficient approach, originally developed for characterizing Gaussian dynamics in XPCS [260], to incorporate non-Gaussian dynamics. This extension leads to $c_2(\vec{q}, t_1, t_2)$ estimates that align more closely with the simulated results. However, it is found that, beyond non-Gaussian dynamics, the cooperative motion of particles must also be considered. While the particle dynamics during yielding remain incompletely understood, the non-Gaussian dynamics approach inspired by this comparison is successfully applied to two common and simpler non-Gaussian dynamic processes: anomalous diffusion induced by memory kernels in the Generalized Langevin Equation and hopping dynamics from an arrested particle cage. By comparing the dynamic

parameters extracted from the proposed analysis with those from simulations, this chapter validates the accuracy and versatility of the approach in analyzing simple dynamic systems with non-Gaussian characteristics. Despite the complexity of non-Gaussian dynamics, the method provides reliable physical insights into the underlying processes.

5.2 Complex Dynamics during Yielding

Concentrated suspensions of such particles exhibit significantly more complex dynamics, often displaying various forms of non-Gaussian behavior. The application of an external drive, such as shear in Rheo-XPCS experiment, further complicates these dynamics by coupling intrinsic particle motion with hydrodynamic interactions and internal stress relaxation, leading to rich and crucial dynamics that governs the property and transient behaviors. However, due to limitations in the existing analytical approaches, these non−Gaussian characteristics are often overlooked, resulting in an approximation as Gaussian dynamics (e.g., see Section 4.2.2). While such simplifications can be convenient, they neglect the critical dynamical features essential for accurately describing the system. In the following section, we analyze the limitations of the Gaussian approximation in describing non-Gaussian dynamics, highlighting its distortion on data interpretation. We then present an improved framework that integrates non-Gaussian dynamics and Co-Dyn, providing a more accurate and comprehensive description of the system.

To make such a demonstration, we simulate a system with an attractive DLVO potential under constant stress deformation (see details in Section 4.3.2). Our results reveal significant dynamical heterogeneity, including variations in both the flow velocity and transport dynamics, manifesting as shear banding (Fig. 4.3). The PDF, obtained by directly averaging particle positions, further confirms substantial deviations from a Gaussian distribution, with pronounced power−law tails indicating the presence of strong non−Gaussian dynamics (Fig. 5.9). The estimation of the NGP demonstrates that changes in non−Gaussian dy-

namics serve as a key indicator during the yielding process. These findings underscore the necessity of incorporating non−Gaussian effects to accurately capture the complexity of the system's dynamics.

In the conventional transport coefficient approach presented in Chapter 3, $c_2(\vec{q}, t_1, t_2)$ at $q = 7$, which approximately corresponds to the particle's unit size $\left(r = \frac{2\pi}{q} \approx 1\right)$ in real space, is computed under the assumption of Gaussian dynamics, incorporating only the MSD and $J(t)$ (Eq. 2.47). However, as shown in Fig. 5.1B, this assumption leads to a significant deviation from the directly computed $c_2(\vec{q}, t_1, t_2)$ obtained via simulations using Eq. 2.14. This discrepancy underscores the necessity of incorporating higher-order statistical features of the displacement distribution. To address this limitation, we employ a Fourier transformation of the probability density function (PDF) to obtain the intermediate scattering function $S(q, t)$ (Eq. 2.12), which better captures non-Gaussian effects. Incorporating this refined $S(q, t)$ into the calculation of $c_2(\vec{q}, t_1, t_2)$ using Eq. 2.13 (Fig. 5.1D) results in an improved agreement with simulations, demonstrating the importance of explicitly accounting for non-Gaussian statistics.

Further comparison between the simulation results and the model analysis reveals a discrepancy at high τ values, where blocks of higher correlation appear and disappear abruptly. To refine the model, it is essential to incorporate the effects of cooperatively rearranging regions (CRR)$^-$localized zones within a material where particles or structural elements undergo correlated motion. This behavior is evident in the spatial distribution of non-affine displacement in Fig. 4.3G, where particle transport dynamics exhibit spatial correlations: particles within the shear band move slowly due to confinement by a densified cage, while those at the band's surface move freely across the void. In particular, CRR is expected to emerge within the densified shear band, where particles experience a glass-like environment and confinement of the surrounding cage.

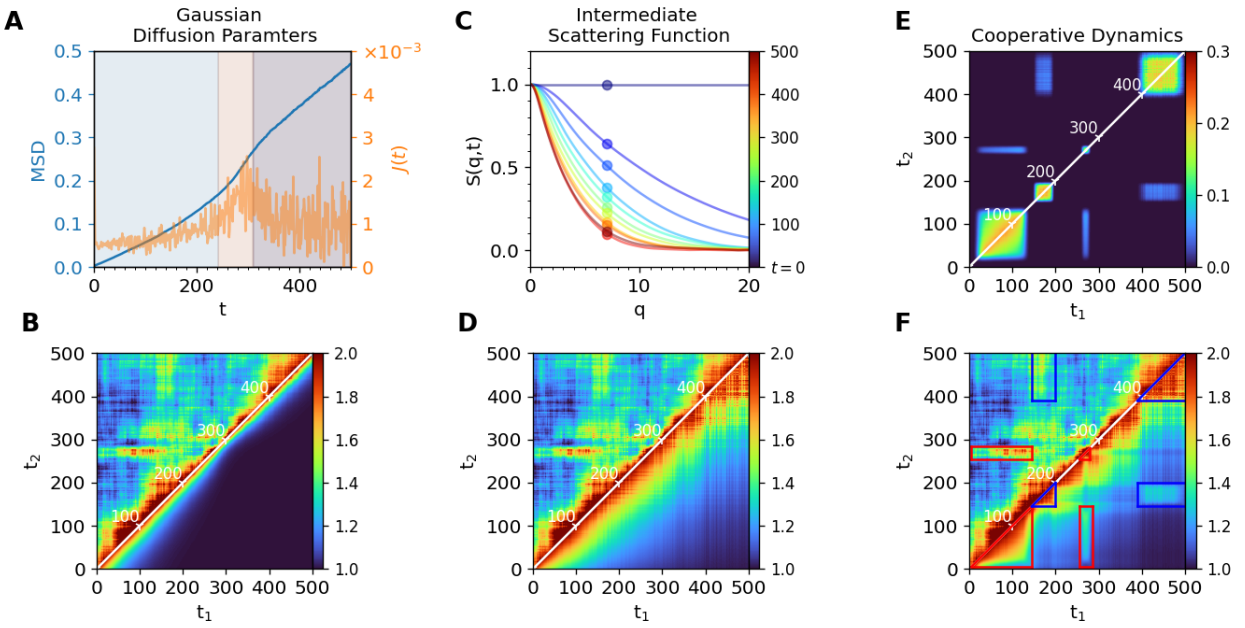

Figure 5.1: **Illustration of Non-Gaussian Dynamics in the Yielding Process and Their Impact on $c_2(\vec{q}, t_1, t_2)$ Observed in XPCS A)** The MSD and $J(t)$ during the three yielding phases—pre-yield, delayed yield, and resolidification (indicated by background colors) are computed using Eq. 2.42 from the PDF shown in Fig. 5.9. **B)** The $c_2(\vec{q}, t_1, t_2)$ (lower triangle) is calculated under the assumption of Gaussian dynamics, using MSD and $J(t)$ in Eq. 2.47. The resulting $c_2(\vec{q}, t_1, t_2)$ significantly deviates from the $c_2(\vec{q}, t_1, t_2)$ obtained directly from simulations using Eq. 2.14, highlighting the breakdown of Gaussian assumption. **C)** To account for non-Gaussian effects, the intermediate scattering function $S(q, t)$ is computed by Fourier transforming the PDF using Eq. 2.12. **D)** The $c_2(\vec{q}, t_1, t_2)$ is then computed from Eq. 2.13 using the refined $S(q, t)$ at $q = 7$ (solid dots at **C)**). This approach improves agreement with simulations by capturing non-Gaussian dynamics. **E)** Incorporating cooperative dynamics due to CRR further refines the $c_2(\vec{q}, t_1, t_2)$ prediction. **F)** Qualitative analysis suggests that two distinct phases of CRR (blue and red box at **E)**) contribute to correlations at high τ values. With both non-Gaussian dynamics and cooperative rearrangements included, the computed $c_2(\vec{q}, t_1, t_2)$ closely matches the simulation results.

In the original Gaussian dynamics model, these CRR were neglected since correlations for $m \neq n$ do not contribute to Eq. 2.5. This assumption was reasonable due to the limited coherence of the incident beam, which caused correlations attributed to CRR to be obscured by noise, leading to a low signal-to-noise ratio. However, this limitation becomes more pronounced when simulating the dynamics of attractive colloidal suspensions, where the incident

beam is assumed to be perfectly coherent. To better capture the behavior of $c_2(\vec{q}, t_1, t_2)$, we include the contribution of CRR in the model via Eq. 2.99. Here, CRR is represented as two additional "shear bands" (blue and red blocks in Fig. 5.1E), supplementing the static and flowing bands in shear banding. For simplicity, we assume that both $J(t)$ and v for CRR are zero, and the change in $c_2(\vec{q}, t_1, t_2)$ (Fig. 5.1E) depends solely on its fraction $f(t)$. This corresponds to a physical picture in which cooperative motion starts and stops abruptly, with CRR appearing and disappearing during the yielding process. By incorporating these collective effects, the refined model produces a $c_2(\vec{q}, t_1, t_2)$ that qualitatively matches the simulation results (Fig. 5.1F). Additionally, CRR contributes to $c_2(\vec{q}, t_1, t_2)$ in other directions as well (Fig. 5.10). However, due to dominant heterodyne effects induced by flow, its impact is less pronounced compared to $c_2(\vec{q}, t_1, t_2)$ observed in the vorticity direction.

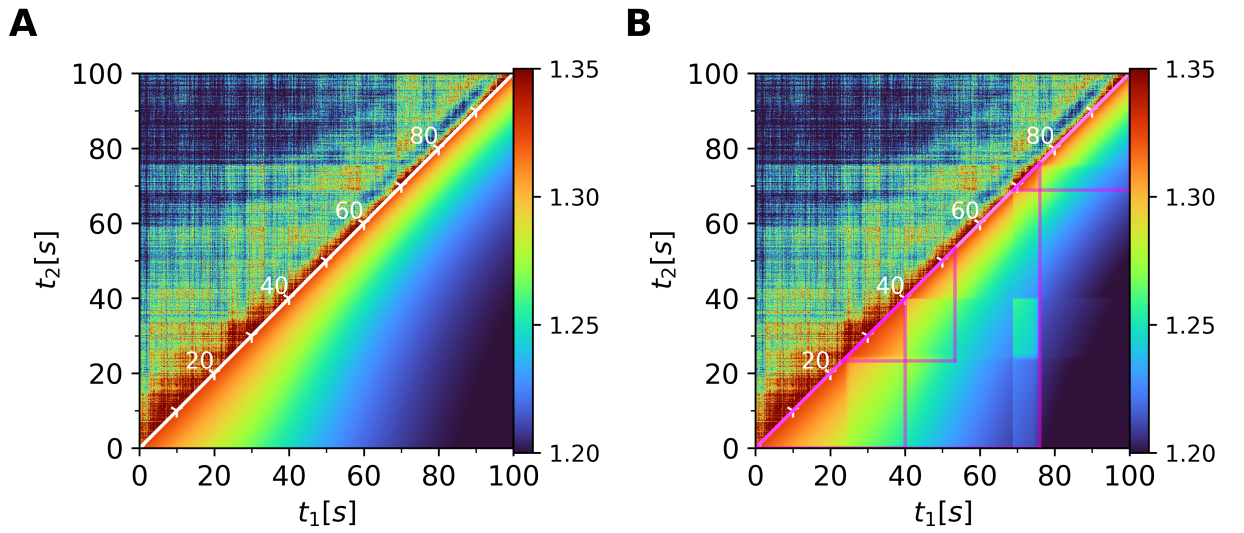

Figure 5.2: **Illustration of incorporating cooperative dynamics into the analysis model improves fitting results and describes the experimental $c_2(\vec{q}, t_1, t_2)$ with higher fidelity. (A)** The $c_2(\vec{q}, t_1, t_2)$ obtained from the experiment (upper triangles) and the fitting results based on the simple transport coefficient approach. Small features in the $c_2(\vec{q}, t_1, t_2)$, such as blocks of $c_2(\vec{q}, t_1, t_2)$ that suddenly appear and disappear, are observed. However, the smooth variations predicted by the simple model fail to capture these transient features. **(B)** By incorporating Co-Dyn, the model provides a better description of the data. It reveals that these correlation blocks originate from a series of Co-Dyn events within CRR (highlighted by magenta squares).

Compared to the simulation, the experimental results exhibit similar behavior, confirming the trends observed in Fig. 5.1. Specifically, in the vorticity direction, as shown in Fig. 4.20 for an attractive colloidal suspension under 110 Pa (See Section 4.3.1), the $c_2(\vec{q}, t_1, t_2)$ obtained from the experiment (upper triangles) is compared with the fitting results from the simple transport coefficient approach. While the model captures the overall trend, it fails to account for small but distinct features in $c_2(\vec{q}, t_1, t_2)$, such as correlation blocks that appear and disappear abruptly. These transient fluctuations indicate the presence of underlying dynamical heterogeneities that are not fully described by a smooth transport process. By incorporating Co-Dyn, the model provides a significantly improved description of the data. The analysis reveals that these correlation blocks are associated with a series of Co-Dyn events occurring within CRR, as highlighted by magenta squares. This finding underscores the crucial role of cooperative dynamics in shaping the observed correlation patterns, highlighting the need for advanced modeling approaches to fully capture the system's complexity.

These findings suggest that single-particle Gaussian diffusive dynamics, non-Gaussian dynamics, and cooperative dynamics must all be considered to accurately describe the microscopic dynamics underlying XPCS measurements in complicated process, such as in yielding systems. Our model successfully captures these dynamics, providing a unified framework for their interpretation. Systematically incorporating non-Gaussian effects and cooperative motion offers a more robust methodology for analyzing experimental XPCS data, particularly in systems exhibiting complex, heterogeneous dynamics.

5.3 Extended Transport Coefficient Approach for Simple and Homogeneous non-Gaussian Dynamics

Analysis of yielding simulation demonstrates that incorporating non-Gaussian dynamics significantly improves the accuracy of the results (Fig. 5.1B to Fig. 5.1D). This insight mo-

tivates the development of an approach to characterize specific non-Gaussian dynamics in homogeneous systems based on Eq. 2.13 and Eq. 2.12. However, since $S(q,t)$ is not well-defined for all processes, a linear combination of Gaussian functions (Eq. 2.130) can be chosen to simulate the actual complex $S(q,t)$ observed in experiments. As demonstrated in Fig. 5.11, analyzing $c_2\left(\vec{q},t_1,t_2\right)$ under this assumption allows for accurate extraction of $S(q,t)$ at the corresponding $q=7$, highlighting the non-Gaussian nature of yielding dynamics. With this extended approach, key physical parameters describing non-Gaussian behavior can be systematically extracted by examining its impact on $c_2\left(\vec{q},t_1,t_2\right)$.

The theoretical background and mathematical derivation of the expectations and observations of non-Gaussian dynamics are detailed in Section 2.8, with analytical approaches thoroughly explained in Section 2.8.5. To validate the effectiveness of the proposed analytical approach in capturing dynamics and extracting meaningful physical insights from non-Gaussian systems, we analyze two classical examples with classical and well-formulated dynamic equations that are widely applied across different fields: anomalous diffusion and cage dynamics. By appropriately defining the parameter n, we systematically examine each system and discuss its physical relevance in experimental contexts.

5.3.1 Anomalous Diffusion

Anomalous diffusion refers to a type of diffusion that deviates from the classical Brownian motion model, where the MSD of particles does not grow linearly with time (MSD $\propto t$), typically characterized by a power-law dependence (MSD $\propto t^{\alpha}$). Depending on the stretch exponent α, anomalous diffusion can be further characterized as sub-diffusion ($\alpha < 1$) or hyper-diffusion ($\alpha > 1$). Anomalous diffusion is important because it is frequently observed in complex systems, such as crowded environments [297], polymer melt [298], biological tissues [299], and soft matter [300], where the motion of particles is constrained or influenced by factors like spatial heterogeneity, obstacles, or memory effects.

There has been consistent effort devoted to formalizing the PDF of anomalous diffusion, such as generalized Langevin equation (GLE). If the memory kernel ($\mathcal{K}$) has a power-law form, the integral in the GLE resembles a fractional derivative in time and its solution in Fourier−Laplace space is [301]

$$\mathbb{P}\left(q,s\right)=\frac{1}{s+sD\mathcal{K}\left(s\right)q^{2}} \tag{5.1}$$

In the special case of Riemann-Llouville (RL) operator, the $\mathcal{K}(s)$ is defined as

$$\mathcal{K}(s)=s^{-\alpha} \tag{5.2}$$

In such case, the PDF is written as [302]

$$\mathbb{P}\left(x,t\right)=\frac{1}{2|x|}\mathbf{H}_{1,1}^{1,0}\left[\begin{array}{c|c}\frac{|x|}{\sqrt{Dt^{\alpha}}} & \begin{array}{c}\left(1,\frac{\alpha}{2}\right)\\ \left(1,1\right)\end{array}\end{array}\right] \tag{5.3}$$

where $\mathbf{H}$ stands for the Fox $\mathbf{H}$-function as a hyper-geometic function [303, 304]. The intermediate scattering function is obtained as,

$$S\left(q,t\right)=\mathbf{E}_{\alpha}\left(q^{2}\sqrt{Dt^{\alpha}}\right) \tag{5.4}$$

where $\mathbf{E}$ stands for the Mittag-Leffler function [305].

Having described the PDF and $S(q,t)$ in Eq. 5.4 and Eq. 5.4, the MSD can be shown as,

$$\mathbb{V}[x(t)]=\frac{2Dt^{\alpha}}{\mathbf{\Gamma}\left(1+\alpha\right)} \tag{5.5}$$

where $\mathbf{\Gamma}$ stands for gamma function. The RL model corresponds to the typical case of anomalous diffusion, where $\alpha<1$ represents sub-diffusion and $\alpha\rightarrow 1$ recovers the usual diffusion.

Provided by the reference[306], when $\alpha = \frac{1}{2}$ as the case of sub-diffusion, $S(q,t)$ and MSD is expressed as

$$\begin{aligned} S(q,t) &= \mathbf{E}_{\frac{1}{2}}\left(q^2\sqrt{Dt^{\frac{1}{2}}}\right) = \mathrm{e}^{-Dq^4t}\mathrm{erf}\left(Dq^2\sqrt{t}\right) \\ \mathbb{V}[x(t,\alpha=\frac{1}{2})] &= \frac{2Dt^{\frac{1}{2}}}{\Gamma(1.5)} = \frac{4}{\sqrt{\pi}}Dt^{\frac{1}{2}} \end{aligned} \tag{5.6}$$

Eq. 5.6 is the reference equation for anomalous diffusion with a power-law memory kernel of $\alpha = \frac{1}{2}$. Using this equation, we can generate and analyze the $c_1(\vec{q}, t_1, t_2)$ for anomalous diffusion by Eq. 2.13. By comparing the extracted physical parameters of α and D with the input, we can verify and demonstrate the analysis approach.

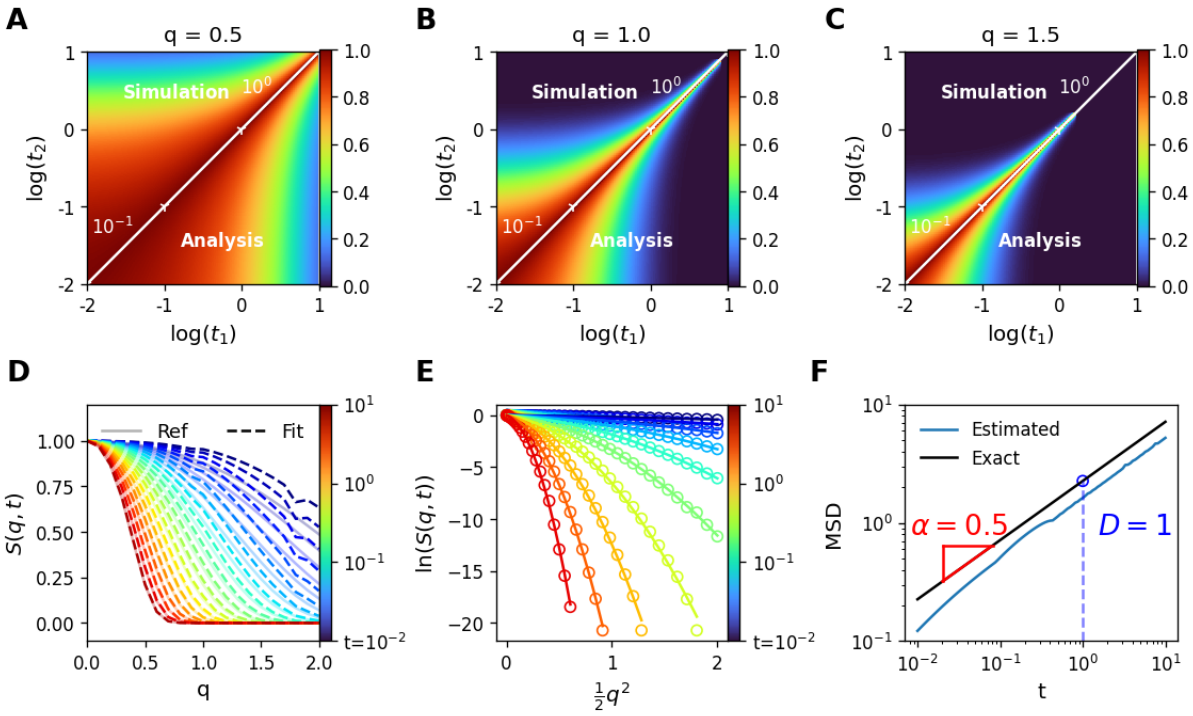

Figure 5.3: **Illustration of the proposed approach for extracting $S(q,t)$ and MSD from the $c_1(\vec{q},t_1,t_2)$ with $\alpha=\frac{1}{2}$ and $D=1$. A)-C)** The $c_1(\vec{q},t_1,t_2)$ is generated from Eq. 5.6 at $q=0.5$ (**A**), 1 (**B**), and 1.5 (**C**), respectively, and is shown in the upper triangle of the $c_1(\vec{q},t_1,t_2)$. These $c_1(\vec{q},t_1,t_2)$ are analyzed using the approach proposed in Section 2.8.5, and the fitting results are plotted in the lower triangle. The consistency between the simulated and fitted $c_1(\vec{q},t_1,t_2)$ demonstrates the capability of the approach to accurately describe complex patterns. **D)** The extracted results from $c_1(\vec{q},t_1,t_2)$ for different q values ranging from 0 to 20 allow us to map $S(q,t)$ over time, indicating the dynamic changes in anomalous diffusion (Fig. 5.3 **D**). The dynamics mapped by the analysis (solid dot line) closely overlap with the reference $S(q,t)$ (faded light background) given in Eq. 5.6. **E)** By performing cumulative fitting of $S(q,t)$ in a log scale corresponding to $\frac{1}{2}q^2$ (solid line), the time-dependent physical parameters that describe the dynamics can be obtained based on Eq. 2.174. **F)** The linear parameters from a cumulant analysis, specifically MSD and $\mathbb{V}[x(t)]$, are obtained with $\alpha=0.53$ and $D=0.72$, closely matching the input values and demonstrating consistency between the analysis results and the input parameters. The observed inconsistencies might be attributed to the fact that the linear combination of Gaussian functions cannot exactly replicate the PDF of anomalous diffusion under the RL operator.

Given the $S(q,t)$ from Eq. 5.6, with Eq. 2.13, the $c_1(\vec{q},t_1,t_2)$ can be computed and shown in Panel **A-C** at Fig. 5.3 with input parameter of $D=1$ and $\alpha=\frac{1}{2}$. To capture the entire dynamics process with fewer points, the $c_1(\vec{q},t_1,t_2)$ has its t_1 and t_2 in log scale,

which is uncommon in comparison to the traditional $c_1(\vec{q}, t_1, t_2)$ in linear scale obtained from XPCS experiment. The consistency between the simulated and fitted $c_1(\vec{q}, t_1, t_2)$ confirms the capability of this approach to capture the underlying complex dynamics. This agreement suggests that the method is robust in describing the correlation decay patterns associated with non−Gaussian processes.

A key aspect of the analysis is the choice of n, which depends on the specific system under study. While a sufficiently large n can accurately fit any PDF, increasing n also raises computational costs. Therefore, an optimal balance must be found by selecting the smallest n that adequately describes the data. A common approach is to plot the fitting residuals as a function of n to determine the most appropriate value. Moreover, in some cases, n carries physical significance. For example, cage dynamics can be well described by $n = 2$, which may indicate the presence of two distinct dynamic processes: particle motion within the cage and escape of particles from the cage (Fig. 5.6).

The extracted results from $c_1(\vec{q}, t_1, t_2)$ for different q values ranging from 0 to 20 allow us to map $S(q,t)$ over time, indicating the dynamic changes in anomalous diffusion (Fig. 5.3 **D**). The dynamics process mapped out by the scatter line are closely overlapping with the reference $S(q,t)$ shown in Eq. 5.6. To better understand the extracted dynamics and distill the information, we perform a cumulative fitting of $c_1(\vec{q}, t_1, t_2)$ in a logarithmic scale corresponding to $\ln(S(q,t))$ (Fig. 5.3 **F**). This allows us to obtain time-dependent physical parameters that characterize the anomalous diffusion, as described by the non-Gaussian expansion in Eq. 2.174. The extracted MSD and variance of displacement, $\mathbb{V}[x(t)]$, from the cumulant analysis exhibit strong agreement with the input parameters as the key parameter of $\alpha = 0.52$ and $D = 0.72$ is obtained, confirming the validity of the approach in quantifying non-Gaussian dynamics (Fig. 5.3 **F**).

However, a slight inconsistency is observed on D, as 0.72 compared to input value of 1, which may be attributed to the limitations of representing the PDF and $S(q,t)$ of anomalous

diffusion using a linear combination of Gaussian functions under the RL operator. This discrepancy highlights the challenges in modeling the non−Gaussian characteristics of the system at short timescales, where deviations from a purely Gaussian approximation becomes significant. Future refinements to the fitting approach, potentially incorporating higher-order corrections or alternative functional forms, could further improve the accuracy in this regime.

5.3.2 Cage Dynamics

Cage dynamics is another common case of non−Gaussian dynamics, referring to the transient confinement of a particle by its surrounding neighbors, a phenomenon commonly observed in dense and glassy systems such as colloidal suspensions [307, 308], supercooled liquids [309, 310], and granular materials [311, 312]. In these systems, a particle undergoes localized vibrations within a "cage" formed by adjacent particles before escaping and engaging in long-range diffusion. This introduces non−Gaussian characteristics to the dynamic process, where the particle exhibits two different types of noise depending on whether it is located inside or outside the cage. Inside the cage, the noise is attributed to collisions with surrounding particles, and the fluctuations of the particle are driven by a noise of amplitude D. If the particle escapes the cage, collisions become more frequent with small solvent molecules, and the diffusion constant changes to D_A. Meanwhile, the intermittent trapping and release process is a hallmark of dynamic heterogeneity and is crucial for understanding the slowing down of dynamics near the glass transition. Studying cage dynamics provides insight into fundamental processes such as structural relaxation, non−Gaussian transport, and the emergence of cooperative motion, making it an essential topic in soft matter physics and materials science.

The cage dynamics has been well-studied in various ways, including theory, simulation

and experiment. The $S(q,t)$ for cage dynamics is provided as [200]:

$$S\left(q,t\right)=\exp\left\{-\frac{\tau_R q\epsilon/\tau_o}{1+\left(q\epsilon\right)^2}\left[\frac{q\epsilon t}{\tau_R}-\arctan\left(q\epsilon f_t\right)\right]\right\}\left[1+\left(q\epsilon f_t\right)^2\right]^{-\frac{\tau_R}{2\tau_o}\frac{(q\epsilon)^2}{1+(q\epsilon)^2}}\mathrm{e}^{-(q\sigma)^2 f_t} \tag{5.7}$$

where f_t is an expression as follow:

$$f_t=1-\mathrm{e}^{-\frac{t}{\tau_R}} \tag{5.8}$$

In Eq. 5.7 and Eq. 5.8, four key parameters define the relevant length and time scales of cage dynamics: τ_o, τ_R, σ, and ϵ. The parameters τ_o and τ_R quantify the mean time between two consecutive hops and the time required for the particle to explore the cage, respectively. The parameter σ represents the typical size of a harmonic cage confining a particle, while ϵ denotes the characteristic hopping length. These parameters are related to the characteristic diffusion rate inside (D) and outside (D_A) the cage as follows:

$$\begin{aligned} D&=\frac{\sigma^2}{\tau_R}\\ D_A&=\frac{\epsilon^2}{\tau_o}\end{aligned} \tag{5.9}$$

The MSD of the cage dynamics can be calculated as

$$\mathbb{V}[x(t)]=2\left(D-D_A\right)\tau_R f_t+2D_A t \tag{5.10}$$

According to Eq. 2.42, by taking the time derivative of MSD, the transport coefficient is obtain as,

$$\begin{aligned} J(t)&=\frac{d}{dt}\left(\mathbb{V}[x(t)]\right)\\ &=2\left(D-D_A\right)f_t+2D_A\\ &=2\left(D-D_A\right)\left(1-\mathrm{e}^{-\frac{t}{\tau_R}}\right)+2D_A\end{aligned} \tag{5.11}$$

with characteristic that

$$\begin{aligned} J(t=0) &= 2D \\ J(t\to\infty) &= 2D_A \end{aligned} \tag{5.12}$$

As defined in Eq. 2.176, the non-Gaussian parameter $\alpha_2(t)$ quantifies the extent of non-Gaussian characteristics in the particle trajectory, providing insight into the structural rearrangements of the system. It is calculated as follows:

$$\alpha_2(t) = \frac{\tau_o}{3\tau_R} \frac{2\mathrm{e}^{-\frac{3t}{\tau_R}} - 9\mathrm{e}^{-\frac{2t}{\tau_R}} + 18\mathrm{e}^{-\frac{t}{\tau_R}} - 11 + \frac{6t}{\tau_R}}{\left[\left(D/D_A - 1\right) f_t + t/\tau_R\right]^2} \tag{5.13}$$

Using equations Eq. 5.7, we can generate and analyze the $c_1\left(\vec{q}, t_1, t_2\right)$ for cage dynamics. After inputting the length and time scales τ_o, τ_R, σ, and ϵ, the MSD ($\mathbb{V}[x(t)]$) and NGP $\alpha_2(t)$ can be extracted either by direct computation using Eq. 5.10 and Eq. 5.13 or by analyzing $c_1\left(\vec{q}, t_1, t_2\right)$. Comparing the extracted MSD and NGP allows for verification and validation of the analysis approach.

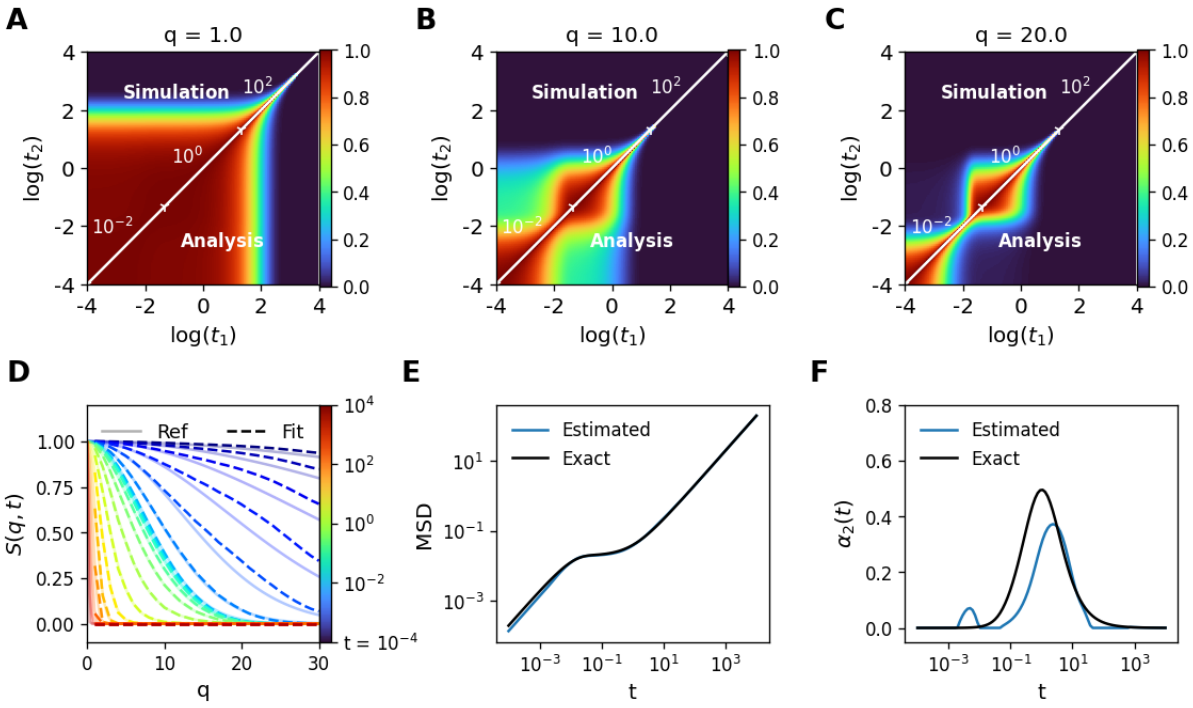

Figure 5.4: **Illustration of the proposed approach for extracting $S(q,t)$ and MSD from the $c_1(\vec{q},t_1,t_2)$ of cage dynamics. A)-C)** The $c_1(\vec{q},t_1,t_2)$ is generated from Eq. 5.7 at $q = 1$ (**A**), 10 (**B**), and 20 (**C**), respectively, and is shown in the upper triangle of the $c_1(\vec{q},t_1,t_2)$. The input parameters are set as $\epsilon = \sigma = 0.1$, $\tau_o = 1$, and $\tau_R = 1$. The $c_1(\vec{q},t_1,t_2)$ are analyzed using the approach proposed in Section 2.8.5, and the fitting results are plotted in the lower triangle. The consistency between the simulated and fitted $c_1(\vec{q},t_1,t_2)$ demonstrates the capability of the approach to accurately describe complex patterns. **D)** The extracted results from $c_1(\vec{q},t_1,t_2)$ for different q values ranging from 0 to 30 allow us to map $S(q,t)$ over time, indicating the dynamic changes in the cage effect (**D**). The dynamics mapped by the analysis (solid scatter dots) closely overlap with the reference $S(q,t)$ (faded light background) given in Eq. 5.7. The mapped-out $S(q,t)$ can be fitted with Eq. 2.174, allowing the extraction of (**E)**) MSD and (**F)**) NGP, which are then compared with the reference values. The close agreement between the extracted MSD and NGP with the input values demonstrates consistency between the analysis and the reference. The observed inconsistencies might be attributed to the fact that the linear combination of Gaussian functions cannot exactly replicate the PDF of cage dynamics.

The proposed approach for extracting $S(q,t)$ and MSD from the $c_1(\vec{q},t_1,t_2)$ of cage dynamics is illustrated in Fig. 5.4. To validate this method, $c_1(\vec{q},t_1,t_2)$ were generated from Eq. 5.7 at different scattering vectors, specifically $q = 1$, 10, and 20 (Fig. 5.4 **A)-C)**). The upper triangle of each $c_1(\vec{q},t_1,t_2)$ presents the generated data, while the lower triangle

contains the corresponding fitting results obtained using the approach outlined in this study. The agreement between the simulated and fitted $c_1(\vec{q}, t_1, t_2)$ demonstrates the effectiveness of the proposed method in capturing complex dynamic patterns, particularly in systems exhibiting cage effects.

By analyzing $c_1(\vec{q}, t_1, t_2)$ over a broad range of q values from 0 to 30, the extracted dynamic structure factor $S(q,t)$ can be mapped as a function of time, revealing the underlying dynamical changes induced by the cage effect. Fig. 5.4 **D** shows a comparison between the extracted $S(q,t)$ (solid dot line) and the reference values obtained from Eq. 5.7 (faded line in background), demonstrating a high level of consistency. This indicates that the proposed methodology successfully reconstructs the temporal evolution of the dynamics and effectively captures the transient confinement of particles within cages. More fundamental physical parameters governing the dynamic process, including ϵ, σ, τ_o, and τ_R, can be extracted by further analyzing $J_{obs}(t)$, obtained by taking the time derivative of MSD. As expected, consistency is observed, as shown in Fig. 5.5.

Further analysis involves fitting the extracted $S(q,t)$ using the first two terms in Eq. 2.174, from which characteristic parameters of the dynamic process such as MSD and NGP are obtained. Fig. 5.4 **E** and **F** illustrate the extracted MSD and NGP over time, respectively, compared with their reference values from Eq. 5.10 and Eq. 5.13. The close agreement between the extracted parameters and the expected values further supports the robustness of this approach. However, minor inconsistencies are observed, particularly at early times, which may be attributed to the limitations of using a linear combination of Gaussian functions to approximate the PDF of cage dynamics. Despite these discrepancies, the overall agreement validates the method as a powerful tool for investigating non-Gaussian dynamics in confined systems.

5.4 Discussion and Conclusion

In this work, we have demonstrated that the yielding of attractive colloidal suspensions is a complex process that requires considering Gaussian, non-Gaussian, and cooperative dynamics for a comprehensive description. While a complete characterization remains challenging, particularly for $c_2\left(\vec{q}, t_1, t_2\right)$ originating from CRR due to cooperative dynamics and structural rearrangements, incorporating non-Gaussian dynamics significantly improves the agreement between model predictions and simulation results.

Building on this idea, we develop an effective approach for characterizing non-Gaussian dynamics observed in XPCS. By modeling the PDF as a linear combination of Gaussian functions, we extract the intermediate scattering function $S(q,t)$ from the analysis of $c_1\left(\vec{q}, t_1, t_2\right)$ or $c_2\left(\vec{q}, t_1, t_2\right)$. Fitting $S(q,t)$ enables the determination of key dynamic parameters, including the mean square displacement (MSD), the non-Gaussian parameter $\alpha_2(t)$, and the transport coefficient $J(t)$, providing a comprehensive description of non-Gaussian dynamics.

To validate this approach, we examined two simple and representative cases: anomalous diffusion and cage dynamics. In well-defined scenarios, the extracted parameters—including MSD, NGP, diffusion constant D, and hopping interval τ_R—show strong agreement with input values, confirming the method's reliability. However, deviations suggest that Gaussian approximations may not fully capture the complexity of the PDF, necessitating higher-order corrections.

Beyond soft matter and colloidal physics, our methodology has broader implications for studying complex systems. Future directions include applying this analysis to real physical systems and experimentally validating the approach across diverse material classes, such as polymeric and active matter systems, to extend its applicability. Additionally, given the multidimensional nature of $c_2\left(\vec{q}, t_1, t_2\right)$, spanning two temporal dimensions (t_1, t_2) and one spatial dimension (q), integrating machine learning techniques could enhance data interpretation and improve quantitative analysis and parameter extraction from the vast amount of

dynamic information.

Overall, this work advances XPCS as a powerful tool for probing mesoscale dynamics by refining analytical techniques for non-Gaussian dynamics. With the significant increase in flux and coherence following the recent beamline upgrade, XPCS can now capture more subtle and detailed dynamics. The synergy between the upgraded beamline and the newly developed analytical approach enables a more precise way to model non-Gaussian dynamics, including intermittent trapping, heterogeneous motion, and dynamic transitions, further establishing XPCS as a crucial technique for studying complex and disordered systems.

5.5 Appendix

5.5.1 Comparison of Extracted and Reference $J(t)$ for Cage Dynamics Analyzed in Fig. 5.4

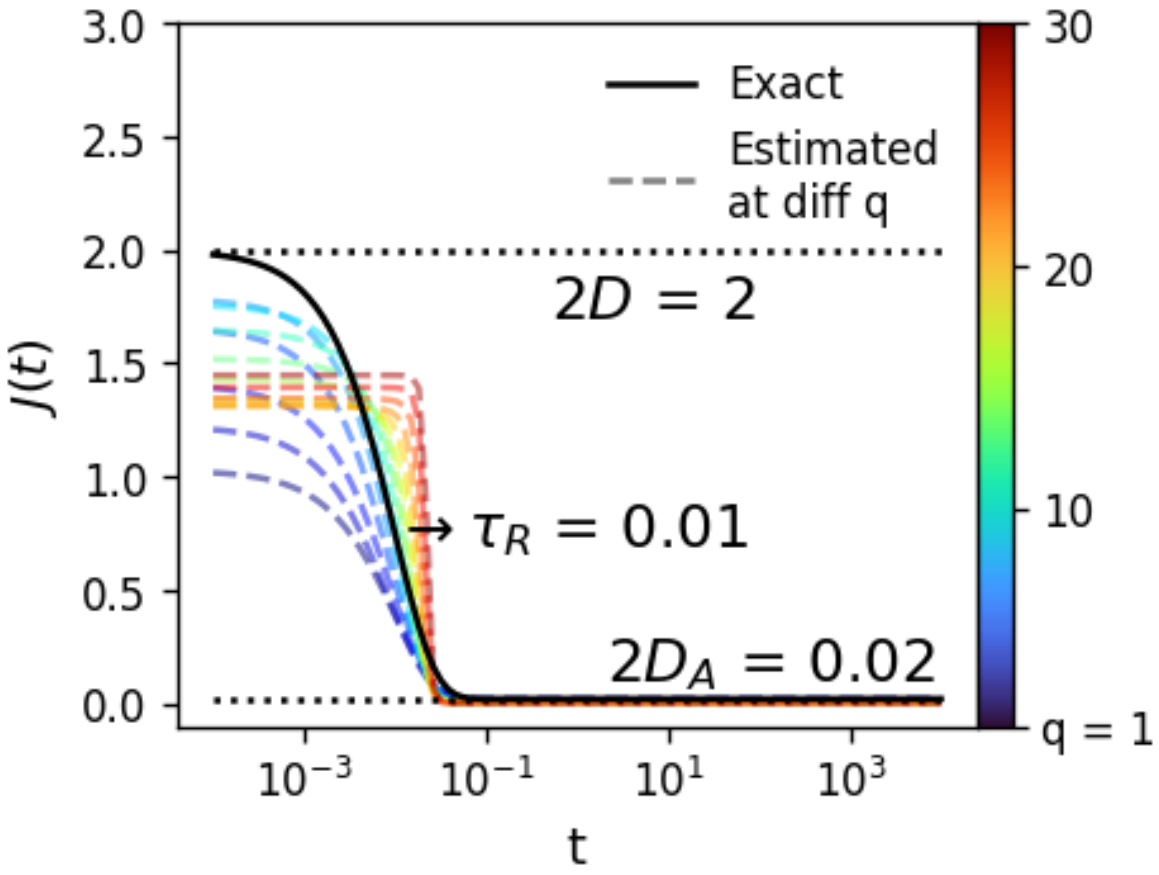

Figure 5.5: **The transport coefficient $J(t)$ from reference and analysis results of cage dynamics.** The $J(t)(t)$ with $\epsilon = \sigma = 0.1$, $\tau_o = 1$, and $\tau_R = 1$, corresponding to the cage dynamics process in Fig. 5.4, is shown as the solid black line based on Eq. 5.11. The input parameters of the dynamics can be extracted and visualized as the transition from the ceiling of $2D$ to the baseline $2D_A$, where τ_R represents the time at which the maximum decay rate is observed. The colored dashed line represents $J_{obs}(t)$, calculated using Eq. 2.148 with parameters obtained from the proposed analysis approach. The behavior of $J_{obs}(t)$ exhibits an initial increase ($1 \leq q \leq 11$) followed by a decrease ($q \geq 11$) as q increases, consistent with the observation that cage dynamics is only prominent within a specific range of q values.

5.5.2 *The residual of fitting from analysis in Fig. 5.4 and Fig. 5.3*

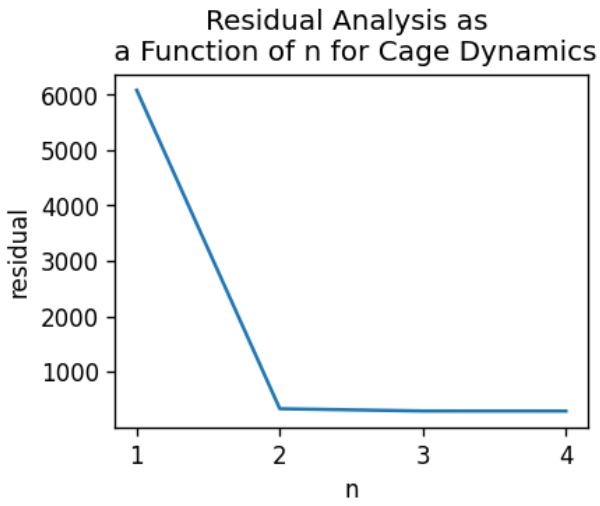

Figure 5.6: **Residual Analysis as a Function of n in the Gaussian Model for Cage Dynamics.** The residual decreases significantly when two Gaussian functions are used in the fitting of $c_1(\vec{q}, t_1, t_2)$ for cage dynamics. However, for $n = 3$ and $n = 4$, the reduction in residual is negligible, indicating that the data is already well-fitted or that additional components may lead to overfitting. Therefore, $n = 2$ is selected as the optimal choice for analyzing the $c_1(\vec{q}, t_1, t_2)$ of cage dynamics. This result is also physically reasonable, as it reflects the presence of two distinct dynamic processes in cage dynamics: diffusion inside and outside the cage.

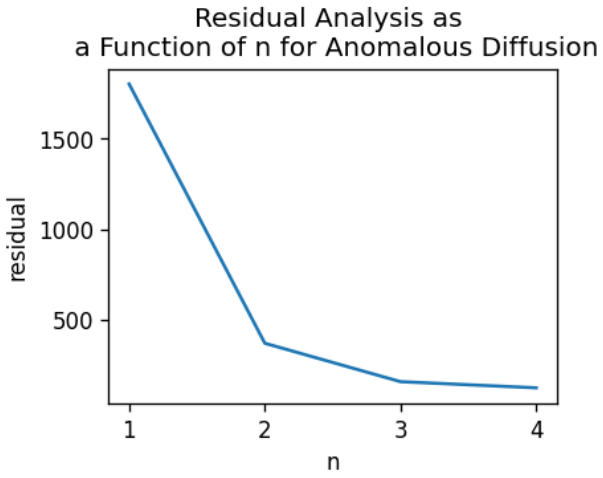

Figure 5.7: **Residual Analysis as a Function of n in the Gaussian Model for Anomalous Diffusion.** The residual decreases significantly when more functions are used in the fitting of $c_1(\vec{q}, t_1, t_2)$ for anomalous diffusion. However, for $n = 4$, the reduction in residual is negligible, indicating that the data is already well-fitted or that additional components may lead to overfitting. Therefore, $n = 3$ is selected as the optimal choice for analyzing the $c_1(\vec{q}, t_1, t_2)$ of anomalous diffusion.

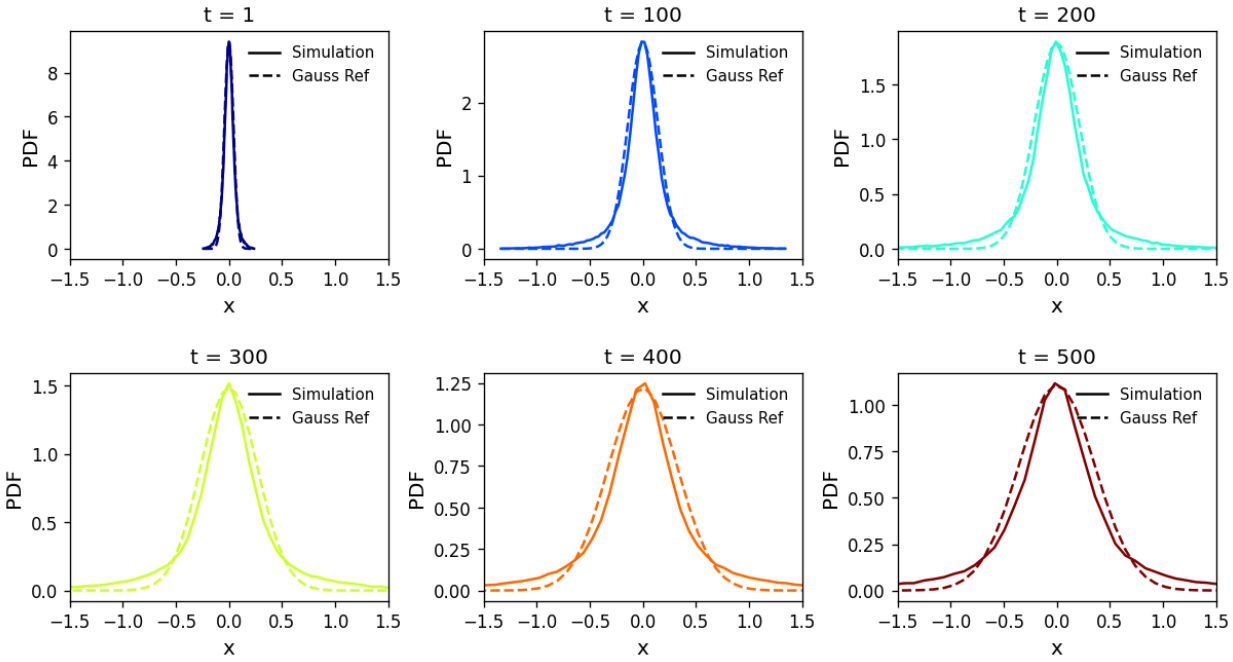

Figure 5.8: **Demonstration of how particle dynamics in the shear banding simulation from Section 4.2.3 deviate from Gaussian behavior over time.** The dashed lines represent the PDF computed at times $t = 1, 100, 200, 300, 400$, and 500 by analyzing particle coordinates within the simulation boxes. The solid lines correspond to Gaussian fits. The growing discrepancy between the computed PDF and the Gaussian fits illustrates the progressive emergence of non-Gaussian dynamics over time.

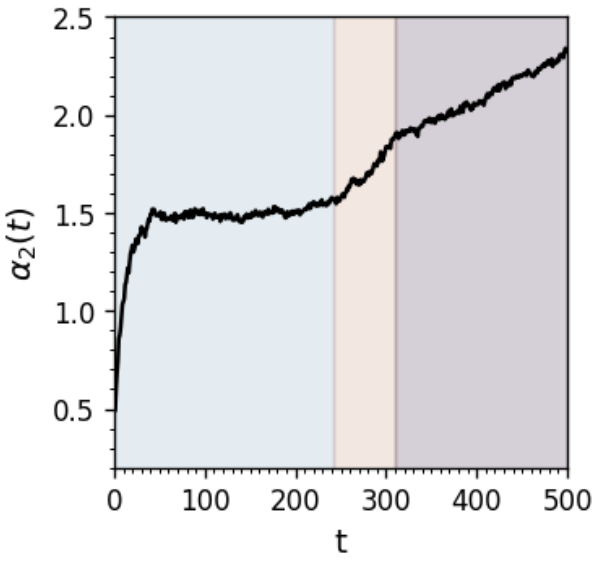

Figure 5.9: **Evolution of the Non-Gaussian Parameter ($\alpha_2(t)$) During the Yielding Process** The $\alpha_2(t)$ is estimated by Eq. 2.176. The background color represents the three phases of the yielding process: pre-yield, delayed yield, and resolidification. The variation of $\alpha_2(t)$ highlights the changes in non-Gaussian characteristics, indicating their contribution to the yielding behavior.

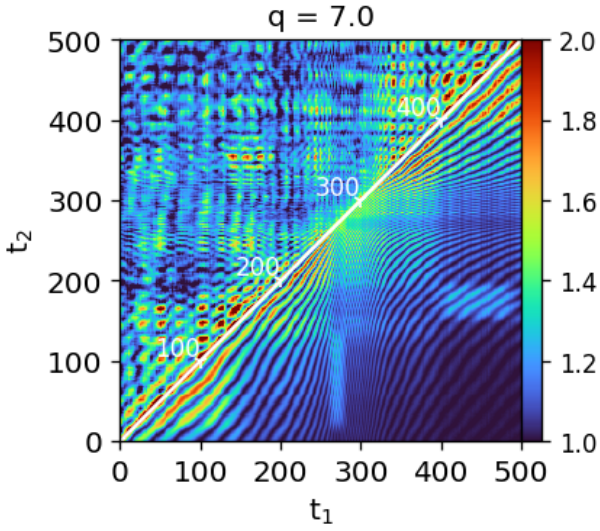

Figure 5.10: $c_2\left(\vec{q}, t_1, t_2\right)$ **in the flow direction with consideration of non-Gaussian dynamics and CRR.** The contribution of CRR to $c_2\left(\vec{q}, t_1, t_2\right)$ is present in the flow direction, as indicated by the bright spots in $c_2\left(\vec{q}, t_1, t_2\right)$. However, due to the dominant heterodyne effects induced by flow, which manifest as an oscillation pattern, this contribution is less pronounced compared to the $c_2\left(\vec{q}, t_1, t_2\right)$ observed in the vorticity direction.

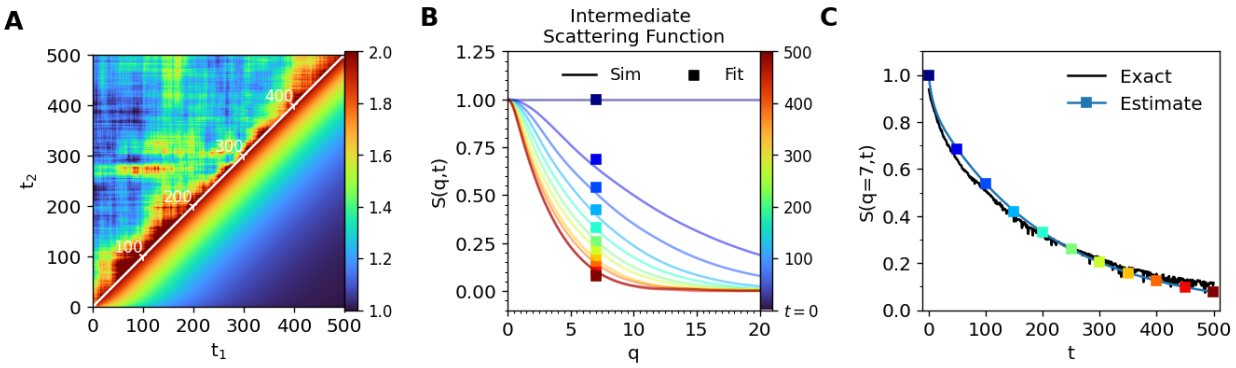

Figure 5.11: **Applying the non-Gaussian approach to extract dynamic information from yielding simulations. (A)** The non-Gaussian approach is applied to the $c_2\left(\vec{q}, t_1, t_2\right)$ from simulations and accurately describes the data. **(B-C)** The intermediate scattering function $S(q,t)$ extracted from the analysis (square dots) closely matches the reference computed directly from PDF of particle coordinates.

CHAPTER 6

OUTLOOK

In this study, we have developed a theoretical framework and analytical approach for extracting dynamical information from XPCS data. This method has been rigorously validated (Chapter 2) and successfully applied to various systems (Chapters 3-5), highlighting its potential as a powerful tool for studying particle dynamics with XPCS. While the approach has proven effective in multiple cases, it remains limited in scope compared to the broad spectrum of dynamic behaviors. It still relies on key assumptions, such as lack of memory in dynamical fluctuations, structural consistency over time, and the absence of spatial correlations in the dynamics. However, our investigation of complex systems reveals that these assumptions do not always hold, particularly in materials undergoing intricate dynamical processes. In the following section, we will provide an outlook on some cases of complex dynamics where each of these assumptions break down and discuss potential strategies for addressing these challenges in future research.

6.1 Memory Effect

In Chapter 5, we briefly discuss how memory effects give rise to non-Gaussian dynamics, leading to anomalous diffusion and complicating the observation of $c_2\left(\vec{q}, t_1, t_2\right)$ in XPCS. Memory effect is a fundamental phenomenon observed across various natural and industrial systems, making its accurate characterization crucial [313, 314].

In Section 5.3, we examine a simple case using the RL model and cage dynamics. In the future work using XPCS, more complex dynamic models can be developed depending on the specific conditions of the system, expanding the analytical capabilities of XPCS for interpreting experimental results. For instance, more intricate scenarios involve distinct memory kernels, such as those in Caputo-Fabrizio (CF) and Atangana-Baleanu (AB), which

follow the formulations presented in [306]:

$$\mathcal{K}_{CP}(s) = \frac{b}{s + \frac{a}{1-a}} \tag{6.1}$$

$$\mathcal{K}_{AB}(s) = \frac{bs^{\alpha-1}}{s^{\alpha} + \frac{\alpha}{1-\alpha}} \tag{6.2}$$

where b is a normalization constant. The $S(q,t)$ for these two models are also included in the reference [306], which, although more complicated, still has a well-defined equation that covers the full range of q and t. It is straightforward to conduct a similar analysis as in Section 5.3.1 for these two dynamic processes. However, since CF and AB are more complex than RL, these models introduce additional complexities due to their long-range temporal correlations, requiring a more refined theoretical framework for accurate analysis.

Beyond theoretical validation, experimental investigations of systems exhibiting similar anomalous diffusion behaviors could provide valuable insights and further test the applicability of the proposed approach. Many active colloidal systems, such as those driven by magnetic fields [151] or light [315], not only exhibit significant anomalous diffusion but also allow for tunable behavior depending on the external field. These systems serve as ideal examples, as the magnitude of the non-Gaussian characteristics can be controlled. Studying such systems would not only help validate memory effect models but also deepen our understanding of the underlying dynamics of these systems.

6.2 Cooperative Dynamics (Co-Dyn)

The current approach focuses solely on capturing the diffusive dynamics ($n = m$) while neglecting correlated motion between individual particles ($n \neq m$). Specifically, in Eq. 2.5, this assumption implies that particle dynamics are ergodic, mutually uncorrelated, and that the system remains homogeneous. Within this framework, the entire dynamical behavior can

be described using a single probability density function (PDF), whether Gaussian, as discussed in Chapter 3, or Non-Gaussian, as explored in Chapter 4. However, this assumption is often overly simplified. In many real-world systems, such as gels [316, 317], fibril networks [318], or crystalline lattices [319, 320], particle dynamics are inherently interconnected with either polymer chains or attractive bonds. In these systems, scatterers interact, whereby the motion of one particle influences the motion of others, giving rise to correlated, cooperative dynamics (Co-Dyn). These Co-Dyn play a crucial role in phenomena such as yielding [321], avalanches [322, 323], and relaxation [324]. Such Co-Dyn often occur locally and heterogeneously within distinct regions, referred to as cooperative rearrangement regions (CRR) [40]. Since our current approach does not account for these localized correlations, it fails to capture the full picture of the system's complex dynamics. To accurately extract dynamic information of CRR, future studies must incorporate Co-Dyn into the analytical framework.

The incorporation of Co-Dyn is theoretically straightforward. As demonstrated in Section 4.2.3, using Eq. 2.99 to account for Co-Dyn leads to a qualitative improvement in the agreement between the computed $c_2\left(\vec{q}, t_1, t_2\right)$ and simulation results. To further isolate and analyze the correlation specifically attributed to Co-Dyn, we can adopt the following equation:

$$\begin{aligned} c_1(\vec{q}, t_1, t_2) &= c_{1,diff-Dyn} + c_{1,Co-Dyn} \\ &= \mathbb{E}\left[\sum_{n=1}^{N} \mathrm{e}^{i\vec{q}\cdot(\vec{r}_n(t_2)-\vec{r}_n(t_1))}\right] + \mathbb{E}\left[\sum_{n=1}^{N}\sum_{m\neq n}^{N} \mathrm{e}^{i\vec{q}\cdot(\vec{r}_n(t_2)-\vec{r}_m(t_1))}\right] \end{aligned} \tag{6.3}$$

Recall that correlations attributed to self-diffusive dynamics ($c_{2,\text{diff-Dyn}}$) can be obtained by fitting $c_2\left(\vec{q}, t_1, t_2\right)$ using our proposed transport approach. The residual from this fitting captures the contributions from Co-Dyn.

$$c_{2,Co-Dyn} = c_2(\vec{q}, t_1, t_2) - c_{2,diff-Dyn} \tag{6.4}$$

By analyzing the difference between $c_2(\vec{q}, t_1, t_2)$ and $c_{2,\text{diff-Dyn}}$, we can quantitatively extract valuable dynamic information associated with the cooperative motion of particles and gain deeper insight into the physical significance of the relaxation process. As demonstrated in Fig. 6.1, $c_2(\vec{q}, t_1, t_2)$ captures the relaxation dynamics of a colloidal suspension following the removal of stress. In addition to the self-dynamic correlations observed along the diagonal of $c_2(\vec{q}, t_1, t_2)$, distinct correlation blocks emerge in the high τ regions (corners of $c_2(\vec{q}, t_1, t_2)$), indicating contributions from Co-Dyn. This contribution, denoted as $c_{2,\text{Co-Dyn}}$ (Fig. 6.1B, upper triangle), is extracted from $c_2(\vec{q}, t_1, t_2)$ using Eq. 6.4, enabling the identification and characterization of CRR. By analyzing these Co-Dyn features, we quantified the fraction of CRR using Eq. 2.99 and tracked its evolution over time in Fig. 6.1C. Two prominent CRR events were observed, one occurring between 0–200 s and another between 400–600 s, each appearing, fluctuating, and eventually dissipating over time. This observation reinforces previous findings that the relaxation of colloidal suspensions is inherently heterogeneous, as consistently reported in prior studies [2]. Incorporating CRR into the model significantly improves the accuracy of $c_2(\vec{q}, t_1, t_2)$ predictions, leading to better agreement with experimental observations.

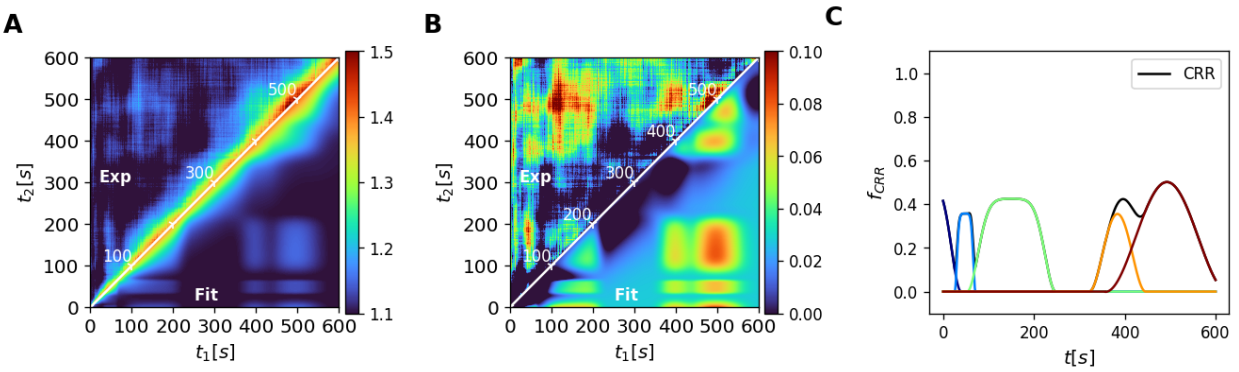

Figure 6.1: **Illustration of Co-Dyn Extraction and Analysis**: **A)** The $c_2\left(\vec{q}, t_1, t_2\right)$ for a relaxation process in colloidal suspension is measured from the Rheo-XPCS experiment. **B)** The $c_2\left(\vec{q}, t_1, t_2\right)$ attributed to Co-Dyn, $c_{2,\text{Co-Dyn}}$, is extracted using Eq. 6.4. **C)** The change in CRR is obtained by analyzing $c_{2,\text{Co-Dyn}}$ from **B)**. The colors of the lines indicate the individual CRR during the dynamics process, and the black line indicates the sum of all CRR over time. The fitting results of $c_{2,\text{Co-Dyn}}$ and $c_2\left(\vec{q}, t_1, t_2\right)$ are shown in the lower triangle in both **A)** and **B)**. Close agreement between $c_2\left(\vec{q}, t_1, t_2\right)$ obtained from the experiment and the analysis indicates a good model and successful analysis.

6.3 Structure-Dynamics Coupling

Beyond the assumption of uncorrelated dynamics over time, another key assumption in our analysis is structure consistency and monodispersity over time for every individual particle in the system, as specified in 6.3. The form factor is assumed to remain constant over time, resulting in the cancellation of structural contributions to $c_2\left(\vec{q}, t_1, t_2\right)$. This simplification was intentional, as our experiments and simulations used hard-core spherical particles to isolate and study fundamental aspects of particle dynamics. Consequently, changes in the correlation function were entirely attributed to dynamics.

While our approach provides valuable insights, it neglects the significant structural transformations that often accompany dynamic changes. Compared to the relatively simplified studies presented in Chapter 3 and 4, many soft matter systems—such as micellar [325, 326], electrolyte complexes [327, 328], and biomacromolecules [329, 121], exhibit intricate structural responses to deformation, including stretching, bending, and localized rearrangements.

Moreover, in scenarios where scatterers deviate from perfect spherical symmetry, translational and rotational diffusion become coupled, complicating the extraction of individual diffusion rates [330]. Existing theoretical frameworks and analytical methodologies are inadequate for addressing these complexities, often failing to accurately capture dynamic processes while ignoring time-dependent variations to the form factor.

Understanding the interplay between structure and dynamics is essential for unraveling the mechanisms underlying time-dependent phenomena, as these factors are often intricately linked and mutually influential. For example, in biological systems such as protein folding [331] and cells under biological flow [332], the simultaneous evolution of structure and dynamics is central to their function. Similarly, in industrial processes, ranging from polymer production [296] to catalytic reactions [333], the coupling between structural transformations and dynamic changes directly impact product quality, performance, and efficiency. This limitation underscores the need for more comprehensive methodologies that integrate structural and dynamic analyses. By combining these perspectives, researchers can achieve a more holistic understanding of complex systems, thereby advancing both fundamental science and industrial applications. Future efforts to address the coupling between structure and dynamics will enhance our ability to study soft matter systems and broaden their practical applications across diverse scientific and technological fields.

6.3.1 Generalized Space-Time Correlation Function

To address these issues, significant efforts have been undertaken in recent years to bridge this gap. Various approaches have been developed to extract structural information from scattering profiles. Notably, the angular X-rays cross-correlation analysis (AXCCA) technique has emerged as a powerful method for quantitatively measuring the angular anisotropy of X-ray diffraction patterns, providing valuable insights into subtle structural changes within the system under investigation [334, 335]. Using a coherent and focused X-ray beam, AX-

CCA enables the characterization of local orientational order and symmetry in colloidal crystals, sparking intensive studies of various dense systems. Alternatively, speckle tracking technique has been developed to analyze deformation-induced patterns, allowing for the investigation of small strain or flow effects [336]. While these approaches represent promising advancements, they remain limited in their scope and applicability, underscoring the need for further development and refinement to achieve a comprehensive understanding of coupled structure-dynamics phenomena.

Looking ahead, future research should aim to bridge this gap by developing experimental and analytical techniques capable of simultaneously resolving both structural and dynamic changes. This will require extending current approaches to regimes comparable to, or even beyond, the capabilities of AXCCA. A promising direction involves advancing to the most fundamental and generalized form of the correlation function between the fields at two different space-time points in the plane parallel light beam: generalized space-time correlation, $c_2\left(\vec{q_1}, \vec{q_2}, t_1, t_2\right)$, defined as [193]:

$$c_2\left(\vec{q_1}, \vec{q_2}, t_1, t_2\right) = \frac{\mathbb{E}\left[I(\vec{q_1}, t_1) I(\vec{q_2}, t_2)\right]}{\mathbb{E}\left[I(\vec{q_1}, t_1)\right] \mathbb{E}\left[I(\vec{q_2}, t_2)\right]} \tag{6.5}$$

This function captures both temporal and spatial correlations simultaneously, producing data with four dimensions: t_1, t_2, $\vec{q_1}$, and $\vec{q_2}$. $c_2\left(\vec{q_1}, \vec{q_2}, t_1, t_2\right)$ is consistent with the time-space correlation function proposed by van Hove in previous studies, known as the van Hove function, but is expressed in reciprocal space via Fourier transform to facilitate its use in scattering experiments [337]. However, due to limitations in experimental tools and the inherent complexity of $c_2\left(\vec{q_1}, \vec{q_2}, t_1, t_2\right)$, it is often computed in a reduced form, where both spatial and temporal dimensions are averaged over delay times and probing lengths. In such cases, $c_2\left(\vec{q_1}, \vec{q_2}, t_1, t_2\right)$ reduces to the commonly observed form, providing limited information about the system's structure or dynamics and often offering less insight than two-point correlation techniques such as XPCS and AXCCA. As a result, its application has

remained largely restricted to a small scope of theoretical studies and simulation [338, 339].

6.4 Future Challenges in Analysis

In the previous section, we highlighted the significance of memory effect, Co-Dyn and structural evolution in physical systems, respectively. We also presented the appropriate modeling and analytical approaches for extracting these complex dynamic and structural correlations from XPCS experiments. Understanding the interplay between Co-Dyn and structure-dynamics coupling is essential for advancing the interpretation of experimental data and refining theoretical frameworks. While the general direction and methodologies for future developments in Co-Dyn and Space-Time Correlation have been outlined, several fundamental challenges persist. In this section, we detail these challenges and explore potential strategies to overcome them, paving the way for more precise and comprehensive studies of complex dynamics in XPCS.

6.4.1 Theoretical Challenges in Modeling Memory Effects

Understanding memory effects in dynamical systems remains a fundamental challenge due to the difficulty in establishing a proper theoretical framework that accurately captures these effects. The non-Gaussian dynamics deviating from classical Brownian motion has been modeled using a variety of theoretical approaches, including:

- Fractional Brownian motion [340]
- Generalized diffusion equations [341]
- Continuous time random walk (CTRW) models [342, 343]
- Generalized Langevin equations (GLE) [344]
- Generalized thermostatistics [345]

- Generalized master equations [346]

Among these, only CTRW models and GLE offer a consistent framework that explicitly incorporate memory effects while preserving the expected form of the PDF for particle displacements. These approaches inherently account for temporal correlations and non-Markovian behavior, making them particularly suitable for describing systems where dynamics are influenced by past states. Their effectiveness has been tentatively demonstrated and discussed in Sections 2.2 and 5.3.1, respectively.

Despite the theoretical foundation of these models, integrating them into the analysis of memory effects observed in XPCS experiments remains a significant challenge. A primary limitation is the absence of a well-defined and consistent PDF that directly links these theoretical frameworks to experimental observables. Without such a formulation, extracting and interpreting memory-dependent dynamics from XPCS data in a physically meaningful manner is challenging. Addressing this gap requires the development of advanced analytical tools that can systematically connect theoretical descriptions of memory effects with experimental measurements, facilitating a more precise characterization of complex dynamical systems. A reasonable starting point for this effort could involve modeling relatively simple processes, such as Lévy flight processes [347]. Additionally, mathematical tools like stochastic matrices could provide valuable insights for refining these models and enhancing their applicability to experimental data.

6.4.2 Limitations in the Description of CRR

In Co-Dyn studies, the primary challenge lies not in the relatively straightforward analytical models but in the precise characterization of CRR. One of the most significant difficulties in studying CRR is the inherently low signal-to-noise ratio, which causes the signal to blend with noise from beam intensity fluctuations and coherence variations, complicating the analysis. While ongoing synchrotron upgrades are expected to enhance signal quality by

improving beam coherence and stability, these advancements alone are insufficient. A reliable methodology is still required to effectively isolate CRR signals from background noise. Addressing this issue demands the development of advanced noise-filtering techniques and improved statistical frameworks to enhance signal extraction. Overcoming these limitations is crucial for achieving more accurate and robust analyses of CRR within Co-Dyn studies.

Another major challenge stems from the inherently unpredictable nature of CRR dynamics. These fluctuations can occur sporadically, with varying durations, phases, and magnitudes, making their characterization particularly difficult. Unlike conventional dynamic processes, there is no universally defined function that accurately describes the occurrence of CRR, posing a fundamental challenge in the analysis. One approach to addressing this issue involves representing CRR as a discrete numerical array, but this requires substantial computational resources. Alternatively, CRR can be approximated using model functions such as a stretched Gaussian, as illustrated in Fig. 6.1C. However, this simplification carries the risk of distorting or omitting critical dynamic features, potentially compromising the accuracy of the analysis. Developing more sophisticated modeling approaches that balance computational efficiency with fidelity to experimental data remains an open challenge in Co-Dyn research.

6.4.3 Understanding the Space-Time Correlation

With advancements in synchrotron radiation sources and X-ray instrumentation, the analysis of the two-point correlation function $c_2\left(\vec{q_1}, \vec{q_2}, t_1, t_2\right)$ has become a significant challenge. The interpretation of this function relies on the continuous development of the theoretical framework in XPCS and AXCCA. Building upon the model developed in this thesis, future approaches could start with the simplest case, such as considering the polydispersity of spherical particle sizes within the dynamic system, and progressively incorporating more structural elements, such as time-evolving changes in particle size, to model the colloidal

nucleation process. Ultimately, it is anticipated that the fusion of these approaches will form the theoretical framework for the analysis of $c_2\left(\vec{q_1}, \vec{q_2}, t_1, t_2\right)$.

Furthermore, the excessive volume of data generated during these analyses presents another significant challenge. For example, a dataset consisting of 100 points can yield up to 100^4 raw $c_2\left(\vec{q_1}, \vec{q_2}, t_1, t_2\right)$ values. Although spatial and temporal symmetries can reduce this number, the reduction is still not substantial. Temporal symmetry alone can halve the number of effective $c_2\left(\vec{q_1}, \vec{q_2}, t_1, t_2\right)$ points, yet an enormous amount of data remains. In typical measurements, tens of thousands of X-ray profiles are collected, generating datasets of immense scale. These large datasets pose significant challenges for visualization and presentation, let alone for understanding and extracting meaningful dynamic and structural information. The sheer complexity and scale of the $c_2\left(\vec{q_1}, \vec{q_2}, t_1, t_2\right)$ data emphasize the urgent need for innovative computational and analytical techniques to effectively manage, interpret, and extract valuable insights from such data.

6.5 Possible Solution: AI-Driven Method

Recent years have witnessed remarkable advancements in artificial intelligence (AI) and ML, revolutionizing data analysis across scientific disciplines. In particular, deep learning techniques such as convolutional neural networks (CNNs), recurrent neural networks (RNNs), and transformer-based architectures have demonstrated exceptional capabilities in recognizing complex patterns, extracting features, and making predictions from high-dimensional datasets [348, 349, 350]. These AI-driven methods have been successfully applied to fields ranging from X-ray imaging [351, 352] to materials science [353, 354], enabling automated interpretation of intricate experimental data. For XPCS studies, these computational tools provide a promising approach to overcoming traditional analysis limitations, such as noise suppression, feature extraction, and high-dimensional data interpretation [355, 356, 357].

Our ongoing work demonstrates the potential of AI-driven methods in addressing the

challenges of Co-Dyn and Space-Time Correlation analysis. With the upgraded beamline, we have observed correlations attributed to Co-Dyn in response to external perturbations, which were previously indistinguishable from noise in earlier studies. By integrating our theoretical models with machine learning (ML) techniques, we quantitatively verified and effectively analyzed regions exhibiting Co-Dyn, extracting key parameters such as the timing, lifetime, and intensity of these events [40, 358]. As illustrated in Fig. 6.2, convolutional neural networks (CNN) were applied to extract crucial insights from XPCS scattering patterns, enabling the automated characterization of both the temporal and spatial features of Co-Dyn. These AI-driven methods provide a robust framework for interpreting CRR within established statistical and stochastic theories, enhancing both descriptive accuracy and predictive capability.

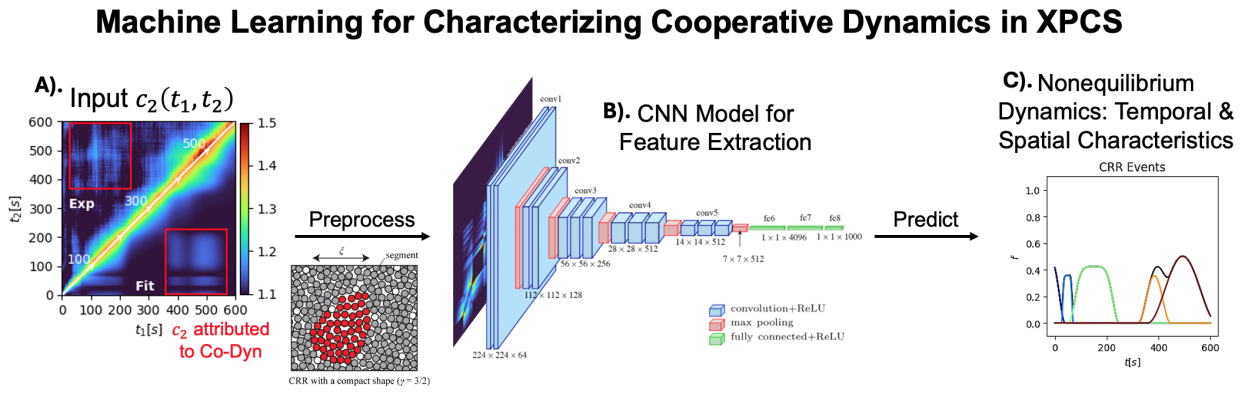

Figure 6.2: **Illustration of how Co-Dyn is automatically identified and quantified using ML. A)** The experimental $c_2(\vec{q}, t_1, t_2)$ (upper triangle) is used as input and fitted (lower triangle) to **B)** a CNN model for feature extraction, leading to **C)** the identification and prediction of CRR events [4] and their evolution over time.

Beyond traditional statistical analysis, AI algorithms have introduced innovative ways to handle the vast and intricate datasets generated by modern X-ray experiments. Techniques such as neural networks, unsupervised clustering, and feature extraction algorithms have proven effective in deciphering the spatial and temporal correlations inherent in $c_2(\vec{q_1}, \vec{q_2}, t_1, t_2)$ datasets [359, 360]. By leveraging AI, researchers can identify underlying patterns, reduce

data dimensionality, and extract meaningful structural and dynamic information from complex scattering datasets. Furthermore, AI-driven approaches enable automation in data processing workflows, significantly reducing computational overhead and making real-time analysis feasible [361, 355]. These advancements underscore the transformative role of AI in tackling the complexities of Co-Dyn and Space-Time Correlation analysis, opening new avenues for precise and high-throughput XPCS studies.

6.6 Closing Remarks

In summary, as my thesis has explored the intricate dynamic changes observed in XPCS through advanced scattering techniques and theoretical frameworks, it has addressed several existing challenges, such as the limitations of structural analysis and the vast complexity of multi-dimensional datasets, and has laid the groundwork for more comprehensive and accurate studies of coupled structure-dynamics phenomena using $c_2\left(\vec{q_1}, \vec{q_2}, t_1, t_2\right)$. Looking ahead, the integration of cutting-edge experimental techniques, such as those enabled by synchrotron radiation, with innovative computational approaches, including artificial intelligence, offers unprecedented opportunities to deepen our understanding of these systems. As the field continues to advance, these developments will not only enhance our ability to probe fundamental processes of dynamics but also pave the way for transformative applications in materials science, biology, and beyond. Inspired by Hilbert's timeless words, *"Wir müssen wissen. Wir werden wissen"* (We must know. We will know), this thesis represents a step forward in unraveling the complexity of dynamic systems and serves as a call to action for future research to continue bridging the gaps between theory, experiment, and data interpretation.

REFERENCES

[1] Oleg G Shpyrko. X-ray photon correlation spectroscopy. Synchrotron Radiation, 21(5):1057–1064, 2014.

[2] Gavin J Donley, Suresh Narayanan, Matthew A Wade, Jun Dong Park, Robert L Leheny, James L Harden, and Simon A Rogers. Investigation of the yielding transition in concentrated colloidal systems via rheo-xpcs. Proceedings of the National Academy of Sciences, 120(18):e2215517120, 2023.

[3] Jake Song, Qingteng Zhang, Felipe de Quesada, Mehedi H Rizvi, Joseph B Tracy, Jan Ilavsky, Suresh Narayanan, Emanuela Del Gado, Robert L Leheny, Niels Holten-Andersen, et al. Microscopic dynamics underlying the stress relaxation of arrested soft materials. Proceedings of the National Academy of Sciences, 119(30):e2201566119, 2022.

[4] Akinori Sato and Takashi Sasaki. Cooperativity of dynamics in supercooled polymeric materials and its temperature dependence predicted from a surface controlled model. European Polymer Journal, 99:485–494, 2018.

[5] Ian Percival and Derek Richards. Introduction to dynamics. Cambridge University Press, 1982.

[6] Clark Robinson. Dynamical systems: stability, symbolic dynamics, and chaos. CRC press, 1998.

[7] Robert H Cannon. Dynamics of physical systems. Courier Corporation, 2003.

[8] David J Tritton. Physical fluid dynamics. Springer Science & Business Media, 2012.

[9] Irving R Epstein and John A Pojman. An introduction to nonlinear chemical dynamics: oscillations, waves, patterns, and chaos. Oxford university press, 1998.

[10] Abraham Nitzan. Chemical dynamics in condensed phases: relaxation, transfer, and reactions in condensed molecular systems. Oxford university press, 2024.

[11] Paul Weiss. Cellular dynamics. Reviews of Modern Physics, 31(1):11, 1959.

[12] Henry Tedeschi. Cell physiology: molecular dynamics. Elsevier, 2012.

[13] Marc A Meyers. Dynamic behavior of materials. John wiley & sons, 1994.

[14] Vitali Nesterenko. Dynamics of heterogeneous materials. Springer Science & Business Media, 2013.

[15] James T Hynes. Molecules in motion: chemical reaction and allied dynamics in solution and elsewhere. Annual review of physical chemistry, 66(1):1–20, 2015.

[16] Raphael D Levine. Molecular reaction dynamics. Cambridge university press, 2009.

[17] Immanuel Velikovsky. Earth in upheaval. Paradigma Ltd, 2009.

[18] Yan Hu, Roland Bürgmann, Paramesh Banerjee, Lujia Feng, Emma M Hill, Takeo Ito, Takao Tabei, and Kelin Wang. Asthenosphere rheology inferred from observations of the 2012 indian ocean earthquake. Nature, 538(7625):368–372, 2016.

[19] RT Pierrehumbert. Large-scale horizontal mixing in planetary atmospheres. Physics of Fluids A: Fluid Dynamics, 3(5):1250–1260, 1991.

[20] Hideyuki Hotta, Yuto Bekki, Laurent Gizon, Quentin Noraz, and Mark Rast. Dynamics of large-scale solar flows. Space Science Reviews, 219(8):77, 2023.

[21] John Zeng Hui Zhang. Theory and application of quantum molecular dynamics. World Scientific, 1998.

[22] Carlo Massobrio, Jincheng Du, Marco Bernasconi, Philip S Salmon, et al. Molecular dynamics simulations of disordered materials, volume 215. Springer, 2015.

[23] Ben Leimkuhler and Charles Matthews. Molecular dynamics. Interdisciplinary applied mathematics, 39(1), 2015.

[24] Issam Jassim, Dieter Stolle, and Pieter Vermeer. Two-phase dynamic analysis by material point method. International journal for numerical and analytical methods in geomechanics, 37(15):2502–2522, 2013.

[25] Patrick Paultre. Dynamics of structures. John Wiley & Sons, 2013.

[26] Michael J Solomon and Qiang Lu. Rheology and dynamics of particles in viscoelastic media. Current opinion in colloid & interface science, 6(5-6):430–437, 2001.

[27] Dan Guo, Guoxin Xie, and Jianbin Luo. Mechanical properties of nanoparticles: basics and applications. Journal of physics D: applied physics, 47(1):013001, 2013.

[28] Junemoo Koo and Clement Kleinstreuer. A new thermal conductivity model for nanofluids. Journal of Nanoparticle research, 6:577–588, 2004.

[29] Dimitri N Basov, Richard D Averitt, Dirk Van Der Marel, Martin Dressel, and Kristjan Haule. Electrodynamics of correlated electron materials. Reviews of Modern Physics, 83(2):471–541, 2011.

[30] George M Beal and Joe M Bohlen. The diffusion process. 1956.

[31] FM Horn, W Richtering, J Bergenholtz, N Willenbacher, and NJ Wagner. Hydrodynamic and colloidal interactions in concentrated charge-stabilized polymer dispersions. Journal of colloid and interface science, 225(1):166–178, 2000.

[32] Yunwei Wang, Li Li, Yiming Wang, Qingshong Yang, Zhishuang Ye, Chen Hua, Yuchuan Tian, Regine von Klitzing, and Xuhong Guo. Interaction among spherical polyelectrolyte brushes in concentrated aqueous solution. Langmuir, 36(12):3104–3110, 2020.

[33] Vladimir A Bershtein, Larisa M Egorova, Pavel N Yakushev, P Pissis, P Sysel, and L Brozova. Molecular dynamics in nanostructured polyimide–silica hybrid materials and their thermal stability. Journal of Polymer Science Part B: Polymer Physics, 40(10):1056–1069, 2002.

[34] JF Mano, JL Gómez Ribelles, NM Alves, and M Salmerón Sanchez. Glass transition dynamics and structural relaxation of plla studied by dsc: Influence of crystallinity. Polymer, 46(19):8258–8265, 2005.

[35] Alejandro Toro-Labbé. Theoretical aspects of chemical reactivity, volume 19. Elsevier, 2006.

[36] Jan Mewis and Norman J Wagner. Colloidal suspension rheology, volume 10. Cambridge university press Cambridge, 2012.

[37] Rudolph Stephen Lenk. Polymer rheology. Springer Science & Business Media, 2012.

[38] Hesam Askari and Ken Kamrin. Intrusion rheology in grains and other flowable materials. Nature materials, 15(12):1274–1279, 2016.

[39] Bartosz A Grzybowski, Krzysztof Fitzner, Jan Paczesny, and Steve Granick. From dynamic self-assembly to networked chemical systems. Chemical Society Reviews, 46(18):5647–5678, 2017.

[40] Mark D Ediger. Spatially heterogeneous dynamics in supercooled liquids. Annual review of physical chemistry, 51(1):99–128, 2000.

[41] Hsuan-Wei Hu and Steve Granick. Viscoelastic dynamics of confined polymer melts. Science, 258(5086):1339–1342, 1992.

[42] Otis R Walton. Particle-dynamics calculations of shear flow. In Studies in Applied Mechanics, volume 7, pages 327–338. Elsevier, 1983.

[43] Nicoletta Gnan and Emanuela Zaccarelli. The microscopic role of deformation in the dynamics of soft colloids. Nature Physics, 15(7):683–688, 2019.

[44] Nikita Morozov and Yuri Petrov. Dynamics of fracture. Springer Science & Business Media, 2013.

[45] Larry D Libersky and Albert G Petschek. Smooth particle hydrodynamics with strength of materials. In Advances in the Free-Lagrange Method Including Contributions on Adaptive Gridding and the Smooth Particle Hydrodynamics Method: Proceedings of the Next Free-Lagrange Conference Held at Jackson Lake Lodge, Moran, WY, USA 3–7 June 1990, pages 248–257. Springer, 2005.

[46] Wolfgang Losert, Lyderic Bocquet, Tom C Lubensky, and Jerry P Gollub. Particle dynamics in sheared granular matter. Physical review letters, 85(7):1428, 2000.

[47] Eugen Axinte. Glasses as engineering materials: A review. Materials & Design, 32(4):1717–1732, 2011.

[48] Richard Zallen. The physics of amorphous solids. John Wiley & Sons, 2008.

[49] Alberto Concellón, Cassandra A Zentner, and Timothy M Swager. Dynamic complex liquid crystal emulsions. Journal of the American Chemical Society, 141(45):18246–18255, 2019.

[50] Amin M'barki, Lydéric Bocquet, and Adam Stevenson. Linking rheology and printability for dense and strong ceramics by direct ink writing. Scientific reports, 7(1):6017, 2017.

[51] Wenyan Xie, Xi Wei, Heemin Kang, Hong Jiang, Zhiqin Chu, Yuan Lin, Yong Hou, and Qiang Wei. Static and dynamic: evolving biomaterial mechanical properties to control cellular mechanotransduction. Advanced Science, 10(9):2204594, 2023.

[52] David Richard Schmidt, Heather Waldeck, and Weiyuan John Kao. Protein adsorption to biomaterials. Biological interactions on materials surfaces: Understanding and controlling protein, cell, and tissue responses, pages 1–18, 2009.

[53] E Pfender and YC Lee. Particle dynamics and particle heat and mass transfer in thermal plasmas. part i. the motion of a single particle without thermal effects. Plasma Chemistry and Plasma Processing, 5:211–237, 1985.

[54] Ask F Jakobsen. Constant-pressure and constant-surface tension simulations in dissipative particle dynamics. The Journal of chemical physics, 122(12), 2005.

[55] Moubin Liu, Paul Meakin, and Hai Huang. Dissipative particle dynamics with attractive and repulsive particle-particle interactions. Physics of Fluids, 18(1), 2006.

[56] Shaghayegh Khani, Safa Jamali, Arman Boromand, Michael JA Hore, and Joao Maia. Polymer-mediated nanorod self-assembly predicted by dissipative particle dynamics simulations. Soft Matter, 11(34):6881–6892, 2015.

[57] Thomas L Beck and R Stephen Berry. The interplay of structure and dynamics in the melting of small clusters. The Journal of chemical physics, 88(6):3910–3922, 1988.

[58] Benjamin J Landrum, William B Russel, and Roseanna N Zia. Delayed yield in colloidal gels: Creep, flow, and re-entrant solid regimes. Journal of Rheology, 60(4):783–807, 2016.

[59] Jean-Pierre Aubin. The legacy of ingenhousz notes on some mathematical translations of uncertainty in living sciences. 2012.

[60] Mark Kac. Random walk and the theory of brownian motion. The American Mathematical Monthly, 54(7P1):369–391, 1947.

[61] Adolf Fick. Ueber diffusion. Annalen der physik, 170(1):59–86, 1855.

[62] Load Rayleigh. On the resultant of a large number of vibrations of the same pitch and of arbitrary phase. Phil. Mag., Series 5, 43(261):259–272, 1880.

[63] Albert Einstein. Über die von der molekularkinetischen theorie der wärme geforderte bewegung von in ruhenden flüssigkeiten suspendierten teilchen. Annalen der physik, 4, 1905.

[64] Jean Perrin. Mouvement brownien et réalité moléculaire. 1909.

[65] Paul Langevin et al. Sur la théorie du mouvement brownien. CR Acad. Sci. Paris, 146(530-533):530, 1908.

[66] Adriaan Daniël Fokker. Die mittlere energie rotierender elektrischer dipole im strahlungsfeld. Annalen der Physik, 348(5):810–820, 1914.

[67] VM Planck. Über einen satz der statistischen dynamik und seine erweiterung in der quantentheorie. Sitzungberichte der, 1917.

[68] M von Smoluchowski. Drei vortrage uber diffusion, brownsche bewegung und koagulation von kolloidteilchen. Zeitschrift fur Physik, 17:557–585, 1916.

[69] Oskar Klein. Zur statistischen theorie der suspensionen und deren zusammenhang mit der brownschen bewegung. Arkiv för Matematik, Astronomi och Fysik, 16(5):1–24, 1921.

[70] H. A. Kramers. Brownian motion in a field of force and the diffusion model of chemical reactions. Physica, 7(4):284–304, 1940.

[71] Norbert Wiener. Differential-space. Journal of Mathematics and Physics, 2(1-4):131–174, 1923.

[72] George E Uhlenbeck and Leonard S Ornstein. On the theory of the brownian motion. Physical review, 36(5):823, 1930.

[73] Ming Chen Wang and George Eugene Uhlenbeck. On the theory of the brownian motion ii. Reviews of modern physics, 17(2-3):323, 1945.

[74] Subrahmanyan Chandrasekhar. Stochastic problems in physics and astronomy. Reviews of modern physics, 15(1):1, 1943.

[75] Lars Onsager. Reciprocal relations in irreversible processes. i. Physical review, 37(4):405, 1931.

[76] Lars Onsager. Reciprocal relations in irreversible processes. ii. Physical review, 38(12):2265, 1931.

[77] Rep Kubo. The fluctuation-dissipation theorem. Reports on progress in physics, 29(1):255, 1966.

[78] Rafail V Abramov and Andrew J Majda. Blended response algorithms for linear fluctuation-dissipation for complex nonlinear dynamical systems. Nonlinearity, 20(12):2793, 2007.

[79] Rouslan L Stratonovich. Nonlinear nonequilibrium thermodynamics I: linear and nonlinear fluctuation-dissipation theorems, volume 57. Springer Science & Business Media, 2012.

[80] Alexandre Tkatchenko, Alberto Ambrosetti, and Robert A DiStasio. Interatomic methods for the dispersion energy derived from the adiabatic connection fluctuation-dissipation theorem. The Journal of Chemical Physics, 138(7), 2013.

[81] Koichi Murase and Tetsufumi Hirano. Hydrodynamic fluctuations and dissipation in an integrated dynamical model. Nuclear Physics A, 956:276–279, 2016.

[82] A Markov. Extension of the law of large numbers to dependent events, isvestia soc. Phys. Math. Kazan, 15(4):135–156, 1906.

[83] A. A. Markov. Extension of the limit theorems of probability theory to a sum of variables connected in a chain. The Notes of the Imperial Academy of Sciences of St. Petersburg VIII Series, Physio-Mathematical College, XXII/9, 1907. In Russian.

[84] Andrei Kolmogoroff. Über die analytischen methoden in der wahrscheinlichkeitsrechnung. Mathematische Annalen, 104:415–458, 1931.

[85] Sydney Chapman. The absorption and dissociative or ionizing effect of monochromatic radiation in an atmosphere on a rotating earth. Proceedings of the Physical Society, 43(1):26, 1931.

[86] Svante Arrhenius. The viscosity of solutions. Biochemical Journal, 11(2):112, 1917.

[87] Jan Hermans Jr. The viscosity of concentrated solutions of rigid rodlike molecules (poly-γ-benzyl-l-glutamate in m-cresol). Journal of Colloid Science, 17(7):638–648, 1962.

[88] Chen-Jung Lin, James H Peery, and WR Schowalter. Simple shear flow round a rigid sphere: inertial effects and suspension rheology. Journal of Fluid Mechanics, 44(1):1–17, 1970.

[89] GK Batchelor and JT0246 Green. The determination of the bulk stress in a suspension of spherical particles to order c2. Journal of Fluid Mechanics, 56(3):401–427, 1972.

[90] RA Lionberger and WB Russel. A smoluchowski theory with simple approximations for hydrodynamic interactions in concentrated dispersions. Journal of Rheology, 41(2):399–425, 1997.

[91] AJ Banchio, J Bergenholtz, and G Nägele. Rheology and dynamics of colloidal suspensions. Physical review letters, 82(8):1792, 1999.

[92] Miriam Siebenbürger, Matthias Fuchs, Henning Winter, and Matthias Ballauff. Viscoelasticity and shear flow of concentrated, noncrystallizing colloidal suspensions: Comparison with mode-coupling theory. Journal of Rheology, 53(3):707–726, 2009.

[93] Dan S Bolintineanu, Gary S Grest, Jeremy B Lechman, Flint Pierce, Steven J Plimpton, and P Randall Schunk. Particle dynamics modeling methods for colloid suspensions. Computational Particle Mechanics, 1:321–356, 2014.

[94] Berni J Alder and Thomas Everett Wainwright. Studies in molecular dynamics. i. general method. The Journal of Chemical Physics, 31(2):459–466, 1959.

[95] Donald L Ermak and J Andrew McCammon. Brownian dynamics with hydrodynamic interactions. The Journal of chemical physics, 69(4):1352–1360, 1978.

[96] John F Brady and Georges Bossis. The rheology of concentrated suspensions of spheres in simple shear flow by numerical simulation. Journal of Fluid mechanics, 155:105–129, 1985.

[97] Louis Durlofsky, John F Brady, and Georges Bossis. Dynamic simulation of hydrodynamically interacting particles. Journal of fluid mechanics, 180:21–49, 1987.

[98] John F Brady, Georges Bossis, et al. Stokesian dynamics. Annual review of fluid mechanics, 20(1):111–157, 1988.

[99] Amit Kumar and Jonathan JL Higdon. Origins of the anomalous stress behavior in charged colloidal suspensions under shear. Physical Review E—Statistical, Nonlinear, and Soft Matter Physics, 82(5):051401, 2010.

[100] Michael Dean Bybee. Hydrodynamic simulations of colloidal gels: Microstructure, dynamics, and rheology. University of Illinois at Urbana-Champaign, 2009.

[101] Amit Kumar. Microscale dynamics in suspensions of non-spherical particles. University of Illinois at Urbana-Champaign, 2010.

[102] Steve Plimpton. Fast parallel algorithms for short-range molecular dynamics. Journal of computational physics, 117(1):1–19, 1995.

[103] Matt K Petersen, Jeremy B Lechman, Steven J Plimpton, Gary S Grest, PR Schunk, et al. Mesoscale hydrodynamics via stochastic rotation dynamics: Comparison with lennard-jones fluid. The Journal of chemical physics, 132(17), 2010.

[104] PJ Hoogerbrugge and Johannes MVA Koelman. Simulating microscopic hydrodynamic phenomena with dissipative particle dynamics. Europhysics letters, 19(3):155, 1992.

[105] Robert D Groot and Patrick B Warren. Dissipative particle dynamics: Bridging the gap between atomistic and mesoscopic simulation. The Journal of chemical physics, 107(11):4423–4435, 1997.

[106] Martin Hecht, Jens Harting, Thomas Ihle, and Hans J Herrmann. Simulation of clay-like colloids. Physical Review E—Statistical, Nonlinear, and Soft Matter Physics, 72(1):011408, 2005.

[107] Hiroshi Noguchi and Gerhard Gompper. Transport coefficients of off-lattice mesoscale-hydrodynamics simulation techniques. Physical Review E—Statistical, Nonlinear, and Soft Matter Physics, 78(1):016706, 2008.

[108] Christoph Junghans, Matej Praprotnik, and Kurt Kremer. Transport properties controlled by a thermostat: An extended dissipative particle dynamics thermostat. Soft Matter, 4(1):156–161, 2008.

[109] RGM Van der Sman. Simulations of confined suspension flow at multiple length scales. Soft Matter, 5(22):4376–4387, 2009.

[110] Masahiro Fujita and Yukio Yamaguchi. Multiscale simulation method for self-organization of nanoparticles in dense suspension. Journal of Computational Physics, 223(1):108–120, 2007.

[111] Denis Semwogerere and Eric R Weeks. Confocal microscopy. Encyclopedia of biomaterials and biomedical engineering, 23:1–10, 2005.

[112] Adaobi Nwaneshiudu, Christiane Kuschal, Fernanda H Sakamoto, R Rox Anderson, Kathryn Schwarzenberger, and Roger C Young. Introduction to confocal microscopy. Journal of Investigative Dermatology, 132(12):1–5, 2012.

[113] Samantha Stehbens, Hayley Pemble, Lyndsay Murrow, and Torsten Wittmann. Imaging intracellular protein dynamics by spinning disk confocal microscopy. Methods in enzymology, 504:293–313, 2012.

[114] Deshpremy Mukhija and Michael J Solomon. Translational and rotational dynamics of colloidal rods by direct visualization with confocal microscopy. Journal of colloid and interface science, 314(1):98–106, 2007.

[115] Marinus T Vlaardingerbroek and Jacques A Boer. Magnetic resonance imaging: theory and practice. Springer Science & Business Media, 2013.

[116] Girish Katti, Syeda Arshiya Ara, and Ayesha Shireen. Magnetic resonance imaging (mri)–a review. International journal of dental clinics, 3(1):65–70, 2011.

[117] Jan Novak and Melanie M Britton. Magnetic resonance imaging of the rheology of ionic liquid colloidal suspensions. Soft Matter, 9(9):2730–2737, 2013.

[118] Philippe Coussot, F Bertrand, and Benjamin Herzhaft. Rheological behavior of drilling muds, characterization using mri visualization. Oil & gas science and technology, 59(1):23–29, 2004.

[119] Hyun Sun Cho, Friedrich Schotte, Valentyn Stadnytskyi, and Philip Anfinrud. Time-resolved x-ray scattering studies of proteins. Current opinion in structural biology, 70:99–107, 2021.

[120] Tomas Rosén, Ruifu Wang, Chengbo Zhan, Hongrui He, Shirish Chodankar, and Benjamin S Hsiao. Cellulose nanofibrils and nanocrystals in confined flow: Single-particle dynamics to collective alignment revealed through scanning small-angle x-ray scattering and numerical simulations. Physical Review E, 101(3):032610, 2020.

[121] Tomas Rosén, Ruifu Wang, HongRui He, Chengbo Zhan, Shirish Chodankar, and Benjamin S Hsiao. Shear-free mixing to achieve accurate temporospatial nanoscale kinetics through scanning-saxs: ion-induced phase transition of dispersed cellulose nanocrystals. Lab on a Chip, 21(6):1084–1095, 2021.

[122] Tomas Rosén, Ruifu Wang, HongRui He, Chengbo Zhan, Shirish Chodankar, and Benjamin S Hsiao. Understanding ion-induced assembly of cellulose nanofibrillar gels through shear-free mixing and in situ scanning-saxs. Nanoscale advances, 3(17):4940–4951, 2021.

[123] Olivier Isnard. A review of in situ and/or time resolved neutron scattering. Comptes Rendus Physique, 8(7-8):789–805, 2007.

[124] Guan-Rong Huang, Yangyang Wang, Bin Wu, Zhe Wang, Changwoo Do, Gregory S Smith, Wim Bras, Lionel Porcar, Péter Falus, and Wei-Ren Chen. Reconstruction of three-dimensional anisotropic structure from small-angle scattering experiments. Physical Review E, 96(2):022612, 2017.

[125] Jianwei Miao, Richard L Sandberg, and Changyong Song. Coherent x-ray diffraction imaging. IEEE Journal of selected topics in quantum electronics, 18(1):399–410, 2011.

[126] JN Clark, X Huang, R Harder, and IK Robinson. High-resolution three-dimensional partially coherent diffraction imaging. Nature communications, 3(1):993, 2012.

[127] J-D Nicolas, Tobias Reusch, Markus Osterhoff, Michael Sprung, FJR Schúlein, Hubert J Krenner, Achim Wixforth, and Tim Salditt. Time-resolved coherent x-ray diffraction imaging of surface acoustic waves. Applied Crystallography, 47(5):1596–1605, 2014.

[128] A Ulvestad, A Tripathi, SO Hruszkewycz, W Cha, SM Wild, GB Stephenson, and PH Fuoss. Coherent diffractive imaging of time-evolving samples with improved temporal resolution. Physical Review B, 93(18):184105, 2016.

[129] B Frick. Neutron backscattering spectroscopy. In Neutron and X-ray Spectroscopy, pages 483–527. Springer, 2006.

[130] Bernhard Frick and Dan Neumann. Neutron backscattering. Neutrons in Soft Matter, pages 183–202, 2011.

[131] Ingo Hoffmann. Neutrons for the study of dynamics in soft matter systems. Colloid and Polymer Science, 292:2053–2069, 2014.

[132] Michael Monkenbusch and Dieter Richter. High resolution neutron spectroscopy—a tool for the investigation of dynamics of polymers and soft matter. Comptes Rendus. Physique, 8(7-8):845–864, 2007.

[133] Jonas Ries and Petra Schwille. Fluorescence correlation spectroscopy. BioEssays, 34(5):361–368, 2012.

[134] Thomas Ohrt, Jörg Mütze, Wolfgang Staroske, Lasse Weinmann, Julia Höck, Karin Crell, Gunter Meister, and Petra Schwille. Fluorescence correlation spectroscopy and fluorescence cross-correlation spectroscopy reveal the cytoplasmic origination of loaded nuclear risc in vivo in human cells. Nucleic acids research, 36(20):6439–6449, 2008.

[135] Salvatore Chiantia, Jonas Ries, and Petra Schwille. Fluorescence correlation spectroscopy in membrane structure elucidation. Biochimica et Biophysica Acta (BBA)-Biomembranes, 1788(1):225–233, 2009.

[136] Jörg Stetefeld, Sean A McKenna, and Trushar R Patel. Dynamic light scattering: a practical guide and applications in biomedical sciences. Biophysical reviews, 8:409–427, 2016.

[137] Benjamin Chu. Laser light scattering: basic principles and practice. Courier Corporation, 2007.

[138] Benjamin Chu, Zhulun Wang, and Jiqun Yu. Dynamic light scattering study of internal motions of polymer coils in dilute solution. Macromolecules, 24(26):6832–6838, 1991.

[139] Bruce J Berne and Robert Pecora. Dynamic light scattering: with applications to chemistry, biology, and physics. Courier Corporation, 2000.

[140] Ferenc Mezei. The principles of neutron spin echo. In Neutron Spin Echo: Proceedings of a Laue-Langevin Institut Workshop Grenoble, October 15–16, 1979, pages 1–26. Springer, 2005.

[141] Ferenc Mezei. Neutron spin echo: A new concept in polarized thermal neutron techniques. Zeitschrift für Physik A Hadrons and nuclei, 255:146–160, 1972.

[142] C Le Coeur and S Longeville. Microscopic protein diffusion at high concentration by neutron spin-echo spectroscopy. Chemical Physics, 345(2-3):298–304, 2008.

[143] K Niedzwiedz, A Wischnewski, W Pyckhout-Hintzen, J Allgaier, D Richter, and A Faraone. Chain dynamics and viscoelastic properties of poly (ethylene oxide). Macromolecules, 41(13):4866–4872, 2008.

[144] A Arbe, D Richter, J Colmenero, and B Farago. Merging of the α and β relaxations in polybutadiene: A neutron spin echo and dielectric study. Physical Review E, 54(4):3853, 1996.

[145] Xiang Luo, Tengfei Cui, and Xiangqiang Chu. Applications of neutron spin echo in soft matter. Frontiers in Physics, 11:1279007, 2023.

[146] Dieter Richter, Michael Monkenbusch, Arantxa Arbe, and Juan Colmenero. Neutron spin echo in polymer systems. Neutron Spin Echo in Polymer Systems: -/-, pages 1–221, 2005.

[147] M Sutton, SGJ Mochrie, T Greytak, SE Nagler, LE Berman, GA Held, and GB Stephenson. Observation of speckle by diffraction with coherent x-rays. Nature, 352(6336):608–610, 1991.

[148] Qingteng Zhang, Guoxiang Hu, Vitalii Starchenko, Gang Wan, Eric M Dufresne, Yongqi Dong, Huajun Liu, Hua Zhou, Hyoungjeen Jeen, Kayahan Saritas, et al. Phase transition dynamics in a complex oxide heterostructure. Physical Review Letters, 129(23):235701, 2022.

[149] Aurora Nogales and Andrei Fluerasu. X ray photon correlation spectroscopy for the study of polymer dynamics. European Polymer Journal, 81:494–504, 2016.

[150] Divya Bahadur, Qingteng Zhang, Eric M Dufresne, Pawel Grybos, Piotr Kmon, Robert L Leheny, Piotr Maj, Suresh Narayanan, Robert Szczygiel, James W Swan, et al. Evolution of structure and dynamics of thermo-reversible nanoparticle gels—a combined xpcs and rheology study. The Journal of Chemical Physics, 151(10), 2019.

[151] Antara Pal, Thomas Zinn, Mohammad Arif Kamal, Theyencheri Narayanan, and Peter Schurtenberger. Anomalous dynamics of magnetic anisotropic colloids studied by xpcs. Small, 14(46):1802233, 2018.

[152] Suan P Quah, Yugang Zhang, Andrei Fluerasu, Xiaoxi Yu, Bingqian Zheng, Xuechen Yin, Weiping Liu, and Surita R Bhatia. Techniques to characterize dynamics in biomaterials microenvironments: Xpcs and microrheology of alginate/peo–ppo–peo hydrogels. Soft matter, 17(6):1685–1691, 2021.

[153] Anastasia Ragulskaya, Vladimir Starostin, Nafisa Begam, Anita Girelli, Hendrik Rahmann, Mario Reiser, Fabian Westermeier, Michael Sprung, Fajun Zhang, Christian Gutt, et al. Reverse-engineering method for xpcs studies of non-equilibrium dynamics. IUCrJ, 9(4):439–448, 2022.

[154] Robert L Leheny, Michael C Rogers, Kui Chen, Suresh Narayanan, and James L Harden. Rheo-xpcs. Current Opinion in Colloid & Interface Science, 20(4):261–271, 2015.

[155] Guangxu Ju, Dongwei Xu, Matthew J Highland, Carol Thompson, Hua Zhou, Jeffrey A Eastman, Paul H Fuoss, Peter Zapol, Hyunjung Kim, and G Brian Stephenson. Coherent x-ray spectroscopy reveals the persistence of island arrangements during layer-by-layer growth. Nature Physics, 15(6):589–594, 2019.

[156] Alexander Schavkan. Dynamics of colloidal systems of magnetic nanoparticles under influence of magnetic fields investigated by XPCS. PhD thesis, Staats-und Universitätsbibliothek Hamburg Carl von Ossietzky, 2017.

[157] Joseph Larmor. Lxiii. on the theory of the magnetic influence on spectra; and on the radiation from moving ions. The London, Edinburgh, and Dublin Philosophical Magazine and Journal of Science, 44(271):503–512, 1897.

[158] Joseph John Thomson. Xl. cathode rays. The London, Edinburgh, and Dublin Philosophical Magazine and Journal of Science, 44(269):293–316, 1897.

[159] John Christopher Dainty. Laser speckle and related phenomena, volume 9. Springer science & business Media, 2013.

[160] Emil Wolf. Coherence properties of partially polarized electromagnetic radiation. Il Nuovo Cimento (1955-1965), 13:1165–1181, 1959.

[161] Julien Lhermitte. Using coherent small angle xray scattering to measure velocity fields and random motion. McGill University (Canada), 2011.

[162] Philip Willmott. An introduction to synchrotron radiation: techniques and applications. John Wiley & Sons, 2019.

[163] Zhang Jiang, Xuefa Li, Joseph Strzalka, Michael Sprung, Tao Sun, Alec R Sandy, Suresh Narayanan, Dong Ryeol Lee, and Jin Wang. The dedicated high-resolution grazing-incidence x-ray scattering beamline 8-id-e at the advanced photon source. Synchrotron Radiation, 19(4):627–636, 2012.

[164] G Grübel, GB Stephenson, C Gutt, H Sinn, and Th Tschentscher. Xpcs at the european x-ray free electron laser facility. Nuclear Instruments and Methods in Physics Research Section B: Beam Interactions with Materials and Atoms, 262(2):357–367, 2007.

[165] Michael Borland, Tim Berenc, Y Sun, and Vadim Sajaev. Lower emittance lattice for the advanced photon source upgrade using reverse bending magnets. Technical report, Argonne National Lab.(ANL), Argonne, IL (United States), 2017.

[166] Melike Abliz, M Jaski, A Xiao, U Wienands, H Cease, M Borland, G Decker, and J Kerby. Septum magnet design for the aps-u. Technical report, Argonne National Lab.(ANL), Argonne, IL (United States), 2017.

[167] R Abela, W Joho, P Marchand, SV Milton, and LZ Rivkin. Design considerations for a swiss light source (sls). In Proceedings of the EPAC92, Berlin, page 486. Citeseer, 1992.

[168] Louis Emery and Michael Borland. Possible long-term improvements to the advanced photon source. In Proceedings of the 2003 Particle Accelerator Conference, volume 1, pages 256–258. IEEE, 2003.

[169] Mrinal Bera, Qingteng Zhang, Xiaobing Zuo, Wei Bu, Joe Strzalka, Steven Weigand, Jan Ilavsky, Eric Dufresne, Suresh Narayanan, and Byeongdu Lee. Opportunities of soft materials research at advanced photon source. Synchrotron Radiation News, 36(2):12–23, 2023.

[170] Robert Pecora. Spectral distribution of light scattered by monodisperse rigid rods. Journal of chemical physics, 48(9):4126–4128, 1968.

[171] Robert Pecora. Spectrum of light scattered from optically anisotropic macromolecules. The Journal of Chemical Physics, 49(3):1036–1043, 1968.

[172] Dewey K Carpenter. Dynamic light scattering with applications to chemistry, biology, and physics (berne, bruce j.; pecora, robert), 1977.

[173] M Corti, V Degiorgio, M Giglio, and A Vendramini. Analysis of macromolecular polydispersity by dynamic light scattering and thermodiffusion. Optics Communications, 23(2):282–284, 1977.

[174] Stephen W. Provencher. Contin: A general purpose constrained regularization program for inverting noisy linear algebraic and integral equations. Computer Physics Communications, 27(3):229–242, 1982.

[175] Ross N Andrews, Suresh Narayanan, Fan Zhang, Ivan Kuzmenko, and Jan Ilavsky. Inverse transformation: Unleashing spatially heterogeneous dynamics with an alternative approach to xpcs data analysis. Applied Crystallography, 51(1):35–46, 2018.

[176] Yihao Chen, Simon A Rogers, Suresh Narayanan, James L Harden, and Robert L Leheny. Microscopic dynamics of stress relaxation in a nanocolloidal soft glass. Physical Review Materials, 4(3):035602, 2020.

[177] Donald B Dingwell and Sharon L Webb. Structural relaxation in silicate melts and non-newtonian melt rheology in geologic processes. Physics and Chemistry of Minerals, 16:508–516, 1989.

[178] Sharon Webb. Silicate melts: Relaxation, rheology, and the glass transition. Reviews of Geophysics, 35(2):191–218, 1997.

[179] Sandra Lerouge, Médéric Argentina, and Jean-Paul Decruppe. Interface instability in shear-banding flow. Physical Review Letters, 96(8):088301, 2006.

[180] Jean-Baptiste Salmon, Annie Colin, Sébastien Manneville, and François Molino. Velocity profiles in shear-banding wormlike micelles. Physical Review Letters, 90(22):228303, 2003.

[181] Michel Cloitre, Régis Borrega, and Ludwik Leibler. Rheological aging and rejuvenation in microgel pastes. Physical Review Letters, 85(22):4819, 2000.

[182] Melissa B Gordon, Christopher J Kloxin, and Norman J Wagner. The rheology and microstructure of an aging thermoreversible colloidal gel. Journal of Rheology, 61(1):23–34, 2017.

[183] Esmaeel Moghimi, Andrew B Schofield, and George Petekidis. Yielding and resolidification of colloidal gels under constant stress. Journal of Physics: Condensed Matter, 33(28):284002, 2021.

[184] Karin A Dahmen, Yehuda Ben-Zion, and Jonathan T Uhl. Micromechanical model for deformation in solids with universal predictions for stress-strain curves and slip avalanches. Physical Review Letters, 102(17):175501, 2009.

[185] Karin A Dahmen, Yehuda Ben-Zion, and Jonathan T Uhl. A simple analytic theory for the statistics of avalanches in sheared granular materials. Nature Physics, 7(7):554–557, 2011.

[186] Ranjini Bandyopadhyay, Dennis Liang, Hasan Yardimci, David A Sessoms, Matthew A Borthwick, Simon GJ Mochrie, James L Harden, and Robert L Leheny. Evolution of particle-scale dynamics in an aging clay suspension. Physical Review Letters, 93(22):228302, 2004.

[187] Oier Bikondoa. On the use of two-time correlation functions for x-ray photon correlation spectroscopy data analysis. Journal of applied crystallography, 50(2):357–368, 2017.

[188] Anastasia Ragulskaya, Vladimir Starostin, Fajun Zhang, Christian Gutt, and Frank Schreiber. On the analysis of two-time correlation functions: equilibrium versus non-equilibrium systems. Applied Crystallography, 57(4), 2024.

[189] Wesley R Burghardt, Marcin Sikorski, Alec R Sandy, and Suresh Narayanan. X-ray photon correlation spectroscopy during homogenous shear flow. Physical Review E, 85(2):021402, 2012.

[190] C Gutt, T Ghaderi, Virginie Chamard, A Madsen, T Seydel, Metin Tolan, M Sprung, G Grübel, and SK Sinha. Observation of heterodyne mixing in surface x-ray photon correlation spectroscopy experiments. Physical Review Letters, 91(7):076104, 2003.

[191] Tomas Rosén, HongRui He, Ruifu Wang, Korneliya Gordeyeva, Ahmad Reza Motezakker, Andrei Fluerasu, L Daniel Söderberg, and Benjamin S Hsiao. Exploring nanofibrous networks with x-ray photon correlation spectroscopy through a digital twin. Physical Review E, 108(1):014607, 2023.

[192] Erich O Schulz-DuBois. Photon Correlation Techniques in Fluid Mechanics: Proceedings of the 5th International Conference at Kiel-Damp, Fed. Rep. of Germany, May 23–26, 1982, volume 38. Springer, 1982.

[193] Rodney Loudon. The quantum theory of light. OUP Oxford, 2000.

[194] P _ G De Gennes. Liquid dynamics and inelastic scattering of neutrons. Physica, 25(7-12):825–839, 1959.

[195] Venkataraman Balakrishnan. Elements of nonequilibrium statistical mechanics, volume 3. Springer, 2008.

[196] Gerd Röpke. Nonequilibrium statistical physics. John Wiley & Sons, 2013.

[197] Gregory F Lawler. Stochastic calculus: An introduction with applications. American Mathematical Society, 2010.

[198] Thomas Kolb and Daphne Klotsa. Active binary mixtures of fast and slow hard spheres. Soft Matter, 16(8):1967–1978, 2020.

[199] BRA Nijboer and A Rahman. Time expansion of correlation functions and the theory of slow neutron scattering. Physica, 32(2):415–432, 1966.

[200] Etienne Fodor, Hisao Hayakawa, Paolo Visco, and Frédéric van Wijland. Active cage model of glassy dynamics. Physical Review E, 94(1):012610, 2016.

[201] Erkan Senses, Siyam M Ansar, Christopher L Kitchens, Yimin Mao, Suresh Narayanan, Bharath Natarajan, and Antonio Faraone. Small particle driven chain disentanglements in polymer nanocomposites. Physical Review Letters, 118(14):147801, 2017.

[202] Hongyu Guo, Gilles Bourret, R Bruce Lennox, Mark Sutton, James L Harden, and Robert L Leheny. Entanglement-controlled subdiffusion of nanoparticles within concentrated polymer solutions. Physical Review Letters, 109(5):055901, 2012.

[203] R Aravinda Narayanan, P Thiyagarajan, S Lewis, A Bansal, LS Schadler, and LB Lurio. Dynamics and internal stress at the nanoscale related to unique thermomechanical behavior in polymer nanocomposites. Physical Review Letters, 97(7):075505, 2006.

[204] Erik Geissler, Katalin Kosik, Andrei Fluerasu, Abdellatif Moussaïd, and Krisztina László. X-ray photon correlation spectroscopy of dynamics in thermosensitive gels. In Macromolecular Symposia, volume 256, pages 73–79. Wiley Online Library, 2007.

[205] Avni Jain, Florian Schulz, Francesco Dallari, Verena Markmann, Fabian Westermeier, Yugang Zhang, Gerhard Grübel, and Felix Lehmkühler. Three-step colloidal gelation revealed by time-resolved x-ray photon correlation spectroscopy. The Journal of Chemical Physics, 157(18), 2022.

[206] Laurence B Lurio, George M Thurston, Qingteng Zhang, Suresh Narayanan, and Eric M Dufresne. Use of continuous sample translation to reduce radiation damage for xpcs studies of protein diffusion. Journal of Synchrotron Radiation, 28(2):490–498, 2021.

[207] Johannes Möller, Michael Sprung, Anders Madsen, and Christian Gutt. X-ray photon correlation spectroscopy of protein dynamics at nearly diffraction-limited storage rings. IUCrJ, 6(5):794–803, 2019.

[208] John W Negele. The mean-field theory of nuclear structure and dynamics. Reviews of Modern Physics, 54(4):913, 1982.

[209] Henrik Flyvbjerg, Kim Sneppen, and Per Bak. Mean field theory for a simple model of evolution. Physical Review Letters, 71(24):4087, 1993.

[210] Robert W Batterman. Why equilibrium statistical mechanics works: Universality and the renormalization group. Philosophy of Science, 65(2):183–208, 1998.

[211] Giovanni Jona-Lasinio. Renormalization group and probability theory. Physics Reports, 352(4-6):439–458, 2001.

[212] Leo P Kadanoff. Scaling and universality in statistical physics. Physica A: Statistical Mechanics and its Applications, 163(1):1–14, 1990.

[213] Peter N Pusey and W Van Megen. Phase behaviour of concentrated suspensions of nearly hard colloidal spheres. Nature, 320(6060):340–342, 1986.

[214] ME Cates, SM Fielding, D Marenduzzo, E Orlandini, and JM Yeomans. Shearing active gels close to the isotropic-nematic transition. Physical Review Letters, 101(6):068102, 2008.

[215] Peter Sollich, François Lequeux, Pascal Hébraud, and Michael E Cates. Rheology of soft glassy materials. Physical Review Letters, 78(10):2020, 1997.

[216] Pierre Jop, Vincent Mansard, Pinaki Chaudhuri, Lydéric Bocquet, and Annie Colin. Microscale rheology of a soft glassy material close to yielding. Physical Review Letters, 108(14):148301, 2012.

[217] Jin Wang. Landscape and flux theory of non-equilibrium dynamical systems with application to biology. Advances in Physics, 64(1):1–137, 2015.

[218] Avishek Das and David T Limmer. Nonequilibrium design strategies for functional colloidal assemblies. Proceedings of the National Academy of Sciences, 120(40):e217242120, 2023.

[219] Megan T Valentine, Peter D Kaplan, D Thota, John C Crocker, Thomas Gisler, Robert K Prud'homme, M Beck, and David A Weitz. Investigating the microenvironments of inhomogeneous soft materials with multiple particle tracking. Physical Review E, 64(6):061506, 2001.

[220] Mohammad Nabizadeh, Farzaneh Nasirian, Xinzhi Li, Yug Saraswat, Rony Waheibi, Lilian C Hsiao, Dapeng Bi, Babak Ravandi, and Safa Jamali. Network physics of attractive colloidal gels: Resilience, rigidity, and phase diagram. Proceedings of the National Academy of Sciences, 121(3):e2316394121, 2024.

[221] Gary P Morriss and Denis J Evans. Isothermal response theory. Molecular Physics, 54(3):629–636, 1985.

[222] Gary P Morriss and Denis J Evans. Application of transient correlation functions to shear flow far from equilibrium. Physical Review A, 35(2):792, 1987.

[223] Zhe Wang, Christopher N Lam, Wei-Ren Chen, Weiyu Wang, Jianning Liu, Yun Liu, Lionel Porcar, Christopher B Stanley, Zhichen Zhao, Kunlun Hong, et al. Fingerprinting molecular relaxation in deformed polymers. Physical Review X, 7(3):031003, 2017.

[224] Suraj Pandey, Richard Bean, Tokushi Sato, Ishwor Poudyal, Johan Bielecki, Jorvani Cruz Villarreal, Oleksandr Yefanov, Valerio Mariani, Thomas A White, Christopher Kupitz, et al. Time-resolved serial femtosecond crystallography at the european xfel. Nature Methods, 17(1):73–78, 2020.

[225] Darren F Arola, Geoffrey A Barrall, Robert L Powell, Kathryn L McCarthy, and Michael J McCarthy. Use of nuclear magnetic resonance imaging as a viscometer for process monitoring. Chemical Engineering Science, 52(13):2049–2057, 1997.

[226] Peter J Lu, Peter A Sims, Hidekazu Oki, James B Macarthur, and David A Weitz. Target-locking acquisition with real-time confocal (tarc) microscopy. Optics express, 15(14):8702–8712, 2007.

[227] Anton Barty, Sébastien Boutet, Michael J Bogan, Stefan Hau-Riege, Stefano Marchesini, Klaus Sokolowski-Tinten, Nikola Stojanovic, Ra'anan Tobey, Henri Ehrke, Andrea Cavalleri, et al. Ultrafast single-shot diffraction imaging of nanoscale dynamics. Nature photonics, 2(7):415–419, 2008.

[228] Alessandro Arcovito, Maurizio Benfatto, Michele Cianci, S Samar Hasnain, Karin Nienhaus, G Ulrich Nienhaus, Carmelinda Savino, Richard W Strange, Beatrice Vallone, and Stefano Della Longa. X-ray structure analysis of a metalloprotein with enhanced active-site resolution using in situ x-ray absorption near edge structure spectroscopy. Proceedings of the National Academy of Sciences, 104(15):6211–6216, 2007.

[229] Margherita Maiuri, Marco Garavelli, and Giulio Cerullo. Ultrafast spectroscopy: State of the art and open challenges. Journal of the American Chemical Society, 142(1):3–15, 2019.

[230] Yao-Hui Wang, Shisheng Zheng, Wei-Min Yang, Ru-Yu Zhou, Quan-Feng He, Petar Radjenovic, Jin-Chao Dong, Shunning Li, Jiaxin Zheng, Zhi-Lin Yang, et al. In situ raman spectroscopy reveals the structure and dissociation of interfacial water. Nature, 600(7887):81–85, 2021.

[231] Jason S Gardner, Georg Ehlers, Antonio Faraone, and Victoria García Sakai. High-resolution neutron spectroscopy using backscattering and neutron spin-echo spectrometers in soft and hard condensed matter. Nature Reviews Physics, 2(2):103–116, 2020.

[232] Daniel Garcia-Sanchez, King Yan Fong, Harish Bhaskaran, Steve Lamoreaux, and Hong X Tang. Casimir force and in situ surface potential measurements on nanomembranes. Physical Review Letters, 109(2):027202, 2012.

[233] Can Liu and Shen Ye. In situ atomic force microscopy (afm) study of oxygen reduction reaction on a gold electrode surface in a dimethyl sulfoxide (dmso)-based electrolyte solution. The Journal of Physical Chemistry C, 120(44):25246–25255, 2016.

[234] GG Fuller, JM Rallison, RL Schmidt, and LG Leal. The measurement of velocity gradients in laminar flow by homodyne light-scattering spectroscopy. Journal of Fluid Mechanics, 100(3):555–575, 1980.

[235] SB Dierker, R Pindak, RM Fleming, IK Robinson, and L Berman. X-ray photon correlation spectroscopy study of brownian motion of gold colloids in glycerol. Physical Review Letters, 75(3):449, 1995.

[236] Anastasia Ragulskaya. Dynamics of liquid-liquid phase separation in protein solutions probed by coherent X-ray scattering. PhD thesis, Universität Tübingen, 2023.

[237] Michael C Rogers, Kui Chen, Matthew J Pagenkopp, Thomas G Mason, Suresh Narayanan, James L Harden, and Robert L Leheny. Microscopic signatures of yielding in concentrated nanoemulsions under large-amplitude oscillatory shear. Physical Review Materials, 2(9):095601, 2018.

[238] Tomoaki Niiyama, Masato Wakeda, Tomotsugu Shimokawa, and Shigenobu Ogata. Structural relaxation affecting shear-transformation avalanches in metallic glasses. Physical Review E, 100(4):043002, 2019.

[239] Erik Miller and Jonathan P Rothstein. Transient evolution of shear-banding wormlike micellar solutions. Journal of Non-Newtonian Fluid Mechanics, 143(1):22–37, 2007.

[240] Zhanzhao Li, Maryam Hojati, Zhengyu Wu, Jonathon Piasente, Negar Ashrafi, José P Duarte, Shadi Nazarian, Sven G Bilén, Ali M Memari, and Aleksandra Radlińska. Fresh and hardened properties of extrusion-based 3d-printed cementitious materials: a review. Sustainability, 12(14):5628, 2020.

[241] Ian Loftus. Chapter 4: Mechanisms of Plaque Rupture, chapter 4. University of Adelaide Press, Adelaide, AU, 2011.

[242] Jingyuan Xu, Virgile Viasnoff, and Denis Wirtz. Compliance of actin filament networks measured by particle-tracking microrheology and diffusing wave spectroscopy. Rheologica acta, 37(4):387–398, 1998.

[243] Thomas G Mason and David A Weitz. Optical measurements of frequency-dependent linear viscoelastic moduli of complex fluids. Physical review letters, 74(7):1250, 1995.

[244] Yeseul Kim, Sunhyung Kim, Byoung Soo Kim, Jeong Hoon Park, Kyung Hyun Ahn, and Jun Dong Park. Yielding behavior of concentrated lithium-ion battery anode slurry. Physics of Fluids, 34(12), 2022.

[245] LS Stephens, Yan Liu, and EI Meletis. Finite element analysis of the initial yielding behavior of a hard coating/substrate system with functionally graded interface under indentation and friction. J. Trib., 122(2):381–387, 2000.

[246] Vincent Grenard, Thibaut Divoux, Nicolas Taberlet, and Sébastien Manneville. Timescales in creep and yielding of attractive gels. Soft matter, 10(10):1555–1571, 2014.

[247] Simon Dagois-Bohy, Ellák Somfai, Brian P Tighe, and Martin Van Hecke. Softening and yielding of soft glassy materials. Soft matter, 13(47):9036–9045, 2017.

[248] Neil J Balmforth, Ian A Frigaard, and Guillaume Ovarlez. Yielding to stress: recent developments in viscoplastic fluid mechanics. Annual review of fluid mechanics, 46(1):121–146, 2014.

[249] Jason R Stokes and William J Frith. Rheology of gelling and yielding soft matter systems. Soft Matter, 4(6):1133–1140, 2008.

[250] Peiran Wei, Ciera Cipriani, Chia-Min Hsieh, Krutarth Kamani, Simon Rogers, and Emily Pentzer. Go with the flow: Rheological requirements for direct ink write printability. Journal of Applied Physics, 134(10), 2023.

[251] Amit Rawat, Simerdeep Singh Gupta, Haripriya Kalluri, Michael Lowenborg, Kuljit Bhatia, and Kevin Warner. Rheological characterization in the development of topical drug products. The Role of Microstructure in Topical Drug Product Development, pages 3–45, 2019.

[252] Saheli Chakraborty, Gurmukh K Sethi, Louise Frenck, Alec S Ho, Irune Villaluenga, Hiroshi Wantanabe, and Nitash P Balsara. Effect of yield stress on stability of block copolymer electrolytes against lithium metal electrodes. ACS Applied Energy Materials, 5(1):852–861, 2021.

[253] Alexander Malkin, Valery Kulichikhin, and Sergey Ilyin. A modern look on yield stress fluids. Rheologica Acta, 56:177–188, 2017.

[254] Daniel Bonn, Morton M Denn, Ludovic Berthier, Thibaut Divoux, and Sébastien Manneville. Yield stress materials in soft condensed matter. Reviews of Modern Physics, 89(3):035005, 2017.

[255] Arif Z Nelson, Kenneth S Schweizer, Brittany M Rauzan, Ralph G Nuzzo, Jan Vermant, and Randy H Ewoldt. Designing and transforming yield-stress fluids. Current Opinion in Solid State and Materials Science, 23(5):100758, 2019.

[256] Thomas Gibaud, Catherine Barentin, Nicolas Taberlet, and Sébastien Manneville. Shear-induced fragmentation of laponite suspensions. Soft Matter, 5(16):3026–3037, 2009.

[257] Ratul Dasgupta, H George E Hentschel, Ashwin Joy, and Itamar Procaccia. Shear banding instabilities in amorphous solids: Predicting the yield strain. In AIP Conference Proceedings, volume 1518, pages 162–169. American Institute of Physics, 2013.

[258] Suzanne M Fielding. Shear banding in soft glassy materials. Reports on Progress in Physics, 77(10):102601, 2014.

[259] Joris Sprakel, Stefan B Lindström, Thomas E Kodger, and David A Weitz. Stress enhancement in the delayed yielding of colloidal gels. Physical review letters, 106(24):248303, 2011.

[260] HongRui He, Heyi Liang, Miaoqi Chu, Zhang Jiang, Juan J de Pablo, Matthew V Tirrell, Suresh Narayanan, and Wei Chen. Transport coefficient approach for characterizing nonequilibrium dynamics in soft matter. Proceedings of the National Academy of Sciences, 121(31):e2401162121, 2024.

[261] Ludovic Berthier, Giulio Biroli, M Lisa Manning, and Francesco Zamponi. Yielding and plasticity in amorphous solids. arXiv preprint arXiv:2401.09385, 2024.

[262] Armand Barbot, Matthias Lerbinger, Anael Lemaitre, Damien Vandembroucq, and Sylvain Patinet. Rejuvenation and shear banding in model amorphous solids. Physical Review E, 101(3):033001, 2020.

[263] John Douglas Eshelby. The determination of the elastic field of an ellipsoidal inclusion, and related problems. Proceedings of the royal society of London. Series A. Mathematical and physical sciences, 241(1226):376–396, 1957.

[264] Giorgio Parisi, Itamar Procaccia, Corrado Rainone, and Murari Singh. Shear bands as manifestation of a criticality in yielding amorphous solids. Proceedings of the National Academy of Sciences, 114(22):5577–5582, 2017.

[265] Michio Tateno and Hajime Tanaka. Power-law coarsening in network-forming phase separation governed by mechanical relaxation. Nature communications, 12(1):912, 2021.

[266] KN Pham, G Petekidis, D Vlassopoulos, SU Egelhaaf, WCK Poon, and PN Pusey. Yielding behavior of repulsion-and attraction-dominated colloidal glasses. Journal of Rheology, 52(2):649–676, 2008.

[267] Esmaeel Moghimi and George Petekidis. Mechanisms of two-step yielding in attractive colloidal glasses. Journal of Rheology, 64(5):1209–1225, 2020.

[268] Peter J Lu, Jacinta C Conrad, Hans M Wyss, Andrew B Schofield, and David A Weitz. Fluids of clusters in attractive colloids. Physical review letters, 96(2):028306, 2006.

[269] Thomas Gibaud, Damien Frelat, and Sébastien Manneville. Heterogeneous yielding dynamics in a colloidal gel. Soft Matter, 6(15):3482–3488, 2010.

[270] Jader Colombo and Emanuela Del Gado. Stress localization, stiffening, and yielding in a model colloidal gel. Journal of rheology, 58(5):1089–1116, 2014.

[271] G Foffi, Cristiano De Michele, Francesco Sciortino, and Piero Tartaglia. Arrested phase separation in a short-ranged attractive colloidal system: A numerical study. The Journal of chemical physics, 122(22), 2005.

[272] Misaki Ozawa, Ludovic Berthier, Giulio Biroli, Alberto Rosso, and Gilles Tarjus. Random critical point separates brittle and ductile yielding transitions in amorphous materials. Proceedings of the National Academy of Sciences, 115(26):6656–6661, 2018.

[273] Misaki Ozawa, Ludovic Berthier, Giulio Biroli, and Gilles Tarjus. Rare events and disorder control the brittle yielding of well-annealed amorphous solids. Physical Review Research, 4(2):023227, 2022.

[274] Dennis L Malandro and Daniel J Lacks. Relationships of shear-induced changes in the potential energy landscape to the mechanical properties of ductile glasses. The Journal of chemical physics, 110(9):4593–4601, 1999.

[275] Daniel J Lacks and Mark J Osborne. Energy landscape picture of overaging and rejuvenation in a sheared glass. Physical review letters, 93(25):255501, 2004.

[276] Misaki Ozawa, Ludovic Berthier, Giulio Biroli, and Gilles Tarjus. Role of fluctuations in the yielding transition of two-dimensional glasses. Physical Review Research, 2(2):023203, 2020.

[277] Vitalij Hieronymus-Schmidt, Harald Rösner, Gerhard Wilde, and Alessio Zaccone. Shear banding in metallic glasses described by alignments of eshelby quadrupoles. Physical Review B, 95(13):134111, 2017.

[278] Thomas Gibaud, Thibaut Divoux, and Sébastien Manneville. Nonlinear mechanics of colloidal gels: Creep, fatigue, and shear-induced yielding. In Statistical and Nonlinear Physics, pages 313–336. Springer, 2022.

[279] Guillaume Ovarlez, Stéphane Rodts, Xavier Chateau, and Philippe Coussot. Phenomenology and physical origin of shear localization and shear banding in complex fluids. Rheologica acta, 48(8):831–844, 2009.

[280] Roberto Benzi, Thibaut Divoux, Catherine Barentin, Sébastien Manneville, Mauro Sbragaglia, and Federico Toschi. Unified theoretical and experimental view on transient shear banding. Physical Review Letters, 123(24):248001, 2019.

[281] Deepak Mangal, Mohammad Nabizadeh, and Safa Jamali. Predicting yielding in attractive colloidal gels. Physical Review E, 109(1):014602, 2024.

[282] Francesco Bonacci, Xavier Chateau, Eric M Furst, Julie Goyon, and Anaël Lemaître. Yield stress aging in attractive colloidal suspensions. Physical Review Letters, 128(1):018003, 2022.

[283] Theyencheri Narayanan, William Chèvremont, and Thomas Zinn. Small-angle x-ray scattering in the era of fourth-generation light sources. Journal of Applied Crystallography, 56(4):939–946, 2023.

[284] William Chèvremont, Thomas Zinn, and Theyencheri Narayanan. Improvement of ultra-small-angle xpcs with the extremely brilliant source. Journal of Synchrotron Radiation, 31(1), 2024.

[285] RC Ball and John R Melrose. A simulation technique for many spheres in quasi-static motion under frame-invariant pair drag and brownian forces. Physica A: Statistical Mechanics and its Applications, 247(1-4):444–472, 1997.

[286] Yun Liu, Wei-Ren Chen, and Sow-Hsin Chen. Cluster formation in two-yukawa fluids. The Journal of chemical physics, 122(4), 2005.

[287] Don S Lemons and Paul Langevin. An introduction to stochastic processes in physics. JHU Press, 2002.

[288] Shaohua Shen, Sarah A Lindley, Xiangyan Chen, and Jin Z Zhang. Hematite heterostructures for photoelectrochemical water splitting: rational materials design and charge carrier dynamics. Energy & Environmental Science, 9(9):2744–2775, 2016.

[289] HaRam Kim, Boghos Taslakjian, Sarah Kim, Matthew V Tirrell, and Mustafa O Guler. Therapeutic peptides, proteins and their nanostructures for drug delivery and precision medicine. ChemBioChem, 25(8):e202300831, 2024.

[290] Alexander E Marras, Jeffrey M Ting, Kaden C Stevens, and Matthew V Tirrell. Advances in the structural design of polyelectrolyte complex micelles. The Journal of Physical Chemistry B, 125(26):7076–7089, 2021.

[291] Jizhou Li, Nikhil Sharma, Zhisen Jiang, Yang Yang, Federico Monaco, Zhengrui Xu, Dong Hou, Daniel Ratner, Piero Pianetta, Peter Cloetens, et al. Dynamics of particle network in composite battery cathodes. Science, 376(6592):517–521, 2022.

[292] Cheng Zeng, Jianing Liang, Can Cui, Tianyou Zhai, and Huiqiao Li. Dynamic investigation of battery materials via advanced visualization: from particle, electrode to cell level. Advanced Materials, 34(52):2200777, 2022.

[293] Bart Vorselaars, Alexey V Lyulin, K Karatasos, and MAJ Michels. Non-gaussian nature of glassy dynamics by cage to cage motion. Physical Review E—Statistical, Nonlinear, and Soft Matter Physics, 75(1):011504, 2007.

[294] Zakiya Shireen and Sujin B Babu. Cage dynamics leads to double relaxation of the intermediate scattering function in a binary colloidal system. Soft matter, 14(45):9271–9281, 2018.

[295] Maram Abadi, Maged F Serag, and Satoshi Habuchi. Entangled polymer dynamics beyond reptation. Nature Communications, 9(1):5098, 2018.

[296] Eric J Bailey and Karen I Winey. Dynamics of polymer segments, polymer chains, and nanoparticles in polymer nanocomposite melts: A review. Progress in Polymer Science, 105:101242, 2020.

[297] Igor M Sokolov. Models of anomalous diffusion in crowded environments. Soft Matter, 8(35):9043–9052, 2012.

[298] W Paul. Anomalous diffusion in polymer melts. Chemical Physics, 284(1-2):59–66, 2002.

[299] M Köpf, C Corinth, O Haferkamp, and TF Nonnenmacher. Anomalous diffusion of water in biological tissues. Biophysical journal, 70(6):2950–2958, 1996.

[300] Scott A McKinley, Lingxing Yao, and M Gregory Forest. Transient anomalous diffusion of tracer particles in soft matter. Journal of Rheology, 53(6):1487–1506, 2009.

[301] Ralf Metzler and Joseph Klafter. The random walk's guide to anomalous diffusion: a fractional dynamics approach. Physics reports, 339(1):1–77, 2000.

[302] Luiz Roberto Evangelista and Ervin Kaminski Lenzi. An introduction to anomalous diffusion and relaxation. Springer, 2023.

[303] Arakaparampil M Mathai, Ram Kishore Saxena, and Hans J Haubold. The H-function: theory and applications. Springer Science & Business Media, 2009.

[304] Francesco Mainardi, Gianni Pagnini, and RK Saxena. Fox h functions in fractional diffusion. Journal of computational and applied mathematics, 178(1-2):321–331, 2005.

[305] Hans J Haubold, Arak M Mathai, and Ram K Saxena. Mittag-leffler functions and their applications. Journal of applied mathematics, 2011(1):298628, 2011.

[306] Angel A Tateishi, Haroldo V Ribeiro, and Ervin K Lenzi. The role of fractional time-derivative operators on anomalous diffusion. Frontiers in Physics, 5:52, 2017.

[307] Eric R Weeks and David A Weitz. Subdiffusion and the cage effect studied near the colloidal glass transition. Chemical physics, 284(1-2):361–367, 2002.

[308] Eric R Weeks and DA Weitz. Properties of cage rearrangements observed near the colloidal glass transition. Physical review letters, 89(9):095704, 2002.

[309] Ranko Richert. Dynamics of nanoconfined supercooled liquids. Annual review of physical chemistry, 62(1):65–84, 2011.

[310] Raffaele Pastore, Antonio Coniglio, and Massimo Pica Ciamarra. From cage-jump motion to macroscopic diffusion in supercooled liquids. Soft Matter, 10(31):5724–5728, 2014.

[311] Pedro M Reis, Rohit A Ingale, and Mark D Shattuck. Caging dynamics in a granular fluid. Physical review letters, 98(18):188301, 2007.

[312] G Marty and Olivier Dauchot. Subdiffusion and cage effect in a sheared granular material. Physical review letters, 94(1):015701, 2005.

[313] Nathan C Keim, Joseph D Paulsen, Zorana Zeravcic, Srikanth Sastry, and Sidney R Nagel. Memory formation in matter. Reviews of Modern Physics, 91(3):035002, 2019.

[314] Jaroslav M Ilnytskyi, Marina Saphiannikova, Dieter Neher, and Michael P Allen. Modelling elasticity and memory effects in liquid crystalline elastomers by molecular dynamics simulations. Soft Matter, 8(43):11123–11134, 2012.

[315] Thomas Zinn, Theyencheri Narayanan, Sai Nikhilesh Kottapalli, Johannes Sachs, Thomas Sottmann, and Peer Fischer. Emergent dynamics of light-induced active colloids probed by xpcs. New Journal of Physics, 24(9):093007, 2022.

[316] Jader Colombo, Asaph Widmer-Cooper, and Emanuela Del Gado. Microscopic picture of cooperative processes in restructuring gel networks. Physical review letters, 110(19):198301, 2013.

[317] Jader Colombo and Emanuela Del Gado. Self-assembly and cooperative dynamics of a model colloidal gel network. Soft matter, 10(22):4003–4015, 2014.

[318] Kiril Tsemekhman, Lukasz Goldschmidt, David Eisenberg, and David Baker. Cooperative hydrogen bonding in amyloid formation. Protein science, 16(4):761–764, 2007.

[319] Cristina Toninelli, Giulio Biroli, and Daniel S Fisher. Cooperative behavior of kinetically constrained lattice gas models of glassy dynamics. Journal of statistical physics, 120:167–238, 2005.

[320] Qingteng Zhang, Eric M Dufresne, Pice Chen, Joonkyu Park, Margaret P Cosgriff, Mohammed Yusuf, Yongqi Dong, Dillon D Fong, Hua Zhou, Zhonghou Cai, et al. Thermal fluctuations of ferroelectric nanodomains in a ferroelectric-dielectric pbtio 3/srtio 3 superlattice. Physical review letters, 118(9):097601, 2017.

[321] Marios D Demetriou, John S Harmon, Min Tao, Gang Duan, Konrad Samwer, and William L Johnson. Cooperative shear model for the rheology of glass-forming metallic liquids. Physical Review Letters, 97(6):065502, 2006.

[322] Yi Jiang, Pieter J Swart, Avadh Saxena, Marius Asipauskas, and James A Glazier. Hysteresis and avalanches in two-dimensional foam rheology simulations. Physical Review E, 59(5):5819, 1999.

[323] Pinaki Kumar, Evangelos Korkolis, Roberto Benzi, Dmitry Denisov, André Niemeijer, Peter Schall, Federico Toschi, and Jeannot Trampert. On interevent time distributions of avalanche dynamics. Scientific reports, 10(1):626, 2020.

[324] KL Ngai and RW Rendell. Cooperative dynamics in relaxation: A coupling model perspective. Journal of Molecular Liquids, 56:199–214, 1993.

[325] Götz Jerke, Jan Skov Pedersen, Stefan Ulrich Egelhaaf, and Peter Schurtenberger. Static structure factor of polymerlike micelles: Overall dimension, flexibility, and local properties of lecithin reverse micelles in deuterated isooctane. Physical Review E, 56(5):5772, 1997.

[326] Santosh L Gawali, Mingming Zhang, Sugam Kumar, Debes Ray, Manidipa Basu, Vinod K Aswal, Dganit Danino, and Puthusserickal A Hassan. Discerning the structure factor of charged micelles in water and supercooled solvent by contrast variation x-ray scattering. Langmuir, 35(30):9867–9877, 2019.

[327] Samanvaya Srivastava and Matthew V Tirrell. Polyelectrolyte complexation. Advances in chemical physics, 161:499–544, 2016.

[328] Jing Yu, Jun Mao, Guangcui Yuan, Sushil Satija, Zhang Jiang, Wei Chen, and Matthew Tirrell. Structure of polyelectrolyte brushes in the presence of multivalent counterions. Macromolecules, 49(15):5609–5617, 2016.

[329] Ung-Jin Kim, Jaehyung Park, Chunmei Li, Hyoung-Joon Jin, Regina Valluzzi, and David L Kaplan. Structure and properties of silk hydrogels. Biomacromolecules, 5(3):786–792, 2004.

[330] Jiajun Tian, Ahmad Reza Motezakker, Ruifu Wang, Andrew J Bae, Andrei Fluerasu, Hengwei Zhu, Benjamin S Hsiao, and Tomas Rosén. Probing the self-assembly dynamics of cellulose nanocrystals by x-ray photon correlation spectroscopy. Journal of Colloid and Interface Science, 683:1077–1086, 2025.

[331] Martin Karplus and David L Weaver. Protein-folding dynamics. Nature, 260(5550):404–406, 1976.

[332] Paul CH Li and D Jed Harrison. Transport, manipulation, and reaction of biological cells on-chip using electrokinetic effects. Analytical chemistry, 69(8):1564–1568, 1997.

[333] Mark A Newton. Dynamic adsorbate/reaction induced structural change of supported metal nanoparticles: heterogeneous catalysis and beyond. Chemical Society Reviews, 37(12):2644–2657, 2008.

[334] Peter Wochner, Christian Gutt, Tina Autenrieth, Thomas Demmer, Volodymyr Bugaev, Alejandro Díaz Ortiz, Agnes Duri, Federico Zontone, Gerhard Grübel, and Helmut Dosch. X-ray cross correlation analysis uncovers hidden local symmetries in disordered matter. Proceedings of the National Academy of Sciences, 106(28):11511–11514, 2009.

[335] Ivan A Zaluzhnyy, Ruslan P Kurta, Marcus Scheele, Frank Schreiber, Boris I Ostrovskii, and Ivan A Vartanyants. Angular x-ray cross-correlation analysis (axcca): Basic concepts and recent applications to soft matter and nanomaterials. Materials, 12(21):3464, 2019.

[336] Mark Sutton, Julien RM Lhermitte, Françoise Ehrburger-Dolle, and Frédéric Livet. High resolution strain measurements in highly disordered materials. Physical Review Research, 3(1):013119, 2021.

[337] Léon Van Hove. Correlations in space and time and born approximation scattering in systems of interacting particles. Physical Review, 95(1):249, 1954.

[338] Peter H Poole, Claudio Donati, and Sharon C Glotzer. Spatial correlations of particle displacements in a glass-forming liquid. Physica A: Statistical Mechanics and its Applications, 261(1-2):51–59, 1998.

[339] Indrajit Tah and Smarajit Karmakar. Signature of dynamical heterogeneity in spatial correlations of particle displacement and its temporal evolution in supercooled liquids. Physical Review Research, 2(2):022067, 2020.

[340] Benoit B Mandelbrot and John W Van Ness. Fractional brownian motions, fractional noises and applications. SIAM review, 10(4):422–437, 1968.

[341] Ben O'Shaughnessy and Itamar Procaccia. Analytical solutions for diffusion on fractal objects. Physical review letters, 54(5):455, 1985.

[342] Joseph Klafter, Michael F Shlesinger, and Gert Zumofen. Beyond brownian motion. Physics today, 49(2):33–39, 1996.

[343] Harvey Scher and Melvin Lax. Stochastic transport in a disordered solid. i. theory. Physical Review B, 7(10):4491, 1973.

[344] V Seshadri and Bruce J West. Fractal dimensionality of lévy processes. Proceedings of the National Academy of Sciences, 79(14):4501–4505, 1982.

[345] Constantino Tsallis, Silvio VF Levy, André MC Souza, and Roger Maynard. Statistical-mechanical foundation of the ubiquity of lévy distributions in nature. Physical Review Letters, 75(20):3589, 1995.

[346] Vasudev M Kenkre, Elliot W Montroll, and Michael F Shlesinger. Generalized master equations for continuous-time random walks. Journal of Statistical Physics, 9:45–50, 1973.

[347] Aleksei V Chechkin, Vsevolod Y Gonchar, Joseph Klafter, and Ralf Metzler. Fundamentals of lévy flight processes. Fractals, Diffusion, and Relaxation in Disordered Complex Systems: Advances in Chemical Physics, Part B, pages 439–496, 2006.

[348] Yogesh Kumar, Apeksha Koul, Ruchi Singla, and Muhammad Fazal Ijaz. Artificial intelligence in disease diagnosis: a systematic literature review, synthesizing framework and future research agenda. Journal of ambient intelligence and humanized computing, 14(7):8459–8486, 2023.

[349] Yifang Ma, Zhenyu Wang, Hong Yang, and Lin Yang. Artificial intelligence applications in the development of autonomous vehicles: A survey. IEEE/CAA Journal of Automatica Sinica, 7(2):315–329, 2020.

[350] Miles Cranmer, Alvaro Sanchez Gonzalez, Peter Battaglia, Rui Xu, Kyle Cranmer, David Spergel, and Shirley Ho. Discovering symbolic models from deep learning with inductive biases. Advances in neural information processing systems, 33:17429–17442, 2020.

[351] Xiangyu Ou, Xue Chen, Xianning Xu, Lili Xie, Xiaofeng Chen, Zhongzhu Hong, Hua Bai, Xiaowang Liu, Qiushui Chen, Lin Li, et al. Recent development in x-ray imaging technology: Future and challenges. Research, 2021.

[352] Scott J Adams, Robert DE Henderson, Xin Yi, and Paul Babyn. Artificial intelligence solutions for analysis of x-ray images. Canadian Association of Radiologists Journal, 72(1):60–72, 2021.

[353] Ying Li and Tianle Yue. Machine Learning for Polymer Informatics. American Chemical Society, 2024.

[354] Chengshi Wang, Yeon-Ju Kim, Aikaterini Vriza, Rohit Batra, Arun Baskaran, Naisong Shan, Nan Li, Pierre Darancet, Logan Ward, Yuzi Liu, et al. Autonomous platform for solution processing of electronic polymers. Nature Communications, 16(1):1498, 2025.

[355] Doga Yamac Ozgulbas, Don Jensen Jr, Rory Butler, Rafael Vescovi, Ian T Foster, Michael Irvin, Yasukazu Nakaye, Miaoqi Chu, Eric M Dufresne, Soenke Seifert, et al. Robotic pendant drop: containerless liquid for μs-resolved, ai-executable xpcs. Light: Science & Applications, 12(1):196, 2023.

[356] James P Horwath, Xiao-Min Lin, Hongrui He, Qingteng Zhang, Eric M Dufresne, Miaoqi Chu, Subramanian KRS Sankaranarayanan, Wei Chen, Suresh Narayanan, and Mathew J Cherukara. Ai-nerd: Elucidation of relaxation dynamics beyond equilibrium through ai-informed x-ray photon correlation spectroscopy. Nature Communications, 15(1):5945, 2024.

[357] Theyencheri Narayanan. Recent advances in synchrotron scattering methods for probing the structure and dynamics of colloids. Advances in Colloid and Interface Science, page 103114, 2024.

[358] Zexin Zhang, Peter J Yunker, Piotr Habdas, and AG Yodh. Cooperative rearrangement regions and dynamical heterogeneities in colloidal glasses with attractive versus repulsive interactions. Physical review letters, 107(20):208303, 2011.

[359] Tatiana Konstantinova, Lutz Wiegart, Maksim Rakitin, Anthony M DeGennaro, and Andi M Barbour. Noise reduction in x-ray photon correlation spectroscopy with convolutional neural networks encoder–decoder models. Scientific Reports, 11(1):14756, 2021.

[360] Sonja Timmermann, Vladimir Starostin, Anita Girelli, Anastasia Ragulskaya, Hendrik Rahmann, Mario Reiser, Nafisa Begam, Lisa Randolph, Michael Sprung, Fabian Westermeier, et al. Automated matching of two-time x-ray photon correlation maps from phase-separating proteins with cahn–hilliard-type simulations using auto-encoder networks. Applied Crystallography, 55(4):751–757, 2022.

[361] Miaoqi Chu, Jeffrey Li, Qingteng Zhang, Zhang Jiang, Eric M Dufresne, Alec Sandy, Suresh Narayanan, and Nicholas Schwarz. pyxpcsviewer: an open-source interactive tool for x-ray photon correlation spectroscopy visualization and analysis. Synchrotron Radiation, 29(4):1122–1129, 2022.

[362] Don S Lemons. An introduction to stochastic processes in physics, 2003.

[363] Julien Lhermitte. Using Coherent X Rays to Measure Velocity Profiles. McGill University (Canada), 2015.

[364] Albert Einstein et al. On the motion of small particles suspended in liquids at rest required by the molecular-kinetic theory of heat. Annalen der physik, 17(549-560):208, 1905.

[365] Michael K Hausmann, Patrick A Ruhs, Gilberto Siqueira, Jőrg Läuger, Rafael Libanori, Tanja Zimmermann, and André R Studart. Dynamics of cellulose nanocrystal alignment during 3d printing. ACS Nano, 12(7):6926–6937, 2018.

[366] Matthias Rebber, Malte Trommler, Irina Lokteva, Samanehalsadat Ehteram, Andreas Schropp, Sandra König, Michael Fröba, and Dorota Koziej. Additive-free, gelled nanoinks as a 3d printing toolbox for hierarchically structured bulk aerogels. Advanced Functional Materials, 32(19):2112914, 2022.

[367] Tianhaozhe Sun, Kelin Wang, Takeshi Iinuma, Ryota Hino, Jiangheng He, Hiromi Fujimoto, Motoyuki Kido, Yukihito Osada, Satoshi Miura, Yusaku Ohta, et al. Prevalence of viscoelastic relaxation after the 2011 tohoku-oki earthquake. Nature, 514(7520):84–87, 2014.

[368] Kunimasa Miyazaki, Hans M Wyss, David A Weitz, and David R Reichman. Nonlinear viscoelasticity of metastable complex fluids. Europhysics Letters, 75(6):915, 2006.

[369] Kasper Masschaele, Jan Fransaer, and Jan Vermant. Flow-induced structure in colloidal gels: Direct visualization of model 2d suspensions. Soft Matter, 7(17):7717–7726, 2011.

[370] Simon A Rogers, Dimitris Vlassopoulos, and PT Callaghan. Aging, yielding, and shear banding in soft colloidal glasses. Physical Review Letters, 100(12):128304, 2008.

[371] V Chikkadi, DM Miedema, MT Dang, B Nienhuis, and P Schall. Shear banding of colloidal glasses: Observation of a dynamic first-order transition. Physical Review Letters, 113(20):208301, 2014.

[372] F Livet, F Bley, F Ehrburger-Dolle, I Morfin, E Geissler, and M Sutton. X-ray intensity fluctuation spectroscopy by heterodyne detection. Journal of synchrotron radiation, 13(6):453–458, 2006.

[373] T Srokowski and A Kamińska. Diffusion equations for a markovian jumping process. Physical Review E, 74(2):021103, 2006.

[374] Evgenii B Aleksandrov, Yu M Golubev, Aleksandr Vladimirovich Lomakin, and VA Noskin. Intensity-fluctuation spectroscopy of optical fields with non-gaussian statistics. Soviet Physics Uspekhi, 26(8):643, 1983.

[375] Andrey Markov. Extension of the limit theorems of probability theory to a sum of variables connected in a chain. Dynam Probabilist Syst, 1:552, 1971.

[376] Sydney Chapman and Thomas George Cowling. The mathematical theory of non-uniform gases: an account of the kinetic theory of viscosity, thermal conduction and diffusion in gases. Cambridge university press, 1990.

[377] Immanuel Kalcher and Joachim Dzubiella. Structure-thermodynamics relation of electrolyte solutions. The Journal of chemical physics, 130(13), 2009.

[378] Chris Benmore, Tekin Bicer, Maria KY Chan, Zichao Di, Dog$^{\smile}$ a Gürsoy, Inhui Hwang, Nikita Kuklev, Dergan Lin, Zhengchun Liu, Ihar Lobach, et al. Advancing ai/ml at the advanced photon source. Synchrotron Radiation News, 35(4):28–35, 2022.

[379] J Colmenero, Fl Alvarez, and A Arbe. Self-motion and the α relaxation in a simulated glass-forming polymer: Crossover from gaussian to non-gaussian dynamic behavior. Physical Review E, 65(4):041804, 2002.

[380] Thomas Schäfer and Vladimir Skokov. Dynamics of non-gaussian fluctuations in model a. Physical Review D, 106(1):014006, 2022.

[381] Rémi Busselez, Ronan Lefort, Aziz Ghoufi, Brigitte Beuneu, Bernhard Frick, Frédéric Affouard, and Denis Morineau. The non-gaussian dynamics of glycerol. Journal of Physics: Condensed Matter, 23(50):505102, 2011.

[382] Markus Bier, René van Roij, Marjolein Dijkstra, and Paul van der Schoot. Self-diffusion of particles in complex fluids: temporary cages and permanent barriers. Physical review letters, 101(21):215901, 2008.

[383] Sujata Dhakal, Zehao Chen, Daniel Estrin, and Svetlana Morozova. Spatially-resolved network dynamics of poly (vinyl alcohol) gels measured with dynamic small angle light scattering. Gels, 8(7):394, 2022.

[384] Jin Huang, Yichao Xu, Shuanhu Qi, Jiajia Zhou, Wei Shi, Tianyi Zhao, and Mingjie Liu. Ultrahigh energy-dissipation elastomers by precisely tailoring the relaxation of confined polymer fluids. Nature Communications, 12(1):3610, 2021.

[385] Alberto Dinelli, Jérémy O'Byrne, Agnese Curatolo, Yongfeng Zhao, Peter Sollich, and Julien Tailleur. Non-reciprocity across scales in active mixtures. Nature Communications, 14(1):7035, 2023.

[386] Mauricio Rojas-Vega, Pablo De Castro, and Rodrigo Soto. Wetting dynamics by mixtures of fast and slow self-propelled particles. Physical Review E, 107(1):014608, 2023.

[387] Robert L Leheny. Xpcs: Nanoscale motion and rheology. Current opinion in colloid & interface science, 17(1):3–12, 2012.

[388] BJ Ackerson, PN Pusey, and RJA Tough. Interpretation of the intermediate scattering function at short times. Journal of Chemical Physics, 76(3):1279–1282, 1982.

[389] Bruce J Ackerson. Correlations for interacting brownian particles. Journal of Chemical Physics, 64(1):242–246, 1976.

[390] Étienne Fodor, Cesare Nardini, Michael E Cates, Julien Tailleur, Paolo Visco, and Frédéric Van Wijland. How far from equilibrium is active matter? Physical review letters, 117(3):038103, 2016.

[391] Zhidong Luo, Qi Yue, Xueyuan Li, Yuchen Zhu, Xuzhao Liu, and Lee A Fielding. Polymer-assisted 3d printing of inductor cores. ACS applied materials & interfaces, 2024.

[392] Gautam Das and Soo-Young Park. Liquid crystalline elastomer actuators with dynamic covalent bonding: Synthesis, alignment, reprogrammability, and self-healing. Current Opinion in Solid State and Materials Science, 27(3):101076, 2023.

[393] NJ Wagner and R Klein. The rheology and microstructure of charged colloidal suspensions. Colloid and polymer science, 269:295–319, 1991.

[394] Michael Fahrländer, Matthias Bruch, Tammo Menke, and Christian Friedrich. Rheological behavior of ps-melts containing surface modified pmma-particles. Rheologica acta, 40(1):1–9, 2001.

[395] Andre R Studart, Esther Amstad, and Ludwig J Gauckler. Colloidal stabilization of nanoparticles in concentrated suspensions. Langmuir, 23(3):1081–1090, 2007.

[396] George V Franks, Zhongwu Zhou, Nanda J Duin, and David V Boger. Effect of interparticle forces on shear thickening of oxide suspensions. Journal of Rheology, 44(4):759–779, 2000.

[397] Anh Vu Nguyen Le, Adrien Izzet, Guillaume Ovarlez, and Annie Colin. Solvents govern rheology and jamming of polymeric bead suspensions. Journal of Colloid and Interface Science, 629:438–450, 2023.

[398] Yoram S Papir and Irvin M Krieger. Rheological studies on dispersions of uniform colloidal spheres: Ii. dispersions in nonaqueous media. Journal of Colloid and Interface Science, 34(1):126–130, 1970.

[399] Gerhard Fritz, Volker Schädler, Norbert Willenbacher, and Norman J Wagner. Electrosteric stabilization of colloidal dispersions. Langmuir, 18(16):6381–6390, 2002.

[400] Yunwei Wang, Li Li, Yiming Wang, Qingsong Yang, Zhishuang Ye, Liang Sun, Fan Yang, and Xuhong Guo. Effect of counterions on the interaction among concentrated spherical polyelectrolyte brushes. Polymers, 13(12):1911, 2021.

[401] Robert D Groot. Electrostatic interactions in dissipative particle dynamics—simulation of polyelectrolytes and anionic surfactants. The Journal of chemical physics, 118(24):11265–11277, 2003.

[402] Thibaut Divoux, Vincent Grenard, and Sébastien Manneville. Rheological hysteresis in soft glassy materials. Physical review letters, 110(1):018304, 2013.

[403] Esmaeel Moghimi, Alan R Jacob, Nick Koumakis, and George Petekidis. Colloidal gels tuned by oscillatory shear. Soft Matter, 13(12):2371–2383, 2017.

[404] Stefano Aime, Laurence Ramos, and Luca Cipelletti. Microscopic dynamics and failure precursors of a gel under mechanical load. Proceedings of the National Academy of Sciences, 115(14):3587–3592, 2018.

[405] Mohammad Nabizadeh and Safa Jamali. Life and death of colloidal bonds control the rate-dependent rheology of gels. Nature Communications, 12(1):4274, 2021.

[406] H Hoekstra, Jan Vermant, Joannes Mewis, and GG Fuller. Flow-induced anisotropy and reversible aggregation in two-dimensional suspensions. Langmuir, 19(22):9134–9141, 2003.

[407] F Camerel, Jean-Christophe P Gabriel, P Batail, P Panine, and P Davidson. Combined saxs- rheological studies of liquid-crystalline colloidal dispersions of mineral particles. Langmuir, 19(24):10028–10035, 2003.

[408] G Petekidis, D Vlassopoulos, and PN Pusey. Yielding and flow of sheared colloidal glasses. Journal of physics: Condensed matter, 16(38):S3955, 2004.

[409] Tatjana Sentjabrskaja, Eleftheria Babaliari, Jan Hendricks, Marco Laurati, George Petekidis, and Stefan Ulrich Egelhaaf. Yielding of binary colloidal glasses. Soft Matter, 9(17):4524–4533, 2013.

[410] Joseph Yerushalmi, Stanley Katz, and Reuel Shinnar. The stability of steady shear flows of some viscoelastic fluids. Chemical Engineering Science, 25(12):1891–1902, 1970.

[411] Ewan J Hemingway and Suzanne M Fielding. Interplay of edge fracture and shear banding in complex fluids. Journal of Rheology, 64(5):1147–1159, 2020.

[412] A. P. Thompson, H. M. Aktulga, R. Berger, D. S. Bolintineanu, W. M. Brown, P. S. Crozier, P. J. in 't Veld, A. Kohlmeyer, S. G. Moore, T. D. Nguyen, R. Shan, M. J. Stevens, J. Tranchida, C. Trott, and S. J. Plimpton. LAMMPS - a flexible simulation tool for particle-based materials modeling at the atomic, meso, and continuum scales. Comp. Phys. Comm., 271:108171, 2022.

[413] Donald J Plazek. Dynamic mechanical and creep properties of a 23% cellulose nitrate solution; andrade creep in polymeric systems. Journal of Colloid Science, 15(1):50–75, 1960.

[414] Nayeon Park, Myungjae Lee, Hyunjoon Jung, and Jaewook Nam. Complex rheological response of li-ion battery anode slurries. Journal of Power Sources, 608:234607, 2024.

[415] Masahiko Ishii and Hiroshi Nakamura. Influence of molecular weight and concentration of carboxymethyl cellulose on rheological properties of concentrated anode slurries for lithium-ion batteries. JCIS Open, 6:100048, 2022.

[416] Srini Raghavan, Manish Keswani, and Renhe Jia. Particulate science and technology in the engineering of slurries for chemical mechanical planarization. KONA Powder and Particle Journal, 26:94–105, 2008.

[417] Catherine Tom, Surya Narayana Sangitra, and Ravi Kumar Pujala. Rheological fingerprinting and applications of cellulose nanocrystal based composites: A review. Journal of Molecular Liquids, 370:121011, 2023.

[418] Dhriti Khandal, Bernard Riedl, Jason R Tavares, Pierre J Carreau, and Marie-Claude Heuzey. Tailoring cellulose nanocrystals rheological behavior in aqueous suspensions through surface functionalization with polyethyleneimine. Physics of Fluids, 31(2), 2019.

[419] MASR Saadi, Alianna Maguire, Neethu T Pottackal, Md Shajedul Hoque Thakur, Maruf Md Ikram, A John Hart, Pulickel M Ajayan, and Muhammad M Rahman. Direct ink writing: a 3d printing technology for diverse materials. Advanced Materials, 34(28):2108855, 2022.

[420] Hao Chang, Pan Zhang, Rui Guo, Yuntao Cui, Yi Hou, Ziqiao Sun, and Wei Rao. Recoverable liquid metal paste with reversible rheological characteristic for electronics printing. ACS applied materials & interfaces, 12(12):14125–14135, 2020.

[421] Joel Ming Rui Tan, Yousef Farraj, Alexander Kamyshny, and Shlomo Magdassi. Fabrication approaches of soft electronics. ACS Applied Electronic Materials, 5(3):1376–1393, 2023.

[422] D Richard, Misaki Ozawa, S Patinet, E Stanifer, B Shang, SA Ridout, B Xu, G Zhang, PK Morse, J-L Barrat, et al. Predicting plasticity in disordered solids from structural indicators. Physical Review Materials, 4(11):113609, 2020.

[423] Ratul Dasgupta, H George E Hentschel, and Itamar Procaccia. Yield strain in shear banding amorphous solids. Physical Review E—Statistical, Nonlinear, and Soft Matter Physics, 87(2):022810, 2013.

[424] Andrea Ninarello, Ludovic Berthier, and Daniele Coslovich. Models and algorithms for the next generation of glass transition studies. Physical Review X, 7(2):021039, 2017.

[425] Joseph Pollard and Suzanne M Fielding. Yielding, shear banding, and brittle failure of amorphous materials. Physical Review Research, 4(4):043037, 2022.

[426] Hugh J Barlow, James O Cochran, and Suzanne M Fielding. Ductile and brittle yielding in thermal and athermal amorphous materials. Physical Review Letters, 125(16):168003, 2020.

[427] Hanyi Yu, Sung Bo Yoon, Robert Kauffman, Jens Wrammert, Adam Marcus, and Jun Kong. Non-gaussian models for object motion analysis with time-lapse fluorescence microscopy images. Modern Statistical Methods for Health Research, pages 15–41, 2021.

[428] Erica J Saltzman and Kenneth S Schweizer. Large-amplitude jumps and non-gaussian dynamics in highly concentrated hard sphere fluids. Physical Review E—Statistical, Nonlinear, and Soft Matter Physics, 77(5):051504, 2008.

[429] Dieter Ammon. Approximation and generation of gaussian and non-gaussian stationary processes. Structural Safety, 8(1-4):153–160, 1990.

[430] Ada Altieri, Pierfrancesco Urbani, and Francesco Zamponi. Microscopic theory of two-step yielding in attractive colloids. Physical review letters, 121(18):185503, 2018.